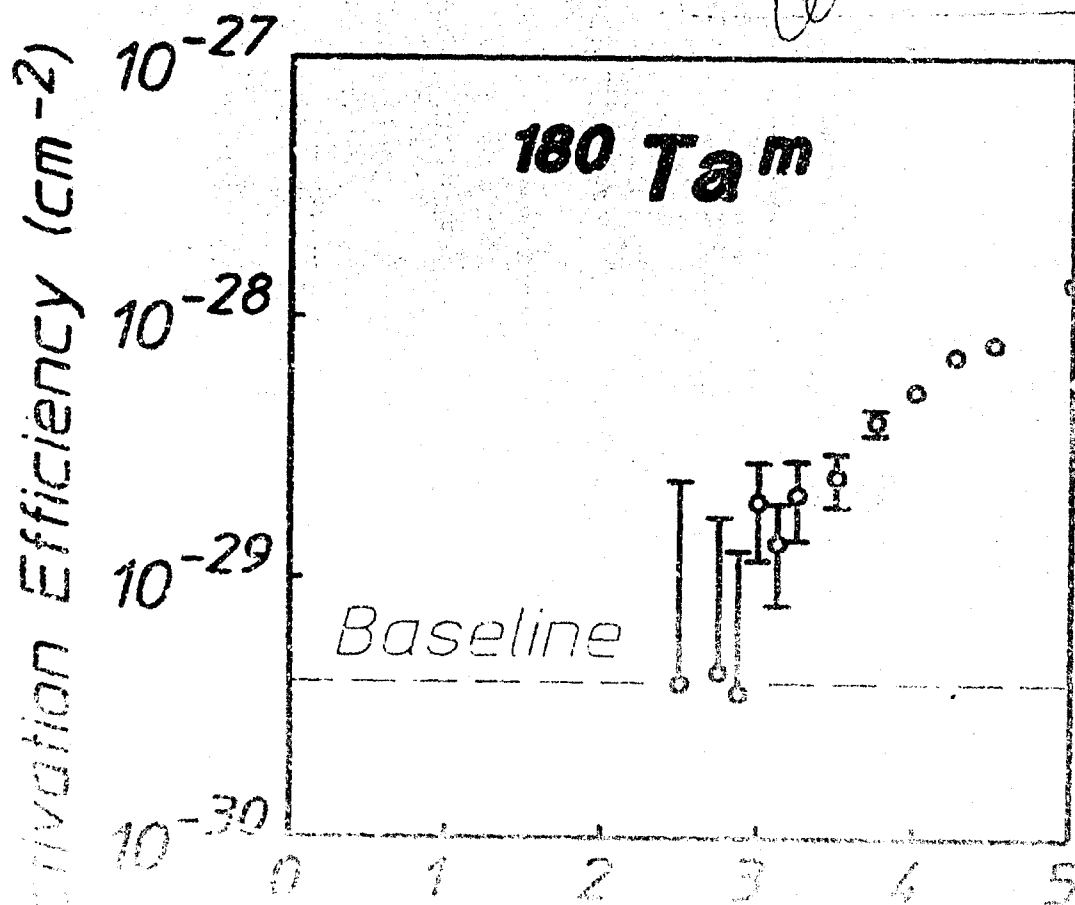


The University of Texas at Dallas
Center for Quantum Electronics
The Gamma-Ray Laser Project
Final Technical Report
1986 - 1989

AD-A219 972



Report GPL/8903

PROOF OF THE FEASIBILITY
OF COHERENT AND INCOHERENT SCHEMES
FOR PUMPING A GAMMA-RAY LASER

Principal Investigator: Carl B. Collins
The University of Texas at Dallas
Center for Quantum Electronics
P.O. Box 830688
Richardson, Texas 75083-0688

March 1990

Final Technical Report
26 September 1986 through 24 December 1989
Contract Number N00014-86-C-2488

This document has been approved
for public release and sale;
its distribution is unlimited.



Prepared for
INNOVATIVE SCIENCE AND TECHNOLOGY DIRECTORATE
OF STRATEGIC DEFENSE INITIATIVE ORGANIZATION

Contracting Officer's Technical Representative
Dr. Paul Kepple, Code 4720
Naval Research Laboratory
4555 Overlook Avenue, SW
Washington, DC 20375-5000

Accession For	
NTIS	QA&I
DTIC TAB	<input checked="" type="checkbox"/>
Unclassified	<input type="checkbox"/>
Justification	
By _____	
Distribution/	
Availability Codes	
Avail and/or	
Dist	Special
A-1	

Reproduction in whole, or in part, is permitted for
any purpose of the United States Government.

REPORT DOCUMENTATION PAGE		READ INSTRUCTIONS BEFORE COMPLETING FORM
1. REPORT NUMBER GRL/8903	2. GCOV ACCESION NO	3. RECIPIENT'S CATALOG NUMBER
4. TITLE (and Subtitle) PROOF OF THE FEASIBILITY OF COHERENT AND INCOHERENT SCHEMES FOR PUMPING A GAMMA-RAY LASER		5. TYPE OF REPORT & PERIOD COVERED Final Technical 9/26/86 - 12/24/89
7. AUTHOR(s) C. B. COLLINS		6. PERFORMING ORG. REPORT NUMBER N00014-86-C-2488
9. PERFORMING ORGANIZATION NAME AND ADDRESS University of Texas at Dallas Center for Quantum Electronics P.O. Box 830688 Richardson, TX 75083-0688		10. PROGRAM ELEMENT, PROJECT, TASK AREA & WORK UNIT NUMBERS
11. CONTROLLING OFFICE NAME AND ADDRESS INNOVATIVE SCIENCE AND TECHNOLOGY DIRECTORATE OF STRATEGIC DEFENSE INITIATIVE ORGANIZATION		12. REPORT DATE March 1990
14. MONITORING AGENCY NAME & ADDRESS (if different from Controlling Office) Dr. Paul Kepple Naval Research Laboratory, Code 4720 4555 Overlook Avenue, SW Washington, DC 20375-5000		15. SECURITY CLASS. (of this report) Unclassified
16. DISTRIBUTION STATEMENT (of the Report) This document has been approved for public release and sale; its distribution is unlimited.		15a. DECLASSIFICATION/DOWNGRADING SCHEDULE
17. DISTRIBUTION STATEMENT (of the abstract entered in Block 20, if different from Report)		
18. SUPPLEMENTARY NOTES		
19. KEY WORDS (Continue on reverse side if necessary and identify by block number) Gamma-ray laser, Ultrashort wavelength laser		
20. ABSTRACT (Continue on reverse side if necessary and identify by block number) Recent approaches to the problem of the gamma-ray laser have focused upon upconversion techniques in which metastable nuclei are pumped with long wavelength radiation. At the nuclear level the storage of energy can approach tera-Joules (10^{12} J) per liter for thousands of years. However, any plan to use such a resource for a gamma-ray laser poses (continue on next page)		

TABLE OF CONTENTS

PREFACE	i
MAJOR MILESTONE REPORT (June 1, 1988)	iii
MAJOR MILESTONE REPORT (June 30, 1988)	v
MAJOR MILESTONE REPORT (March 21, 1989)	vii
MAJOR MILESTONE REPORT (November 23, 1989)	ix
→ THERMAL ECONOMY OF A GAMMA-RAY LASER by C. B. Collins	1 Gomaa, gomaa'
→ PHOTOEXCITATION OF NUCLEAR ISOMERS BY (γ,γ) REACTIONS by J. J. Carroll, M. J. Byrd, D. G. Richmond, T. W. Sinor, K. N. Taylor, W. L. Hodge, Y. Paiss, C. D. Eberhard, J. A. Anderson, and C. B. Collins University of Texas at Dallas	15
E. C. Scarbrough and P. P. Antich University of Texas Southwestern Medical Center	
F. J. Agee, D. Davis, G. A. Huttlin, K. G. Kerris, M. S. Litz, and D. A. Whittaker Aurora Simulator Facility, Harry Diamond Laboratories	
→ ADAPTATION OF A FIXED ENERGY ELECTRON ACCELERATOR TO PRODUCE VARIABLE ENDPOINT BREMSSTRAHLUNG by M. J. Byrd, J. J. Carroll, and C. B. Collins University of Texas at Dallas	63
→ DETERMINATION OF GATEWAY STATES IN ^{197}Au WITH A COMPTON x-RAY SPECTROMETER by C. D. Eberhard, J. A. Anderson, M. J. Byrd, J. J. Carroll, and C. B. Collins University of Texas at Dallas	87
LIST OF DISSERTATIONS PRODUCED UNDER THIS CONTRACT	115
APPENDIX Reprints of articles published during this Contract	117
→ "Calibration of Pulsed Bremsstrahlung Spectra with Photo-nuclear Reactions of ^{75}Se and ^{79}Br ," by J. A. Anderson and C. B. Collins, Rev. Sci. Instrum. 58, 2157-2160 (1987).	
→ "Scaling to High Average Powers of a Flash X-Ray Source Producing Nanosecond Pulses," by F. Davanloo, T. S. Bowen, and C. B. Collins, Rev. Sci. Instrum. 58, 2103-2109 (1987).	
→ "Frequency Modulation Spectrometer for Mössbauer Studies," by P. W. Reittinger, T. W. Sinor, S. S. Wagal, and C. B. Collins, Rev. Sci. Instrum. 59, 362-367 (1987).	
→ "Calibration of Pulsed X-Ray Spectra," by J. A. Anderson and C. B. Collins, Rev. Sci. Instrum. 59, 414-419 (1987).	

"Depopulation of the Isomeric State $^{180}\text{Ta}^m$ by the Reaction $^{180}\text{Ta}^m(\gamma, \gamma')^{180}\text{Ta}$," by C. B. Collins, C. D. Eberhard, J. W. Glesener, and J. A. Anderson, Phys. Rev. C 37, 2267-2269 (1988).

"Diamond-like Carbon Films Prepared with a Laser Ion Source," by S. S. Wagal, E. M. Juengerman, and C. B. Collins, Appl. Phys. Lett. 53, 187-188 (1988).

"Activation of $^{115}\text{In}^m$ by Single Pulses of Intense Bremsstrahlung," by C. B. Collins, J. A. Anderson, Y. Paiss, C. D. Eberhard, R. J. Peterson, and W. L. Hodge, Phys. Rev. C 38, 1852-1856 (1988).

"Flash X-Ray Source Excited by Stacked Blumlein Generators," by F. Davanloo, J. J. Coogan, T. S. Bowen, R. K. Krause, and C. B. Collins, Rev. Sci. Instrum. 59, 2260-2264 (1988).

"Activation of $^{111}\text{Cd}^m$ by Single Pulses of Intense Bremsstrahlung," by J. A. Anderson, M. J. Byrd, and C. B. Collins, Phys. Rev. C 38, 2838-2842 (1988).

"Comment on 'Mössbauer Sidebands from a Single Parent Line,'" by C. B. Collins, P. W. Reittinger, and T. W. Sinor, Phys. Rev. B 39, 9655-9659 (1989).

"Large Scale Effects of the Magnetic Phase Modulation of Recoilless Gamma Transitions," by T. W. Sinor, P. W. Reittinger, and C. B. Collins, Phys. Rev. Lett. 62, 2547-2551 (1989).

"Laser Plasma Source of Amorphic Diamond," by C. B. Collins, F. Davanloo, E. M. Juengerman, W. R. Osborn, and D. R. Jander, Appl. Phys. Lett. 54, 216-218 (1989).

"Mössbauer Isomer Shift Measurements without Mechanical Tuning," by T. W. Sinor, P. W. Reittinger, and C. B. Collins, Rev. Sci. Instrum. 60, 3258-3261 (1989).

"Accelerated Decay of $^{180}\text{Ta}^m$ and ^{176}Lu in Stellar Interiors through (γ, γ') Reactions," by J. J. Carroll, J. A. Anderson, J. W. Glesener, C. D. Eberhard, and C. B. Collins, Astrophys. J. 344, 454-459 (1989).

PREFACE

The dramatic successes enjoyed in this project over the past four years have tended to emphasize the approach to the gamma-ray laser that depends upon incoherent pumping. We first reported the giant resonance for the dumping of the $^{180}\text{Ta}^m$ isomer by pumping samples with flash x-rays of relatively modest intensities from a 6 MeV linac in a scheme which is the nuclear analog of the ruby laser. This particular material, the worst of the 29 actual candidates for a gamma-ray laser, showed the largest integrated cross section ever reported for interband transfer in any nuclear material, $4 \times 10^{-22} \text{ cm}^2 \text{ eV}$. This was an enormous value for bandwidth funneling to a fluorescent level, corresponding to about 0.5 eV of useful width for the absorption of the pump x-rays.

Subsequent studies showed that these giant pumping resonances occur with a gratifying frequency throughout the table of nuclides. Concern had first arisen that these seemingly favorable structures might lie at high energies of excitation near the threshold for neutron evaporation, and so be associated in some way with the high density of nuclear states expected there. This has not proven to be the case. The definitive experimental series culminated in a major milestone achievement in which nineteen isomers were successfully pumped with the bremsstrahlung from a 4 MeV linac. The density of nuclear states near 4 MeV should be exponentially reduced from values expected near 6 MeV, and yet most isomers were excited with comparable efficiencies by linacs operated at the two energies. The two poorest of the 29 candidates for a gamma-ray laser, $^{180}\text{Ta}^m$ and $^{123}\text{Te}^m$, showed the least variation in excitation when the end point of the bremsstrahlung was lowered from 6 to 4 MeV. Still, no other candidates are available, but results for these two would encourage expectations that the great width associated with pumping candidate isomers is concentrated at relatively few discrete transition energies. As usual with these experiments, no significant contributions were made by spurious neutrons evaporated from environmental materials.

The inability to vary the spectrum of the x-rays pumping the isomers generally prevented us from locating the precise energies necessary to excite the giant resonances. Just at the end of this contract we obtained access to the only linac with a variable endpoint energy and enough intensity, the superconducting injector to the storage ring at Darmstadt in West Germany. By setting the endpoint energy of the bremsstrahlung to successively higher values, the sudden increase in activation of a sample could be clearly seen when the giant pumping resonance was reached. The resulting data are shown on the cover of

this report. Analyses concluded after the end of this contract showed that the sudden onset of the dumping of $^{180}\text{Ta}^m$ occurred through two gateways. The lowest opened at 2.8 MeV with an integrated cross section of 17,000 on the usual scale ($\times 10^{-29} \text{ cm}^2 \text{ keV}$) where 10 describes a fully allowed process and the other was accessed at 3.6 MeV through a cross section of 57,000.

So much attention has been paid to the direct approach to the pumping of a gamma-ray laser that it has tended to eclipse the sustained progress enjoyed in our other approaches. One of the most difficult breakthroughs was realized in the last year along the more complex direction of coherent pumping. In this process the intent is to mix the quantum properties of long-lived nuclear states with those able to radiate freely. In this way the metastability of an isomeric state could be "switched off." The critical experiment was to show that some laboratory level coherent input power can affect the properties of a nuclear level. Reported recently in Phys. Rev. Lett. was the demonstration that large levels of modulation of the phases of nuclear states can be obtained with relatively modest input powers.

As has been the case since 1982, there are still no known factors which inhibit the realization of a gamma-ray laser. Neither the level of pump fluence required for laser threshold nor the waste heat to reject presents any particular problem in idealized materials. A gamma-ray laser is feasible if the right combination of energy levels occurs in some real material. When actually tested, the two poorest of the 29 candidate nuclei did surprisingly well, performing 1,000 to 10,000 times better than expected. The overriding question in resolving the feasibility of the nuclear analog to the ruby laser is whether or not one of the better of the 29 has its isomeric level in a position sufficiently near the ideal.

This final report has been prepared from three components. First are the reports of major milestone achievements realized under this contract, followed by the individual articles elaborating upon results that have not yet been published in technical journals. Finally, in the Appendix are found reprints of those results already appearing in the reviewed journals. In this regard, I wish to thank again all our staff for their splendid efforts in supporting the preparation of these manuscripts to a rather demanding timetable.

- C. B. Collins, Director
- Center for Quantum Electronics

MAJOR MILESTONE REPORT

Strengthening the Feasibility of the Tuning and Stimulation of Nuclear Radiation

June 1, 1988

C. B. Collins, Center for Quantum Electronics, University of Texas at Dallas

Achievement

Tunable sidebands have been produced on gamma-ray transitions by directly modulating the phases of nuclear states at levels far exceeding any noise contributed by magnetoacoustic effects.

Technical Background

The approach to the gamma-ray laser with the greatest potential efficiency depends upon the mixing of nearly resonant nuclear states with interaction energies developed by the external modulation of the hyperfine fields. In this way stored isomeric populations could be dumped into freely radiating states.

The first milestone would be a demonstration that significant interaction energies can be developed at the nuclear level by externally applied fields. Overseas efforts have shown that a magnetic field oscillating at radiofrequencies can directly modulate the phase of a nuclear state by coupling to its magnetic moment. In the frequency domain such modulation is observed as sidebands on gamma-ray transitions originating on the state, but the effect is very small at all reasonable levels of applied power.

The conceptual key to thousandfold enhancements lies in the use of small fields to manipulate the greater magnetic fields arising from the natural correlations of individual magnons in ferromagnetic materials. For several years we have observed the production of sidebands to Mössbauer transitions on such a large scale in ferromagnetic materials, but the concern has lingered that the dominant effect might have actually arisen from periodic Doppler shifts produced by vibrations in the host lattice driven by magnetostriction.

Report

As a basis for comparison, sidebands were excited on the unsplit absorption transition of ^{57}Fe nuclei at 14.4 keV in a stainless steel foil by sinusoidal vibrations injected with a piezoelectric source as shown in Fig. 1a. In the usual longitudinal geometry for a transmission experiment a convenient level of input power produced a reference level of sideband development in which the 4th order contained 20% of the intensity remaining in the parent line. In the transverse geometry the effect of phonons transported in the foil about 1 cm around a bend of 90 degrees could not be detected, even with a tenfold increase in power above the reference level.

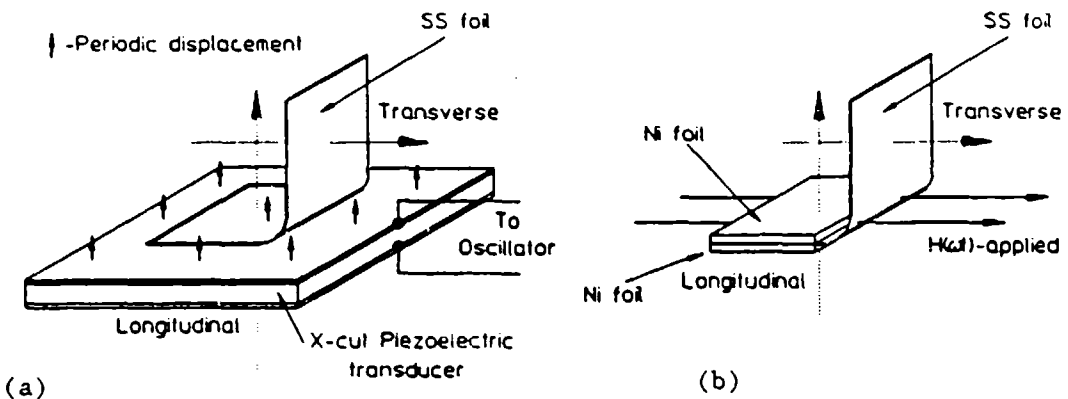


Figure 1: Schematic representation of the mounting of the enriched stainless steel foil 2.5 μm thick used in these transmission experiments. The vectors of the propagation of the gammas from sources to detectors are shown by the dotted arrows for the longitudinal and transverse arrangements shown.

a) (left) Sidebands driven by phonons from an X-cut quartz crystal.
 b) (right) Sidebands driven by the oscillating magnetization of the two Ni foils immersed in the applied H field shown.

Replacing the piezoelectric source with a pair of 2.5 μm foils of ferromagnetic Ni sinusoidally magnetized as shown in Fig. 1b, gave the opportunity to launch what we believe are large amplitude spin waves into the magnon fluid in the paramagnetic stainless foil. Boundary effects known as flux refractions favor the transfer of ferromagnetic magnetization of the Ni across the interface where it can serve as a source term for local alignment of the magnons in the stainless foil. The longitudinal geometry was used to set the same reference level of sideband development at the source. In the transverse geometry at this same level of input power, the first order sidebands were found to have 20% of the intensity of the parent line, a level 10 times the threshold for detection and hence, 100 times any component contributed by acoustic phonons.

Significance

There is a twofold significance to this major milestone experiment.

- 1) In stainless steel spin waves can be transported more efficiently than phonons, thus providing a means for studying the direct modulation of nuclear states in an environment free from acoustic noise.
- 2) Even with transport the intensities of magnetic sidebands are greatly enhanced by ferromagnetic sources meaning that relatively large interaction energies can be developed at the nuclear level with modest applied powers.

MAJOR MILESTONE REPORT

Strengthening the Feasibility of a Gamma-Ray Laser

June 30, 1988

C. B. Collins, Center for Quantum Electronics, University of Texas at Dallas

Achievements

Giant resonances for pumping isomeric nuclei with flash x-rays have been found in many isotopes, but the best x-ray energies for exciting them have been impossible to determine. Now, one has been located in a demonstration nucleus with an enormous cross section at a practical value of x-ray energy.

Technical Background

The nuclear analog of the ruby laser embodies the simplest concepts for a gamma-ray laser. Not surprisingly, the greatest rate of achievement in the quest for a subAngstrom laser continues in that direction. For ruby the identification and exploitation of a bandwidth funnel were the critical keys in the development of the first laser. There was a broad absorption band linked through efficient cascading to the narrow laser level.

Recently we reported a major milestone which showed that comparable structure existed at the nuclear scale in the first of the 29 candidate isomers available for tests, $^{180}\text{Ta}^m$. Populations of the isomer were successfully pumped down with flashes of x-rays absorbed through an astonishingly large cross section of 40,000 on the usual scale ($\times 10^{-29} \text{ cm}^2 \text{ keV}$) where 10 describes a fully allowed process. Then we discovered that these giant funnels for pumping isomers occurred rather frequently. We found them in the second of the 29 candidates, $^{123}\text{Te}^m$, as well as in other demonstration nuclei such as ^{197}Au and ^{195}Pt . However, until now, no experiment could pinpoint the location of such giant resonances in the scheme of energy levels for any nucleus.

Reported here is success in locating at 2600 keV the giant resonance for pumping $^{197}\text{Au}^m$ with flash x-rays through an integrated cross section of 3700 units. Another discrete resonance was found at a more difficult energy of 4800 keV, but it had an even larger cross section of 100,000 units.

Report

The inability to vary the spectrum of the x-rays pumping the isomers had previously prevented us from locating the precise energy necessary to reach the giant resonances. The spectrum of intensities normally used is the bremsstrahlung from a 6 MeV linac shown in Fig. 1 by the solid curve. In this major milestone experiment we obtained other spectral distributions from the Compton scattering of those primary x-rays through different angles. One example is shown in Fig. 1 by the dotted curve.

Samples of gold foils were run in pneumatic shuttles through the scattered x-rays and into the well of a NaI(Tl) crystal where the $^{197}\text{Au}^m$ nuclei were detected by the emission of fluorescent photons. The unique combination of a short lifetime for the isomer and a giant resonance for pumping it enabled us to obtain statistically significant numbers of fluorescent photons from such a weakened pump source as resulted from the Compton scattering.

Previously we had reported a simple procedure for obtaining possible values of integrated cross sections for pumping isomers as functions of the energy at which the gateway state might be assumed to lie. Used upon the yields of $^{197}\text{Au}^m$, we got a different curve of cross section as a function of energy for each of the five angles at which scattered radiation could be accessed. Such curves should pass through points corresponding to real gateway states and the intersection of two is shown in Fig. 2. The other three curves crossed at the higher energy gateway.

Significance

There is a threefold significance to this milestone result.

- 1) The giant resonance in ^{197}Au for bandwidth funneling to the isomer is the largest ever demonstrated below 3 MeV. The previous record had been the 430 unit cross section found in ^{87}Sr in 1967 at 2.7 MeV. It had been considered anomalous, being 10 X larger than all others.
- 2) This first giant funnel to be located in energy was found at a value comparable to the excitation energies of some of the higher lying isomers. This shows that the accidental resonance of such an ideal pumping level and an isomer is possible.
- 3) The strength of this giant resonance for pumping was concentrated at a discrete energy rather than being distributed at a low level over the whole continuum. This makes it much easier to pump the nuclear levels in one layer while passing the waste heat into another for disposal.

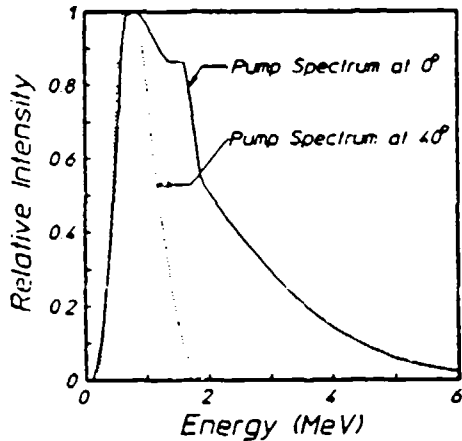


Figure 1: Two of the five spectra available for pumping $^{197}\text{Au}^m$ in this experiment. The solid curve describes the unscattered bremsstrahlung from the 6 MeV linac and the dotted curve plots the intensities computed to be present after scattering through 40° by an iron cylinder 25 mm in diameter and 25 mm long.

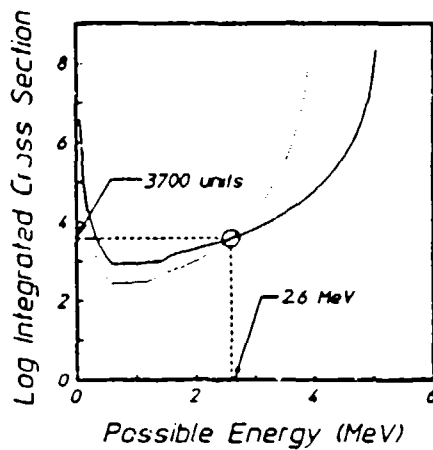


Figure 2: Integrated cross sections for the (γ, γ') reactions pumping $^{197}\text{Au}^m$ through an unknown gateway state as functions of the energies at which they could be assumed to lie. Units are $10^{-29} \text{ cm}^2 \text{ keV}$. Dotted and solid curves plot results obtained with radiation scattered through 24° and 16° , respectively. The intersection locates the new gateway.

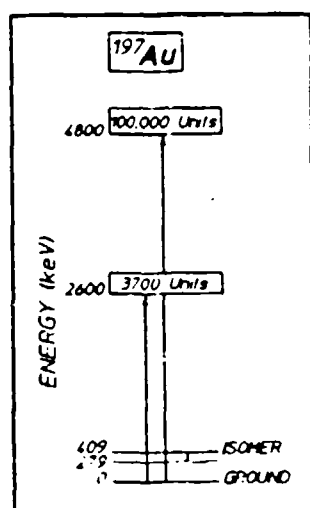


Figure 3: Energy level diagram of the newly discovered states dominating the production of the isomer, $^{197}\text{Au}^m$. The great widths of these resonances are indicated schematically by the widths of the rectangles and the actual cross sections are given for excitation by the transitions represented by the upward arrows. The downward arrow locates a transition useful in the detection of the isomer.

MAJOR MILESTONE REPORT

Strengthening the Feasibility of a Gamma-Ray Laser

March 21, 1989

C. B. Collins, Center for Quantum Electronics, University of Texas at Dallas

Achievement

Discovered in the first two of the 29 candidate isomers to be tested for a gamma-ray laser were giant pumping resonances which enabled performances to approach the ideal when used with hard x-ray pump sources. Now, these same resonances have been excited with much softer x-rays emitted by a 4 MeV linac.

Technical Background

The nuclear analog of the ruby laser embodies the simplest concepts for a gamma-ray laser. Not surprisingly, the greatest rate of achievement in the quest for a subAngstrom laser continues in that direction. For ruby the identification and exploitation of a bandwidth funnel were the critical keys in the development of the first laser. There was a broad absorption band linked through efficient cascading to the narrow laser level.

Last year we reported a major milestone which showed that comparable structure existed at the nuclear scale in the first of the 29 candidate isomers available for testing, $^{180}\text{Ta}^m$. Populations of the isomer were successfully pumped down with flashes of x-rays absorbed through an astonishingly large cross section of 40,000 on the usual scale ($\times 10^{-29} \text{ cm}^2 \text{ keV}$) where 10 describes a fully allowed process. This corresponded to a partial width for useful absorption of 0.5 eV, even better than what had been assumed for idealized nuclei. Then we discovered that these giant funnels for pumping isomers occurred rather frequently. We found them in the second of the 29 candidates, $^{123}\text{Te}^m$, as well as in other demonstration nuclei such as ^{197}Au and ^{195}Pt . However, until now, no experiment could pinpoint the location of such giant resonances in the scheme of energy levels for any of the candidate isomers nor determine whether they lay at small enough energies to be practical.

Reported here is success in pumping the two candidate isomers, $^{180}\text{Ta}^m$ and $^{123}\text{Te}^m$ with a 4 MeV linac through the same giant gateways that had been previously accessed with a 6 MeV device.

Report

The inability to vary the spectrum of the x-rays pumping the isomers generally prevent us from locating the precise energies necessary to reach the giant resonances. The spectrum of intensities previously used was the bremsstrahlung from a 6 MeV linac shown in Fig. 1. In this major milestone experiment we obtained another spectral distribution as seen in Fig. 1 from a 4 MeV linac.

Samples with relatively short-lived signatures were run in pneumatic shuttles through the linac x-rays and into the well of a NaI(Tl) crystal where the pumped nuclei were detected. Materials with longer-lived signatures were simply carried to the counting chamber after the pumping terminated. Some non-candidate control nuclei, such as ^{77}Se and ^{89}Y , could only be activated through giant resonances by the 6 MeV linac. However, to within uncertainties in the spectral intensities from the two sources the same levels of activation per unit dose were found in changing from one linac to the other for both the candidates, ^{180}Ta and ^{123}Te . This means that the giant resonances for pumping those two candidates lie at the lower energies common to both pump sources.

Significance

There is a threefold significance to this milestone result.

- 1) The giant resonances for pumping the candidate isomers $^{180}\text{Ta}^m$ and $^{123}\text{Te}^m$ can be reached at gateway energies well below 4 MeV. These candidates have the largest integrated cross sections for pumping with x-rays ever found below 4 MeV in any nuclei.
- 2) Concern had lingered that the giant pumping resonances previously found with the 6 MeV linac might need the full 6 MeV of energy for excitation. At such values the density of states is high and the onset of evaporation of particles from nuclei is near. Either would make the resonances useless to laser development but neither detrimental effect can occur at energies as low as 4 MeV.
- 3) The two poorest of the 29 candidates are the only ones available for testing and they continue to outperform even the most optimistic expectations. The likelihood for the full feasibility of one of the better candidates continues to be raised by the successes enjoyed with the least attractive of the 29 candidates.

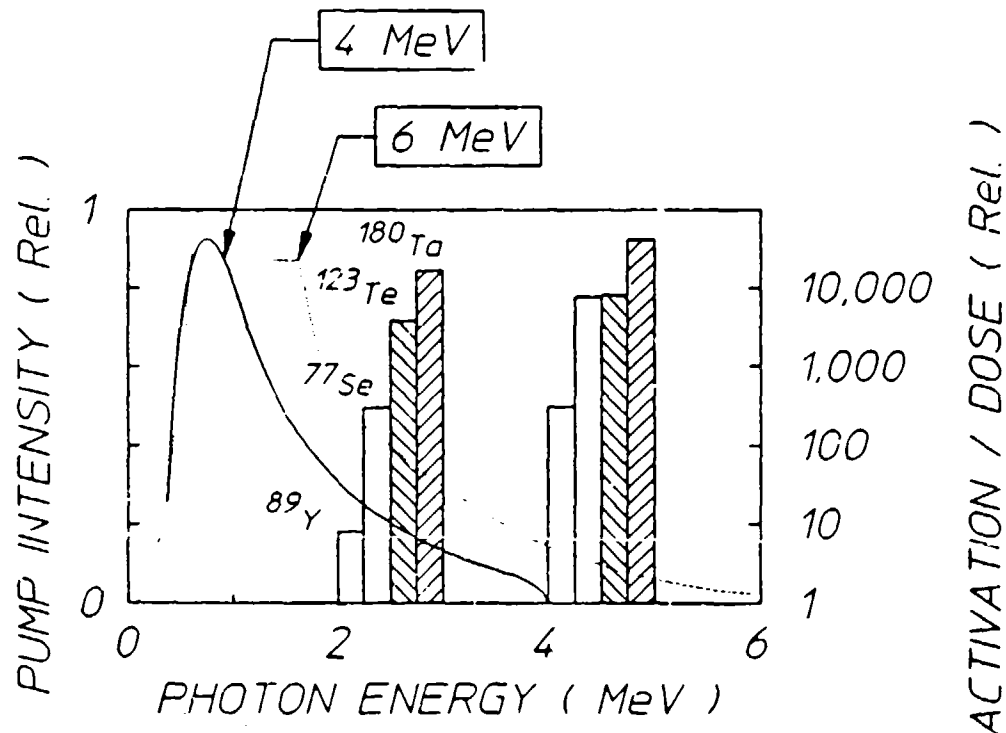


Figure 1: Solid and dotted curves plot the relative spectral intensities in photons/cm²/keV/sec as functions of photon energies that are expected from the two linac sources identified by the endpoint energies used in these experiments. Bars plot the isomeric activation, or deactivation in the case of $^{180}\text{Ta}^m$, on the rightmost scale as determined from the nuclear fluorescence observed after pumping with x-rays from the linacs. The leftmost set of bars give results from the 4 MeV linac and the rightmost were obtained with the 6 MeV source. Precise values of the gateway energies remain unknown and the placement of the bars is only to indicate that they lie below 4 or 6 MeV, respectively. Hatched bars identify actual candidate isomers and open bars pertain to non-candidate comparison nuclides.

MAJOR MILESTONE REPORT

Strengthening the Feasibility of a Gamma-Ray Laser

November 23, 1989

C. B. Collins, Center for Quantum Electronics, University of Texas at Dallas

Achievement

Giant resonances for pumping isomeric nuclei with flash x-rays have been found in many isotopes, but the best x-ray energies for exciting them have been impossible to determine. Now, one has been pinpointed at the ideal energy for pumping the first candidate isomer available for testing.

Technical Background

The nuclear analog of the ruby laser embodies the simplest concepts for a gamma-ray laser. Not surprisingly, the greatest rate of achievement in the quest for a subAngstrom laser continues in that direction. For ruby the identification and exploitation of a bandwidth funnel were the critical keys in the development of the first laser. There was a broad absorption band linked through efficient cascading to the narrow laser level.

Last year we reported a major milestone which showed that comparable structure existed at the nuclear scale in the first of the 29 candidate isomers available for tests, $^{180}\text{Ta}^m$. Populations of the isomer were successfully pumped down with flashes of x-rays absorbed through an astonishingly large cross section. Then we discovered that these giant funnels for pumping isomers occurred rather frequently. We found them in the second of the 29 candidates, $^{123}\text{Te}^m$, as well as in other demonstration nuclei such as ^{197}Au and ^{195}Pt . However, until now, no experiment could determine the location of such giant resonances in the scheme of energy levels for any nucleus.

Reported here is success in locating at 2500 keV the giant resonance for pumping isomeric populations of $^{180}\text{Ta}^m$ through an integrated cross section of 70,000 on the usual scale ($\times 10^{-29} \text{ cm}^2 \text{ keV}$) where 10 describes a fully allowed process.

Report

The inability to vary the spectrum of the x-rays pumping the isomers had previously prevented us from locating the precise energy necessary to reach the giant resonances. The spectrum of intensities used earlier had been the bremsstrahlung from a linac with a fixed endpoint energy. In this major milestone experiment we obtained access to the only existing linac with a variable endpoint energy, the superconducting injector to the storage ring at Darmstadt in West Germany. By setting the endpoint energy of the bremsstrahlung to successively higher values, the sudden increase in activation of a sample could be clearly seen when the giant pumping resonance was reached.

We had reported earlier that when $^{180}\text{Ta}^m$ is dumped with flash x-rays it cascades to the ground state which has a half-life of 8.1 hrs against transmutation to hafnium. The most dependable signature for the deexcitation of the $^{180}\text{Ta}^m$ has been the detection of K_{α} lines of the ^{180}Hf daughter of the ground state in an otherwise pure sample of Ta.

In this experiment a 127 μm thick foil of tantalum containing 0.012% of naturally occurring $^{180}\text{Ta}^m$ was exposed for 4-hour intervals to bremsstrahlung with successively higher endpoints. After each exposure the activation of the foil was counted with a Ge(Li) spectrometer. The x-ray lines in the resulting spectra were fitted to determine the intensity of the fluorescence from the ^{180}Hf daughter. The onset of activation above background levels was clearly seen at 2500 keV.

Significance

There is a threefold significance to this milestone result.

- 1) The giant resonance for dumping the candidate isomer $^{180}\text{Ta}^m$ is clearly shown by the abrupt edge at 2.5 MeV in the excitation function for the transmutation debris. Such a sharp onset shows that the entire pumping strength is concentrated in a single resonance in energy. This arrangement is the ideal nuclear analog to the ruby laser.
- 2) To within experimental resolution of ± 100 keV the giant funneling state for dumping $^{180}\text{Ta}^m$ was found at the same energy of excitation as is already contained by some of the higher lying isomers at neighboring mass numbers. This shows that an accidental resonance of such an ideal pumping level with an isomer is likely in this mass region.
- 3) The isomer $^{180}\text{Ta}^m$ is the poorest of the 29 candidates for a gamma-ray laser, but it is the only one available for dumping in tests. It continues to outperform even our most optimistic expectations. The likelihood for the full feasibility of one of the better candidates is raised substantially by the great strength and low excitation energy demonstrated for the bandwidth funnel in this worst case.

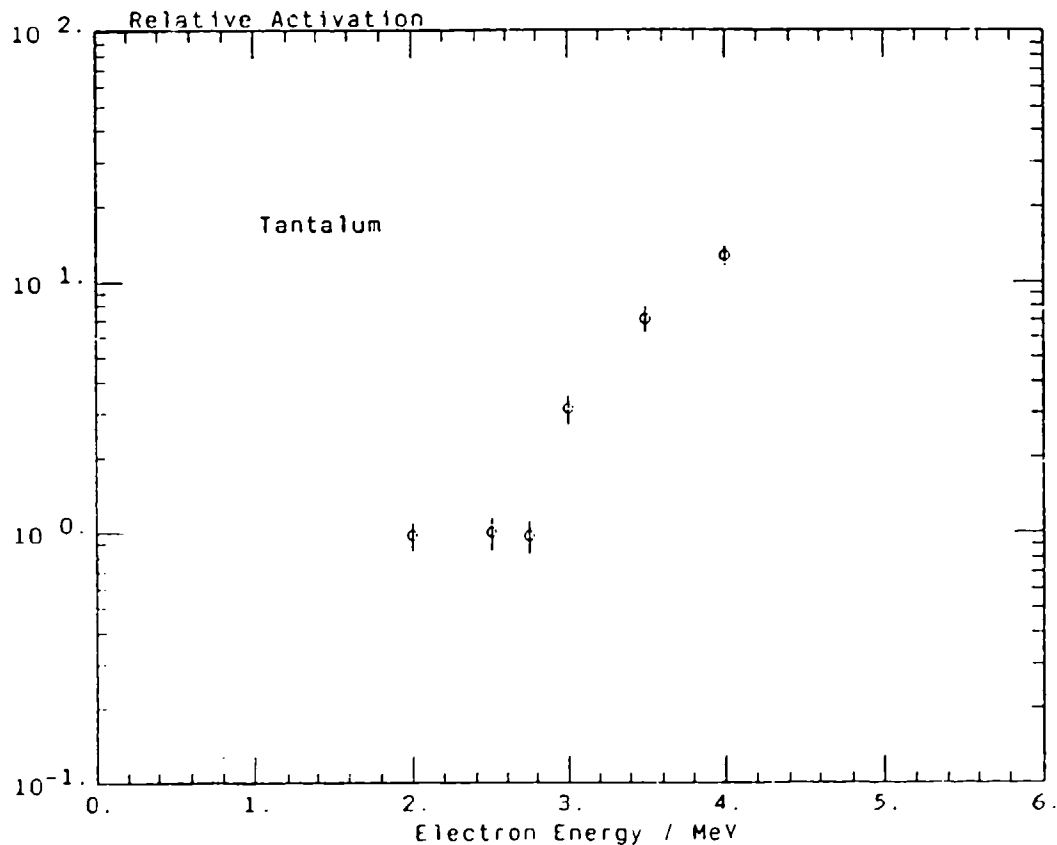


Figure 1: Deactivation function of $^{180}\text{Ta}^m$. Graph shows normalized yields of K_{α} photons from the Hf debris produced by dumping isomeric populations with bremsstrahlung x-rays having the endpoint energies shown on the abscissa. Points are normalized to the background value of unity. Each was obtained by irradiating a $127 \mu\text{m}$ thick foil of Ta containing 0.012% of the isomer for 4 hours with bremsstrahlung from the superconducting accelerator at the Technische Hochschule Darmstadt in West Germany.

THERMAL ECONOMY OF A GAMMA-RAY LASER

by C. B. Collins

One of the most inhibiting factors in the development of a gamma-ray laser has been the heavy load of theoretical dogma¹ which confounds the start of each experiment. Too obvious to warrant proof, these tenents of faith are often believed to frustrate even the more positive modeling we reported² in 1982. While sometimes combined in various packagings, the barriers to the realization of a gamma-ray laser are usually purported to be fourfold:

- 1) The electrons will screen the nuclei so analogs of optical pumping will not work for nuclear states.
- 2) The absorption widths which nuclei display toward pump photons cannot exceed 1 μ eV in any useful cases.
- 3) The isomeric states which would be the most attractive to pump cannot be dumped by photons because they have angular momenta which are too different from the freely radiating levels.
- 4) The waste heat associated with any pumping process will lodge in the host lattice and destroy the Mössbauer effect needed for a sharpened cross section for stimulated emission.

The sequence of experimental results we reported in 1987 completely destroyed the first three of these tenents of faith. Achieving a first major milestone, we reported³ the experimental observation of eleven orders of magnitude of increase in the amount of fluorescence which could be obtained when narrow nuclear levels of ^{79}Br and ^{77}Se were pumped with flash x-rays through broad states able to funnel their populations down to the radiating level. Those results confirmed the existence at the nuclear level of the analogs of the processes of bandwidth funneling which made the first ruby laser possible. Clearly the first barrier had been only an illusion.

The second and third articles of faith were destroyed by our more recent major milestone report of the successful dumping of some of the population of a nuclear isomer, $^{180}\text{Ta}^m$. Offset by eight quanta of angular momenta from the normal rotational bands, populations of this

state were dumped into the freely radiating system of levels through an enormous integrated cross section approaching $10^{-21} \text{ cm}^2 \text{ eV}$ by pumping them with flash x-rays.⁴ This result implies a useful absorption width of about 0.5 eV for the interband transfer of population from isomeric to radiating level systems. Experimentally, the occurrence of these giant resonances for mixing levels across such great spans of angular momenta was subsequently shown to be a rather common occurrence among nuclides.^{5, 6, 7}

At this point we have realized nearly seventeen orders-of-magnitude of increase in feasibility over the pessimistic evaluation¹ from which the current renaissance in this field departed. Present capabilities exceed even the more optimistic projection² upon which our project is based. However, the concern for the thermal economy has persisted.

In 1986 we reported a study⁸ which showed that the waste heat associated with the pumping of nuclei with flash x-rays presented a manageable problem to the design of a device. However, that work received little attention and even the most recent studies⁹ pursued elsewhere admit no domain in parameter space in which a threshold level of inversion could be pumped without the concomitant loss of the recoilless fraction of the output transitions. Of course, without the recoilless fraction the cross section for stimulated emission would be so reduced by broadening as to be impossible to excite.

Perhaps, unrecognized, is the fact that the critical parameter in the thermal economy is the average excess energy, E by which the energies of the dominant nuclear transitions exceeds the K-edge energy of the electrons of the material. In the early stages the waste heat is almost entirely contained in the primary photoelectron population produced either by the pump radiation or by the internal conversion of the various nuclear transitions. To have a hopeless situation one need only to limit studies to the rather few instances in which the kinetic energy, E of the primary photoelectrons is so small that the range of such particles is less than the dimensions of the layer being pumped. Then, they cannot escape and the waste energy will be degraded to heat precisely in the sensitive area in which the population inversion is developed. Just such a failure mode was built into the unfortunate

example of the excitation of the 14.4 keV transition of ^{57}Fe in an iron matrix.⁹

It is the purpose of this manuscript to explore the problem of the thermal economy of the ruby-laser analog in systems benefitting from the new discoveries which remove the first three traditional inhibitions to the design of a gamma-ray laser. It will be seen that for a wide margin of material parameters, the problem of the waste heat is readily manageable. As a consequence, the fourth and last of the traditional tenets of dogma is destroyed as a paramount concern. Reduced to the level of an engineering challenge, the solution to the problem of waste heat remains to be tailored to the particular characteristics of the nuclear system finally employed.

Whether or not the initial state to be pumped is isomeric, the principal figure of merit for bandwidth funneling is the partial width for the transfer, $b_a b_o \Gamma$. Constituent parameters are identified in Fig. 1 where it can be seen that the branching ratios b_a and b_o specify the probabilities that a population pumped by absorption into the i -th broad level will decay back into the initial or fluorescent levels, respectively. It is not often that the sum of branching ratios is unity, as channels of decay to other levels are likely. However, the maximum value of partial width for a particular level i occurs when $b_a = b_o = 0.5$.

The actual measurement of partial widths has involved the correlation of fluorescence yields excited by a pulse of x-rays in the scheme of Fig. 1 with those expected from the expression,^{4,9}

$$N_f = N_o \sum_i \xi_i \frac{\varphi_i}{A} \quad , \quad (1a)$$

where N_o and N_f are the numbers of initial and fluorescent nuclei respectively, (φ_i/A) is the spectral intensity of the pump radiation in keV/keV/cm² at the energy E_i of the i -th pump band, and the summation is taken over all of the possible pump bands capable of cascading to the same fluorescence level of interest. The ξ_i is a combination of nuclear parameters including the partial width $b_a b_o \Gamma$ in keV,

$$\xi_i = \frac{(\pi b_a b_o \Gamma \sigma_0 / 2)_i}{E_i} \quad (1b)$$

where σ_0 is the peak of the Breit-Wigner cross section for the absorption step. The combination of parameters in the numerator of Eq. (1b) is termed the integrated cross section for the transfer of population according to the scheme of Fig. 1.

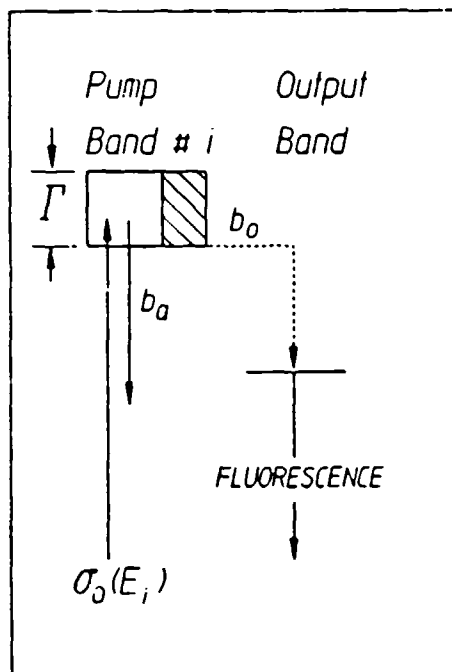


Figure 1: Schematic representation of the decay modes of a gateway state of width Γ sufficiently large to promote bandwidth funneling. The initial state from which population is excited with an absorption cross section σ_0 can be either ground or isomeric, in principle.

The Breit-Wigner cross section peaks at

$$\sigma_0 = \frac{\lambda^2}{2\pi} \frac{2I_e+1}{2I_g+1} \frac{1}{a_p+1} \quad (2)$$

where λ is the wavelength in cm of the gamma ray at the resonant energy, E_i ; I_e and I_g are the nuclear spins of the excited and initial states,

respectively; and α_p is the total internal conversion coefficient for the two-level system comprised by the initial and pump levels. The value of α_p is essentially zero for a transition which is highly allowed; and even were it not, α_p would be reduced further and the partial width would become correspondingly larger so that the quantity ξ_i would remain unaffected.

In this development it has been assumed that the width of the pump spectrum is sufficiently greater than Γ that the pump can be considered to be continuous and without structure over the width of the absorption line. Other than this assumption the development, so far, is general. Restrictive assumptions necessary for the management of the thermal economy can be explicitly stated as follows:

- 1) The pump band i in Fig. 1 is one of the newly discovered giant pumping resonances with a partial width of $b_s b_0 \Gamma = 1$ eV.
- 2) The pump transition is centered on an energy $E_i = 30$ keV.
- 3) The initial state is assumed to be isomeric with an excitation energy so high that 2) is possible.
- 4) The output transition is around 100 keV.
- 5) The nuclei are diluted in a thin film of diamond.
- 6) The Borrman effect contributes a factor of 10 to the enhancement of the ratio of cross sections for resonant to non-resonant transitions.

An immediate issue is the plausibility of these assumptions. While the widths for pumping interband transfer of population to and from isomers have been shown to approach 1 eV in many cases,^{4,7} it had not been previously demonstrated that such a width corresponded to a discrete level. Described in the Major Milestone Report for this quarter is the use of a Compton spectrometer to search for a gateway energy, E_i through which the photon pumping reaction, $^{197}\text{Au}(\gamma, \gamma')^{197}\text{Au}^*$ proceeds. As described elsewhere in this quarterly report the enormous integrated cross section of 3700 in the usual units ($\times 10^{-29} \text{ cm}^2 \text{ keV}$) was found to be localized at an energy 2.6 MeV above the ground state. Al-

least in this case, the experiment supported the identification of such favorable pumping resonances with a discrete, well-defined pump energy so that Assumption 1) is plausibly supported.

Plausibility of the second and third assumptions must be considered together. The range of excitation energies over which isomers can be found is very large, reaching 6 MeV if one considers the shape isomers proposed by Weiss et al.¹⁰ We have already shown that isomers can be dumped into the freely radiating system, even through $\Delta J = 8$, so the only doubt here is a statistical one; whether or not a giant pump resonance can be found within 30 keV of an isomer.

Assumption 4) is quite likely and the feasibility of 5) has been greatly increased by a recent "breakthrough" in the deposition of thin film diamond from laser plasmas. As described in one of the following manuscripts, we have been able to grow very uniform thin films of amorphic diamond from the plasma ablated from a carbon target in an environment especially suited to doping with nuclei of interest to the gamma-ray laser. While proper single crystal substrates have not yet been used to try to organize the growth of single crystal diamond, the largest step of fabricating a diamond film has been accomplished. However, until a single lattice is demonstrated the combination of assumptions 5) and 6) remains uncertain. By itself, the anticipation of a factor of ten reduction in the ratio of probabilities for non-resonant to resonant absorption is modest but still questionable for diamond at this time. As a consequence, single crystal Be is also modeled as a second preference. Thus, it can be reasonably asserted that the six assumptions upon which rest the model reported here are plausible and consistent.

Following our development² of 1982 under small signal conditions the overall logarithmic amplification, α for a single pass down the length, z of the strip of pumped material shown in Fig. 2, is,

$$\alpha = N_f \sigma_R z - N_o \sigma_{NR}^{(m)} z - N_d \sigma_{NR}^{(d)} z \quad , \quad (3)$$

where N_f is the number of nuclei in the fluorescent level which it is desired to pump to threshold, and where σ_R and σ_{NR} denote the cross sections for the resonant emission given by Eq. (2) evaluated at the output wavelength (100 keV) and for the non-resonant absorption in the

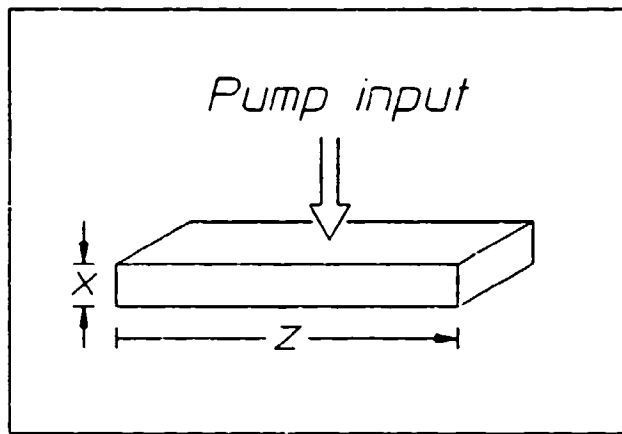


Figure 2: Geometry of the thin strip of diamond doped with the nuclei to be pumped with flash x-rays.

medium, (m) and diluent, (d), respectively. To reach the threshold for laser output, α must become positive so that the minimal condition is

$$0 \leq N_f \sigma_{NR} z - N_o \sigma_{NR}^{(m)} z - N_d \sigma_{NR}^{(d)} z \quad , \quad (4)$$

which necessitates,

$$\frac{N_f}{N_o} \geq \frac{\sigma_{NR}^{(m)}}{\sigma_R} \left(1 + \frac{N_d}{N_o} \frac{\sigma_{NR}^{(d)}}{\sigma_{NR}^{(m)}} \right) \quad . \quad (5)$$

For estimations to within a factor of two the latter term in the parentheses can be neglected for concentrations greater than 3%. At the 100 keV output transition,

$$\sigma_{NR}^{(d)} (\text{Be}) = 0.13 \text{ cm}^2/\text{gr} \quad , \quad (6a)$$

$$\sigma_{NR}^{(d)} (\text{C}) = 0.15 \text{ cm}^2/\text{gr} \quad , \quad (6b)$$

$$\sigma_{NR}^{(m)} (\text{Ta}) = 4.3 \text{ cm}^2/\text{gr} \quad , \quad (6c)$$

where Ta has been arbitrarily selected as representative of the region of nuclides where the better candidates for a gamma-ray laser medium may be found. So it can be seen that at 3% concentration by mass, losses in the diluent increase the right hand side by a factor of 2x.

Simplifying Eq. (5) gives,

$$\frac{N_f}{N_0} \geq \frac{\sigma_{NR}^{(m)}}{\sigma_R} , \quad (7)$$

so that the fraction pumped must exceed the ratio of the cross sections for non-resonant loss to resonant stimulated emission. Unfortunately the dependence of the right hand side of Eq. (7) upon nuclear parameters is tedious and structured. Baldwin¹ has presented a convenient review which shows Eq. (7) is optimized for an output energy of 100 keV as assumed here. Values range from 10^{-2} to 10^{-4} and can be assumed to be improved (lowered) by the Borrman effect. To be consistent with the earlier assumptions, the Borrman effect is supposed to enhance the mid-range value of 10^{-3} yielding a requirement of 10^{-4} for the pumped fraction,

$$\frac{N_f}{N_0} \geq 10^{-4} , \quad (8)$$

This sets the pump intensity needed for threshold, and with it the amount of waste heat to dissipate.

Substituting into Eq. (8) from Eq. (1a) and assuming the single giant resonance dominates so that the sum is unnecessary, gives,

$$\frac{\pi b_a b_0 \Gamma \sigma_c F_i}{2} \geq 10^{-4} , \quad (9a)$$

where

$$F_i = \frac{\varphi_i}{E_i A} , \quad (9b)$$

that is, F_i is the pump flux integrated over the lifetime of the fluorescent level in units of photons/cm²/eV, if Γ is now in eV. Assuming $I_e = I_g$ in Eq.(2) and $\alpha = 0$, then at 30 keV, $\sigma_0 = 2.72 \times 10^{-18}$ cm² and letting $\pi b_a b_0 \Gamma / 2 = 1$ eV gives

$$F_i \geq 3.7 \times 10^{13} \text{ photons/cm}^2/\text{eV} , \quad (10a)$$

or since each photon is 30 keV,

$$\Phi_i \geq 177 \text{ mJ/cm}^2/\text{eV} \quad . \quad (10b)$$

In the geometry of Fig. 2, it is next important to determine the thickness, x of the pumped layer. At the level of 10% concentration, $N_0 = 5.5 \times 10^{21} \text{ cm}^{-3}$ so the extinction coefficient for pumping is,

$$\sigma_0 N_0 = 1.5 \times 10^4 \text{ cm}^{-1} \quad , \quad (11a)$$

and so,

$$x \approx (\sigma_0 N_0)^{-1} = 0.67 \mu\text{m} \quad . \quad (11b)$$

At the 30 keV pump energy

$$k_{NR} (\text{Be}) = 0.332 \text{ cm}^{-1} \quad , \quad (12a)$$

$$k_{NR} (\text{diamond}) = 0.900 \text{ cm}^{-1} \quad , \quad (12b)$$

$$k_{NR} (10\% \text{ Ta}) = 35.4 \text{ cm}^{-1} \quad , \quad (12c)$$

where the k_{NR} are the extinction coefficients for the non-resonant absorption of the pump x-rays. It is important to notice that this is a typical case in which the pump radiation is not particularly close to an absorption edge. In this case the emerging photoelectrons will have some kinetic energy, and may escape from the region being pumped. Had the example been arranged to be more pathological as in the recently reported case⁹ of the ⁵⁷Fe, Eq. (12c) would have given a much larger absorption coefficient. As it is, the non-resonant absorption by the working medium in the $0.67\mu\text{m}$ layer is only,

$$f_1 = k_{NR} (10\% \text{ Ta}) x = 2.4 \times 10^{-3} \quad , \quad (13)$$

where f_1 is the fraction of the incident fluence stopped in the laser medium by non-resonant absorption. However, this fraction is reduced further by the escape of the primary photoelectrons from the pumped layer.

Figure 3 shows the mean extrapolated ranges, $E/(dE/dx)$ computed by standard techniques¹² for the escape of photoelectrons having the energies shown in the materials indicated. In this case the Ta is considered to be in the normal (100%) concentration. In the 10% concentration being assumed the ranges would be 10x greater and so the

contribution of the working medium to the absorption of the primary photoelectrons would be dominated by the effects of the diluent.

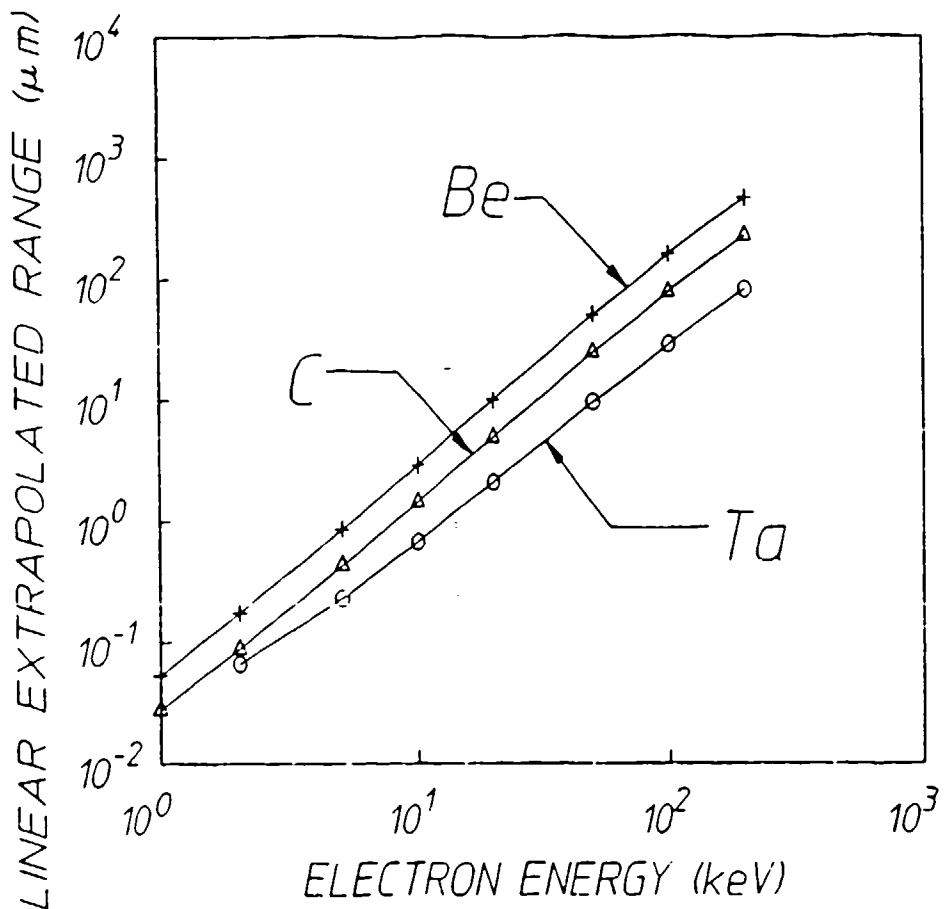


Figure 3: Plot of the linear extrapolated range of electrons in foils of the materials shown.

For the likely cases of rare earth or platinide elements the pump energy we assume lies below the K-edge and about 15 keV above the L-edge. As a result, the primary photoelectrons resulting from the non-resonant absorption in the active medium should have energies of the order of 15 keV and ranges of 6.0 and 3.0 μm in Be and C, respectively. Thus, only about 10% and 20% respectively, of the primaries, should be stopped in the 0.67 μm thick host films of Be or diamond. Multiplying the fraction of Eq. (13) by these probabilities for collision of the primary in the foil gives the fractions.

$$f_2 (\text{Be}) = 2.4 \times 10^{-4} \quad , \quad (14a)$$

$$f_2 (\text{C}) = 4.8 \times 10^{-4} \quad , \quad (14b)$$

for the fraction of the energy from the incident pump degraded into heat in the laser film because of non-resonant absorption.

Considering that edge filters or ablation layers could reduce the bandwidth of the pump radiation to 3 keV, before reaching the doped layer of Fig. 2, the incident fluence lying outside the bandwidth for resonant absorption would be 3000 \times greater than the value of Eq. (10b). However, only the fractions of Eqs. (14a) and (14b) are capable of being degraded into heat in the sensitive layer. The resulting energy balance can then be summarized at threshold:

Lattice	Be	C(diamond)
Resonant input fluence	177 mJ/cm ²	177 mJ/cm ²
Fluence degraded to heat	12 mJ/cm ²	255 mJ/cm ²

There is an additional potential for heating in the resonant term as well. Reference to Fig. 1 will show that for each absorption to the giant funneling state, a cascade is started that reaches finally to the level being inverted. Since the isomer may start at several MeV, while the output transition accounts for only 100 keV, there is the possibility of exciting a sequence of radiative transitions emitting a total of several MeV for each nuclei inverted. Were this to occur in a sequence of many soft transitions of a few keV these could be internally converted to give low energy electrons which would then be unable to escape the 0.67 μm layer being pumped. They would deposit their energies in the layer as heat.

For a number of reasons a significant contribution to the heating from cascades following resonant absorption is unlikely. The most probable spontaneous transitions are those spanning larger gaps of energy and those are seldom converted internally. The ones that are converted will give electrons of higher energies which Fig. 3 shows to have higher probabilities of escape from the layer. It is most reasonable to expect the dominant source of heat to be the energy lying in the broader bandwidth of the pump continuum as discussed above.

The elements of the energy economy tabulated above are the fluences stopped in the thin working layer in which the nuclear populations are being inverted. Dividing those fluences by the $0.67\mu\text{m}$ thickness gives the energy loading of the laser film,

Lattice	Be	C(diamond)
Resonant energy density	2.6KJ/cm^3	2.6KJ/cm^3
The real loading	1.9KJ/cm^3	3.8KJ/cm^3

These values are quite significantly below the levels of heating required to degrade the recoil free fractions in the case of the diamond lattice. Baldwin has summarized¹³ the involved dependence of the recoil free fraction of gamma transitions upon recoil energy, lattice parameters and temperature. He shows that even at a temperature, T equal to the Debeye temperature, Θ_0 the recoil free fraction is not significantly degraded (by more than a factor of 2) for a transition even as energetic as to give a classical recoil energy of $0.14\Theta_0$. In diamond with $\Theta_0 = 2230^\circ\text{ K}$ this means a transition of 100 keV is little affected by a temperature increase up to $T = \Theta_0$.

It is a textbook computation¹⁴ to estimate that the energy content of the phonons of a material with $\Theta_0 = 2230^\circ\text{ K}$ at a temperature of $T = \Theta_0$ is about 11KJ/cm^3 . Comparing this with the estimated loading of 3.8KJ/cm^3 gives a "safety factor" of almost 3x. A comparable margin is obtained for the Be.

To summarize, it is convenient to recast the threshold fluence of Eq. (10b) into more tangible terms. The spectral fluence of $177\text{mJ/cm}^2/\text{eV}$ corresponds to 530 J/cm^2 if the bandwidth of the pump x-rays is arranged to be 3 keV, a practical separation which might be filtered between K-edges. Even if pumped instantaneously, so that no waste heat were transported away, the thermal loading would reach only $1/3$ of the way to the limit for retaining the Mössbauer effect. If derived from an x-ray line of 30 eV width, the threshold fluence would be only 5.3 J/cm^2 . In that case the thermal loading would reach only $1/300$ of the critical limit for a diamond lattice.

Even beyond this point much can be done to reduce heating further. All calculations so far were done for the instantaneous generation of the waste heat. The time for the transport of a phonon across the $0.67\mu\text{m}$ thickness of the working layer is of the order of only 100 psec so that the transport of significant amounts of heat from that layer into a diamond heat sink is possible on a nanosecond time scale. Yet the lifetimes of most of the fluorescent levels of interest for inversion² have lifetimes of tens of nsec to tens of μsec . This is many times the period for the transport of phonons out of the inverting layer so that more orders of magnitude can be realized in reducing the thermal loading further below the limits specified so far. However, all these techniques require precise knowledge about the energy levels and absorption edges of the materials involved. Until the identity of the best candidate for a gamma-ray laser is known, the exact specifications of the solution to the disposal of the waste heat cannot be generally articulated. The examples considered here show that there are many orders of magnitude in the safety margin between likely amounts of heating and the much larger amounts which can be tolerated in stiff lattices such as Be and diamond.

The greatest significance is that the fourth and last of the tenets of theoretical dogma inhibiting the development of a gamma-ray laser is eliminated by these arguments. There is no need to melt the host lattice in order to pump a nuclear system to the laser threshold. *There are no a priori obstacles to the realization of a gamma-ray laser.* A gamma-ray laser is feasible if the right combination of energy levels occurs in some real material. The overriding question to resolve is whether or not one of the better of the 29 candidates has its isomeric level within a few tens or even hundreds of keV of one of the giant resonances for dumping angular momenta, such as found in $^{180}\text{Ta}^m$ and $^{123}\text{Te}^m$.

REFERENCES

1. G. C. Baldwin, J. C. Solem, and V. I. Goldanskii, *Rev. Mod. Phys.* 53, 687 (1981).
2. C. B. Collins, F. W. Lee, D. M. Shemwell, and B. D. DePaola, *J. Appl. Phys.* 53, 4645 (1982).
3. J. A. Anderson and C. B. Collins, *Rev. Sci. Instrum.* 58, 2157 (1987).
4. C. B. Collins, C. D. Eberhard, J. W. Glesener, and J. A. Anderson, *Phys. Rev. C* 37, 2267 (1988).
5. C. D. Eberhard, J. W. Glesener, Y. Phiss, J. A. Anderson, C. B. Collins, W. L. Hodge, E. C. Scarbrough, and P. O. Antich, *Phys. Rev. C* (pending).
6. C. B. Collins, J. A. Anderson, C. D. Eberhard, J. F. McCoy, J. J. Carroll, E. C. Scarbrough, and P. P. Antich, in *Center for Quantum Electronics Report #GRL 8703*, University of Texas at Dallas, 1987 (unpublished), pp 35-53.
7. J. A. Anderson, C. D. Eberhard, J. F. McCoy, K. N. Taylor, J. J. Carroll, M. J. Byrd, C. B. Collins, E. C. Scarbrough and P. P. Antich, in *Center for Quantum Electronics Report #GRL 8704*, University of Texas at Dallas, 1988 (unpublished) pp 11-35.
8. C. B. Collins in *Center for Quantum Electronics Report #GRL 8601*, University of Texas at Dallas, 1986 (unpublished) pp 1-14.
9. D. A. Swallow, *Bull. Am. Phys. Soc.* 33, 1017 (1988), Presentation GC3.
10. M. S. Weiss, *Bull. Am. Phys. Soc.* 33, 1017 (1988), Presentation GC4.
11. S. S. Wagal, E. M. Juengerman and C. B. Collins, *Appl. Phys. Lett.* 53, 187 (1988).
12. G. Knop and W. Paul, in: Alpha, Beta and Gamma-Ray Spectroscopy (ed. Kai Siegbahn, North-Holland Co., Amsterdam, 1965), p 1-25.
13. See Ref 1, Fig. 14.
14. C. Kittel, Introduction to Solid State Physics, 6th ed. (Wiley, New York, 1986), p. 106.

PHOTOEXCITATION OF NUCLEAR ISOMERS BY (γ, γ') REACTIONS

by J. J. Carroll, M. J. Byrd, D. G. Richmond, T. W. Sinor,
K. N. Taylor, W. L. Hodge, Y. Paiss, C. D. Eberhard, J. A. Anderson,
and C. B. Collins

E. C. Scarbrough and P. P. Antich
The University of Texas Southwestern Medical Center at Dallas

F. J. Agee, D. Davis, G. A. Hutlin, K. G. Kerris, M. S. Litz,
and D. A. Whittaker
Aurora Simulator Facility, Harry Diamond Laboratories

INTRODUCTION

Because the photon carries relatively little momentum, (γ, γ') reactions must proceed through resonant channels for excitation with rather narrow widths. This aspect distinguishes photoexcitation from related processes such as (γ, n) . The generation of an additional particle with which to conserve momentum provides a threshold of energy above which all incident photons can mediate the reaction. This facilitates the study of processes such as (γ, n) by increasing product yields and richly detailed results have been reported in the literature.¹ In contrast, the difficulties in exciting the narrow resonances through which (γ, γ') reactions must proceed have inhibited investigations and relatively few results have been published in the past 50 years over which such processes have been known.^{2,3}

In the region of energies from 0.1 to 11.0 MeV photon sources are either fixed in energy or continuous in nature and the opportunity to probe (γ, γ') reactions with a tunable source of narrow width does not exist at practical levels of intensity. Generally experiments have been done with continua either intentionally, or unavoidably because of the degradation of line spectra by Compton scattering in actual geometries in which γ -sources are employed.

If threshold phenomena are being investigated, results are sensitive only to the integrals of the illuminating spectra as functions of energy and impressive precision can be achieved in the reaction cross sections finally reported.¹ Conversely, (γ, γ') reactions which must be excited through narrow windows of energy, depend upon details of the spectra of input intensities. Since the width of the reaction is usually much less than the scale over which any significant variations of intensity can occur, results are reported in terms of the integrated cross sections, $(\sigma\Gamma)_f$,

$$(\sigma\Gamma)_f = \int_{\text{width}} \sigma_f(E) dE \quad , \quad (1)$$

where Γ is the width of the reaction channel, $\sigma_f(E)$ is the cross section for exciting the product state, f , and E is the energy of the incident photon.

The yield of such a (γ, γ') reaction will depend upon the product $I(E)(\sigma\Gamma)_f$, where $I(E)$ is the spectral density of the irradiation in units such as photons/cm²-keV. Thus, the accuracy in reporting integrated cross sections can be no better than the state of knowledge of $I(E)$. The difficulties in characterizing such spectra have provided for decades of critical controversy.

The most tractable (γ, γ') reactions for study are those for the photoexcitation of isomeric states. These live long enough to be readily examined after termination of the input irradiation with its high level of concomitant noise. The archetypical case has been the reaction $^{111}\text{Cd}(\gamma, \gamma')^{111}\text{Cd}^m$. Three of the most recent measurements of the integrated cross section, $\sigma\Gamma$ were conducted in 1979, 1982, and 1987 with results of 35, 5.8, and 14 as reported in Refs. 4-6, respectively, in the usual units of 10^{-29} cm²-keV. Probable errors were quoted as varying

only from 7 to 14% and yet, no two of the measurements were even within a factor of 2 of each other.

Recently, the technology has become available^{7,8} to measure directly the spectrum of a source of pulsed bremsstrahlung, together with greatly improved computer codes¹⁰ with which to calculate spectra expected in complex, but realistic geometries. These advances made it possible to resolve¹¹ the persisting controversies in the reaction $^{111}\text{Cd}(\gamma, \gamma')^{111}\text{Cd}^m$, as well as those¹² in $^{115}\text{In}(\gamma, \gamma')^{115}\text{In}^m$. As expected, it was found^{11,12} that both $^{115}\text{In}^m$ and $^{111}\text{Cd}^m$ were excited by predominantly resonant absorption through intermediate states, called gateway states, near 1 MeV which were broadened by their relatively short lifetimes. The sharp onset of the (γ, γ') reactions with increasing energy relegated to less than 3% any contributions from non-resonant processes and indicated that the gateway states were reasonably well connected by radiative transitions to both the ground states and the isomers. It appears that the principle cause for the large discrepancy between previous measurements was the difficulty in adequately characterizing the spectra of the irradiation, as mentioned above. This was particularly true for radioactive sources since all spectral contributions away from the resonance lines were necessarily due to Compton continua generated by environmentally sensitive radiation transport processes.

The model for the photoexcitation of isomeric nuclei confirmed in this recent work^{11,12} is shown in Fig. 1. Only two gateway levels are drawn as examples and the number actually participating depends upon the sequence of energy levels and transition probabilities for the particular nucleus being considered. In the resolution of previous conflicts in ^{111}Cd and ^{115}In the values finally confirmed lay within the scatter of earlier measurements and generally conformed to expectations based upon nuclear parameters measured by other means.¹³ However, when studies were extended to the deexcitation of an isomeric sample through the reverse of the sequence shown in Fig. 1, quite unexpected results were obtained¹⁴ for the reaction $^{180}\text{Ta}^m(\gamma, \gamma')^{180}\text{Ta}$.

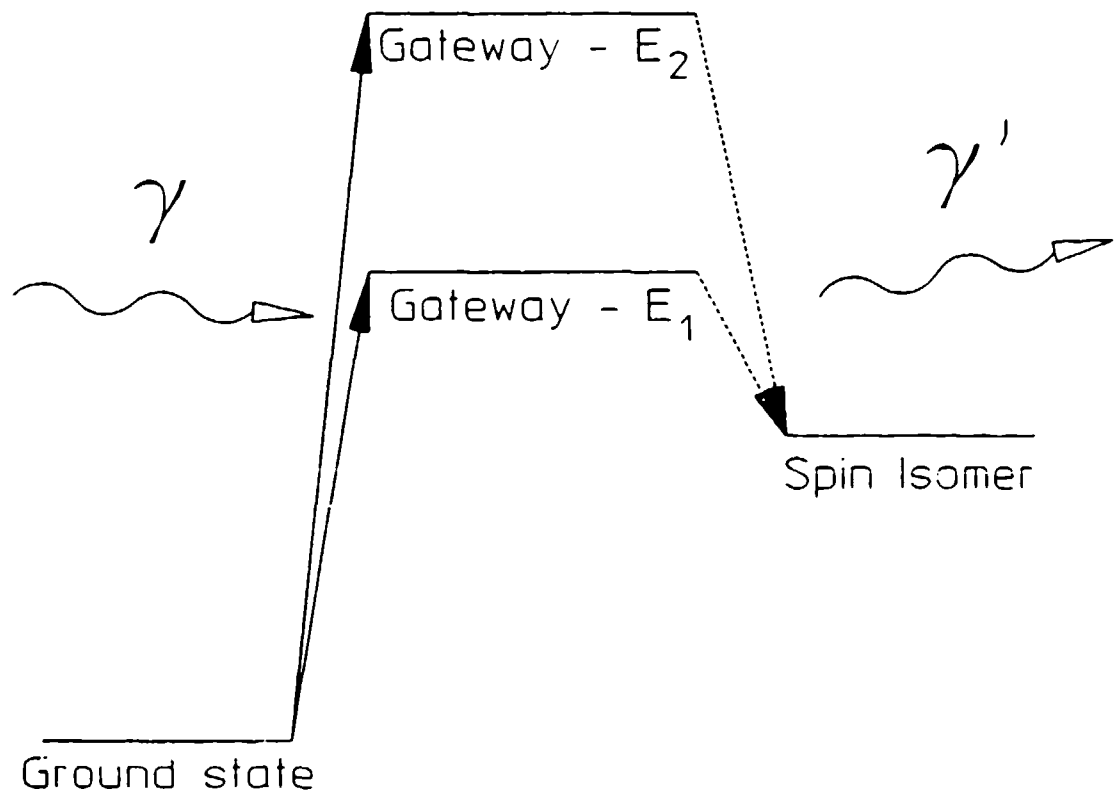


Figure 1: Schematic representation of the (γ, γ') reactions used to populate isomeric states in these experiments. The resonant absorption of bremsstrahlung x-rays denoted as γ , excite populations of gateway states. Two are shown at excitation energies of E_1 and E_2 but the actual number will vary for each nuclide. Parts of the populations of the gateway states make transitions to the final state either directly or as part of a cascade of radiative transitions ending on the final state as indicated by the dashed arrows.

The isomer $^{180}\text{Ta}^m$ is nature's rarest naturally occurring isotope.¹⁵ Requiring an unlikely change of $\Delta J = 8$, the isomer was dumped to the ground state by bremsstrahlung having an endpoint of about 6 MeV. The partial width for this reaction was found¹⁴ to be at least 0.5 eV, an enormous value exceeding any previous reports for (γ, γ') reactions by two to three orders of magnitude. The amount of deexcitation of the isomer observed was astonishing, corresponding to a total integrated cross section in excess of $4 \times 10^{-25} \text{ cm}^2\text{-keV}$. This strength of the dumping reaction $^{180}\text{Ta}^m(\gamma, \gamma')^{180}\text{Ta}$ was qualitatively confirmed¹⁶ with bremsstrahlung from the injector to the Darmstadt superconducting electron machine operated at 4.6 MeV. In this work the extension of these results to endpoint energies as low as 4.0 MeV will be described. Even more recently the reaction $^{176}\text{Lu}(\gamma, \gamma')^{176}\text{Lu}^m$ was reported to proceed with an integrated cross section of comparable magnitude.¹⁷

It was the purpose of the work reported here to examine the systematics of these giant resonances for the photoexcitation of isomeric states to determine whether such results were curiosities associated only with ^{176}Lu and $^{180}\text{Ta}^m$ or whether they were part of a more generally prevalent phenomena. To the extent possible it was intended to try to learn whether the large integrated cross sections were the results of a large number of reaction channels of more conventional size or rather, a few of unprecedented magnitude.

Unfortunately, the type of continuously variable electron accelerators that provided bremsstrahlung spectra with endpoint energies that could be selected in classical investigations¹⁸ of (γ, γ') reactions is no longer available. For the experiments reported here we could arrange access only to a combination of accelerators, some with limited variability of endpoint energies such as DNA/PITHON at Physics International and DNA/Aurora at Harry Diamond Laboratories. Additional capabilities were contributed by two medical Linacs having fixed endpoint energies of 4 and 6 MeV. This enabled us to examine the photoexcitation of 19 isomeric nuclei, most of them over the full range from 0.5 to 11 MeV. The diversity of accelerators and locations contributed an operational benefit by tending to minimize the possibility of inadvertently introducing any systematic bias which might have been associated with any particular machine or its environment.

METHODOLOGY

Analytic Approach

The probability $P(i \rightarrow f)$ that a nucleus undergoes a transition from the state i to the state f due to an x-ray exposure is the sum of the interaction probabilities for each (γ, γ') reaction which contributes to this process. This may be written as

$$P(i \rightarrow f) = \frac{N_f}{N_i} = \int_0^{E_{\text{end}}} \sigma(E) \frac{d\Phi(E)}{dE} dE, \quad (2)$$

where N_f is the number of final states produced and N_i is a statistically large population of nuclei originally in the state i . The irradiation is described by its endpoint energy E_{end} , and its spectral density $d\Phi(E)/dE$, or $I(E)$, in photons/cm²-keV. This is conveniently expressed as the product of the total photon flux Φ_0 in photons/cm² and a relative spectral intensity function $F(E)$ in keV⁻¹ which is normalized according to the condition

$$\int_0^{E_{\text{end}}} F(E) dE = 1, \quad (3)$$

so that

$$\frac{d\Phi(E)}{dE} = I(E) = \Phi_0 F(E). \quad (4)$$

In practice, the resonant gateways are sufficiently narrow in comparison to any features of the input spectra that Eq. (2) can be simplified as suggested by Eq. (1),

$$\frac{N_f}{N_i} = \sum_j (\sigma\Gamma)_{fj} \frac{d\Phi(E_j)}{dE}. \quad (5)$$

Here, E_j is the energy of the j^{th} gateway level mediating the transition and the summation includes all which lie below E_{end} . The symbol $(\sigma\Gamma)_{fj}$ represents the integrated cross section in cm²-keV for production of

this final state through the j^{th} gateway and includes contributions from all cascades which lead to f .

The integrated cross section is often expressed as $(\pi b_s b_o \sigma_0 \Gamma / 2)$, where b_s and b_o are the branching ratios for decay from the gateway level to the initial and final states, respectively. The Γ_j represents the natural width of the j^{th} state, whose lifetime τ_j gives $\Gamma_j = h/\tau_j$, and so $(b_s b_o \Gamma)_j$ is the partial width for the transition. The quantity σ_0 is the amplitude of the Breit-Wigner cross section for the absorption,

$$\sigma_0 = \frac{\lambda^2 I_j + 1}{2\pi I_i + 1} \frac{1}{\alpha_p + 1}, \quad (7)$$

where λ is the wavelength in cm of the γ -ray at the resonant energy, I_j and I_i are the nuclear spins of the gateway and initial states, and α_p is the internal conversion coefficient of the absorption transition.

The above general development could be applied to most of the nuclei studied in this work by identifying i and f with the ground state and the isomer, respectively. In this direction a transition is said to pump the isomeric population. One nucleus, that of the tantalum isotope ^{180}Ta , is naturally abundant as the isomer rather than the ground state which has a relatively short lifetime. In this instance the initial level is the isomer; the final level is the ground state and the transition is considered as dumping the isomeric population.

Each of the isomers pumped in this work was identified by the emission of signature photons¹⁹ with the exception of $^{176}\text{Lu}^m$ which decayed by β^+ emission, as described later. The yields of final state populations were determined from the numbers of counts, C , collected in the corresponding peaks in pulse height spectra. These raw data were then corrected in a standard manner for the photopeak detector efficiency, η , the fraction of fluorescence photons per decay, q , and the finite times of sample transport and counting, D_1 . The latter factor used literature values of the half-lives.¹⁹ It was also necessary to account for some attenuation of the fluorescence photons within the samples themselves because of absorption and scattering events. This effect was accommodated by a transparency factor A which was determined by Monte-Carlo calculations made for each sample. These corrections were confirmed by comparing the activations obtained from targets containing identical

materials, but in different geometries. The number of isomers produced in an exposure was then calculated from the expression,

$$N_f = \frac{C}{D_1 q \eta A} . \quad (8)$$

The definition of the term D_1 restricts the utility of Eq. (8) to photoexcitation which occurs at a particular instant in time. This is acceptable when considering exposures made with "flash" x-ray devices such as nuclear simulators since the durations of those pulses are extremely short compared to the lifetimes of the isomers.

A further modification was necessary to correct the number of isomers produced by continuously operating (cw) devices which generate a uniformly spaced series of flashes. Fortunately, in the linacs used in this work both the durations of individual pulses and the times between them were very short. Also, the numbers of nuclei excited by each flash were small relative to the total numbers of target nuclei. It was therefore only necessary to consider the decays of independent populations during the irradiation period. This was done by introducing another factor, D_2 , into the denominator of Eq.(8) equal to the fraction of all isomers produced that survived until the end of the exposure. This allowed the quantity D_1 to be retained as previously defined. In this way the activations, N_f/N_i were quantitatively obtained from the experimental data.

Substituting Eq. (4) into Eq. (5) and dividing by Φ_0 gives an expression for a type of excitation function,

$$\frac{N_f}{N_i \Phi_0} = \sum_j (\sigma \Gamma)_{fj} F(E_j) . \quad (9)$$

which can be useful as a sensitive indication for the opening of (γ, γ') channels whenever photons of the requisite energies, E_j become available. A change of the endpoint energy, E_{end} of the bremsstrahlung spectrum modulates the spectral intensity function $F(E_j)$ in Eq. (9) at all of the important gateway energies, E_j . The largest effect in the excitation function occurs when E_{end} is increased from a value just below some gateway at $E_j = E_k$ to one exceeding it so that $F(E_k)$ varies from zero to some finite value. In earlier work¹⁸ plots of quantities equivalent to Eq. (9) as functions of the endpoint energies of the

irradiating spectra showed very pronounced activation edges which appeared as sharp increases at the energies, E_j , corresponding to excitation of new gateways.

In the work reported here the ratios of activations, N_f/N_i to the irradiation doses were examined as functions of E_{end} . The relationships between dose which was measured directly, and Φ_0 which had to be derived from it depended upon $F(E)$. The normalization to dose rather than Φ_0 was chosen to avoid any dependence of the features of the excitation function upon interpretative models. Unfortunately, the relatively coarse mesh onto which endpoint energies could be set prevented any precise definition of the energies at which activation edges occurred for most nuclei studied here. However, their existence was very clearly indicated in the data.

A useful guide to interpolation was constructed in a second level of analysis. Previous works had shown that the integrated cross sections of higher lying resonances are generally larger than those of lower energy states.¹⁸ Therefore, the highest gateway below the endpoint tended to dominate the photoexcitation process. A reasonable estimate for that level, if one existed, was obtained from Eq. (9) by assuming that only a single state mediated the transition at some unknown gateway energy E , so that

$$(\sigma\Gamma) = \frac{N_f}{N_i \Phi_0 F(E)} . \quad (10)$$

The effective cross section, $\sigma\Gamma$ determined in this way from data produced by irradiation with a single endpoint, E_{end} was not unique. Rather, it was a collection of possible values that depended upon the spectral intensity of the radiation at the energy the dominant gateway might be assumed to lie. Plotted as a curve, the locus of such values varied from a minimum at the energy for which $F(E)$ was maximal to an unbounded asymptote as $E \rightarrow E_{end}$ and $F(E) \rightarrow 0$. These plots were of particular utility when several sets of such numbers were obtained from different endpoint exposures and were then examined together. In some cases the intersections of those loci suggested at about what energies dominant gateways might lie.

Experimental Details

Sample materials were exposed to photons having energies up to 1.5 MeV with the DNA/PITHON nuclear simulator at Physics International. This device was a flash x-ray source using a single transmission line pulsed by a Marx generator. Since the endpoint energy could be varied to some degree by changing the charging voltage of the Marx, photoexcitation from 0.5 to 1.5 MeV could be investigated with a resolution limited by the available endpoint energies. The samples were placed in front of a converter foil which terminated the transmission line and were aligned to face the photon flash. These were exposed in complex packages to activate many materials in each shot, an important detail since DNA\PITHON could be fired no more than hourly. All the sample packages were backed with Thermoluminescent Dosimeters (TLD's) to measure accurately the dosage which each target received.

The 1.5 to 6 MeV range was studied with two fixed endpoint medical linacs at the Department of Radiology of the University of Texas Southwestern Medical Center at Dallas. Irradiations with nominal 4 MeV bremsstrahlung were obtained with a Varian Clinac 4/100 linac which provided a dose rate of 200 rad(H_2O)/min at 101.2 cm from the converter target. Bremsstrahlung having a nominal endpoint of 6 MeV was obtained with a Varian Clinac 1800 linac operating in the 6 MeV mode. This device produced 400 rad(H_2O)/min at 101.5 cm from the converter target. For both machines, the dose rate was determined by in-line ion chambers whose calibrations can be directly traced to NIST. Samples were exposed in packages confined to the region of most uniform dose distribution. Therefore, TLD's were not used with these accelerators.

Irradiations in the 6 to 11 MeV range were provided with the DNA/Aurora nuclear simulator, the world's largest flash x-ray accelerator,²⁰ located at the Harry Diamond Laboratories. Powered by a Marx bank, photons were generated by converter foils which terminated four separate transmission lines. These converged on a target volume of roughly 0.1 m³ in which the photon field was most intense. Again, the Marx charging voltage was varied to provide irradiations with different endpoint bremsstrahlung. Samples were suspended within the high intensity spot and were backed by TLD's. These packages were oriented to face the centerline of the machine rather than any particular transmission line.

The spectra of these four machines have been well characterized, particularly the linacs which are committed to patient treatment. Photon spectra of the DNA/PITHON and DNA/Aurora accelerators were obtained through use of the Integrated TIGER Series (ITS) computational program.¹⁰ This coupled electron-photon transport code is well documented and widely used in the flash x-ray community. Results obtained in this way are usually calibrated by matching the endpoint energy and the total dosage to the shape of the calculated spectrum. The DNA/PITHON device could also be cross-calibrated by the activation technique described in Refs. 7 and 8. Typical spectra are given in Fig. 2 which shows the relative intensity function $F(E)$, on the meshes of energies for which data were available. For the DNA/PITHON shot shown, $\Phi_0 = 4 \times 10^{14}$ photons/cm² and for the DNA/Aurora shot, $\Phi_0 = 5 \times 10^{13}$ photons/cm².

The output spectra of the medical linacs employed in this work were calculated with the established EGS4 code developed at SLAC.⁹ Unfortunately, the relative spectral intensity functions of these devices that were found in the literature²¹ contained a computational artifact. To minimize that feature the spectra had to be modeled as part of this work. Results are shown in Fig. 3, together with the literature values for a typical case.²¹ The total fluxes at 100 cm were 3.23×10^{11} photons/cm²·min for the nominally 4 MeV device, and 5.35×10^{11} photons/cm²·min for the Clinac 1800 in the 6 MeV mode.

The isotopes studied in these experiments are listed in Table I along with some relevant physical parameters. The techniques employed to obtain measurements of activation depended upon the lifetimes of the isomeric states and whether or not these were long enough to transport the irradiated samples by simple means.

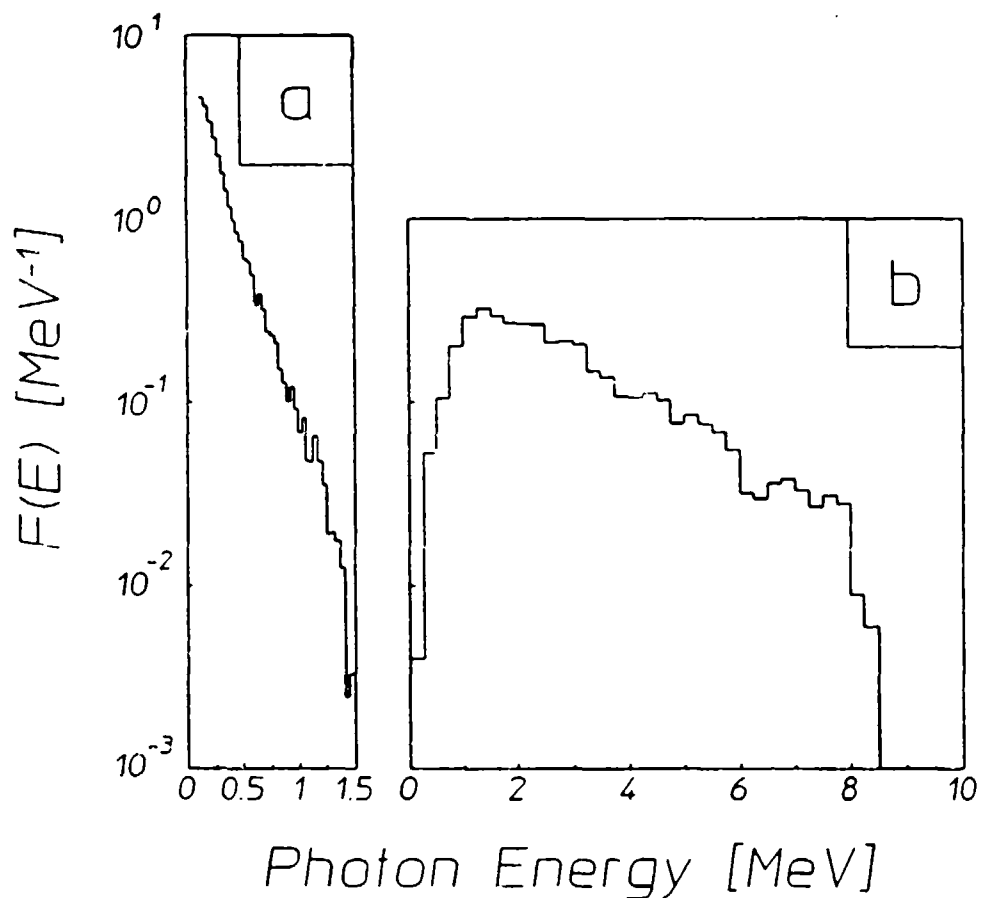


Figure 2: Relative spectral intensities, $F(E)$, of the bremsstrahlung typically produced by nuclear simulators used to irradiate samples in these experiments. The curves are normalized so that the areas under the curves are unity. The devices employed were:
a) DNA/PITHON, with an endpoint of 1.5 MeV.
b) DNA/AURORA, with an endpoint of 8.5 MeV.

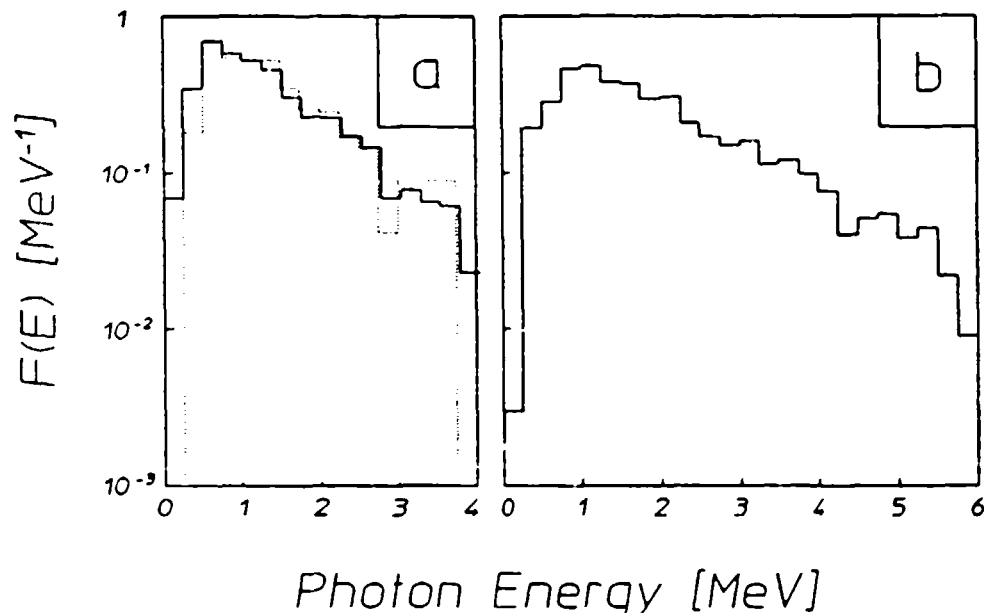


Figure 3: Relative spectral intensities, $F(E)$ of the bremsstahlung produced by the medical linacs used to irradiate samples in these experiments. The curves are normalized so that the areas under the curves are unity. The solid lines indicate empirical fits to the calculated spectra as discussed in the text. The devices employed were:

- a) Varian Clinac 4/100, with a nominal endpoint of 4 MeV. The dotted curve shows the spectrum obtained from Ref. 21 which contains a large spurious artifact at about 3 MeV.
- b) Varian Clinac 1800, operated in the nominal 6 MeV endpoint mode.

Table I. Summary of isomeric nuclei studied. Nuclei marked * were present in isotopically enriched samples. In the sample column, R refers to samples contained in rabbits, P to flat planchettes, F to metallic foils, and B to scintillation bottles. The ¹⁸⁰Ta sample consisted of a dusting of oxide on a thin aluminum plate, referred to by D. In the case of the ¹⁷⁶Lu sample, β -particles were observed instead of fluorescence photons; the NA in the transparency column indicates that this factor was not applicable for ¹⁷⁶Lu.

Nuclide	Abundance [%]	Sample Form	T _{1/2}	Principal Fluorescence [keV]	Transparency
¹⁶⁷ Er	91.54 *	Er ₂ O ₃ (R)	2.28 sec	207.79 (41.70%)	57.90
⁷⁹ Br	50.69	LiBr (R)	4.86 sec	207.20 (75.80%)	84.90
¹⁹¹ Ir	37.30	Ir (R)	4.94 sec	129.43 (25.70%)	10.50
¹⁹⁷ Au	100.00	Au (R)	7.80 sec	279.11 (73.00%)	92.70
⁸⁹ Y	100.00	YF ₃ (R)	16.06 sec	909.15 (99.14%)	94.70
⁷⁷ Se	94.38	Se (R)	17.45 sec	161.92 (52.40%)	72.28
¹⁷⁹ Hf	13.63	HfO ₂ (R)	18.68 sec	214.31 (94.20%)	52.40
¹⁹⁹ Hg	16.90	Hg ₂ Cl ₂ (R)	43.20 sec	158.40 (53.00%)	43.96
¹³⁷ Ba	11.74	BaF ₂ (R)	153.12 sec	661.66 (90.10%)	95.50
¹¹¹ Cd	12.80	Cd (F)	48.6 min	245.49 (94.00%)	76.35
¹¹³ In	4.30	In (F)	1.66 hr	391.69 (64.20%)	98.30
⁸⁷ Sr	7.00	SrF ₂ (P)	2.81 hr	388.40 (82.30%)	95.78
¹⁷⁶ Lu	2.59	LuCl ₂ (B)	3.63 hr	beta	NA
¹¹⁵ In	95.70	In (F)	4.49 hr	336.26 (45.80%)	98.00
¹⁸⁰ Ta	4.00 *	TaO ₂ (D)	8.15 hr	55.79 (36.00%)	100.00

¹³⁵ Ba	6.60	BaF ₂ (P)	1.20 d	268.27 (15.60%)	94.33
¹⁹⁵ Pt	33.80	Pt (Coin)	4.02 d	98.88 (11.40%)	4.76
¹¹⁷ Sn	7.70	Sn (F)	13.6 d	158.56 (86.40%)	92.89
¹²³ Te	0.908	Te (P)	119.7 d	158.99 (84.00%)	62.68

Isomers of the first nine nuclides listed in Table I have half-lives of less than three minutes and therefore required special treatment. These samples consisted of either powders or metallic foils enclosed in cylindrical polyethylene vials, termed rabbits, which were pneumatically transported to a well-type NaI(Tl) detector after exposure. The low energy resolution of this detector necessitated some care in the identification of the prominent features in the pulse height spectra. In all cases, confirmations that these were the fluorescence signatures of the isomers were made by determining the half-lives of the populations emitting these lines for comparision with literature values. This was made possible by simultaneously acquiring data through two Ortec 918A ADCAM multichannel buffers controlled by a personal computer. While one ADCAM served to produce a pulse height spectrum, the other collected a record of the total counts received in the preset dwell interval as a function of time. A typical example of the data obtained in this way is given in Figs. 4 and 5, showing measurements for the isomer $^{167}\text{Fr}^m$.

The remaining nuclides in Table I were investigated in a less hurried, but similar fashion, with the exception of ^{176}Lu . The isomers of those nuclei have half-lives longer than 48.6 min, so they were transported by hand to a nearby solid-type NaI(Tl) detector for counting. Samples containing particularly long-lived isomers like $^{123}\text{Te}^m$ ($T_{1/2} = 119.7$ days) and $^{117}\text{Sn}^m$ ($T_{1/2} = 13.61$ days) were transported to the Center for Quantum Electronics where they were counted using a high-purity, n-type germanium (HPGe) detector. The physical form of the materials in this slower class consisted either of thin metallic disks or metallic chips or chemical compounds contained within flat polyethylene planchettes.

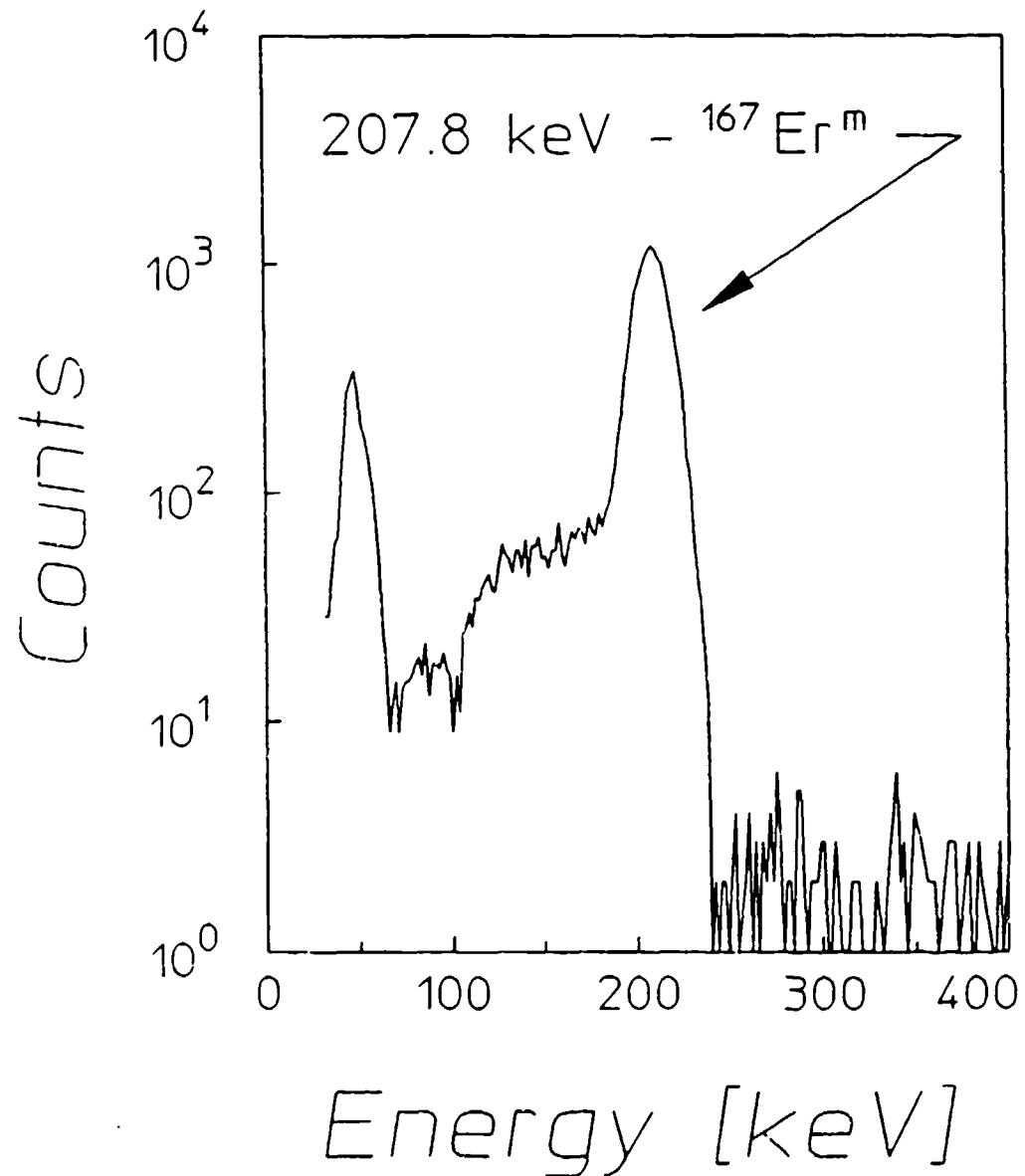


Figure 4: A typical pulse height spectrum showing the 207.8 keV fluorescence line from the decay of $^{167}\text{Er}^m$ following a 6 MeV exposure. The spectrum was obtained with a 7.6 cm \times 7.6 cm diameter NaI(Tl) detector having a 5.1 cm \times 2.5 cm diameter well. The sample was irradiated for 25 sec and the counting period was 5 sec in duration. The transport time from the end of irradiation to the start of counting was 2.06 sec.

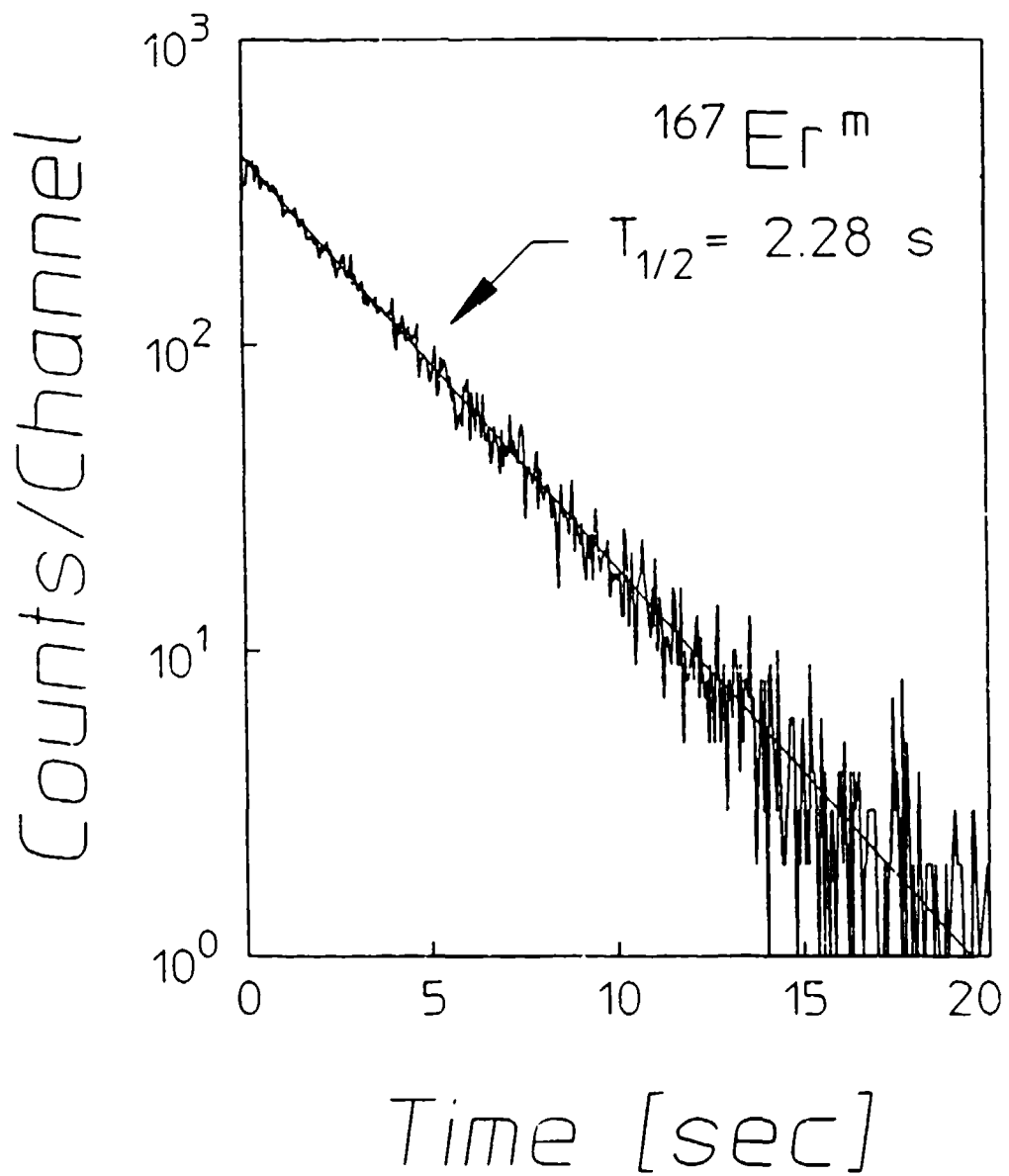


Figure 5: Data typical of the total counting rate measured for $^{167}\text{Er}^m$ as a function of the time elapsed from the start of the counting interval following a 6 MeV exposure. The solid line indicates the decay expected from the literature value of the half-life, 2.28 sec. The spectrum was obtained by recording the number of counts observed in successive dwell intervals of 0.05 sec with a multichannel scalar, and all events above a chosen lower level of discrimination were measured. The counting device was a 7.6 cm \times 7.6 cm diameter NaI(Tl) detector having a 5.1 cm \times 2.5 cm diameter well.

Since the HPGe detector provided greater resolution it was not so necessary to monitor the time decay in detail. For some samples however, energy spectra were acquired after several different elapsed times to provide additional confirmation of the signature identifying the product. This concern was exemplified in measurements of the isomer $^{123}\text{Te}^m$. A pulse height spectrum following a 6 MeV exposure is shown in Fig. 6. The fluorescence line at 159 keV is well defined and gives 5% counting statistics. This was rewarding since there was some concern that the activation might be hidden by the natural background of the counting chamber. Since this was the longest lived isomer ever reported to be excited by a (γ, γ') reaction, the time decay was experimentally determined from a sequence of energy spectra taken after a 6 MeV exposure. The decay of the count rate is shown in Fig. 7. A fit to this data gives a half-life which is in excellent agreement with the literature value.

The remaining nuclide, ^{176}Lu , was examined with a different detection scheme. The ground state of this isotope β^- decays with an endpoint energy of 565 keV and the isomer β^- decays with endpoint energies of 1313 keV (39.6%) and 1225 keV (60.4%). Since the isomer does not return to the ground state by a radiative transition, the number of excited nuclei must be measured by the detection of either β^- particles or the signature photons from the daughter nucleus. This type of deexcitation process is similar to that of ^{180}Ta , which decays by both electron capture and β^- modes.

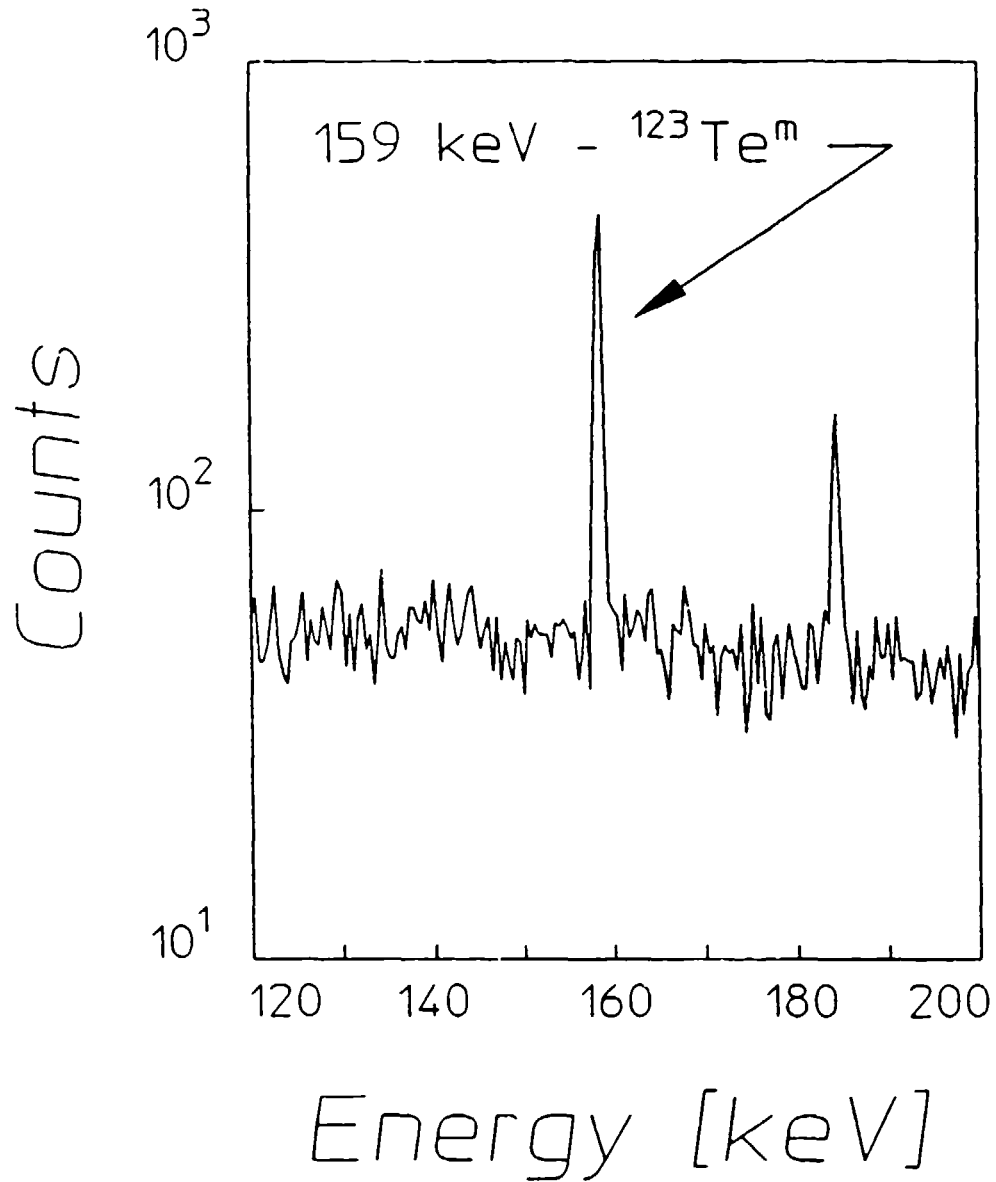


Figure 6: A typical pulse height spectra showing the 159 keV fluorescence line from the decay of $^{123}\text{Te}^m$ following a 6 MeV exposure. The spectrum was obtained with an n-type high purity germanium detector. The sample was irradiated for 2 hours and the counting period was 10 hours. The delay time from the finish of the irradiation to the beginning of the counting period was 22.98 hours.

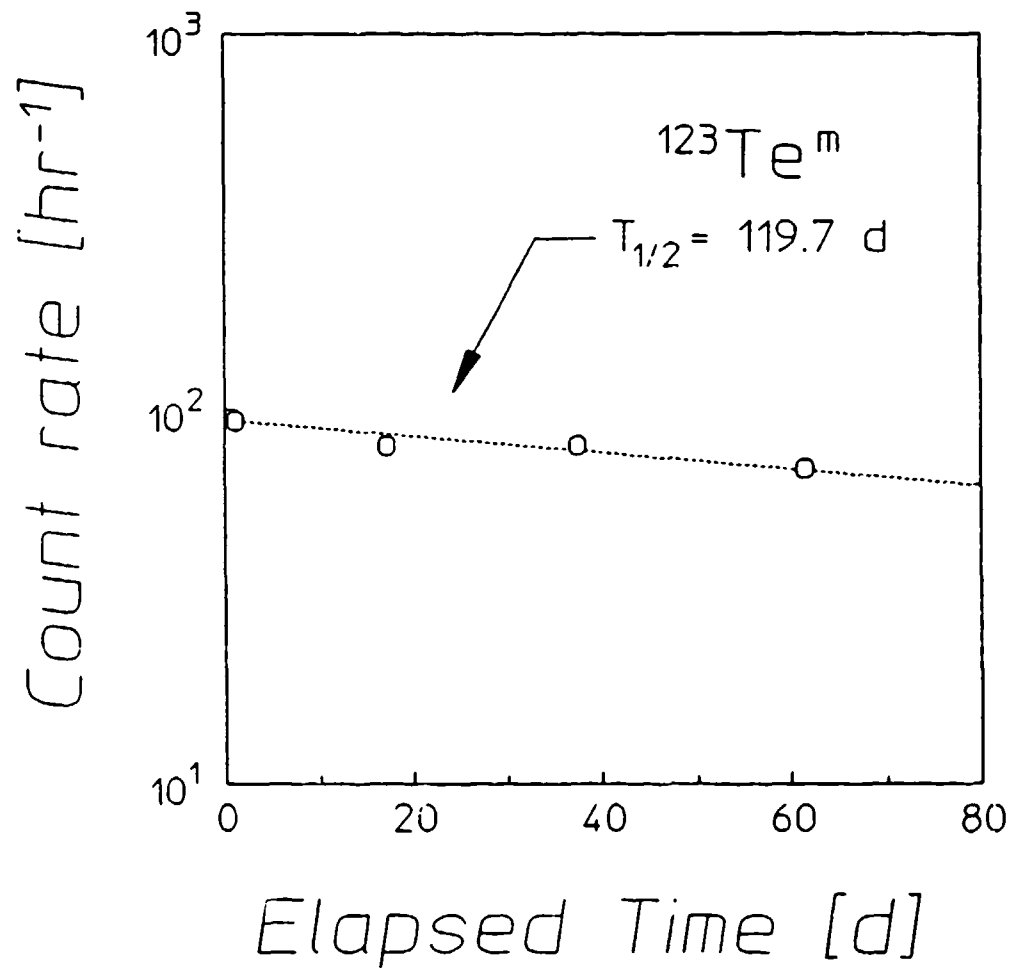


Figure 7: Plot of the time decay of the 159 keV fluorescence line from the decay of $^{123}\text{Te}^m$ following exposure to bremsstrahlung from the 6 MeV linac. The points represent the counting rate observed in several pulse height spectra performed at different elapsed times. The sizes of the symbols are comparable to one standard deviation and the counting periods were all 10 hours. The dashed line indicates the expected decay for a half-life of 119.7 days, taken from the literature, and is in good agreement with the measurements.

In the case of ^{176}Lu , the β^- decay energies allowed the use of a Cerenkov detector. Samples consisting of LuCl_3 , dissolved in distilled water, were contained in polyethylene scintillation bottles. The Cerenkov threshold in water is about 250 keV and β^- particles emitted in the decay of the isomeric states were nearly 10 times more efficient in producing Cerenkov events than those emitted from ground state nuclei. Photons from these events were measured by a system consisting of two RCA 8850 photomultiplier tubes in EG&G bases. The tubes were used in a coincidence mode by connecting their time synchronized outputs through a 150 MHz Phillips 755 logic unit, thereby recognizing only coincident signals from the Cerenkov photons produced by single β^- particles. These output pulses were recorded as functions of elapsed time in multichannel scalar spectra where each channel represented a dwell time of 40 sec. The detector was calibrated with ^{40}K decays from a KCl solution of known activity, since the resulting β^- particles had roughly the same endpoint energy as those from $^{176}\text{Lu}^m$. In these measurements, the individual count rates were monitored to avoid contributions from accidental coincidences triggered by separate β^- events or by thermoluminescence from the material of the bottle. A fit to the experimental data shown in the typical spectrum of Fig. 8 produced a value for the half-life for $^{176}\text{Lu}^m$ of 3.58 ± 0.05 hours, which was in good agreement with the literature value of 3.63 hours. The observed count rate was corrected back to the time immediately following the exposure and the number of isomers was determined as previously described.

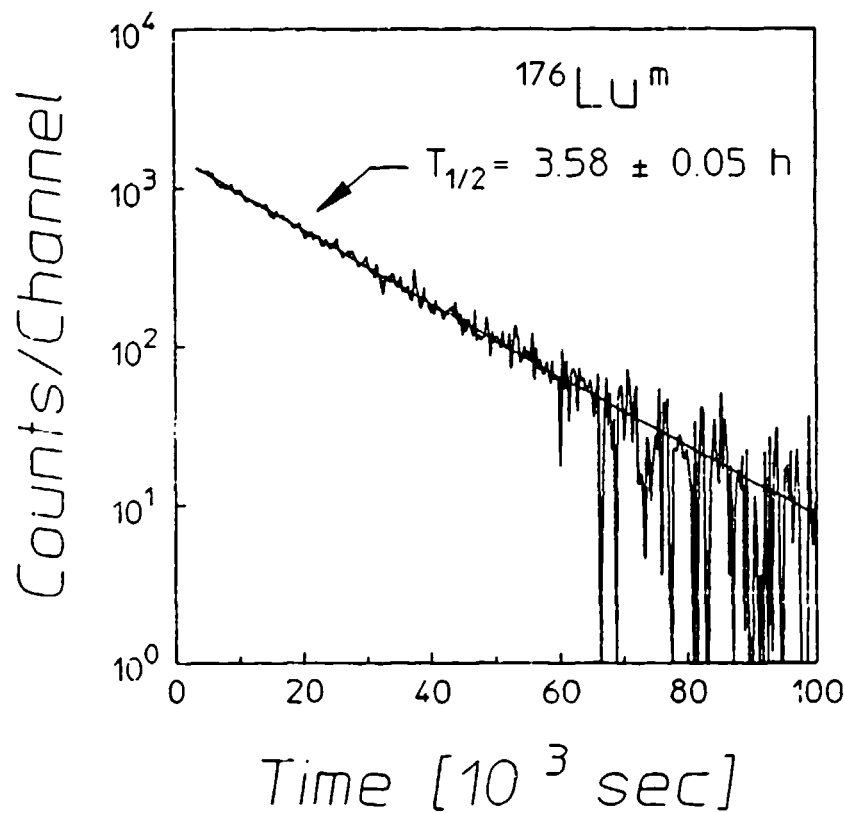


Figure 8: Data typical of the total counting rate measured for $^{176}\text{Lu}^-$ as a function of the time elapsed from the start of the counting interval following a 6 MeV exposure. This result was obtained by recording the number of counts observed in successive dwell time intervals of 320 sec with a multichannel scalar. The device used to make these measurements consisted of two RCA 8850 photomultiplier tubes operated in a coincidence mode as discussed in the text. The sample was irradiated for 40 minutes and the delay time from the finish of the irradiation to the beginning of the counting period was 53 minutes. A fit to the data is shown by the solid line and gives a half-life of 3.58 ± 0.05 hours, in good agreement with the literature value of 3.63 hours.

RESULTS

Strontium as a Benchmark

Normalized activation measurements obtained from all four accelerators for $^{87}\text{Sr}^m$ are shown in Fig. 9, which also indicates the threshold energy for (γ, n) reactions, E_n , at 8.428 MeV. The datum at 1.2 MeV represents an upper limit since no fluorescence photons were observed above the background level. Although lacking in resolution in the critical range from 1.2 to 6 MeV, the data allows several conclusions to be drawn about the photoexcitation process. Most important is that, even though the amount of normalized activation above 1.2 MeV is surprising, there is no evidence to support the significant participation of any non-resonant processes. This type of mechanism, if present, would be heavily dependent upon the density of nuclear states, which rises sharply at energies approaching E_n . The slow increase in the excitation function above 6 MeV relative to the change seen below 4 MeV would seem to preclude this as the dominant means of photoexcitation.

The large increase in normalized activation from 1.2 to 4 MeV indicates that at least one resonant gateway of significant magnitude lies in that range. The experimental resolution, however, does not allow a clear observation of the activation edges so the details of these states cannot be directly determined. Nevertheless, some inferences can be drawn from the plot of Fig. 10, which shows the effective integrated cross sections determined from both 4 and 6 MeV measurements as obtained from Eq. (10). The intersection near the 4 MeV asymptote implies that the two sets of data are the result of photoexcitations dominated by different gateways. Therefore, an additional gateway with an integrated cross section larger than any lying below 4 MeV must exist between 4 and 6 MeV.

Fortunately, the isomer $^{87}\text{Sr}^m$ is distinguished by the degree to which its photoexcitation has been characterized in the literature. An early work,¹⁸ which used an x-ray source of the type no longer available, examined the production of this isomer by bremsstahlung with endpoints which could be varied up to 3 MeV. The tunability of that device allowed three distinct gateways to be identified at 1.22, 1.88, and 2.66 MeV, and their integrated cross sections to be measured. In the usual units of $10^{-29} \text{ cm}^2\text{-keV}$, these were found to be $(8.5 + 4 - 3)$, $(16 + 8 - 5)$ and $(380 + 200 - 100)$, respectively.

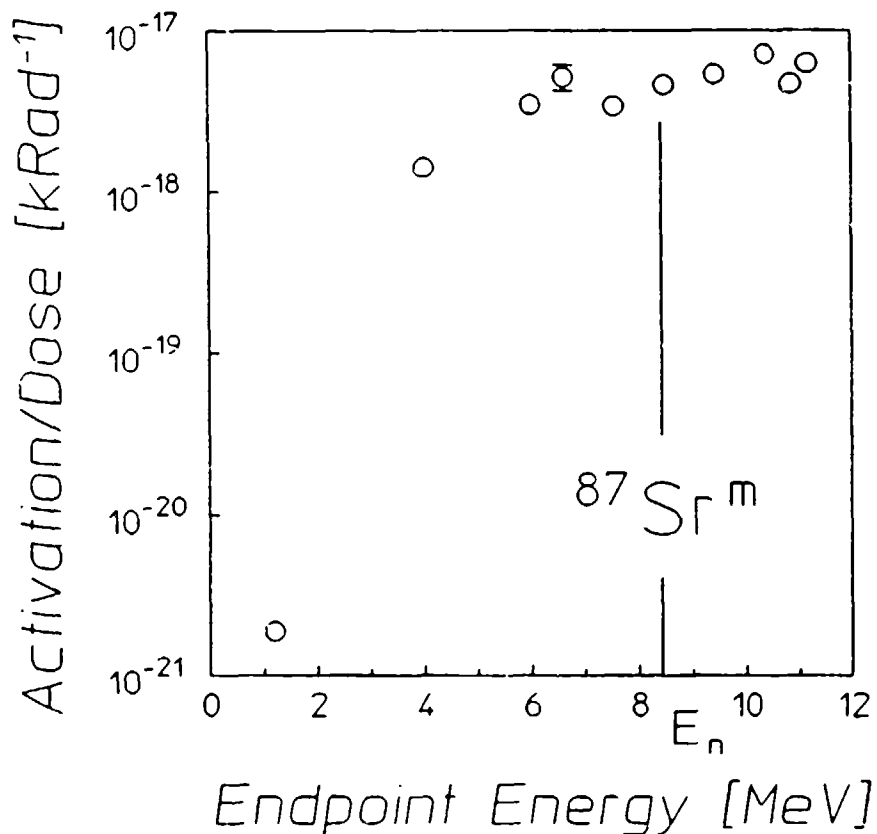


Figure 9: Normalized activation obtained from irradiations with all four accelerators for $^{87}Sr^m$. The size of the symbols is comparable to the standard deviation except where error bars are explicitly shown. The point at 1.2 MeV determined from a DNA/PITHON exposure is an upper bound on the excitation since no fluorescence photons were observed above the level of background. The vertical line indicates the neutron evaporation threshold at $E_n = 8.4$ MeV.

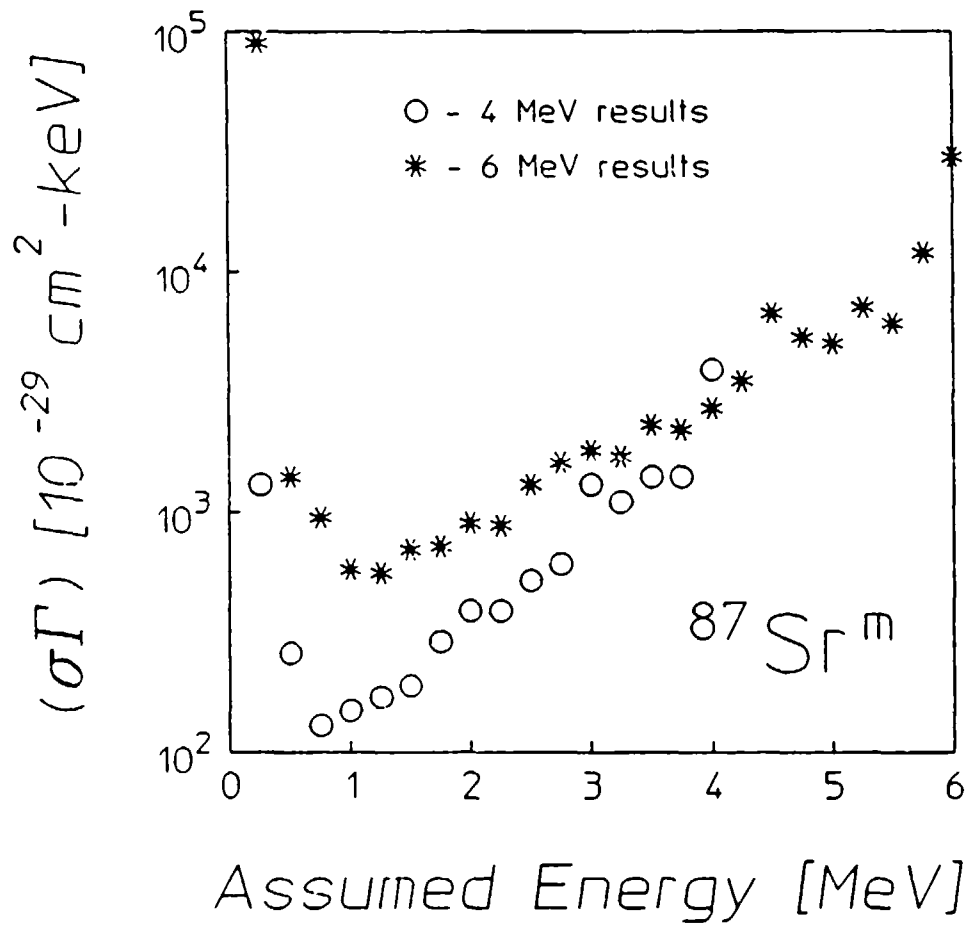


Figure 10: Integrated cross sections for the reaction $^{87}\text{Sr}(\gamma, \gamma')^{87}\text{Sr}^m$ through single, unknown gateway states as functions of the energies at which these states could be assumed to lie. The circles indicate the results of measurements using the 4 MeV linac while the asterisks show those from the 6 MeV experiments.

Figure 11a shows the ^{87}Sr data together with the normalized activations that should have been excited through the known gateways by photons with energies below 4 MeV. These values were calculated from Eq. (5) for many endpoint energies by using typical bremsstrahlung spectra scaled from those shown in Fig. 3. The composite graph produced in this way exhibits the required activation edges at 1.22 and 2.66 MeV in agreement with the actual measurements. No edge is apparent at 1.88 MeV, but this is due to the comparable magnitude and proximity of this level to the one at 1.22 MeV.

The correlation of the expected values near 4 MeV with the datum there indicates that no new states are required to explain all of the normalized activation obtained with the 4 MeV linac. This is in agreement with the preliminary conclusions reached by considering Fig. 9, as discussed above. Figure 10 gives an integrated cross section of $610 \times 10^{-29} \text{ cm}^2\text{-keV}$ for a single state lying between 2.5 and 2.75 MeV, only about one standard deviation above the known dominant level. Although this is an overestimation due to contributions of the other states, it is acceptable when compared to the literature value of $(380 \pm 100) \times 10^{-29} \text{ cm}^2\text{-keV}$. This agreement is far better than that between the measurements of Refs. 4-6.

The data above 6 MeV in Figs. 9 and 11a significantly exceed the photoexcitation which could have been produced through the three known gateways. This extra activation must have therefore represented (γ, γ') reactions which proceeded through one or more unidentified levels. The simplest picture which matches the data is that of a single gateway near 5 MeV with an integrated cross section of the order of $4000 \times 10^{-29} \text{ cm}^2\text{-keV}$. The normalized activation expected from this state, as well as those previously identified, is shown in relation to the experimental data in Fig. 11b.

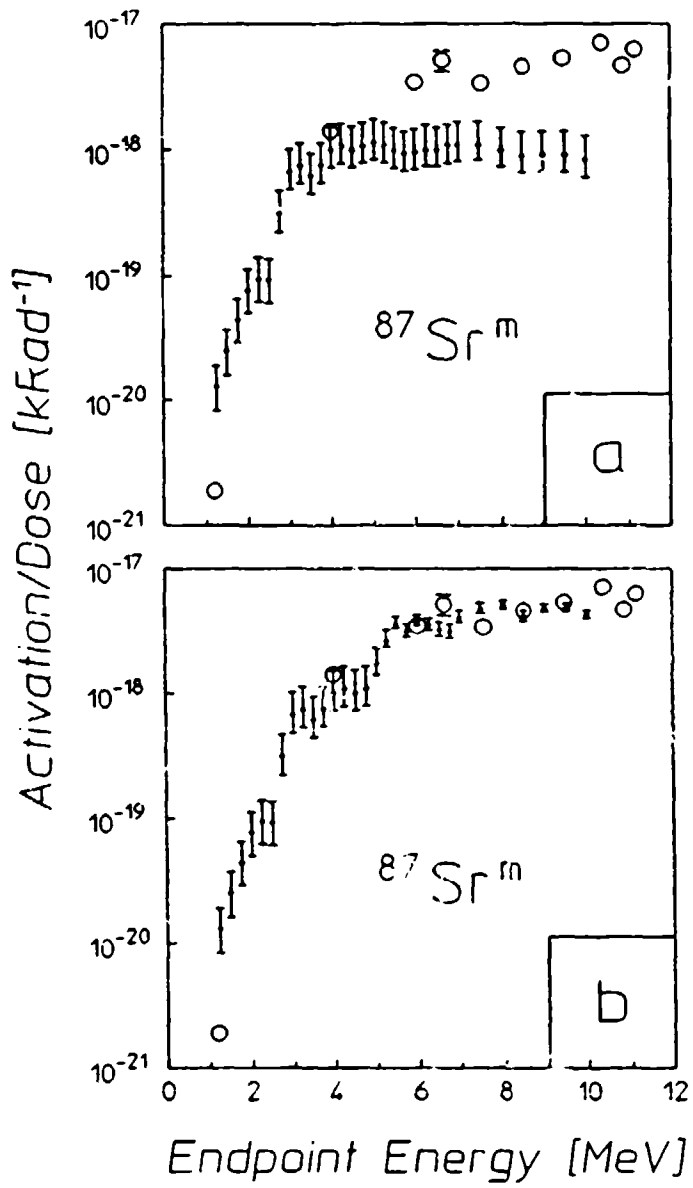


Figure 11: Normalized activation obtained from irradiations with all four accelerators for $^{87}\text{Sr}^m$ as previously shown in Fig. 9. Also displayed are excitation functions calculated from Eq. (5) for:

- Expected photoexcitation through only the three known gateways of Ref. 18. The error bars indicate the uncertainties in the measurements of $(\sigma\Gamma)$ in that work.
- Expected photoexcitation through the three known gateways plus that of a hypothetical state near 5 MeV with integrated cross sections on the order of $4000 \times 10^{-29} \text{ cm}^2\text{-keV}$. The error bars indicate only the uncertainties in the measured $(\sigma\Gamma)$ of Ref. 18.

The nuclide ^{87}Sr provides a benchmark for other (γ, γ') studies since this is the only instance in which the current work can be compared with earlier experiments over a significant range of energies. It is rewarding that the present measurements of the photoexcitation of $^{87}\text{Sr}^m$ below 4 MeV are completely explained by resonant absorption of photons through gateways already reported in the literature.¹⁸ The previous identification of these states has provided a means of validating the interpretive approach described above. Clearly, data as shown in Figs. 9 and 10 can give useful indications of the locations and integrated cross sections of participating resonances even when insufficient experimental resolution is available for a precise determination of these quantities.

Nuclide Survey

All of the nuclei of Table I were irradiated with the DNA/PITHON accelerator. The normalized activations we observed were generally on the order of 10^{-21} krad⁻¹, even after exposures made with bremsstrahlung having the highest available endpoint energy for that device. For most of the materials there was little variation in the normalized activations measured over a range of shots. Therefore, in the context of exploring the systematics of the larger resonances responsible for higher energy photoexcitations, these measurements are of limited usefulness. Although they cannot be employed to identify activation edges, they can serve to provide a baseline of activation below the onset of any of the giant gateways. A typical example of this utility is shown in Fig. 12 which displays data obtained for the isomer $^{167}\text{Er}^m$ along with those for $^{87}\text{Sr}^m$.

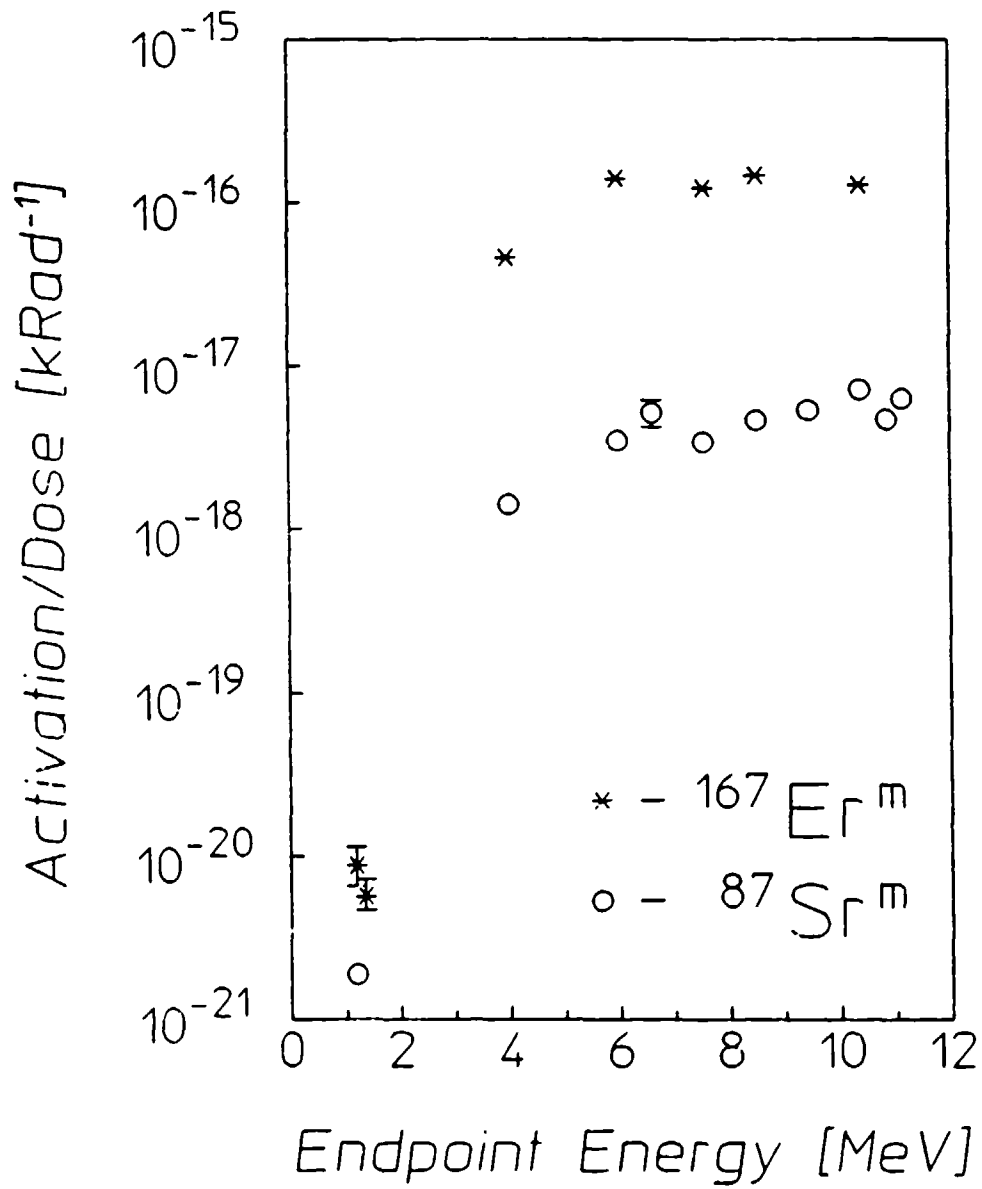


Figure 12: Normalized activation obtained from irradiations with all four accelerators for $^{167}Er^m$. Also included for the purpose of comparison are those values for $^{87}Sr^m$. The size of the symbols is comparable to one standard deviation except where error bars are explicitly shown. The point at 1.2 MeV determined from a DNA/PITHON exposure is an upper bound on the excitation since no fluorescence photons were observed above the level of background. The neutron evaporation thresholds are not indicated for ^{167}Er and ^{87}Sr , but are 6.4 and 8.4 MeV, respectively.

An examination of this plot indicates some interesting behavior. Although the normalized activation achieved with ^{167}Er nuclei is nearly two orders of magnitude larger than that of the ^{87}Sr benchmark, both isomers display similarly slow increases in activation above 6 MeV. This is surprising since non-resonant processes might be expected to be more significant for the photoexcitation of a nucleus as massive as that of ^{167}Er . Nevertheless, resonant absorption appears to be the dominant means of isomeric production for this nucleus as it was for the benchmark nuclide. The increase in normalized activation between the 4 and 6 MeV data strongly imply that a large gateway lies in this range. The magnitude of the data near 1.2 MeV suggests that a smaller activation edge lies below this energy. However, the small number of irradiations makes this assumption difficult to verify.

The measurements obtained from several nuclides, ^{77}Sr , ^{79}Br , ^{111}Cd , and ^{115}In did allow the identification of several resonances below 1.5 MeV. The integrated cross sections of these were found to be on the order of 1 to 10×10^{-29} $\text{cm}^2\text{-keV}$, and these results were reported previously.^{7,8,11,12} A final isotope, ^{179}Hf , while not providing such detailed information, did indicate an activation edge at about 1.1 MeV for its isomer $^{179}\text{Hf}^m$ ($T_{1/2} = 18.68$ sec). Its excitation function is displayed in Fig. 13 and again the relatively slow rise at high energies suggests resonant photoexcitation even for this large nucleus.

With the exceptions of ^{111}Cd , ^{77}Se , and ^{199}Hg , for which data are still being reduced, plots like those of Figs. 9, 12, and 13 for the remaining isotopes in Table I are qualitatively similar. Again, in the context of this study, primary importance is placed on the amount of variation occurring between different endpoint measurements since this may suggest the necessity of particular gateways. This information is given in Table II, in the form of $\sigma\Gamma$ values from Eq. (10). The fractional changes between 4 and 6 MeV measurements and between 6 and 10.4 MeV are also shown as κ_1 and κ_2 , respectively.

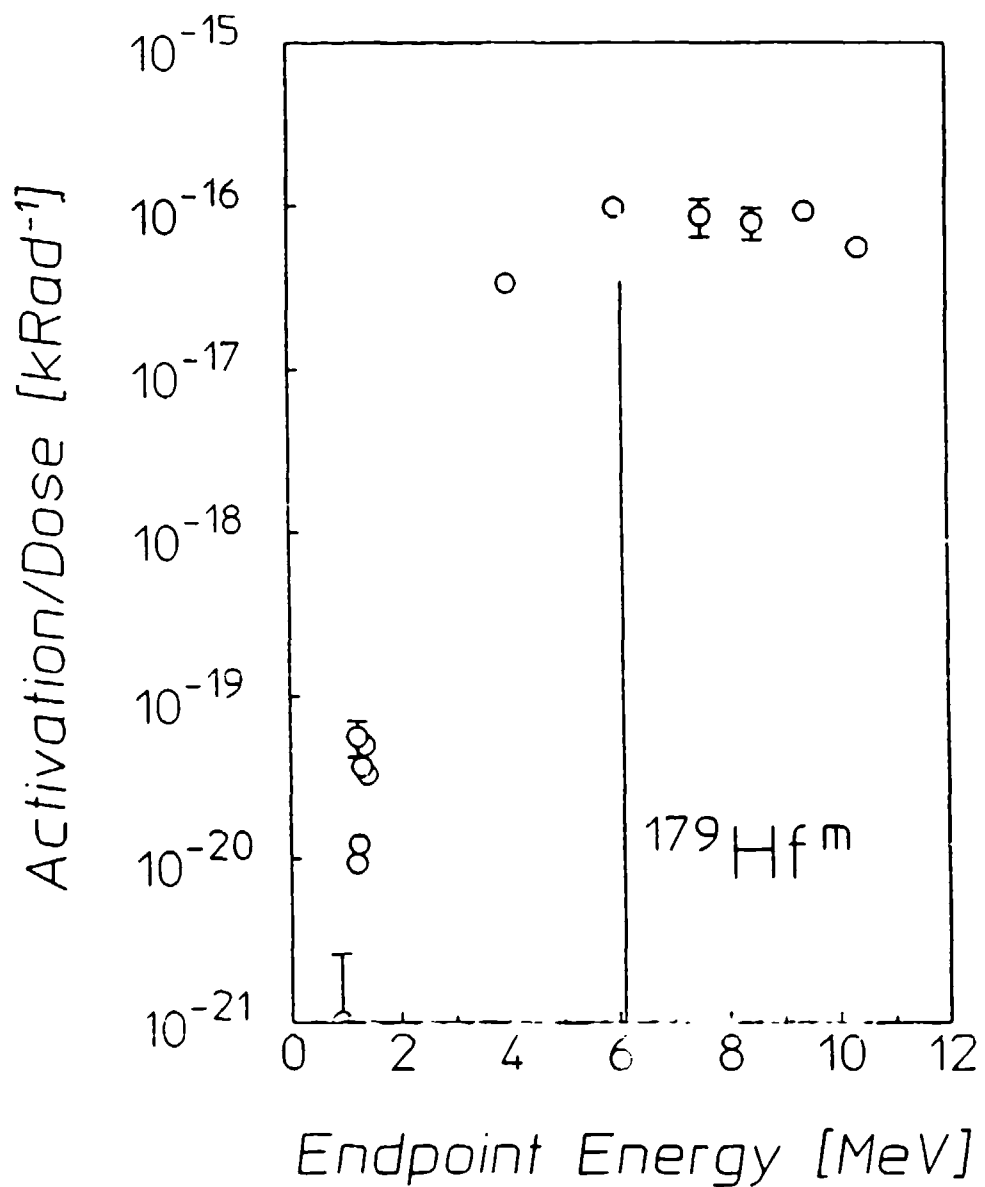


Figure 13: Normalized activation obtained from irradiations with all four accelerators for $^{179}\text{Hf}^m$ ($T_{1/2} = 18.68$ sec). The size of the symbols is comparable to one standard deviation except where error bars are explicitly shown. The vertical line indicates the neutron evaporation threshold at $E_n = 6.1$ MeV.

Table II. Summary of experimental results. The quantity ΔJ is the change in spin between ground state and isomer. For both 4 and 6 MeV irradiations, the integrated cross sections of a single gateway state at the reference energy of 2.125 MeV are given as $(\sigma\Gamma)$ and have been corrected for thermal and epithermal neutron contaminations. The term "units" is used for the sake of brevity to represent units of $10^{-29} \text{ cm}^2\text{-keV}$. The ratio of 6 MeV values to those at 4 MeV are given as κ_1 . The ratio of integrated cross sections obtained from 10.4 MeV to 6 MeV measurements is κ_2 . Also given is the fraction of thermal and epithermal neutron contamination in the total activation, A_n/A_{tot} . The comment NA is used in the column for A_n/A_{tot} when no naturally abundant parent is available for (n,γ) reactions. An entry NA in the κ_2 column indicates that this information is not currently available.

Nuclide	ΔJ	4 MeV			6 MeV			κ_1	κ_2
		$(\sigma\Gamma)$ [units]	A_n/A_{tot} [%]		$(\sigma\Gamma)$ [units]	A_n/A_{tot} [%]			
^{167}Er	3	4600 ± 110	0.01		34000 ± 360	0.32	7.4	1.0	
^{79}Br	3	660 ± 17	NA		1900 ± 23	NA	2.9	1.5	
^{191}Ir	4	7600 ± 610	NA		36000 ± 960	NA	4.7	NA	
^{197}Au	4	2600 ± 40	NA		13000 ± 64	NA	5.0	NA	
^{89}Y	4	9 ± 5	NA		260 ± 8	NA	29	2.9	
^{77}Se	3	330 ± 4	0.03		6500 ± 32	0.76	20	NA	
^{179}Hf	4	9400 ± 120	0.04		25000 ± 110	6.41	2.7	1.1	
^{137}Ba	4	330 ± 23	<0.01		1900 ± 23	0.07	5.8	1.4	
^{199}Hg	6	260 ± 10	0.05		1400 ± 42	5.40	5.4	NA	
^{111}Cd	5	920 ± 12	<0.01		2500 ± 44	0.07	2.7	NA	
^{113}In	4	1300 ± 59	NA		4700 ± 180	NA	3.6	0.71	
^{87}Sr	4	390 ± 13	<0.01		870 ± 18	0.89	2.2	2.3	
^{176}Lu	6	14000 ± 95	0.01		35000 ± 2300	1.51	2.5	NA	
^{115}In	4	1800 ± 16	NA		6700 ± 14	NA	3.7	1.5	
^{180}Ta	8	18000 ± 6600	NA		35000 ± 650	NA	1.9	NA	
^{135}Ba	4	1300 ± 62	<0.01		6000 ± 110	0.3	4.6	4.0	
^{195}Pt	4	3000 ± 160	<0.01		14000 ± 220	0.03	4.7	NA	
^{117}Sn	5	320 ± 47	<0.01		880 ± 26	0.07	2.8	0.84	
^{123}Te	5	4200 ± 730	<0.01		6800 ± 320	1.45	1.6	NA	

Figure 14 displays the effective integrated cross sections for $^{123}\text{Te}(\gamma, \gamma')^{123}\text{Te}^m$ reduced from 4 and 6 MeV measurements. This is the only isotope for which such curves clearly intersect at a location distinct from the 4 MeV asymptote. This plot suggests that normalized activations at both 4 and 6 MeV may have been produced by photoexcitation through the same gateway state near 3 MeV, with an integrated cross section on the order of $14000 \times 10^{-29} \text{ cm}^2\text{-keV}$.

Neutron Excitations

All of the accelerators used, other than DNA/PITHON, were capable of evaporating neutrons from the operational environment. Since neutrons can also excite nuclei into their isomeric states it was important to determine the amount of normalized activation which was attributable to these particles. In principle, two types of neutron reactions could have occurred: inelastic (n, n') reactions which would have required hot neutrons and neutron capture (n, γ) processes driven by fluxes of thermal or epithermal neutrons. Both would have required a primary source of neutrons to have been active during the bremsstrahlung irradiation.

At the photon energies available to the medical linacs, only eight isotopes have thresholds for (γ, n) reactions. Four of these are unlikely and can be reasonably excluded from consideration. The materials used in the irradiation devices and facility were documented, and in these only ^2H , ^9Be , ^{13}C , and ^{17}O were expected to serve as sources of neutrons in the linac environments.

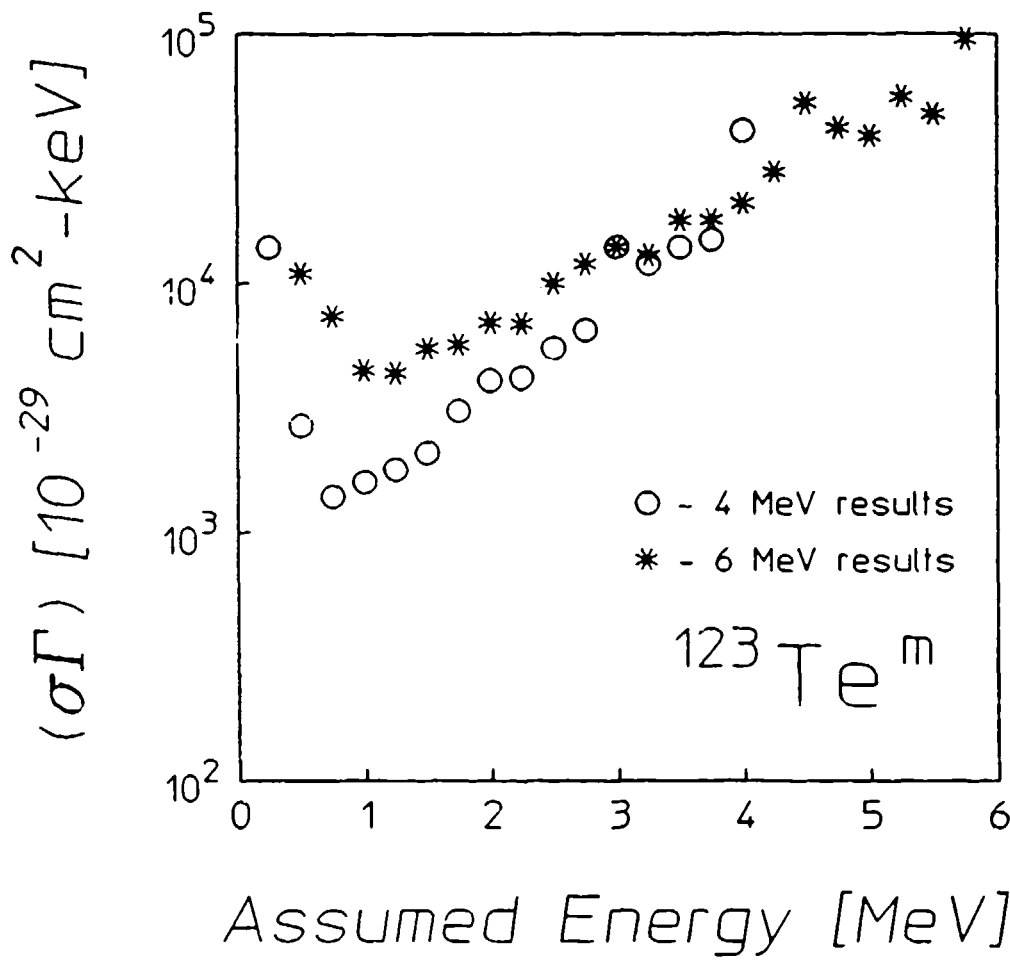


Figure 14: Integrated cross sections for the reaction $^{123}\text{Te}(\gamma, \gamma')^{123}\text{Te}^m$ through a single, unknown gateway state as a function of the energies at which this state could be assumed to lie. The circles indicate the results of measurements using the 4 MeV linac while the asterisks show those from the 6 MeV experiments.

The photon intensity was monitored throughout the course of these experiments, so the flux of primary photoneutrons could be calculated with reasonable accuracy from the following potential sources:

- 1.) a 0.025 cm thick Be window located below the bremsstrahlung converter target in the 6 MeV linac.
- 2.) the ^2H in the cooling water in the bremsstrahlung converter target.
- 3.) the ^2H in the humidity in the chamber and the ^{13}C and ^{17}O in the volume of atmosphere incidentally irradiated.
- 4.) the ^2H , ^{13}C and ^{17}O in the concrete used in construction.

Of these, the first dominated by orders-of-magnitude, giving an expected flux of 10^3 neutrons/cm²-sec at the position of the experimental samples.

The potential activation produced by such a flux is difficult to estimate because the cross sections for (n,n') reactions are poorly known. However, if it is assumed that all of the flux carries at least threshold energy, the cross section $\sigma_{n,100\%}$ necessary to produce all of the measured activation from neutrons can be calculated. These resulting values are summarized in Table III in units of barns and values can be seen to range from tens to thousands. This is to be compared with the few hundreds of millibarns that describe (n,n') reactions in those few cases where measurements have been reported in the literature.

Total neutron cross sections, which certainly must be greater than the inelastic component, are available for all of the materials studied.²² They are summarized in Table III, together with any other cross sections which might bound more closely the value expected for relevant (n,n') reactions that might have contributed in producing the observed isomers.²³⁻³⁰ Finally, in Table III is tabulated the ratio, Ω , which compares the most restrictive upper limit to $\sigma_{n,100\%}$, the cross section for inelastic neutron excitation which would be necessary to explain all of the observed yield.

Table III. Summary of fast neutron contamination limits for 6 MeV irradiations. The fast neutron cross section, $\sigma_{n,100\%}$ is that required to produce 100% of the observed activations. Maximum values for the true total neutron cross section of the element of interest, σ_{tot} , are shown for the energy range 0.1 to 6 MeV. When available, the non-elastic cross section for the element has been shown in parentheses following the elastic cross section. The most restrictive additional cross section, σ_{lim} , for the particular isotope or element is given with its type and E_{max} , the energy up to which it was determined. Cross section types are as follows: ie - inelastic in element; i - inelastic in isotope; n - non-elastic in isotope; fi - inelastic in isotope, average for fission spectrum. The factor Ω is the ratio of the most specific observed cross section to the cross section required for a 100% contamination effect, and thus represents an upper limit for contamination of the neutron effects.

Nuclide	$\sigma_{n,100\%}$ [b]	σ_{tot} [b]	σ_{lim} [b]	Ref.	Type	E_{max} [MeV]	Ω [%]
¹⁶⁷ Er	2700	9	-	-	-	-	0.30
⁷⁹ Br	140	7.5	-	-	-	-	5.4
¹⁹¹ Ir	2590	10.3	-	-	-	-	0.40
¹⁹⁷ Au	95	10	1.3	32	i	5.3	1.4
⁸⁹ Y	20	11.5	0.2	27	i	4.0	1.0
⁷⁷ Se	490	8.3(2.4)	0.73	26	fi	-	0.15
¹⁷⁹ Hf	1940	20	0.4	31	i	1.6	0.02
¹⁹⁹ Hg	120	10(2.6)	0.14	33	i	2.1	0.12
¹³⁷ Ba	130	7.3(2)	0.66	30	i	3	0.51
¹¹¹ Cd	210	8	0.23	26	fi	-	0.11
¹¹³ In	320	6.3	0.047	28	i	1.0	0.01
⁸⁷ Sr	60	10	0.11	26	fi	-	0.18
¹⁷⁶ Lu	2638	7	-	-	-	-	0.27
¹¹⁵ In	430	6.3	0.38	29	i	5.3	0.09
¹⁸⁰ Ta	3016	8.5(2.9)	1.8	32	ie	1.8	0.06
¹³⁵ Ba	420	7.3(2)	-	-	-	-	0.48
¹⁹⁵ Pt	1350	10	0.68	32	ie	1.8	0.05
¹¹⁷ Sn	70	6.8(2)	-	-	-	-	2.9
¹²³ Te	530	6	-	-	-	-	1.1

In effect Ω in Table III is the maximum fractional contamination through the fast neutron channel of the photoexcitation yield. As can be seen, values are generally smaller than 1% and exceptions occur only in cases for which restrictive estimates of (n, n') cross sections are unavailable. For those nuclides the only available values were those describing total processes which certainly bound the (n, n') reactions, but generously so. There is no reason to suspect that the unmeasured inelastic reactions are uniformly so large and that only the smallest appear in the literature. The best resolved are those limiting neutron contributions to a few tenths of a percent. It seems reasonable to conclude that in all cases examined in this work the (γ, γ') channels dominated over (n, n') by orders-of-magnitude for the linac irradiations.

The fast neutron flux expected in these experiments, 10^3 neutrons/cm² sec was too small to confirm by direct measurement at such high levels of irradiation. Nevertheless, in order to completely exclude the possibility of an undocumented emplacement of some strong photoneutron source such as ²³⁵U in the irradiation environment, a measurement was attempted using standard procedures.^{31,32} The (n, p) reactions of ⁴⁶Ti, ⁴⁷Ti, and ⁵⁸Ni are well-documented and provide clear signature photons for convenient periods of decay. These nuclei are not affected by the photon beam in this energy range but they are sensitive to fast neutrons, producing the daughters ⁴⁶Sc, ⁴⁷Sc, and ⁵⁸Co respectively.

In this measurement, the foils were irradiated, removed to the HPGe detector and counted to obtain pulse height spectra. In these spectra no signature photon peaks from the daughters were evidenced at any levels above the background of the counting chamber. It was therefore possible to obtain from this null result only an upper bound on the fast neutron flux at the sample position, which was 7×10^4 neutrons/cm²-sec.

As can be seen, the limit established by measurement is not particularly restrictive, being 70 times larger than the calculated values of fast neutron flux. Even if the limits of contamination in Table III are raised by this factor of 70, at least half of the samples would still be affected by errors of less than 10%. Only in the case of unknown inelastic cross sections for (n, n') reactions which closely approach the total values shown in Table III could an undocumented sample of rare material have produced a level of fast neutron flux sufficient to

contaminate the results of the (γ, γ') reactions being studied. Such occurrences would have required the coincidence of very improbable circumstances and merit no further consideration. That so little fast neutron contamination occurred from use of the 6 MeV linac precluded any possibility of significant effects of fast neutrons in the 4 MeV experiments.

Contributions to the observed activations from (n, γ) reactions could be directly determined. The thermal and epithermal neutron fluxes due to the 6 MeV linac, Φ_{th} and Φ_{ep} , were measured in that environment by irradiating two thin indium foils, one of which was shielded from thermal neutrons by a cadmium cover. In accordance with standard techniques,³³ energy spectra obtained from these foils were examined after exposure for signature photons from the isomer $^{116}\text{In}^m$, which is produced by a branch of the reaction $^{115}\text{In}(n, \gamma)^{116}\text{In}^m$.⁹ The magnitudes of the fluorescence lines observed in both the bare and the shielded samples allowed the determination of the neutron fluxes $\Phi_{th} = 12$ neutrons/cm²-sec and $\Phi_{ep} = 6$ neutrons/cm²-sec from literature values of the thermal and epithermal neutron cross sections.³⁴ The neutron fluxes from the 4 MeV linac were bounded in a similar way. A bare indium foil was exposed, but later showed no photopeaks from $^{116}\text{In}^m$ above the background. Upper bounds for the neutron fluxes were found by assuming for the 4 MeV environment the same 2:1 ratio of thermal to epithermal neutrons found at 6 MeV. The activation was taken to be just below the level of noise and gave $\Phi_{th} \leq 6$ neutrons/cm²-min and $\Phi_{ep} \leq 3$ neutrons/cm²-min during operation of the 4 MeV linac. The small amount of activation of each of the isomers due to these neutrons was subtracted from the total activation observed. In no case did the contribution from thermal and epithermal neutrons in the 4 MeV environment exceed 0.05%. The thermal and epithermal neutron fluxes in the 6 MeV chamber produced contributions below 1.5% for all isomers except for $^{179}\text{Hf}^m$ (6.4%) and $^{199}\text{Hg}^m$ (5.4%). Even in these materials, it is apparent that photoexcitation was the dominant mechanism for the observed activation. The contributions to the activation from thermal and epithermal neutrons is summarized in Table II for each of the 19 nuclides studied.

In the DNA/Aurora environment the target chamber consisted of a large concrete room in which the most intense and high energy photons propagated in an essentially horizontal direction.^{35,36} The most intense spot was centered at about 30 cm from the face of the machine, and was located approximately 1.2 meters above the floor of the 5 meter high

chamber. The wall towards which the beam was directed was 19.5 meters away from the sample position. This geometry contributed two factors of importance. First, if fast neutrons were produced by (γ, n) reactions in the bremsstrahlung field, the lack of dense moderators near the samples made it unlikely that a significant thermal or epithermal neutron flux was present. Second, of the materials within the target chamber only ^2H , ^{17}O , ^{13}C , and ^{181}Ta were likely neutron sources since their neutron binding energies are less than the maximum photon energy produced by the accelerator, about 11 MeV. Clearly the most probable source of fast neutrons in the target chamber was the tantalum, with a neutron binding energy of 7.61 MeV. This assumption allowed the maximum neutron energies to be found from the endpoint energies of the bremsstrahlung produced at different charge voltages. Table IV lists these values.

A determination of the slow neutron flux was made by examining the energy spectra of samples containing natural abundances of the isotopes ^{197}Au and ^{115}In . These nuclei are susceptible to the capture of thermal and epithermal neutrons and produce the daughter nuclei ^{198}Au and ^{116}In , whose decays are marked by distinct signature lines. The spectra of the gold samples showed no evidence of full energy peaks above the level of the background at the fluorescence energies of either the ground or isomeric states of ^{198}Au . On the other hand, spectra of indium samples obtained following shots at 100 kV charge voltage did contain very small peaks at the fluorescence energy of 1097.29 keV from the decay of $^{116}\text{In}^m$ ($T_{1/2} = 54.15$ min). The numbers of counts in these peaks were used to calculate the normalized activation of this species for 100 kV shots and the slow neutron flux which corresponded to this amount of excitation, $\Phi_{\text{slow}} = (1680 \pm 310)$ neutrons/cm²-krad. The latter calculation was made by using the thermal neutron cross section rather than the larger epithermal resonance integral.³⁴ This was done in order to achieve an upper bound on the number of slow neutrons since it was not possible to determine the proportions of thermal to epithermal neutrons from the targets exposed.

Table IV. Summary of various energy parameters estimated for the charge voltages employed in these experiments. The values given for E_{end} are the approximate endpoint energies of the bremsstrahlung produced by DNA/Aurora. The quantity E_{max} indicates the maximum possible energy for neutrons produced through (γ, n) reactions.

Charge Voltage [kV]	E_{end} [MeV]	E_{max} [MeV]
70	6.61	0.00
80	7.56	0.00
90	8.50	0.89
100	9.44	1.83
110	10.39	2.78
115	10.86	3.25
118	11.14	3.53

The projected number of slow neutrons produced during a 118 kV shot was found by scaling the 100 kV value by a factor of 1.92 which represented the rise in maximum neutron energy between these charges. The slow neutron flux for the 118 kV shot was determined to have been (3240 ± 610) neutrons/cm²·krad. The measurements of photoexcitation for the nuclei ⁷⁹Br, ⁸⁹Y, ¹¹³In, ¹¹⁵In, and ¹⁸⁰Ta were free from slow neutron contamination since there are no naturally abundant parents for (γ ,n) reactions.³⁷ The largest neutron capture cross section for the production of the remaining isotopes in Table I is 100 barns,³⁴ the resonance cross section for ¹⁶⁷Er, and therefore at the highest charge voltage the amount of isomeric activation due to slow neutrons was only 3.24×10^{-19} krad⁻¹. Thus even in the most critical case, less than 1% of the total activation, on the order of 10^{-16} krad⁻¹, was provided by slow neutrons.

The number of fast neutrons produced in the target chamber was found in a similar way. Spectra of samples which contained natural abundances of ⁸⁰Se, ⁸²Se, ¹⁰⁹Ag, and ¹¹⁶Cd were examined for any sign of the decay signatures of the daughter nuclei ⁸⁰As, ⁸²As, ¹⁰⁹Pd, and ¹¹⁶Ag which are produced by (n,p) reactions. No such signatures were found above the background level. Nevertheless, it was possible to obtain an upper bound on the numbers of each daughter produced by considering the maximum size of a fluorescence peak which could be hidden by statistical fluctuations of the background. The (n,p) reaction cross sections²² appropriate to the maximum neutron energies were then used to determine upper bounds on the fast neutron flux. When the scaling of the maximum neutron energies was taken into account, the most restrictive upper bound was obtained for the reactions ⁸⁰Se(n,p)⁸⁰As and ⁸²Se(n,p)⁸²As at 100 kV. The fast neutron flux at this charge was found to be $\phi_{\text{fast}} = (2090 \pm 660)$ neutrons/cm²·krad. The number of fast neutrons scaled to 118 kV was then (2660 ± 840) neutrons/cm²·krad. The largest fast neutron cross section for the elements examined in these experiments are on the order of tens of barns, values much greater than the inelastic cross sections for the particular isotopes in question. The amount of fast neutron activation of these nuclei was therefore on the order of 10^{-20} krad⁻¹, and again the neutron contamination was negligible.

CONCLUSIONS

The principal conclusion of this work is that a combination of technical and computational advances has made possible the study of (γ, γ') reactions with greater precision than had been possible in the classical works appearing in the literature. The pernicious lack of convergence of those earlier measurements is now understood to have been a consequence of unexpected intensities of continua in the spectra of the photon sources being used. The results reported here show that when the most current technology is applied to the characterization of the irradiations, the amounts of activation achieved with different accelerators are consistent. Moreover, in the uncontested case¹⁸ of the reaction $^{87}\text{Sr}(\gamma, \gamma')^{87}\text{Sr}^m$ the current results from the four accelerators are in complete agreement with the literature.

This reaction for the photoexcitation of $^{87}\text{Sr}^m$ is particularly important as a benchmark. Up to a bremsstrahlung endpoint energy of 4 MeV, the activations produced in the strontium samples were completely consistent with the 1967 measurements¹⁸ of three gateways at 1.22, 1.89, and 2.66 MeV. This was shown in Fig. 11a. As seen in Fig. 11b, only one additional gateway was needed between 4 and 6 MeV to explain all of the remainder of the data up to 11 MeV.

Since the density of excited states increases exponentially with excitation energy, it might have been reasonably expected that the number of gateway states for the photoexcitation of isomers would also increase to very high values. However, such a possibility does not seem to be supported by the data obtained in our experiments, as typified in Figs. 9 and 11a. There seems to be a discrete state or compact band of states in the 4 to 11 MeV range contributing the single jump in activation observed between 4 and 6 MeV. A phenomenon so localized in energy can be usefully described in terms of an effective integrated cross section, $\sigma\Gamma$, for the photoexcitation of isomers, as was defined in Eq. (10). Of course, for a nuclide such as ^{87}Sr where there are two major gateways, the value of $\sigma\Gamma$ obtained with bremsstrahlung having an endpoint energy great enough to excite both will be larger than what would be measured with bremsstrahlung able to excite only one. Just this result is seen in Table II for ^{87}Sr , as well as for several other nuclides.

The most surprising conclusions of this work is that some of the integrated cross sections for exciting isomers are extraordinarily large, approaching 10^{-21} $\text{cm}^2\text{-eV}$. Typified by the reaction $^{167}\text{Er}(\gamma, \gamma')^{167}\text{Er}^m$, these also seem to occur through discrete gateways or through narrow bands of gateway states. The data of Fig. 12 has a compelling resemblance to that for the excitation of one of the gateways in ^{87}Sr . The same sharp jump in activation with increasing x-ray endpoint is followed by relatively level yield up to 11 MeV. It is possible to fit the data of Fig. 12 with a single gateway near 4 MeV but more detailed considerations suggest there are two gateways in ^{167}Er . On the other hand, the excitation function for the reaction $^{179}\text{Hf}(\gamma, \gamma')^{179}\text{Hf}^m$ shown in Fig. 13 seems compelling in suggesting a single jump in activation at energies below 4 MeV.

Figures 10 and 14 show plots of the integrated cross sections of single gateway states as functions of the energies at which they might lie as found in both 4 and 6 MeV linac experiments. An examination of these graphs reveals the interesting feature that the 4 and 6 MeV curves intersect. The curves must always cross at some energy less than or equal to 4 MeV since each is generated in part by inverting the function $F(E)$. Whenever the crossing point falls at 4 MeV, this behavior is simply due to the linear independence of the two irradiating spectra: above 4 MeV, $F(E)$ is zero for the output of the 4 MeV linac while $F(E)$ is non-zero for the 6 MeV spectrum. This provides an asymptote at 4 MeV for curves generated for all isotopes. However, in cases where the intersection point lies below 4 MeV some information regarding the location of a dominant gateway may be inferred. Assuming, for example, that photoexcitation in some nuclide is dominated by a single gateway at 2.5 MeV for photon energies up to 6 MeV, the 4 and 6 MeV integrated cross section curves will become equal near 2.5 MeV. The appearance of such a crossing in the results of experimental observations can be due to other factors, but in some instances may suggest the location of a single, dominant resonant state.

All of the materials studied show some variation in the location of the intersection point, but most lie close to 4 MeV as in the case of ^{167}Er . These likely convey no information about the energy of a dominant gateway. The lowest energy for such a crossing occurs for production of the isomer $^{123}\text{Te}^m$. Examination of Fig. 14 shows that the integrated cross section curves become equal in the vicinity of 3 MeV. This would imply the existence of a single mediating level having an integrated

cross section of 14000×10^{-29} cm²-keV. If this is indeed the case, ¹²³Te^m may form the cornerstone of an extension of the spectral calibration technique used in Refs. 7 and 8 for energies up to 6 MeV.

Of the nuclides examined in this work, those most likely to have single gateway states are those which had the smallest increases in activation in changing from 4 MeV bremsstrahlung to 6 MeV. The ratios of values of $(\sigma\Gamma)$ which determine the activations with 6 MeV endpoints to those from 4 MeV endpoints are shown in Table II as κ_1 . The smaller values represent the behaviors seen in Fig. 14 that suggests single gateway states.

The difficulties in explaining the sizes of the integrated cross sections reported in this work accrue from the large changes in angular momentum, J separating ground states from isomers. Most of the larger values belong to nuclei which are spheroidal and the projections of angular momentum, K, upon the axes of elongation further inflame the difficulties. With an absorption transition of reasonable probability changes in J and K are limited to $\Delta J \leq 2$ and $\Delta K \leq 2$. While the first might be satisfied by making a transition from the ground state to a high member of a rotational band built upon the final state, the second would be violated because K is conserved within a rotational band. What is needed is a mechanism to mix K values of nuclear levels belonging to rotational bands built upon initial and final states of the (γ, γ') reaction.

It is interesting to speculate that this might occur as a result of couplings to states built upon cores of non-fissioning shape isomers.³⁸ Such states show double minima in energy as functions of elongation, even at low values of spin. At some values of excitation energy the shape of such a nucleus would be unstable and projections upon its principal axes would no longer be conserved. In this way the transition from a K value characteristic of the ground state to one consistent with the isomer might occur by mixing with such a state. In any case the pervasiveness found for the giant values of integrated cross sections for photoexcitation found in this work argues for some type of core property varying slowly with increasing nuclear size. Further work is needed to resolve the precise cause of this phenomenon.

REFERENCES

1. See for example the review, S. S. Dietrich and B. L. Berman, At. Data and Nuc. Data Tables 38, 199 (1988).
2. B. Pontecorvo and A. Lazard, C. R. Acad. Sci. 208, 99 (1939).
3. G. B. Collins, B. Waldman, E. M. Stubblefield and M. Goldhaber, Phys. Rev. 55, 507 (1939).
4. Y. Watanabe and T. Mukoyama, Bull. Inst. Chem. Res. 57, 72 (1979).
5. M. Krcmar, A. Ljubicic, K. Pisk, B. Logan and M. Vrtar, Phys. Rev. C 25, 2097 (1982).
6. I. Bikit, J. Slivka, I. V. Anicin, L. Marinkov, A. Ruydic and W. D. Hamilton, Phys. Rev. C 35, 1943 (1987).
7. J. A. Anderson and C. B. Collins, Rev. Sci. Instrum. 58, 2157 (1987).
8. J. A. Anderson and C. B. Collins, Rev. Sci. Instrum. 59, 414 (1988).
9. *The EGS4 Code System*, Walter R. Nelson, Hideo Hirayama and David W. O. Rogers, SLAC Report 265 (Stanford Linear Accelerator Center, Stanford, Calif. 1985).
10. *ITS: The Integrated TIGER Series of Coupled Electron/Photon Monte Carlo Transport Codes*, J. A. Halbleib and T. A. Mehlhorn, Sandia National Laboratories, SAND84-0573 (1984).
11. J. A. Anderson, M. J. Byrd and C. B. Collins, Phys. Rev. C 38, 2838 (1988).
12. C. B. Collins, J. A. Anderson, Y. Paiss, C. D. Eberhard, R. J. Peterson and W. L. Hodge, Phys. Rev. C 38, 1852 (1988).
13. *Evaluated Nuclear Structure Data File* (Brookhaven National Laboratory, Upton, New York, 1986).
14. C. B. Collins, C. D. Eberhard, J. W. Glesener and J. A. Anderson, Phys. Rev. C 37, 2267 (1988).

15. A. G. W. Cameron, in *Essays in Nuclear Astrophysics*, edited by C. A. Barnes, D. D. Clayton and D. N. Schramm (Cambridge, Univ. Press, Cambridge, 1982), p. 23.
16. A. Richter and W. Ziegler, Private communication.
17. J. J. Carroll, J. A. Anderson, J. W. Glesener, C. D. Eberhard, and C. B. Collins, *Astrophys. J.* 344, 454 (1989).
18. E. C. Booth and J. Brownson, *Nucl. Phys.* A98, 529 (1967).
19. E. Browne and R. B. Firestone, *Table of Radioactive Isotopes*, edited by V. S. Shirley (Wiley, New York, 1986).
20. B. Bernstein and I. B. Smith, *IEEE Trans. Nucl. Sci.* NS-20, 294 (1973).
21. R. Mohan, C. Chui and L. Lidofsky, *Med. Phys.* 12, 595 (1985).
22. *Neutron Cross Sections: Volume II, Curves*, Third Edition, D. I. Garber and R. R. Kinsey, BNL 325 (National Neutron Cross Section Center, Brookhaven National Laboratory, Upton, New York, 1976).
23. A. Calamand, "Cross Sections for Fission Neutron Spectrum Induced Reactions" in *Handbook of Nuclear Activation Cross Sections*, International Atomic Energy Agency Technical Report Series No. 156 (IAEA, Vienna, 1974).
24. E. Ramstrom, *Nucl. Phys.* A315, 143 (1979).
25. H. A. Grench and H. O. Menlove, *Phys. Rev.* 165, 165 (1968).
26. H. C. Martin, B. C. Diven and R. F. Taschek, *Phys. Rev.* 93, 199 (1954).
27. C. P. Swann and F. R. Metzger, *Phys. Rev.* 100, 1329 (1955).
28. G. L. Sherwood, A. B. Smith and J. G. Whalen, *Nucl. Sci. & Eng.* 39, 67 (1970).
29. J. B. Guernsey and A. Wattenberg, *Phys. Rev.* 101, 1516 (1956).
30. K. Sakurai and I. Kondo, *Nucl. Inst. and Meth.* 187, 649 (1981).

31. *ASTM Standard Method for Determining Neutron Flux, Fluence and Spectra by Radioactivation Techniques*, Publication E 261-77 (American Society for Testing and Materials, Philadelphia, 1987), and references cited there.
32. K. H. Beckurts and K. Wirtz, *Neutron Physics*, Trans. by L. Dresner (Springer-Verlag, New York, 1964).
33. *ASTM Standard Method for Determining Thermal Neutron Reaction and Fluence Rates by Radioactivation Techniques*, Publication E 262-86 (American Society for Testing and Materials, Philadelphia, 1987) and references cited there.
34. *Chart of the Nuclides*, Thirteenth Edition, F. W. Walker, D. G. Miller, and F. Feiner, Eds. (General Electric Company, San Jose, Calif. 1983).
35. *The Aurora Bremsstahlung Environment*, K. G. Kerris, Harry Diamond Laboratories Report No. HDL-TM-81-18, Harry Diamond Laboratories, 1981 (unpublished).
36. *Aurora User Guide*, Harry Diamond Laboratories, 1987 (unpublished).
37. *Nuclear Wallet Cards*, J. K. Tuli, (National Nuclear Data Center, Brookhaven National Laboratory, 1985).
38. M. Girod, J. P. Delaroche, D. Gogny, and J. F. Berger, *Phys. Rev. Lett.* 62, 2452 (1989).

ADAPTATION OF A FIXED ENDPOINT ELECTRON ACCELERATOR TO PRODUCE VARIABLE ENDPOINT BREMSSTRAHLUNG

by M. J. Byrd, J. J. Carroll, and C. B. Collins

Center for Quantum Electronics, University of Texas at Dallas

Introduction

The study of the photoexcitation of nuclear isomers through (γ, γ') reactions has been underway for more than fifty years^{1,2} and has yielded a few interesting results. However, in this time the techniques of nuclear spectroscopy employed in these studies have never reached the level of precision that is associated with the analogous optical methods. Experiments carried out in the latter realm are heavily dependent on the use of intense, monochromatic photon sources which are well-characterized over a tunable range of wavelengths. This type of device is not available for (γ, γ') studies since the energies at which these reactions take place are generally on the order of a few MeV. The lack of such a seemingly vital experimental tool is not due to insufficient technology, but is a consequence of the general properties of matter encountered at these higher energies.

Everything is relatively transparent to the high energy photons necessary for photoexcitation studies. For example, even a heavy element like lead has a mass attenuation coefficient of no more than $0.045 \text{ cm}^2/\text{gm}$ for 2 MeV x-rays compared to a value of $123 \text{ cm}^2/\text{gm}$ at 10 keV. This behavior precludes the construction of straightforward devices like x-ray filters or mirrors for use in the MeV range. Also,

the correspondingly small wavelengths make the development of a high energy monochromator impossible. There are no material lattice spacings which produce dispersion of such x-rays.

Another unavoidable factor regards the conversion of the kinetic energy of electrons to photons. Accelerators which produce nearly monochromatic electron beams of a few MeV are commercially available and it is indeed possible to vary the particle energies in these machines. This can be simply accomplished by changing the accelerating field parameters or by using a variable current electromagnet and a leaded slit to select from the distribution of electron velocities available. The magnet would serve to separate electrons having different velocities, and the slit would allow only particles having the desired energy to exit the device. However, the generation of photons introduces a polychromaticity which cannot be avoided due to the particular physical mechanism which governs this process.

Highly energetic, light, charged particles, such as electrons and positrons, interact with matter through the Coulomb field of the nucleus and outer electrons of atoms within a target. This may be described as the exchange of a single virtual photon between the atomic field and the free particle. Bremsstrahlung is produced when energy is lost in the collision through the emission of a real photon.³ The x-ray created in this way will have an energy given by the difference between those of the incident and scattered particles. The probability that a particular energy is lost by an electron in this process is given by the Kulenkampff approximation.⁴ This distribution is a monotonically decreasing function which reaches zero at the kinetic energy of the incident electron. Therefore, even if only one interaction occurs per particle, as in a thin converter target, a continuous bremsstrahlung spectrum is produced which resembles the Kulenkampff function. In contrast, a thicker target produces a more complex spectrum, since there is an increased possibility of multiple interactions. In general, electrons in the original beam lose some, but not all, of their energy in the primary collisions. If secondary bremsstrahlung events occur, each produces photons according to probability distributions with lower endpoints. The final photon spectrum is therefore the result of a convolution of many Kulenkampff distributions arising from both primary and secondary interactions.

There is obviously no way to avoid the polychromicity inherent in MeV photon sources. The only recourse left to an experimenter interested in precise (γ, γ') reaction studies is to use a variable x-ray device which produces a continuum distribution of photon energies up to the endpoint. Machines with this property come in many types, ranging from nuclear simulators driven by Marx banks like the DNA/PITHON and DNA/AURORA accelerators, to variable endpoint linacs like that at NRCC, and the superconducting accelerator at the Technische Hochschule Darmstadt. Each of these can be used to uncover important information by exposing samples to bremsstrahlung having different endpoint energies. In this type of study, the energy range of interest is scanned by tuning the source and the amount of photoexcitation observed reflects the processes through which the (γ, γ') reactions proceeded. If resonant absorption of the incident photons at the energy E provides the dominant channel of excitation in a certain isotope, no activation can be measured following exposure to photons having energies less than E . When bremsstrahlung with an endpoint larger than E is used, activation of the sample can be detected. The sharp rise in the amount of excitation as greater endpoint irradiations are used allows the measurement of both the location and the integrated cross section for the state. Conversely, if the photoexcitation proceeds through a non-resonant channel, the activation rises in a continuous and accelerating fashion as the endpoint energy is increased.

Experiments of the above type have been performed and are documented in the literature,⁵⁻¹³ but their numbers are limited due to the scarcity of these variable endpoint x-ray sources. More numerous are commercial fixed endpoint devices such as medical linacs, and extensive studies have been performed on some nuclides with both 4 and 6 MeV machines.¹⁴⁻²⁵ However, much of the information gained in this way is inferential since only a limited comparison is possible between the activations observed following the irradiations. It is clear that the complete determination of the nature of (γ, γ') reaction processes requires the in-house development of a tunable bremsstrahlung source capable of energies up to at least 4 MeV.

This report describes the hypothetical modification of a linac having an endpoint fixed at 4 MeV in order to accomplish this goal. The tunability can be achieved by a combination of low Z electron beam moderators and a bending magnet. The important problem of characterizing the output of such a device and guiding further refinements in its

design is solved by extensive use of the Electron Gamma Shower code, EGS,²⁶ to simulate the complex electron-photon transport.

Design

There are several key requirements which an x-ray source must satisfy in order to be useful for extensive and detailed photoexcitation studies. These are, in the order of their importance:

- 1) Range of tunability. Previous studies have examined (γ, γ') reactions for photon energies up to about 11 MeV,¹³ but a more detailed examination of photoexcitation from 1 to 6 MeV is needed. The device under consideration here must be sufficiently tunable to scan either all of this range, or a large portion thereof.
- 2) Resolution. Photoexcitation through (γ, γ') reactions proceeds primarily by resonant absorption below 6 MeV.¹⁶ In order to accurately locate the resonances and measure the integrated cross sections of these states, the device must allow good resolution between measurements obtained from different endpoint bremsstrahlung. The maximum allowable step size by which the endpoint may be changed to provide this resolution is chosen to be 0.125 MeV. Of course, an ideal machine would be continuously tunable.
- 3) Intensity. Previous experiments have shown that, for many isomers, the integrated cross sections for excitation through resonant states below 6 MeV are on the order of $10^{-27} \text{ cm}^2\text{-keV}$.¹⁶ Therefore, statistically significant levels of activation can only be reached with a spectral intensity on the order of $10^8 \text{ photons/cm}^2\text{-keV-sec}$ at the resonance energy.
- 4) Experimental convenience. The modification of the original accelerator should not preclude other modes of operation. Also, the changeover procedure between modes should be convenient.

These criteria may be met by modifying a fixed endpoint linac similar to commercially available units designed for medical purposes. Figure 1 shows a sketch of the beam head of a treatment linac configured

in the photon mode. A converter target is placed in the path of the electron beam resulting in the production of intense bremsstrahlung. The conversion efficiency from electrons to photons is roughly 100 to 1 when an x-ray target is used. The resulting field is predominantly forward-lobed, particularly at higher energies, so cone shaped filters are centered in the x-ray path to flatten the photon distribution. Collimating jaws are used to confine the region of treatment. As outlined in the introduction, the endpoint energy of a photon distribution may not be changed. Therefore, a machine being adapted for these purposes must be capable of producing an undisturbed electron beam.

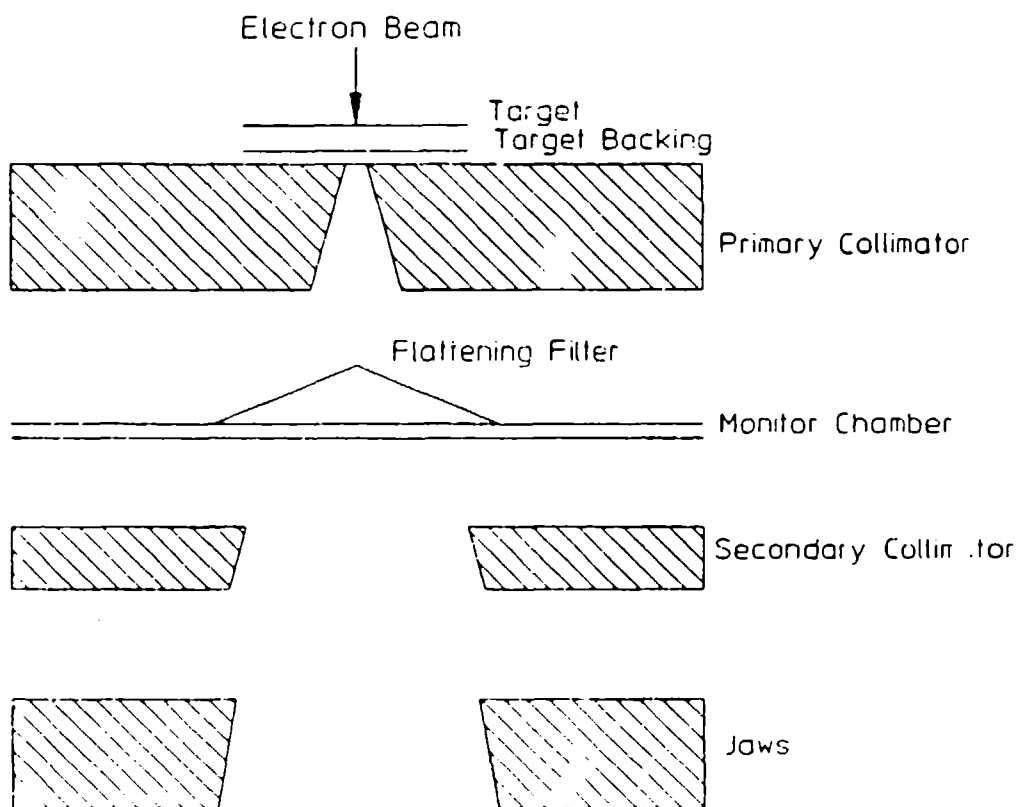


Figure 1: Cutaway view of the beam head of a typical medical treatment linear accelerator operating in the photon mode.²⁷

Although there are medical devices available which yield electrons, they do not conform to the prerequisites listed. First, the beam current is reduced by a factor of 100 to bring the electron induced dose down to a level commensurate with that delivered in the photon mode. Also, a thin foil in the beam path serves to spatially spread the electrons without reducing their energies. Both of these actions tend to limit the intensity of any device based on such a source to levels not useful for (γ, γ') studies.

The foremost alteration of the device then is to secure full beam current in the electron mode without a scattering foil. This is simply accomplished by overriding certain interlocks, a perfunctory change to a device not dedicated to medical applications.

The endpoint energy of a bremsstrahlung distribution depends on the maximum energy of electrons impinging on the converter target. Therefore, the tunability requirement may be fulfilled by demanding that the electron endpoint be variable. The most straightforward means of accomplishing this is to use low Z moderators to degrade the endpoint of the electron distribution prior to conversion.

The energy loss of electrons as they pass through matter is dominated by two processes. One of these mechanisms, termed collisional loss, results in an exchange of energy between the incident particle and the target atom, producing either excitation or ionization. The alternative channel is called radiative loss and corresponds to a transfer of energy from an electron to the surrounding electromagnetic field in the form of a real photon. Each of these processes has a corresponding stopping power, or average energy loss per unit path-length.

When an efficient conversion of electrons to photons is desired, the ratio of radiative to collisional stopping powers should be high. Between 1 and 6 MeV, this ratio is approximately proportional to the atomic number, Z. Therefore, a high Z material is appropriate for the efficient production of bremsstrahlung. Tungsten is the material most often selected for this task.

Conversely, if it is desirable to reduce an electron's energy while minimizing the production of radiation, a low Z material is more

appropriate. In the energy range of interest, the minimum energy loss of an electron passing through such a medium is approximately inversely proportional to the thickness of such a degrader. This is how tunability is achieved in this design. Furthermore, resolution is only restricted by the thinnest increments of degrader material available.

Consider an electron beam incident on a slab of low Z material. Even though the photon flux at the exit plane is very low, the beam on that side is comprised of both photons and electrons. Some of these photons have energies greater than the reduced electron endpoint and are defined as contamination for purposes of this work. A more complex design is therefore necessary in order to separate the degraded electrons from the contaminant photon beam prior to conversion.

Removal of the electrons from the mixed beam is accomplished by applying a magnetic field perpendicular to the beam axis. The magnetic field strength required to bend a 4.0 MeV electron 90 degrees with a radius of curvature of 3.0 cm is 5.0 kG, indicating an electromagnet of very reasonable size. After this bend and some displacement from the converter site, the remaining kinetic energy of the electrons is converted into photons. The geometry is further improved by placing lead collimators between the converter and the sample to be irradiated. Contaminant photons produced at high enough angles to pass through the converter are attenuated by extending the distance between the converter foil and the sample. An overhead view of the final design is shown in Fig. 2, including some simulated electron and photon trajectories.

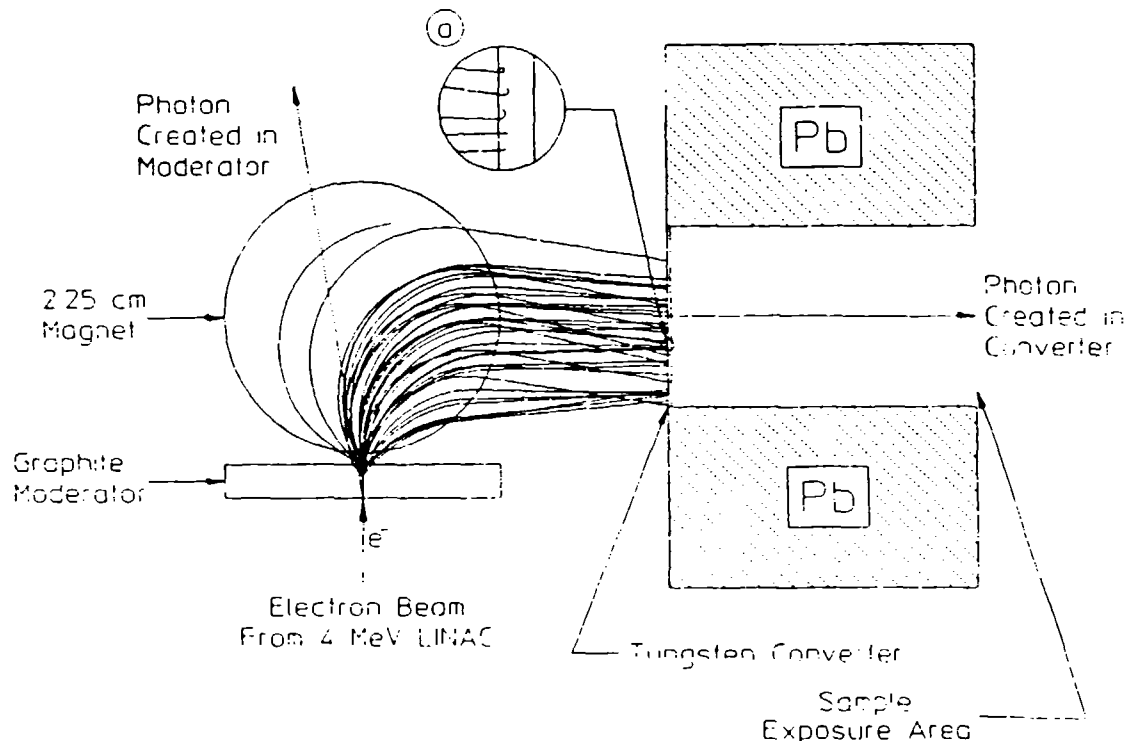


Figure 2: Cross sectional view of variable endpoint bremsstrahlung source. Electron trajectories are shown in solid lines while the dashed lines represent photons. Inset (a) is a closeup of electrons in the converter foil.

This configuration meets the design criteria listed above. However, it is necessary to thoroughly simulate the transport of electrons and photons through all components of this system. These results extend confidence in this design and return quantitative results regarding the actual photon distribution at the sample exposure position.

Simulation Procedures

Most of the computing described here was performed on the Hewlett Packard 9000 Model 560, configured with 4 megabytes of memory and three 32 bit CPU's, each with built-in floating point coprocessors. This computer performed these types of tasks at about 25% the rate of a Convex C1 (CPU time, without implementation of optimizing compiler directives) and at roughly 20 times the rate of an IBM PC/AT with an 80287 math coprocessor.

The coupled electron-photon transport code used is version 4 of the Electron Gamma Shower Code (EGS4), a very general transport program that allows the user to control the initialization, input, output, and geometry checking routines. The actual transport is governed by sophisticated internal electron and photon subroutines. Scattering cross sections, stopping powers, and various other material data are prepared by another program called PEGS (pre-EGS). The PEGS data necessary for this study were generated on a micro-Vax at the University of Texas Southwestern Medical Center.

Earlier versions of EGS were originally intended for higher energy transport than the region of interest here. One artifact of this was carried into version 4 and requires particular attention. Specifically, electron step sizes are too large in the default mode. The authoritative article on the subject²⁸ suggests the remedy of limiting the step size to correspond to a user defined percentage change in the energy of the electron. The procedure that accomplishes this, FIXTMX, was implemented in all of the simulations. Care was taken, in accordance with Ref. 28, to make sure that multiple scattering was not "turned off" by setting the percentage energy change, ESTEPE, too low. Appropriate cutoff energies for secondary electron production, as defined in Ref. 28, were used to prevent the appearance of spurious artifacts in the photon spectra.

Geometry subroutines and macros are included with the EGS4 distribution tape to assist the user in writing the geometry checking routines. Two of those routines, PLANE1 and CYLNDR, were used extensively. The first of these returns whether or not a plane is intercepted by the current particle trajectory, and if so, the distance to the inter-

section. The second is similar, except that it operates on cylinders centered on the z axis. DNEAR is a global variable in EGS that represents the distance to the nearest boundary crossing. The user can override boundary checking when a particle's shortest distance to a boundary is greater than the current step size by setting this variable. This was implemented in some regions, sometimes with as much as a 25% increase in the rate of calculation.

The prototype moderator was modeled first. Graphite was selected as the degrader because it has a low atomic number, is moderately dense, and is commercially available in thin slabs. Our calculations showed that beryllium might be about 35% more efficient for the degradation of the 4 MeV electrons to those around 2.5 MeV, but unfortunately requires special handling because of its toxicity. Also, the question of neutron evaporation can be avoided altogether by using graphite as the moderator material, since its evaporation threshold is 4.95 MeV (for the ^{13}C isotope) while that of beryllium is 1.67 MeV.²⁹ The graphite density used for all calculations was 2.0 g/cm³.

Figure 3 shows the energy distribution for electrons exiting graphite degraders of varying thicknesses. For each of the distributions shown here, 100,000 incident electrons were input. Figure 4 represents the contamination produced in the degrader, showing the angular distribution of photons with energy above the electron endpoint, as registered immediately on the exit plane of the graphite. The results of 750,000 histories were computed and normalized to the estimated beam current of the LINAC, 25 micro-Amps. Channels corresponding to higher angles registered 0 or 1 counts, indicating a very low likelihood of producing contaminant photons at high angles. This feature is used, along with collimator design, to eliminate the possibility of contamination reaching the sample exposure area.

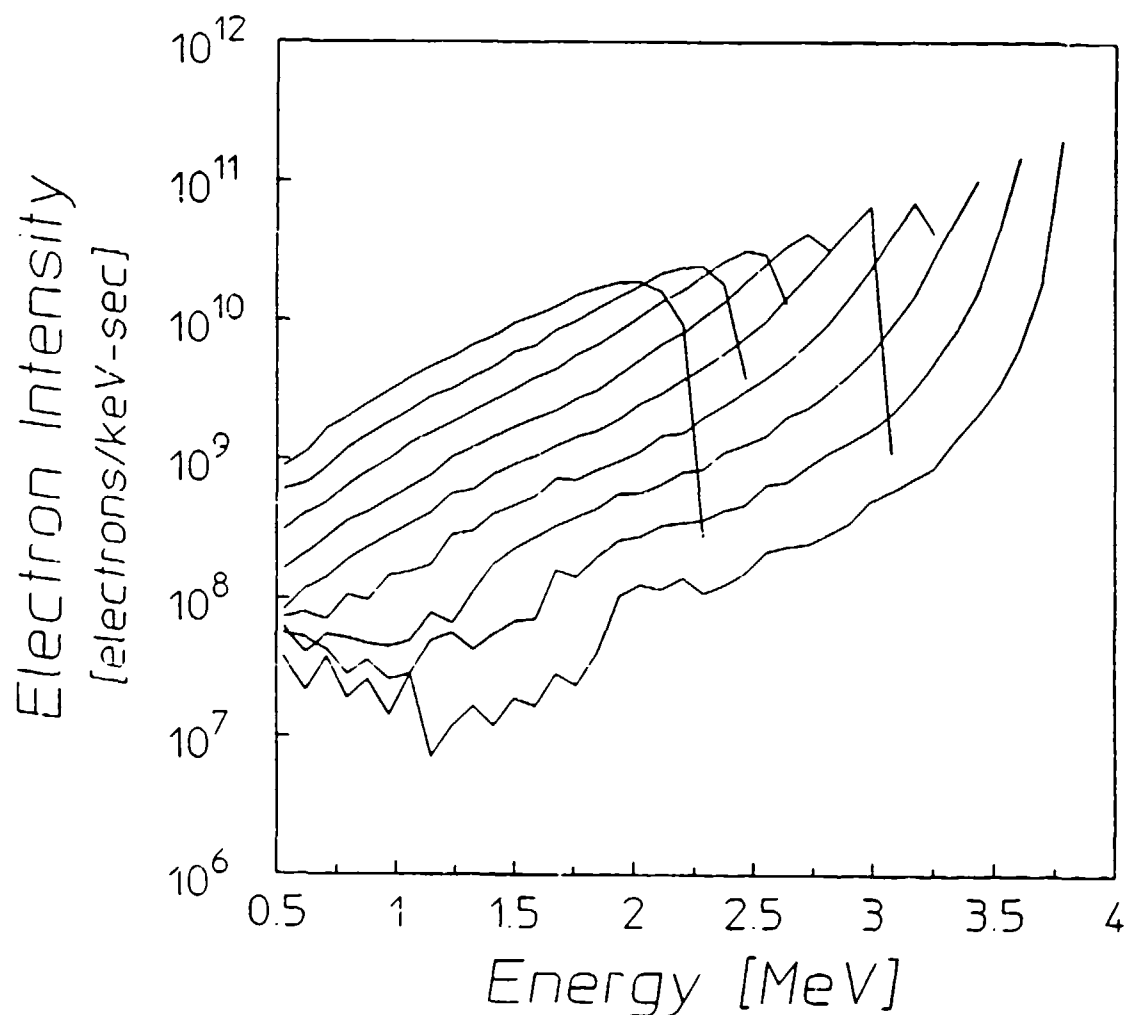


Figure 3: Electron distributions on the exit plane of the degrader slab composed of graphite. Degrader thicknesses vary from 0.07 to 0.63 cm in increments of 0.07 cm. For each curve, 100,000 histories were simulated and the results normalized to a time averaged beam current of 25 μ A.

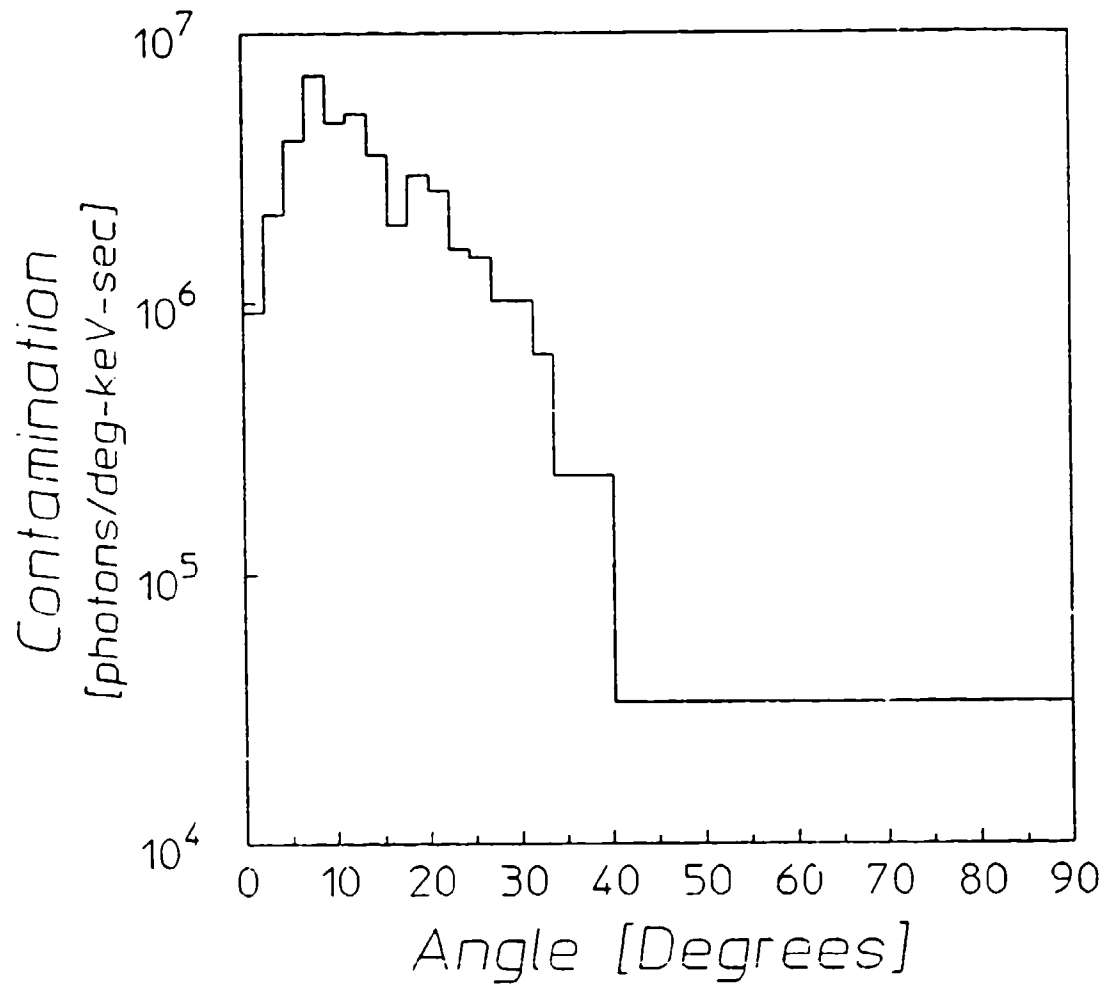


Figure 4: Photons produced in the degrader of energy greater than the electron endpoint. This graph represents the output of 750,000 4 MeV electrons incident on a 0.42 cm slab of graphite, corresponding to an endpoint energy of about 3 MeV. To obtain the same units as Fig. 6, simply divide by $0.11 \times r^2$, where r is the distance from the point of incidence of the electrons on the moderator to the point of observation.

Other segments of the design were then introduced into the simulation, one region at a time. The first of these was the magnetic transport region. Electrons exiting the degrader were transported through a small air interval to a cylindrical region of constant magnetic field in the negative z direction. Field strengths, typically of about 5 kG, were chosen to optimally bend and focus electrons very close to the end-point energy of the electron distributions shown in

Fig. 3. This favors the high end of the output spectrum for reasons that will become apparent in the following applications section.

The magnetic field region is bounded above and below by magnet pole caps assumed to be composed only of iron. The pole spacing was computed using a quadratic least squares fit to data given by the distributor concerning the maximum attainable field strength for a given pole gap.³⁰ The gap between the poles was originally presumed to be air-filled, just as in the magnetic field transport problem outlined in the EGS4 manual.²⁶ The step size required for accurate magnetic field transport, however, was so short that a majority of the simulation time was spent on this region. Most of the electron trajectories in air using the EGS method did not seem to differ much from the paths they would travel in a vacuum. It was therefore decided to model the magnet gap as being a vacuum and to calculate the exit position and direction of the electron based its initial energy, position, and direction (the energy, of course, would remain constant).

Electrons striking the pole pieces in the air-filled gap model were transported until they either exited or fell below the cutoff energy. These electrons did not affect, in most cases, the final output intensity at the sample exposure plane. They did however introduce the possibility of a photon being produced in the magnet pole and passing through the converter to that area. An electron striking the pole in the evacuated gap model was discarded immediately since these do not contribute greatly to the output spectrum. A benchmark case between the two methods is shown in Fig. 5. Note that just below the endpoint energy, the intensity for the vacuum model is consistently about five times that of the air model. The present magnetic field transport subroutine indicates that data acquisition times might be cut by a factor of 5 by the evacuation of the volume the electrons travel through. The difference between the models is probably attributable to the degrading effect of air on the electron energy.

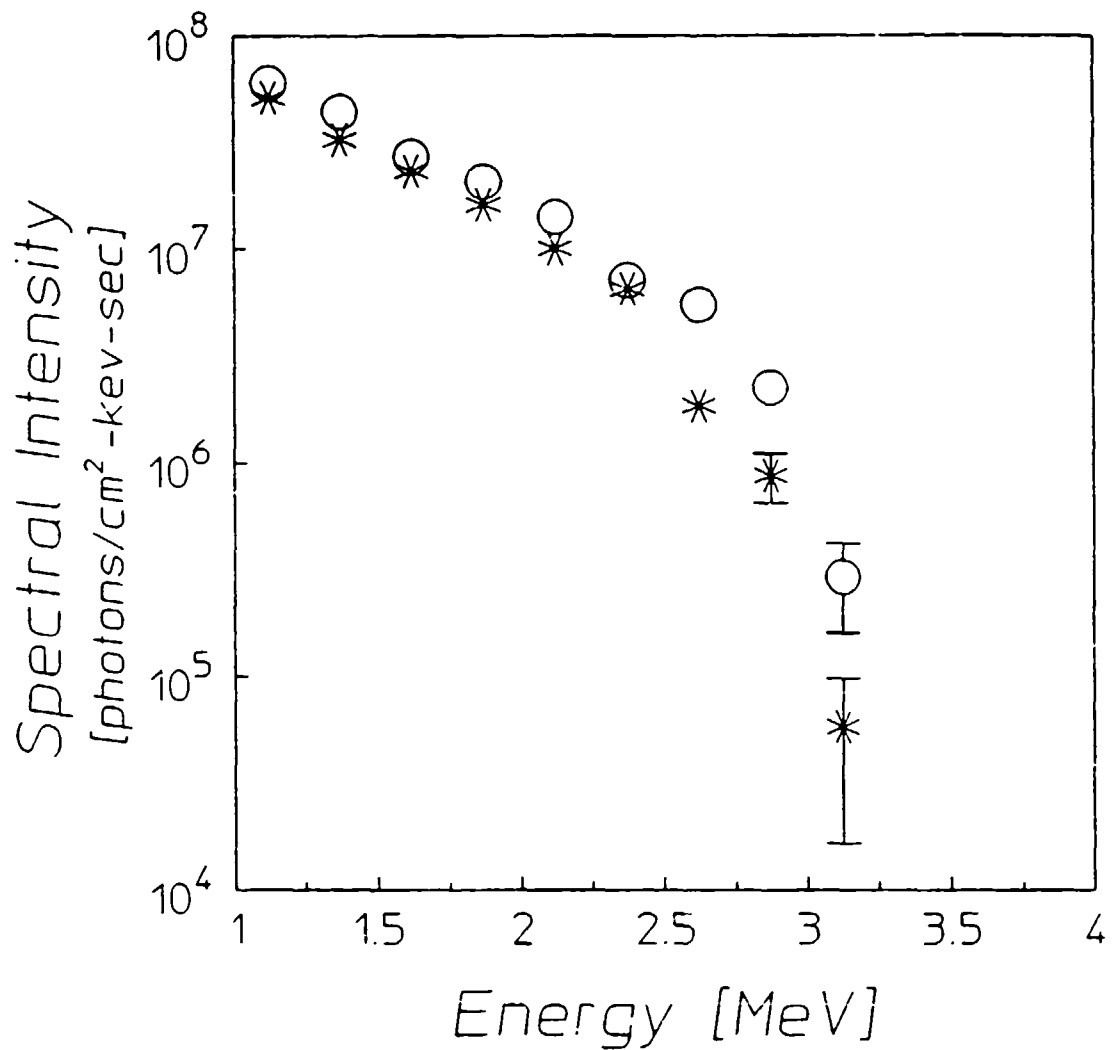


Figure 5: Comparison between air-filled and evacuated models of the magnetic field transport region. The circles represent the results of a vacuum model while the asterisks correspond to the air model spectrum. Where bars are not shown, the uncertainty is bounded by the size of the plotting symbol.

Upon exiting the magnetic field region of the spectrophotometer, most of the electrons impinge upon the tungsten converter, assumed to be 0.056 cm thick. A small percentage of these are converted into photons and travel down a column of air surrounded by lead that serves to

greatly reduced the probability of a contaminant photon reaching the sample exposure area, as mentioned before. For these runs, the distance between the converter and the sample exposure plane was about 5 cm, but should probably be increased in the future to allow for more dispersion of the photons and better protection from contamination. The sample exposure area was a square of 6 cm per side, corresponding to the largest target sample we routinely use for the excitation of isomers. A root-mean-square radius from the center of this area for photons passing through this plane was typically about 1.3 cm, where 2.1 cm corresponds to an exactly even distribution over a circle of radius 3 cm.

Output spectra for several device settings are shown in Fig. 6 and those settings identified in Table I. Finally, to explore the overall efficiency of this device, the results of a 3 MeV endpoint spectrum are compared with the Varian CLINAC 4/100 output obtained from another source,³¹ shown graphically in Fig. 7. The 4 MeV spectrum is obtained by correcting the normalized photon distribution by a time-averaged beam current of 25 μ A and a sample position 65 cm from the converter foil. These two spectra are very similar up to about 2 MeV, where the contrast between them is ascribed to the difference between their endpoint energies.

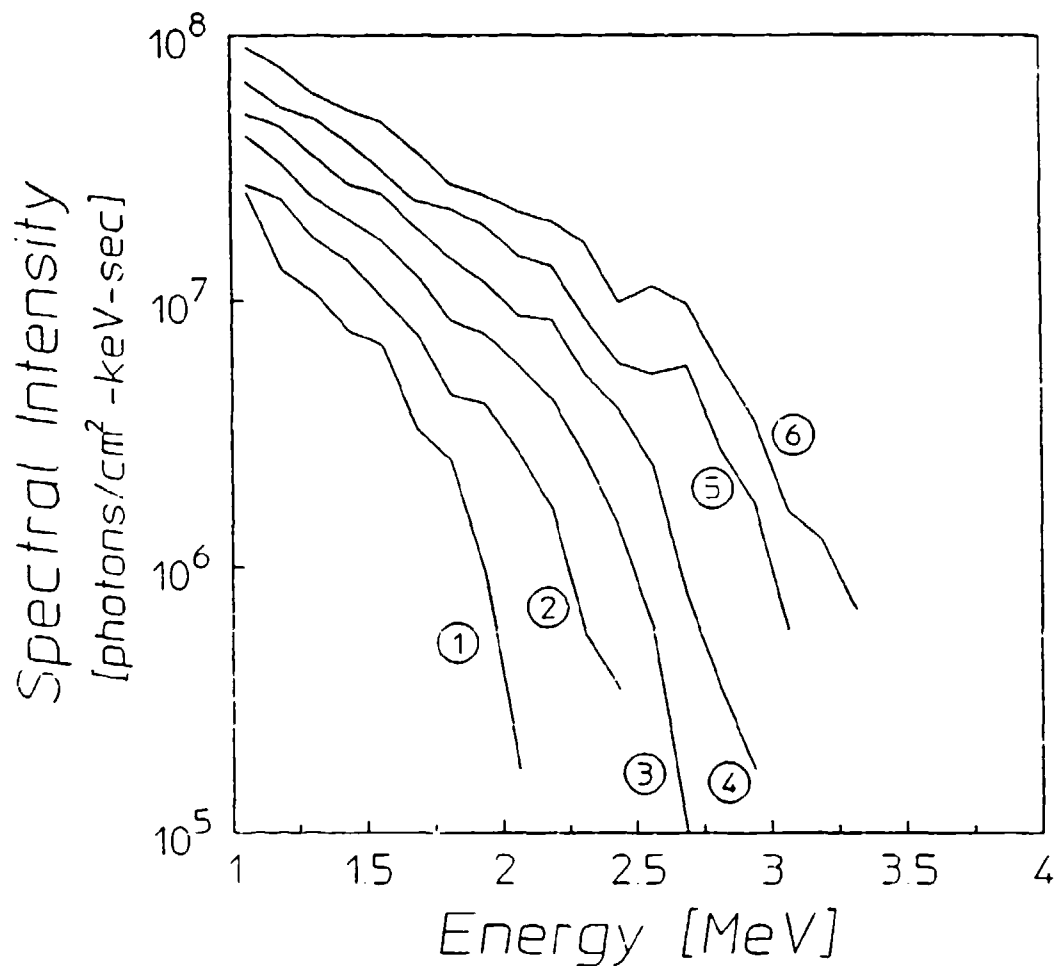


Figure 6: Spectra corresponding to different device settings tuned for varying endpoints. The settings for each spectra are shown in Table I, identified by the circled number next to each curve.

Table I: Summary of spectrophotometer settings for spectra of Fig. 6.

Spectrum Number	Thickness of Degrader [cm]	Magnetic Field [kGauss]	Magnet Pole Spacing [cm]	End-Point Energy [MeV]	Histories Run [$\times 10^5$]
1	0.56	3.63	2.58	2.125	4
2	0.49	4.01	2.43	2.500	5
3	0.42	4.38	2.30	2.750	7
4	0.35	4.76	2.17	3.000	4
5	0.28	5.13	2.04	3.125	3
6	0.21	5.50	1.92	3.375	3

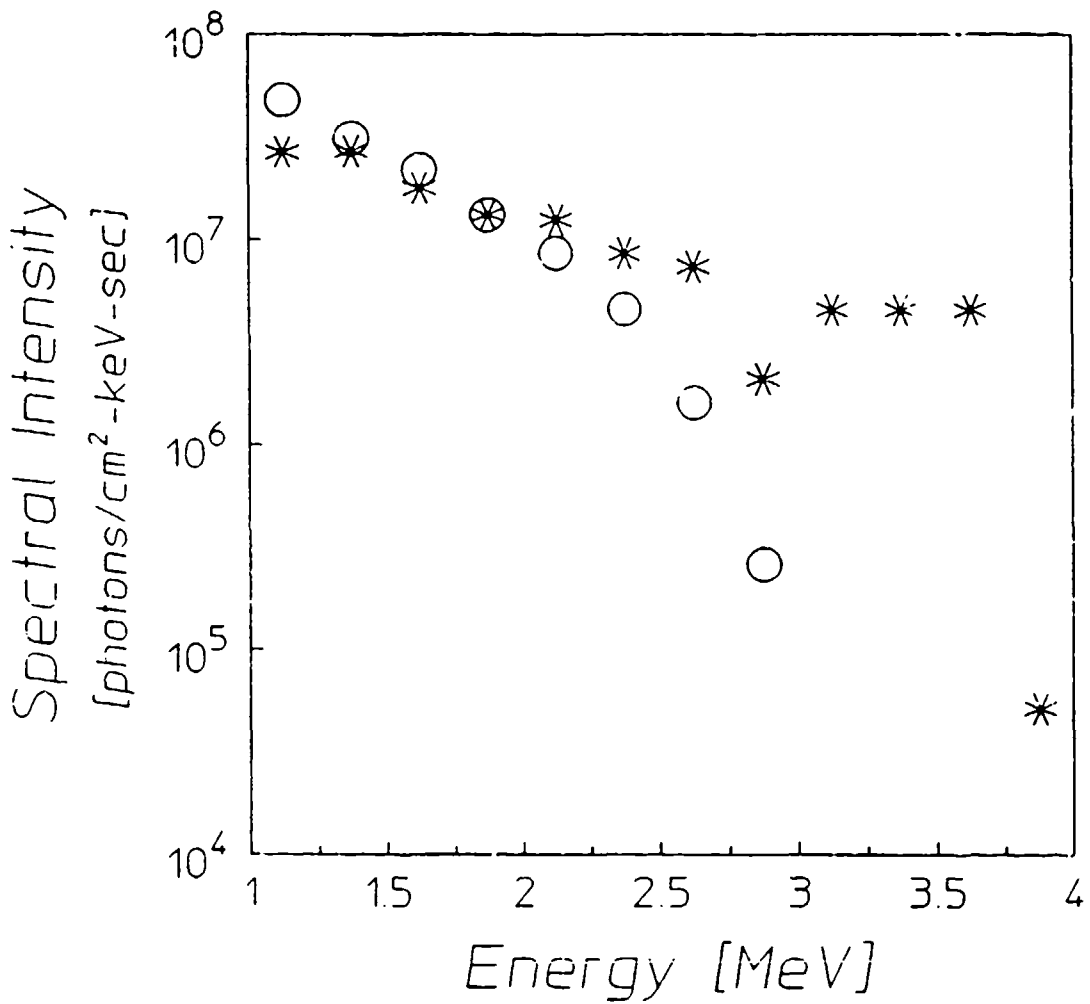


Figure 7: Comparison of 3.0 MeV endpoint results obtained by the design under consideration and CLINAC 4/100 spectrum obtained by using the normalized spectral distribution of Ref. 31 at a distance of 65 cm.

Application - ^{87}Sr

To understand more thoroughly the practicality of this geometry as it relates to (γ, γ') spectroscopy, a test was devised using common experimental parameters. This computational experiment used the isotope most characterized over the energy range of interest³², ^{87}Sr . The goals of this exercise were to confirm that reasonable exposure

times could be expected and to obtain an upper limit on the width of the energy range in which a state of moderate cross section can be identified.

Some background concerning (γ, γ') reactions is required to understand the implications of the results of this conceptual experiment. After exposure of an isotope to certain radiation, activation of a metastable level may be observed. Since the transition between the ground and the metastable states is highly forbidden, this photoexcitation must take place through a higher lying intermediary state, sometimes called a gateway state. These states are narrow relative to the spectra of any available sources.

For a continuous source like a linac, the activation rate, or fractional number of nuclei activated per unit time, is related to the integrated cross section by

$$\frac{N_{\text{excited}}}{N_t} = \sum_i (\sigma\Gamma)_i \left(\frac{d\Phi}{dE} \right)_i , \quad (1)$$

where $(\sigma\Gamma)_i$ is the integrated cross section of the i^{th} resonant excitation channel and $(d\Phi/dE)_i$ is the spectral intensity rate in photons/ $(\text{cm}^2\text{-keV-sec})$ at the sample position and at the i^{th} resonance location. N_{excited} is the number of excited nuclei and N_t represents the total number of nuclei. Experimentally the activation rate is given by

$$\frac{N_{\text{excited}}}{N_t} = \frac{C}{D\eta A f T_{\text{irr}}} , \quad (2)$$

where C is the number of counts registered in a full energy fluorescence peak by a detector of efficiency η , D is the finite count time correction, and f is the quantum efficiency associated with fluorescent decay from the metastable state to the ground state. The exposure time is T_{irr} and A is the self absorption correction coefficient.

The pertinent values for the three gateway states identified in Ref. 32 are shown in Table II. These were used, in conjunction with the spectra of Fig. 6, to calculate the expected activation which could be observed for each endpoint. The number of peak counts corresponding to these activations were then computed using the reasonable experimental parameters given in Table III. A Poisson deviate was then taken of this number of counts to simulate random decay results.

Table II: Locations and magnitudes of gateways identified in ^{87}Sr by Booth and Brownson.³²

Energy [MeV]	Integrated Cross Section [10^{-29} cm 2 -keV]
1.22	8.5
1.88	16.0
2.66	380.0

Table III: Experimental parameters used to project the number of counts observed in a 3X3 NaI detector caused by the activation of ^{87}Sr .

Halflife	2.8 h
Irradiation Time	2.0 h
Travel Time	10.0 m
Count Time	1.0 h
Fluorescence Energy	388.4 keV
Gamma Intensity	82.3 %
Self Absorption	3.2 %
Detector Efficiency	3.4 %

From the results of the computer experiment, the activation was then derived back from this skewed number of counts with the parameters of Table III, as though there was no prior knowledge of either the locations or the integrated cross sections for any gateways. Figure 7 shows this randomly deviated activation as a function of the endpoint energy of the x-ray source. From the figure, a sharp rise in activation between 2.5 and 2.75 MeV can be clearly observed, indicating that a gateway of this size is readily measurable. A discussion of more sensitive methods of measuring the exact locations and cross sections of the gateways lies outside the scope of this computational effort.

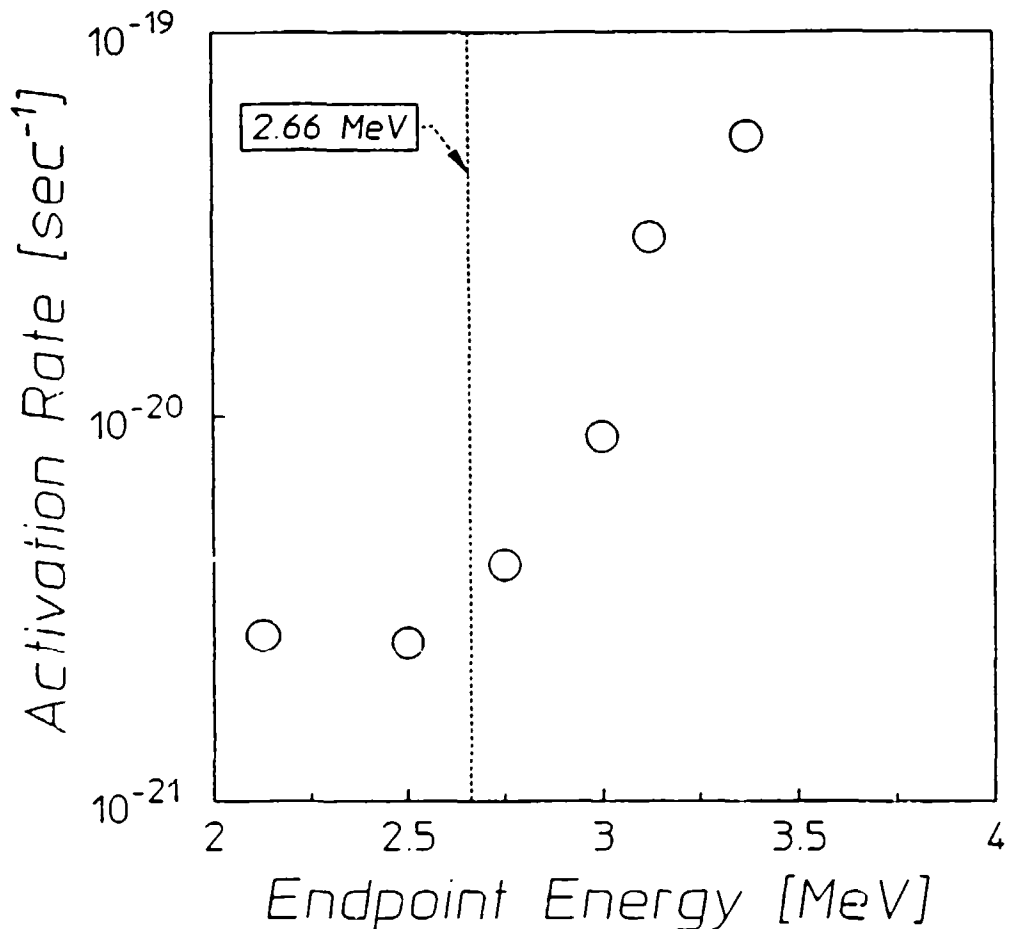


Figure 8: Activation rate due to hypothetical 2 hour exposures of ^{87}Sr to the variable endpoint bremsstrahlung source for each of the endpoints of Table I. The vertical dashed line denotes the position of the 380 unit gateway at 2.66 MeV, where a unit is defined as $10^{-29} \text{ cm}^2\text{-keV}$.

Conclusion

The viability has been demonstrated of economically and effectively converting a fixed endpoint electron linear accelerator into a variable endpoint photon source using simple materials and equipment such as graphite, tungsten, lead, and an electromagnet for bending the beam. Furthermore, the proposed modification meets the criteria of tunability, resolution, intensity, and experimental convenience required for such a source to be useful in (γ, γ') studies.

The test case of ^{87}Sr has shown that, for integrated cross sections of about 400 units, the device can serve to locate the energies of the gateway states. For these and the much larger cross sections already observed below 4 MeV,²³ statistically significant results can be expected with very reasonable data acquisition times.

Computational resolution can be improved further by the implementation of the EGS code system on more sophisticated machines than the one currently used. One such computer is the Cray available through the University of Texas Center for High Performance Computing on which microtasking may be exploited. This involves placing a compiler directive before a loop that then feeds the interior of that loop to a large number of processors. Each processor then runs a copy of the code independently and the results are added at the end of the cycle. Monte Carlo methods can benefit tremendously from such microtasking if proper steps are taken to ensure that randomness is maintained between the processors and that the results are added correctly.

Precision will also be improved by advances expected with the release of EGS version 5, expected in the Fall of 1989.³³ In the low energy ranges of interest here, this new code should run about 3-6 times faster and with greater accuracy than the version presently available to us.³⁴ It will also allow the cutoff energy to be increased, improving the statistical certainty at high energies while maintaining reasonable run times. Nevertheless, all of the anticipated improvements represent refinements which cannot affect the basic results reported here. The adaptation of a fixed endpoint linear accelerator for the production of variable endpoint bremsstrahlung is an attractive and cost-effective option.

References

1. B. Pontecorvo and A. Lazard, *C. R. Acad. Sci.* 208, 99 (1939).
2. G. B. Collins, B. Waldman, E. M. Stubblefield and M. Goldhaber, *Phys. Rev.* 55, 507 (1939).
3. S. M. Seltzer, "Cross Sections for Bremsstrahlung Production and Electron-Impact Ionization," in *Monte Carlo Transport of Electrons and Photons*, Ed. T. M. Jenkins, New York: Plenum Press 1988.
4. E. U. Condon, in *Handbook of Physics*, Ed. E. U. Condon and H. Odishaw, New York: McGraw-Hill 1967.
5. J. A. Anderson and C. B. Collins, Center for Quantum Electronics Report #GRL/8602, University of Texas at Dallas, 1987 (unpublished) pp. 29-46.
6. Center for Quantum Electronics Report #GRL/8603, University of Texas at Dallas, 1987 (unpublished) pp. 31-43.
7. C. B. Collins, J. A. Anderson, Y. Paiss, C. D. Eberhard, R. J. Peterson, and W. L. Hodge, Center for Quantum Electronics Report #GRL/8702, University of Texas at Dallas, 1987 (unpublished) pp. 45-56.
8. C. B. Collins, J. A. Anderson, Y. Paiss, C. D. Eberhard, R. J. Peterson, and W. L. Hodge, *Phys. Rev. C* 38, 1852 (1988).
9. J. A. Anderson, M. J. Byrd, and C. B. Collins, Center for Quantum Electronics Report #GRL/8702, University of Texas at Dallas, 1987 (unpublished) pp. 57-70.
10. J. A. Anderson, M. J. Byrd, and C. B. Collins, *Phys. Rev. C* 38, 2838 (1988).
11. J. A. Anderson, K. N. Taylor, J. M. Carroll, J. F. McCoy, J. J. Carroll, M. J. Byrd, and C. B. Collins, Center for Quantum Electronics Report #GRL/8704, University of Texas at Dallas, 1988, pp. 36-54.

12. C. D. Eberhard, J. A. Anderson, M. J. Byrd, J. J. Carroll, and C. B. Collins, Center for Quantum Electronics Report #GRL/8801, University of Texas at Dallas, 1988, pp. 15-41.
13. J. J. Carroll, J. A. Anderson, M. J. Byrd, K. N. Taylor, D. G. Richmond, T. W. Sinor, and C. B. Collins, Center for Quantum Electronics Report #GRL/8901, University of Texas at Dallas, 1989, pp. 1-31.
14. C. D. Eberhard, J. W. Glesener, Y. Paiss, J. A. Anderson, C. B. Collins, W. L. Hodge, E. C. Scarbrough, and P. P. Antich, Center for Quantum Electronics Report #GRL/8702, University of Texas at Dallas, 1987, pp. 89-103.
15. C. B. Collins, C. D. Eberhard, J. W. Glesener, and J. A. Anderson, Phys. Rev. C 37, 2267 (1988).
16. J. J. Carroll, J. A. Anderson, M. J. Byrd, K. N. Taylor, D. G. Richmond, T. W. Sinor, W. L. Hodge, Y. Paiss, C. D. Eberhard, C. B. Collins, E. C. Scarbrough, and P. P. Antich, Phys. Rev. C (pending).
17. C. B. Collins, C. D. Eberhard, J. W. Glesener, and J. A. Anderson, Center for Quantum Electronics Report #GRL/8703, University of Texas at Dallas, 1988, pp. 21-28.
18. J. W. Glesener, C. D. Eberhard, and C. B. Collins, Center for Quantum Electronics Report #GRL/8703, University of Texas at Dallas, 1988, pp. 29-35.
19. C. B. Collins, J. A. Anderson, C. D. Eberhard, J. F. McCoy, and J. J. Carroll, Center for Quantum Electronics Report #GRL/8703, University of Texas at Dallas, 1988, pp. 37-56.
20. J. A. Anderson, C. D. Eberhard, J. F. McCoy, K. N. Taylor, J. J. Carroll, M. J. Byrd, and C. B. Collins, Center for Quantum Electronics Report #GRL/8704, University of Texas at Dallas, 1988, pp. 11-35.
21. J. A. Anderson, K. N. Taylor, J. J. Carroll, M. J. Byrd, and C. B. Collins, Center for Quantum Electronics Report #GRL/8803, University of Texas at Dallas, 1988, pp. 1-17.

22. J. J. Carroll, J. A. Anderson, J. W. Glesener, C. D. Eberhard, and C. B. Collins, Center for Quantum Electronics Report #GRL/8803, University of Texas at Dallas, 1988, pp. 19-36.
23. J. J. Carroll, J. A. Anderson, M. J. Byrd, K. N. Taylor, D. G. Richmond, T. W. Sinor, W. L. Hodge, Y. Paiss, C. D. Eberhard, and C. B. Collins, Center for Quantum Electronics Report #GRL/8804, University of Texas at Dallas, 1989, pp. 1-29.
24. J. A. Anderson, C. D. Eberhard, M. J. Byrd, J. J. Carroll, C. B. Collins, E. C. Scarbrough, and P. P. Antich, Nucl. Instrum. Methods in Physics Research, Proceedings of the Tenth International Conference on the Application of Accelerators in Research and Industry, ed. J. L. Duggan and I. L. Morgan, (North Holland, Amsterdam, 1989) pp. 452-454.
25. J. J. Carroll, J. A. Anderson, J. W. Glesener, C. D. Eberhard, and C. B. Collins, *Astrophys. J.* (pending).
26. *The EGS Code System*, Walter R. Nelson, Hideo Hirayama, and David W. O. Rogers, SLAC Report 265, (Stanford Linear Accelerator Center, Stanford Calif. 1985).
27. R. Mohan, "Monte Carlo Simulation of Radiation Treatment Machine Heads," in *Monte Carlo Transport of Electrons and Photons*, Ed. T. M. Jenkins, New York: Plenum Press (1987).
28. D. W. O. Rogers, *Nucl. Inst. and Meth. in Phys. Res.* 227, 535 (1984).
29. M. D. Goldberg and J. A. Harvey, "Neutrons," in *American Institute of Physics Handbook*, Ed. D. E. Gray, New York: McGraw-Hill, 1972.
30. GMW Associates, Ian Walker, Private communication.
31. R. Mohan, C. Chui and L. Lidofsky, *Med. Phys.* 12, 595 (1985).
32. E. C. Booth and J. Brownson, *Nucl. Phys.* A98, 529 (1967).
33. D. W. O. Rogers, Private communication.
34. A. F. Bialajew, D. W. Rogers, "Electron Step-Size Artefacts and PRESTA," in *Monte Carlo Transport of Electrons and Photons*, Ed. T. M. Jenkins, New York: Plenum Press (1987).

DETERMINATION OF GATEWAY STATES IN ^{197}Au WITH A COMPTON γ -RAY SPECTROMETER

by C. D. Eberhard, J. A. Anderson, M. J. Byrd, J. J. Carroll
and C. B. Collins

Center for Quantum Electronics, University of Texas at Dallas
and E. Scarbrough and P. P. Antich
University of Texas Southwestern Medical Center

Introduction

Recent experiments^{1,2,3,4} have shown that cross sections for (γ, γ') reactions that populate nuclear isomers can be orders of magnitude larger than previously expected at excitation energies above about 2 MeV. These results were obtained by pumping nuclear populations with the bremsstrahlung radiation from a Varian CLINAC 1800 linear accelerator normally employed for radiation therapy treatments. Unfortunately, such bremsstrahlung sources are inherently continuous and cannot be used to selectively probe for the intermediate gateway states through which the isomeric excitation occurs. Moreover, not even the endpoint energy of this particular device can be varied around its operating point of 6 MeV. Thus, in this previous work there was no direct way of identifying the gateway levels which mediated the population of the observed isomeric states. To facilitate this identification process, a technique has been developed in which Compton scattering is used to progressively modify the energy endpoint and spectral distribution of the incident radiation. The current work describes this method and discusses its application to the study of the gateway states through which the reaction $^{197}\text{Au}(\gamma, \gamma')^{197}\text{Au}^*$ is excited.

The Compton Effect

The Compton effect⁵ describes the collision of a primary photon of energy E_0 with an essentially unbound atomic electron assumed to be initially at rest. The process is named for A. H. Compton, who established it quantitatively in 1923 after careful spectroscopic measurements of x-rays scattered through various angles by light elements. In the collision, the incident momentum and energy must be conserved between the scattered photon and the struck electron, which recoils. The scattered photon has less momentum and energy than the primary photon, with the remaining momentum and energy being imparted to the electron. The consequences of this phenomena can be quantitatively described by a rather straightforward approach.

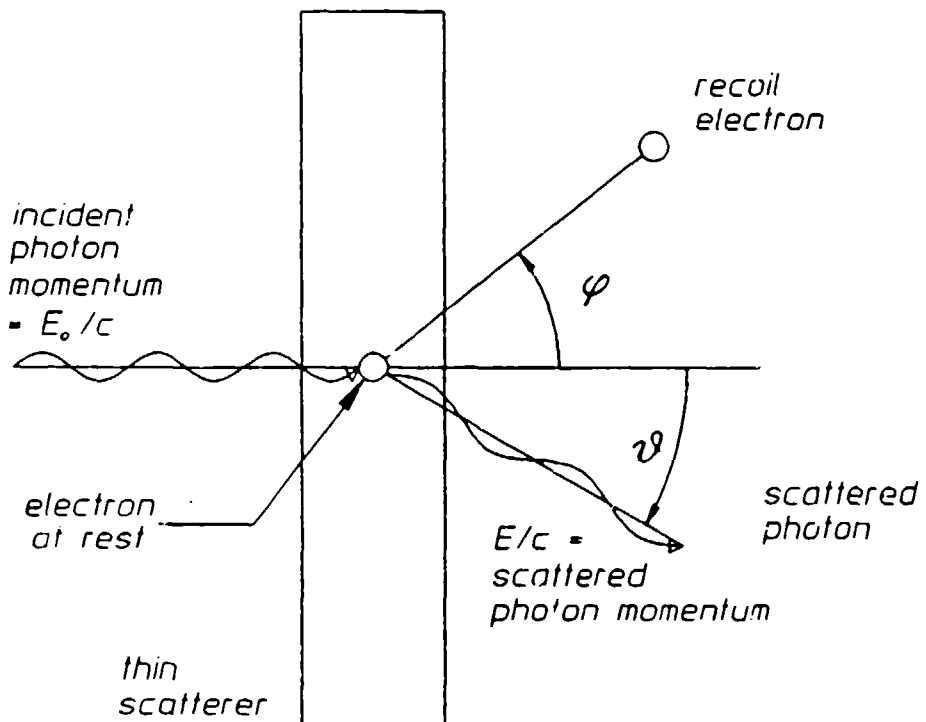


Figure 1: Diagram of the initial and final momenta for Compton scattering.

Let the angle between the propagation vectors of the primary and scattered photons be denoted by θ as shown in Fig. 1. From the relativistic energy-momentum relation and the conservation of energy and momentum, the energy of the scattered photon is found to be given by

$$E = \frac{E_0}{[1 + (E_0/mc^2)(1 - \cos \theta)]}, \quad (1)$$

where mc^2 is the rest mass of the electron. There is a one-to-one correlation between the energy of the scattered photon and the angle θ for a given primary photon energy E_0 . Therefore, photons from a monochromatic source which are scattered into a given angle from a point scatterer will be monochromatic. This leads to the possibility of performing nuclear spectroscopy with Compton scattered radiation having a known spectral distribution. A configuration for a Compton spectrometer to be used in the study of the activation of short lived isomers is shown in Fig. 2.

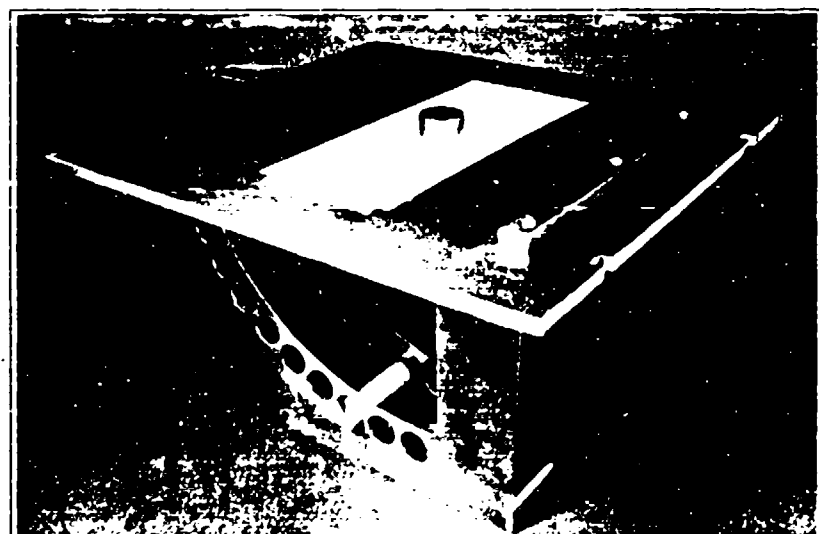


Figure 2: Irradiation fixture of the Compton spectrometer showing a sample in the $\theta = 8^\circ$ position. The pneumatic tubing of the transport system passed through the holes in the sample holder so that the sample was positioned as shown. The tubing was moved from site to site manually.

In the theory of the Compton effect, the struck electron is considered to be free or unbound. This limits the theory to cases for which the atomic binding energy of the electron is small compared with E_0 , which is the case for the primary photon spectrum considered here. Also, the electron is assumed to be at rest. Although the general case of non-zero electron momentum can be obtained from this special case by a Lorentz transformation, this refinement is generally not considered necessary. In 1928 the complete theory for the effect was worked out by Klein and Nishina using Dirac's relativistic theory of the electron. The differential cross section obtained for the scattering of unpolarized incident photons of energy E_0 into the solid angle $d\Omega$ at the polar angle θ is given by

$$\frac{d\sigma}{d\Omega} = r_0^2 \left(\frac{1}{1 + \alpha_i(1 - \cos \theta)} \right)^2 \left(\frac{1 + \cos^2 \theta}{2} \right) \times \left(1 + \frac{\alpha_i^2(1 - \cos \theta)^2}{(1 + \cos^2 \theta)[1 + \alpha_i(1 - \cos \theta)]} \right) \quad (2)$$

where $\alpha_i = E_0/mc^2$ is the incident photon energy in units of mc^2 and $r_0 = e^2/mc^2$ is the classical radius of the electron. The differential scattering cross section is defined through the relationship

$$dR(\theta, E_0) = dI_i(E_0) N_{sc} \frac{d\sigma}{d\Omega}(E_0, \theta) d\Omega(\theta) \quad (3)$$

where

dR = number of photons per second scattered into solid angle $d\Omega$ at θ ,

N_{sc} = number of electrons per cm^3 in the scatterer, and

$dI_i(E_0)$ = incident photon flux with energy E_0 in photons per cm^2 per s.

After substitutions for the solid angle,

$$d\Omega = 2\pi \sin \theta \, d\theta \quad , \quad (4)$$

and the area at the target location at radius r intersected by the conical fan described by $d\Omega$,

$$dA = 2\pi r^2 \sin \theta \, d\theta \quad , \quad (5)$$

Eq. (3) may be rewritten for the scattered flux as

$$dI_f = \frac{dR}{dA} = dI_i \frac{d\sigma}{d\Omega} \frac{1}{r^2} \quad . \quad (6)$$

A real experimental source is not monochromatic, but a small portion of the spectrum can be represented by

$$dI_i = \frac{dI_i}{dE} dE \quad , \quad (7)$$

where dI_i/dE is the spectral density of the incident flux. Written in terms of the spectral density, Eq. (6) becomes

$$dI_f = \frac{dI_i}{dE_i} \frac{d\sigma}{d\Omega} \frac{1}{r^2} dE_i \quad , \quad (8)$$

The energy spread of the scattered photons relative to the energy spread of the incident photons is found by differentiating equation (1),

$$dE = dE_i [1 + \alpha_i(1 - \cos \theta)]^{-2} \quad . \quad (9)$$

Equation (8) becomes

$$\frac{dI_f}{dE} = \frac{dI_i}{dE_i} \frac{d\sigma}{d\Omega} (\theta, E_0) \frac{[1 + \alpha_i(1 - \cos \theta)]^2}{r^2} \quad (10)$$

The quantity dI_f/dE is the output spectral density, a function of θ and E , the scattered photon energy. Thus for a non-monochromatic incident spectrum, the output spectral density can be calculated on a point-by point basis.

The preceding discussion assumed a point scatterer and a point absorber at which one could calculate the spectral density of the scattered radiation. As shown in Fig. 2, both scatterer and absorber have finite volumes which must be accommodated in the calculation of the output spectral density. Since the scattering target must in practice be chosen large enough to produce a significant scattered photon flux, it cannot be considered to be thin in comparison to the mean free path of a photon. Therefore there will be significant multiple scattering in a real target. Although the correct solution of this problem requires a full radiation transport calculation, a first approximation has been made in this work by treating the scattering target as a collection of individual point scatterers and using a simple attenuation calculation to adjust the incident and scattered intensities from each point. This in effect assumes that all secondary scattering events result in absorption. The output spectral density at a given point in the absorber is then the summation of the contributions from all the volume elements in the scatterer. Since the output spectrum is sensitive to position within the absorber, it is necessary to average this output spectral density over the volume of the absorbing sample. A more complete, Monte Carlo based calculation is in progress.

The source of primary photons used in this work was a Varian Clinac 1800 linear accelerator designed for medical applications. Electrons accelerated to an energy of 6 MeV impact a copper target to produce a photon beam with a well characterized bremsstrahlung spectrum⁶. The spatial variation of this bremsstrahlung spectrum over the area of the scatterer has been measured and is negligible⁷.

The output spectral density for the Compton spectrometer was calculated using Eq. (10). For every pair of volume elements in the scatterer and absorber, the geometrical factors r and $\cos \theta$ were determined. Then, for each value of the output energy to be considered,

the corresponding E_0 was found, and the input spectral density was obtained from a piecewise-continuous fit generated from the results of Mohan et al. This spectrum was adjusted for exponential attenuation of the incident radiation by applying the factor $\exp(-\mu(E_0)z)$, where z is the vertical distance of the scattering point from the top of the scattering target and $\mu(E_0)$ is the mass attenuation coefficient at incident photon energy E_0 . After the application of Eq. (10) to obtain the spectrum dI_f/dE of the Compton scattered radiation, a second attenuation correction of $\exp(-\mu(E)d)$ was made. Here, d is the path-length the scattered photon of energy E travels as it exits the scattering target. These results were summed over the scatterer volume and averaged over the absorber volume to produce the spectral density seen by the absorber. In order to test the sensitivity of the model to the geometrical assumptions, the output spectral density at $\theta = 16^\circ$ was calculated for the following four possible geometrical cases:

1. Point scatterer/point absorber: the masses of the scatterer and absorber were considered to be concentrated at the respective geometrical centers. Attenuation in the scatterer was calculated using the appropriate path lengths from the boundary of the scatterer to its center.
2. Extended scatterer/point absorber: the scatterer was divided into volume elements but only the central point of the absorber was considered.
3. Point scatterer/extended absorber: the scatterer was concentrated at its center but the absorber was considered to have an extended volume. Attenuation in the scatterer was calculated using the appropriate path lengths from the boundary of the scatterer to its center.
4. Extended scatterer/extended absorber: the finite dimensions of both scatterer and absorber were considered in this model.

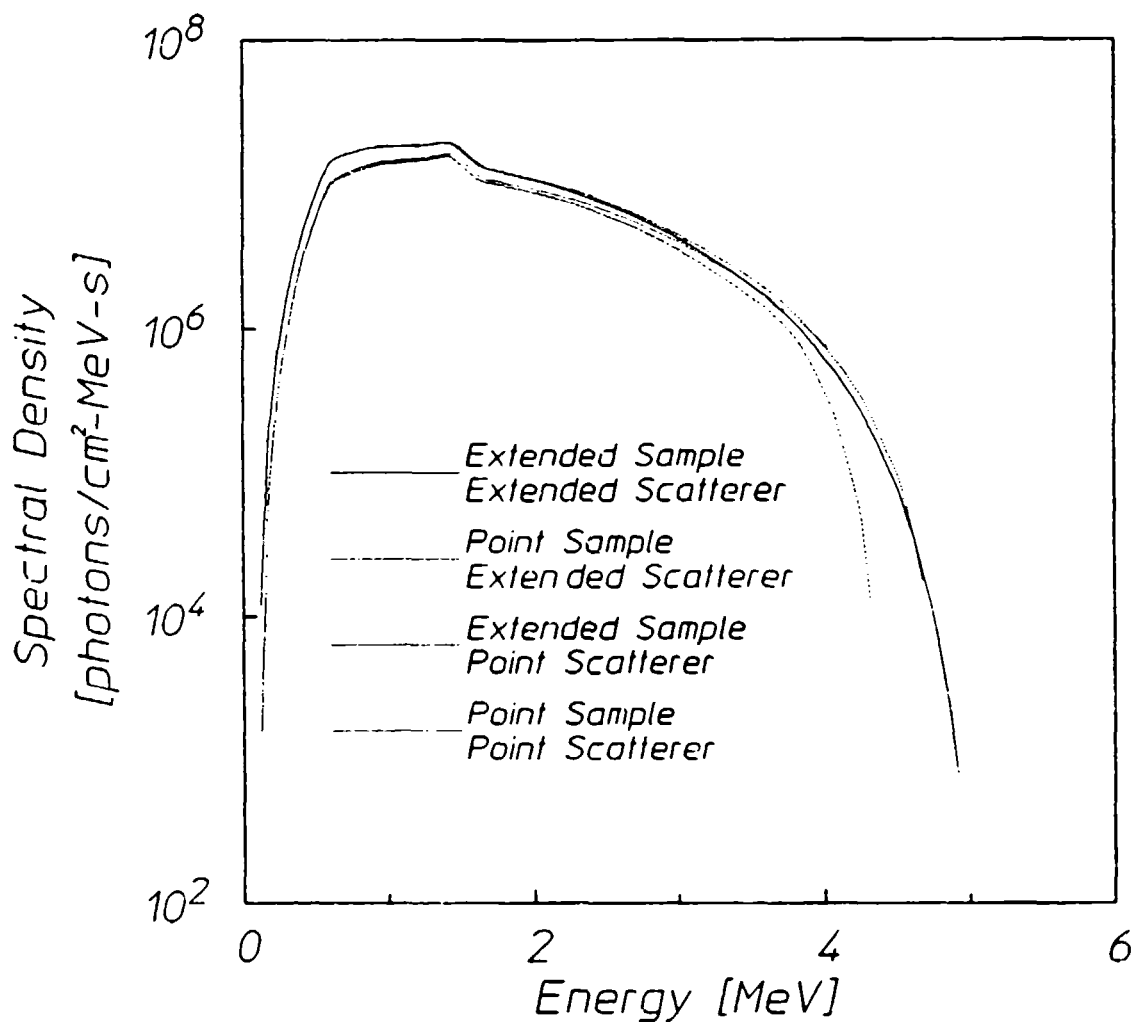


Figure 3: Modelled output spectral densities at the position of the absorber at the 16° spectrometer position for the four geometrical assumptions.

The results of these calculations are shown in Fig. 3. It should be noted that the single-point scatterer models underestimate the low energy portion of the spectrum because of the relatively long absorption path from the center of the scattering target to its boundary. Inclusion of the finite extent of the absorber sample increased the maximum photon energy incident on the absorber because it allowed contributions from lower scattering angles in the Compton process to be made for a given central angle θ . The extended source/extended scatterer model was used throughout the remainder of the work. These extended geometry calculations were performed for scattering angles of 0°, 16°, 24°, 32°

and 40°. The Compton scattered spectral densities are shown plotted in Fig. 4.

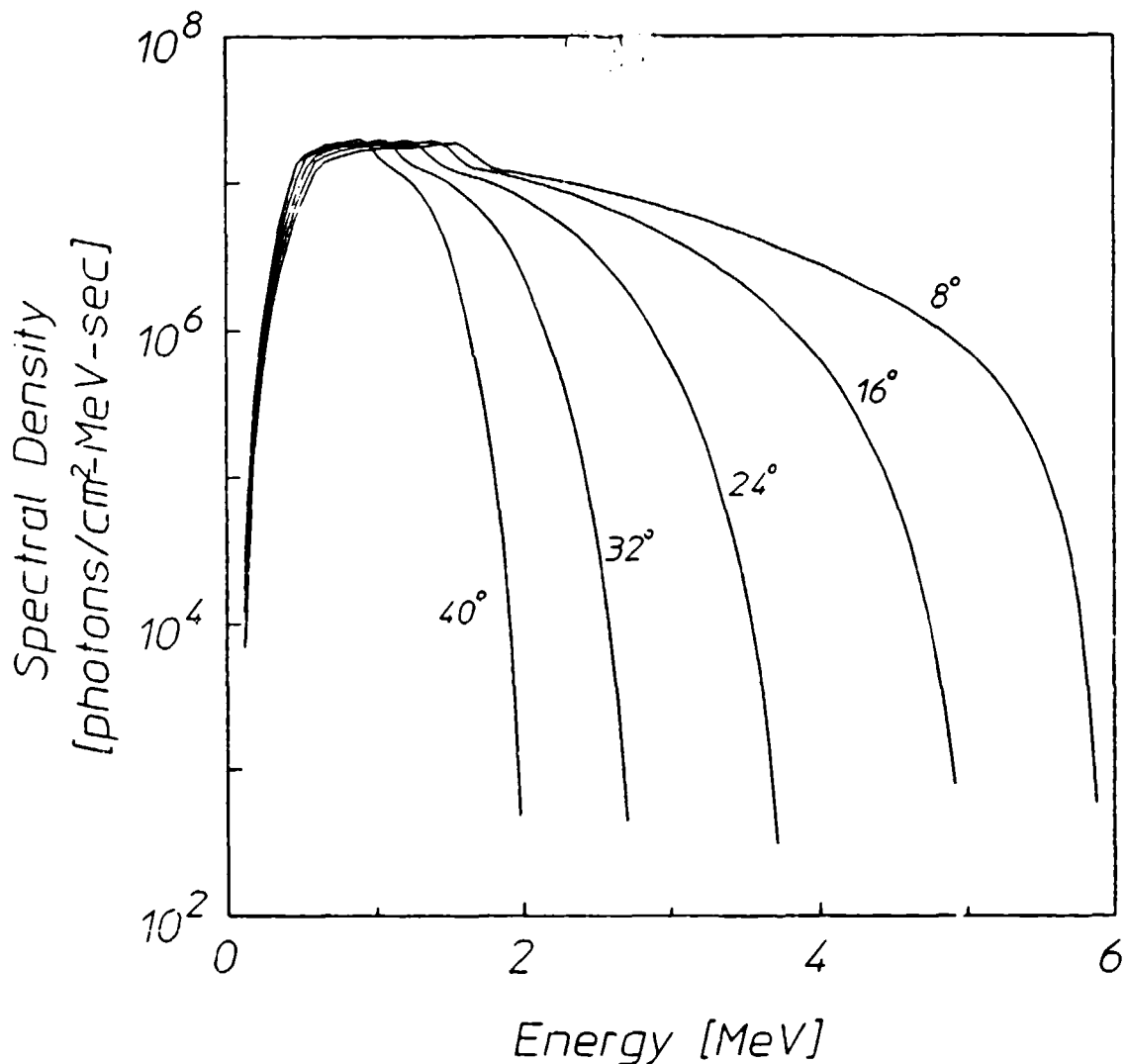


Figure 4. Modelled output spectral densities of the extended scatterer/extended absorber geometry for the scattering angles of 0°, 8°, 16°, 24°, and 32°.

A point of interest concerning the output spectrum is the end-point energy, or that point above which there is no spectral density. By the point-to-point model, the end-point energy, E_{\max} , is given by Eq. (1). However, due to the extended geometry of the scatterer and target, lower angles are encountered which contribute energies higher than the

point-to-point value, increasing the maximum energy of the radiation illuminating the sample. A comparison of the calculated E_{\max} for the point-to-point case and the extended geometry model is shown in Table I.

Table I

End-point energies for extended and point-to-point and geometry calculations.

Angle	E_{\max} Extended Geometry	E_{\max} Point-to-Point Geometry
0°	6.00	6.00
8°	5.88	5.38
16°	4.92	4.12
24°	3.72	2.98
32°	2.70	2.16
40°	1.98	1.60

Long lived isomeric states can be activated either directly or through one or more gateway⁸ states as shown in Fig. 5. The long halflife of the isomeric state leads to a very narrow linewidth. Since the excitation of a particular state is proportional to the linewidth, direct activation of the isomer is considered to be negligible. A gateway state must be excited from the ground state by the absorption of a single photon. Some fraction of the decays from the gateway state then leads to the isomeric state either directly or through a multi-step cascade.

If the activation of the metastable state is assumed to proceed through one gateway state, then the total number of activations is given by

$$N_m = b_0 N_t T \int_0^{\infty} \sigma(E) dI(E) = b_0 N_t T \int_0^{\infty} \sigma(E) \frac{dI(E)}{dE} dE \quad , \quad (11)$$

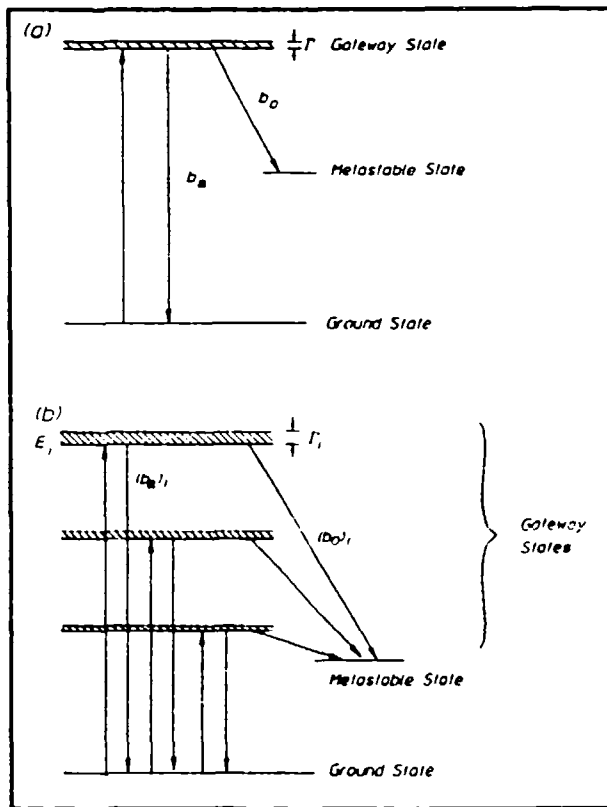


Figure 5(a): Energy level diagram of a single gateway isotope. (b): Energy level diagram of a multiple gateway isotope.

where b_0 is the branching ratio of the decay of the gateway state into the metastable state, T is the irradiation time, and $dI(E)$ is the differential increment of flux with energy between E and $E + dE$. The Breit-Wigner cross section $\sigma(E)$ for the absorption of a photon when the resonant transition energy is E_r is given by

$$\sigma(E) = \frac{\lambda^2}{8\pi} \frac{2I_f + 1}{2I_i + 1} \frac{\Gamma_0 \Gamma}{[(E - E_r)^2 + (\Gamma/2)^2]} \quad , \quad (12A)$$

$$= \frac{\sigma_0}{4} \frac{b_a \Gamma^2}{[(E - E_r)^2 + (\Gamma/2)^2]} \quad , \quad (12B)$$

where the symbols are defined as follows:

λ = photon wavelength,

I_i, I_f = initial and final angular momenta of the nucleus,

Γ = total level width of the gateway state,

$\Gamma_a = b_a \Gamma / (1 + \alpha_p)$ = partial width of the gateway state for electromagnetic transitions to the ground state,

α_p = total internal conversion coefficient for the absorption transition, and

$$\sigma_0 = \frac{\lambda^2}{2\pi} \frac{2I_f + 1}{2I_i + 1} \frac{i}{(\alpha_p + 1)} \quad ,$$

This nomenclature is consistent with that used in the Mossbauer spectroscopy community.

If the spectral density (dI/dE) can be considered to be constant in the vicinity of the absorption line, the integral in Eq. (11) becomes

$$N_m = N_t b_0 \left. \frac{dI}{dE} \right|_{E_r} T \int_0^\infty \sigma(E) dE \quad (13)$$

$$= N_t (\pi \sigma_0 b_a b_0 \Gamma / 2) \left. \frac{dI}{dE} \right|_{E_r} T \quad ,$$

where $(dI/dE)|_{E_r}$ is the spectral density evaluated at the resonance energy, E_r . Thus the effective cross section for this activation is given by

$$\sigma_{\text{eff}} = \pi b_a b_o \sigma_o \Gamma / 2 \quad \text{cm}^2\text{-keV} \quad , \quad (14)$$

and the activation A may be written

$$A = (N_m / N_t) = \sigma_{\text{eff}} \left. \frac{dI}{dE} \right|_{E_r} T \quad . \quad (15)$$

When there are two or more gateway states which may decay into the metastable level, the integral in Eq. (11) is replaced by a summation of integrals, one for each of the i gateway states, and it must be rewritten as

$$N_m = N_t T \sum_i \left[\sigma_{\text{eff}}(E_i) \left. \frac{dI}{dE} \right|_{E_i} \right] \quad . \quad (16)$$

While some gateway energies have been found through the use of variable end-point devices^{9,10}, in many cases the gateways have not been identified. The spectra shown in Fig. 4 indicate that by using a Compton spectrometer one may achieve results similar to those obtained with a variable end-point device, provided that the scattered radiation has adequate intensity. That is, although the scattered intensity will be substantially reduced from that in the primary beam, it must still be sufficient to produce statistically significant activation within the lifetime of the fluorescent level. As an example of this potential application, the spectra of Fig. 4 were used to generate sample activation results for several configurations of gateway states. These numbers correspond to the time corrected activations which would be observed in the samples after irradiation at the appropriate Compton angle. Based on the output spectral density dI/dE of the spectrometer as a function of angle, the effective cross section is obtained from Eq. (15) as

$$\sigma_{\text{eff}} = \frac{N_m}{N_t} = \frac{A}{\left. \frac{dI}{dE} \right|_T} \quad . \quad (17)$$

A family of these curves based on the assumption that there is only one gateway state producing the isomer is shown in Fig. 6. These

curves are seen to intersect at the one energy corresponding to that of the gateway state. When there are two possible gateways, the family of curves similar to those seen in Fig. 7 is generated. This hypothetical case has one gateway at 2 MeV having a cross section of 10^{-26} cm²·keV and a second gateway at 4 MeV with a corresponding cross section of 10^{-25} cm²·keV. The family of curves obtained demonstrates considerably more complexity and the contributing gateways cannot be visually identified as they were in Fig. 6.

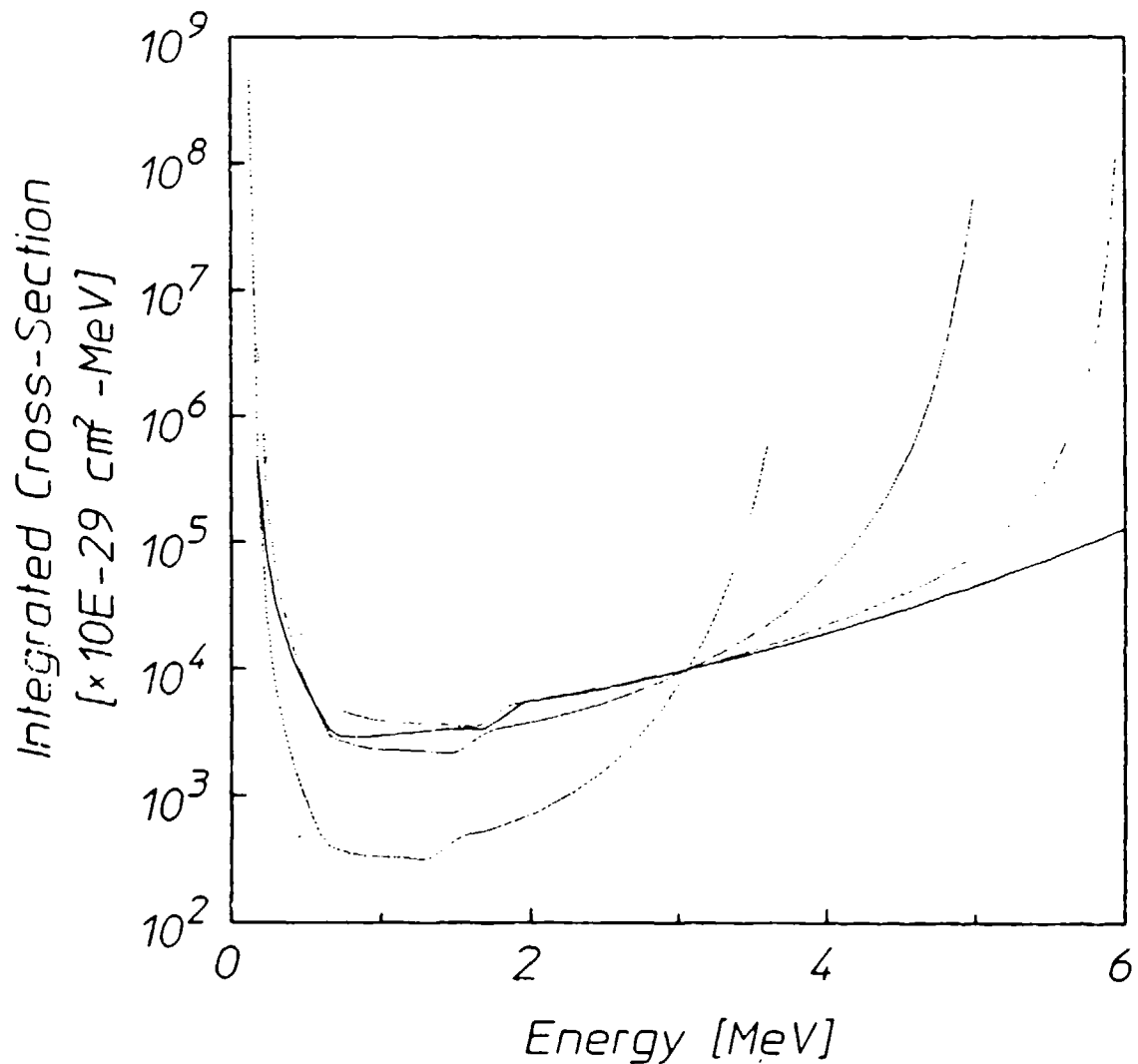


Figure 6: Synthetic curves of the cross section in units of 10^{-29} cm²·keV as a function of gateway energy for the case of a single gateway state. The assumed spectral densities were those shown in Figure 4.

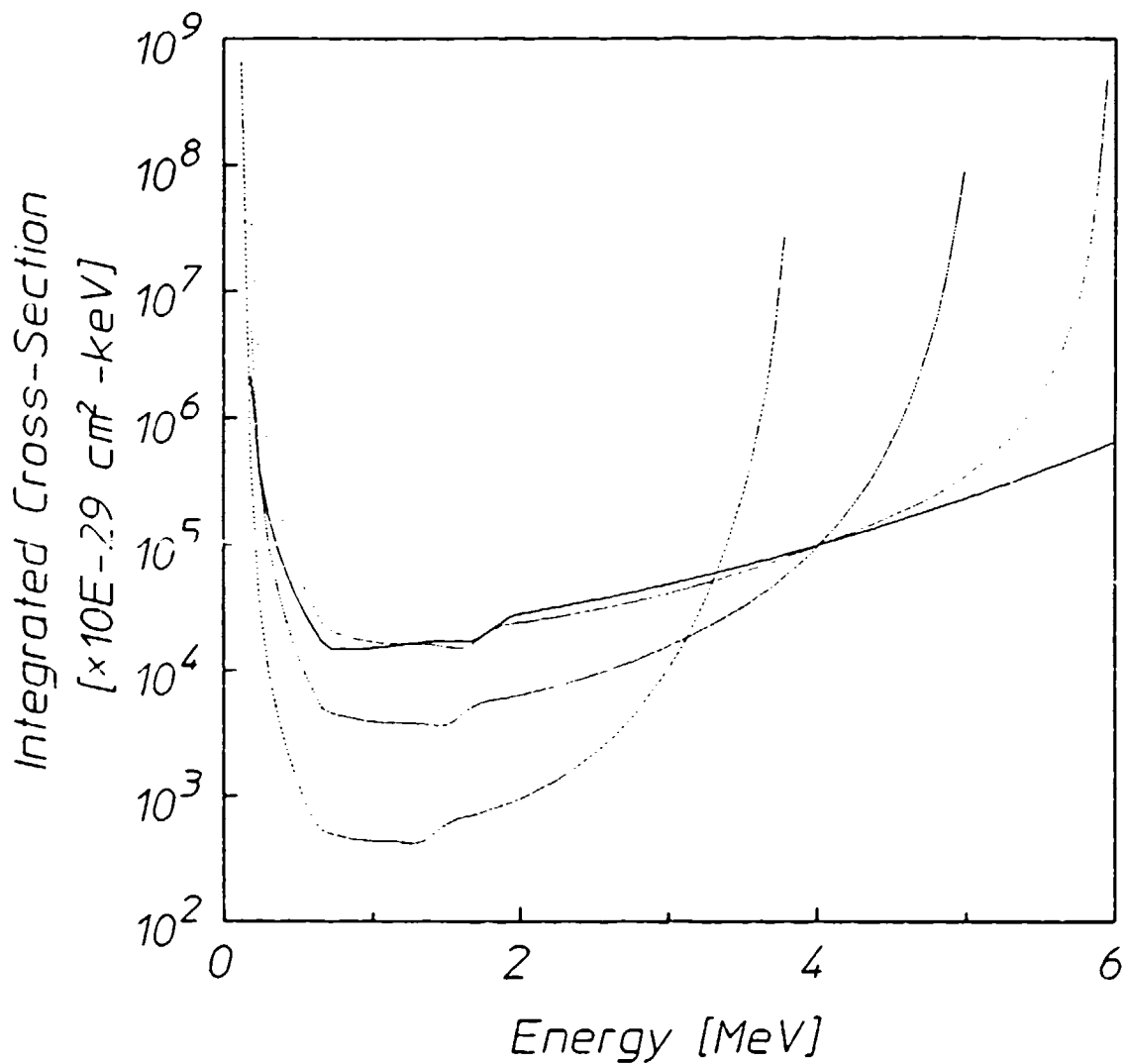


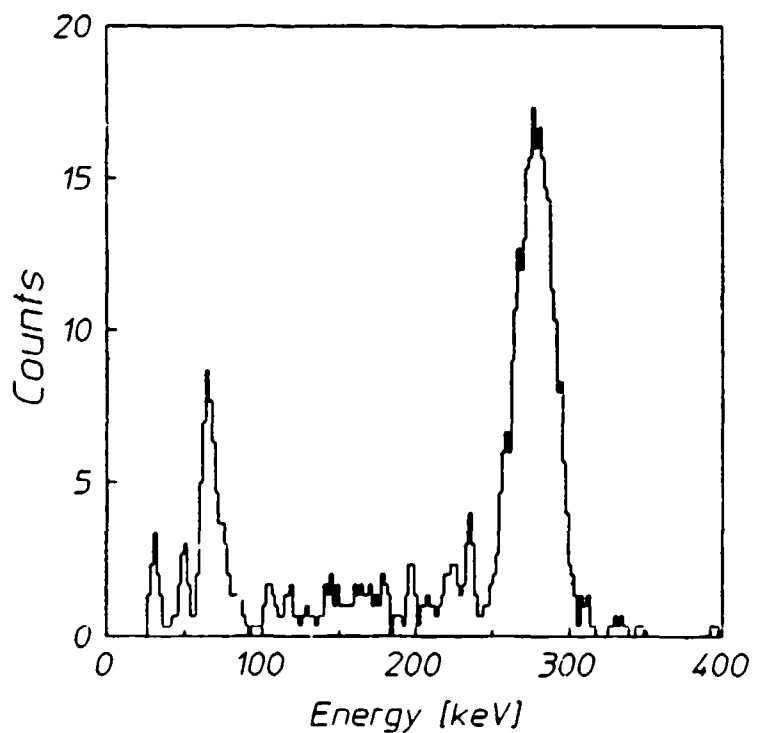
Figure 7: Synthetic curves of the cross section in units of 10^{-29} $\text{cm}^2\text{-keV}$ as a function of gateway energy for the case of two gateway states.

Experimental Details

The irradiation fixture pictured in Fig. 2 was constructed to hold the samples during exposure. This jig was mounted at the filter tray position of the Varian Clinac 1800 linac employed for this work, thus holding the scattering center 65 cm from the x-ray converter target. The total incident photon flux at this position is $2.2 \cdot 10^{10}$ ph-

tons/cm²·sec. A layer of 5 cm of lead shielding was placed in the plane of the Compton target to prevent radiation scattered off the Clinac collimators from reaching the sample positions and contaminating the experiment. The 2.54 cm diameter by 2.54 cm long stainless steel cylinder used as the scattering element nested in an aperture through this secondary shield. Bremsstrahlung radiation from the linac was restricted by the machine collimators until it illuminated only the scattering center.

The fixture had provisions for placing samples at angles corresponding to integral multiples of 8°. Samples were held inside a pneumatic transfer tube at a radial distance of 20.3 cm from the center of the scattering target. The wall thickness of the aluminum transfer tube was only 0.025 cm, presenting a negligible attenuation in the energy range of interest (>1 MeV) in this experiment. A valve on the pneumatic system also allowed the sample to be transferred back to the irradiation site. This was a great convenience, since entry into the CLINAC cell to relocate the sample for exposure would have otherwise required an additional 2 minutes per irradiation.



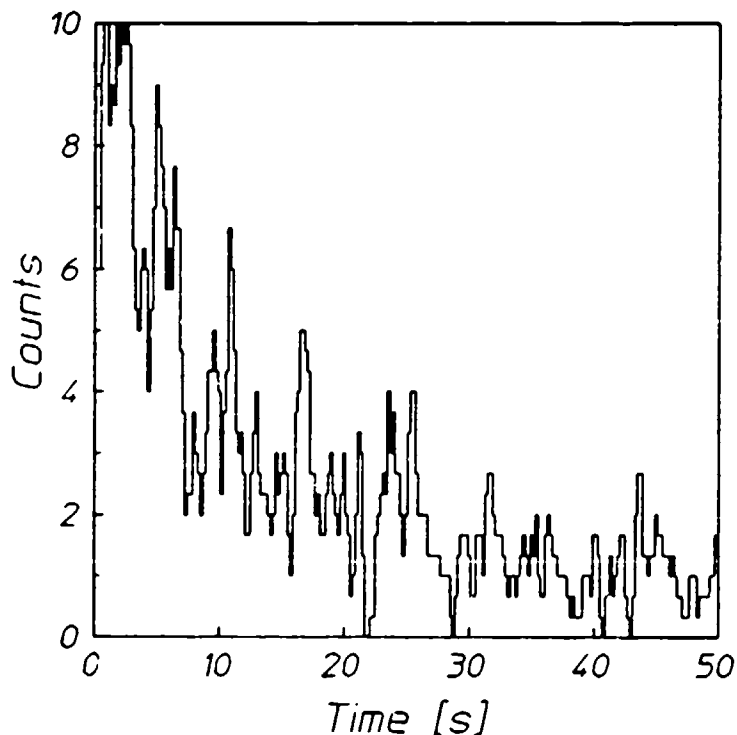


Figure 9: Time decay spectrum of the decay of the $^{197}\text{Au}^m$ produced by the exposure to the Compton scattered spectrum of the LINAC.

In each trial, the sample was exposed for 60 s. Immediately after the irradiation, the sample was automatically transferred from the exposure position to the detector, where it was counted for 20 s. A timer was started at the end of the exposure and stopped by the arrival of the sample at the detector. This timing information was used to correct the observed number of counts for losses during the transit interval.

The detector used in this work was a 7.62 cm x 7.62 cm NaI(Tl) detector with a 2.54 diameter well 5.08 cm deep. Data acquisition began automatically upon arrival of the sample at the detector. A pulse

Figure 8 (Opposite): Pulse height spectrum of the decay of the $^{197}\text{Au}^m$ produced by the exposure of the Compton scattered spectrum of the LINAC.

automatically upon arrival of the sample at the detector. A pulse height spectrum and a time decay spectrum were simultaneously obtained for each case. Examples of these spectra are shown in Figs. 8 and 9. The pulse height spectra were used to obtain the results discussed here. Absolute counting efficiencies for this system were obtained by calibration against standardized sources. The observed counts in the 279 keV peak of $^{197}\text{Au}^m$ were corrected for absolute efficiency, self-absorption of the emitted gamma-rays, counting losses during irradiation and transit, and for the gamma-ray intensity to obtain the total number of excitations occurring during the exposure. Table II contains the number of trials made at each angle, the transit time for each trial, the number of photopeak counts observed, and the number of excitations produced. Table III lists the characteristic parameters for the gold sample used in this work. From the measured values, the product

$$\sigma_{\text{eff}} \times \frac{dI}{dE} = \frac{N_m}{N_t T} \quad (18)$$

was calculated for each observed angle for use in the analysis that has been previously described.

Table II

Summary of data from the Compton spectrometer experiments. Corrections to the observed photopeaks were made as described in the text. Photopeak areas were obtained using the commercial peak analysis program GDR Version 4.0

Angle (deg)	Number of Trials	Transit Time(s)	Total Photopeak	Average Isomeric
0*	1	1.87	19374	$1.08 \times 10^6 \pm 7.3 \times 10^3$
8	1	1.90	244	$3.51 \times 10^3 \pm 2.2 \times 10^2$
16	2	1.82	84	$6.00 \times 10^2 \pm 6.6 \times 10^1$
24	4	1.82	78	$2.86 \times 10^2 \pm 3.2 \times 10^1$
32	4	1.87	40	$1.44 \times 10^2 \pm 2.3 \times 10^1$
40	4	1.80	45	$1.57 \times 10^2 \pm 2.4 \times 10^1$

* No scatterer, exposed to primary beam. ⁴

Table III

Sample parameters for this work.

Sample Composition	99+	% Au
Sample Mass	31.6	g
Isotopic Abundance	100	%
Number of Target Nuclei	9.52×10^{22}	
Gamma-ray energy	279	keV
Gamma-ray intensity @ 279 keV	73.11	%
Self-absorption factor	0.305	

Data Analysis

The spectral intensity was calculated using the techniques described above for each of the sample positions used in the experiment. As previously discussed, the input spectrum used in this work was a piecewise-continuous curve fitted to the results of Mohan et al.⁶ Expected uncertainties associated with the spectral intensity calculation were obtained by fitting a second piece-wise continuous curve to the reported uncertainties in Mohan's work. The two curves representing the envelope of the input model spectrum plus and minus these fitted uncertainties are plotted in Fig. 10 with the original results from Mohan. The envelope curves bound the Monte Carlo results and are consistent with their error bars. Uncertainties in the Compton scattered intensities were obtained by repeating the extended geometry calculations with the envelope curves of Fig. 10 as input data. The results for the case $\theta = 16^\circ$ are shown in Fig. 11.

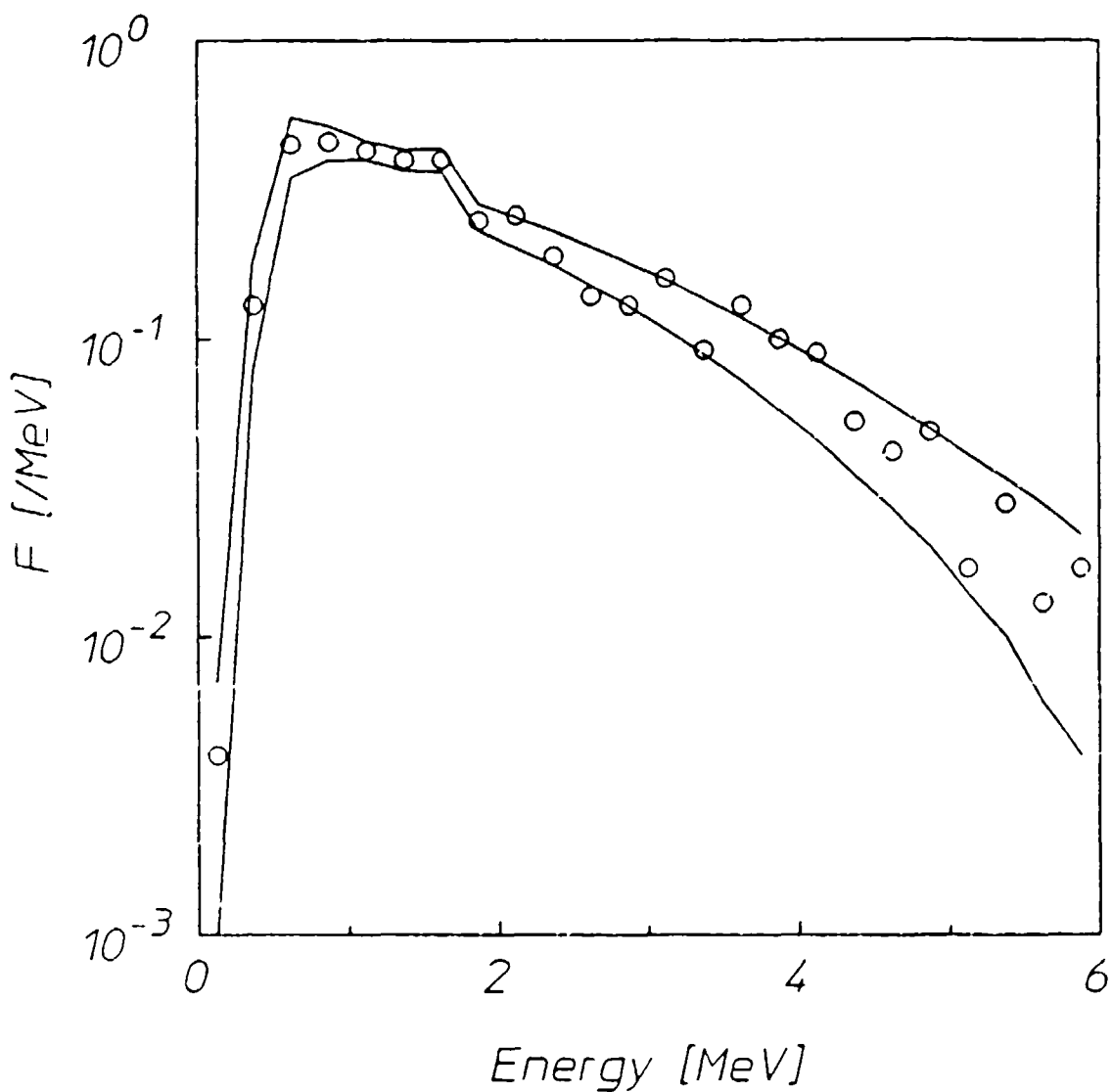


Figure 10: Curves representing the envelope of uncertainty of the input spectral density. This was obtained by fitting piece-wise continuous curves to the uncertainties of the spectrum generated by Mohan. The open circles represent the most probable values of the spectral density as generated by Mohan.

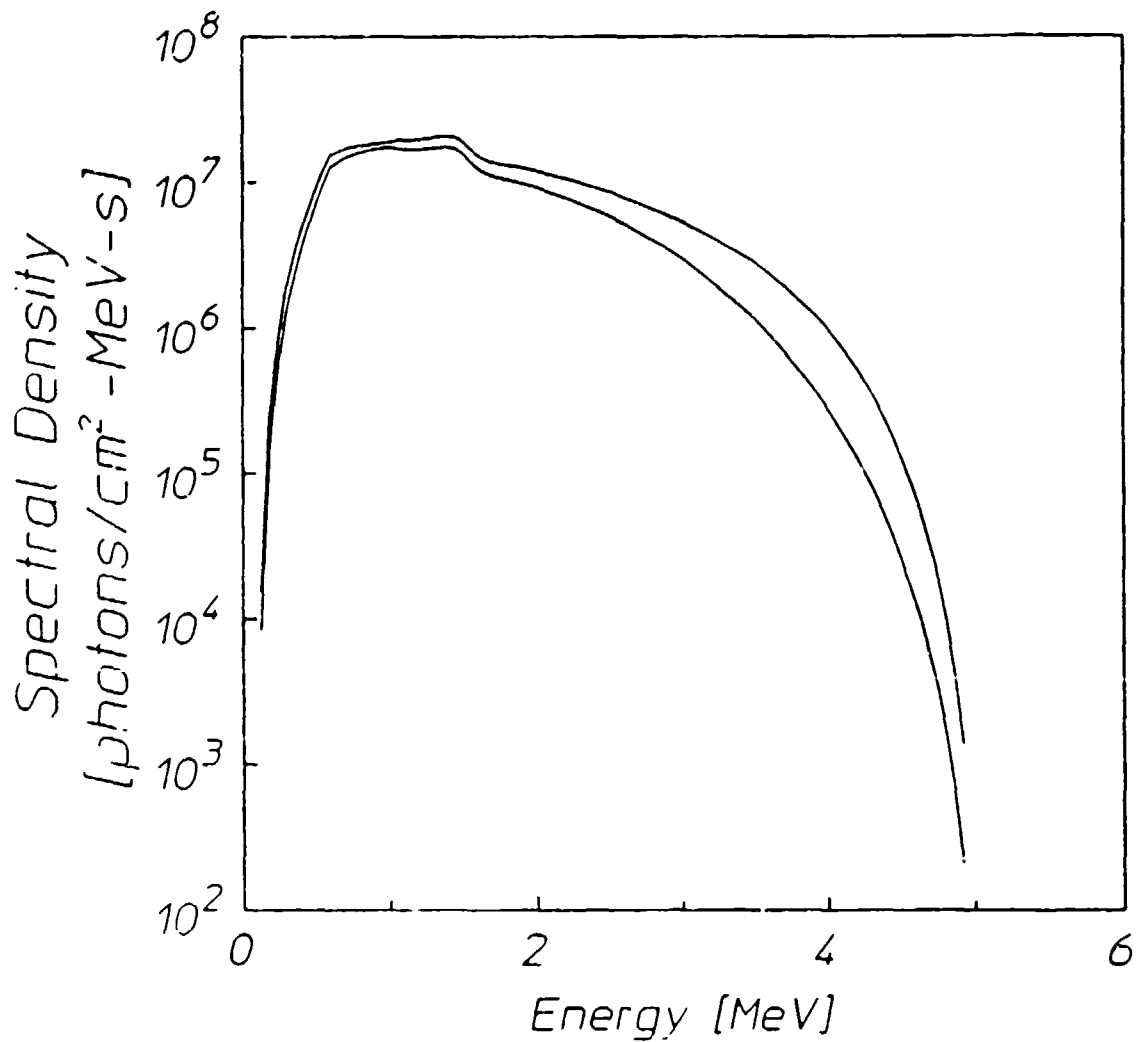


Figure 11: The uncertainty envelope of the compton scattered spectral density at 16° calculated with the extended scatterer/extended absorber geometry.

From the activation data of Table 11, the product of cross section and spectral intensity was calculated using Eq. 18. Based on the assumption of a single gateway, a plot of σ_{eff} versus the gateway energy was made for each value of θ by utilizing the modeled spectral intensities and Eq. 17. The family of curves obtained by the employing this procedure for Compton spectrometer angles of 8°, 16°, and 24° is shown in Fig. 12. Also included in this figure is the curve obtained by a similar analysis of the activation due to the direct exposure of the gold sample to the primary beam of the linac.

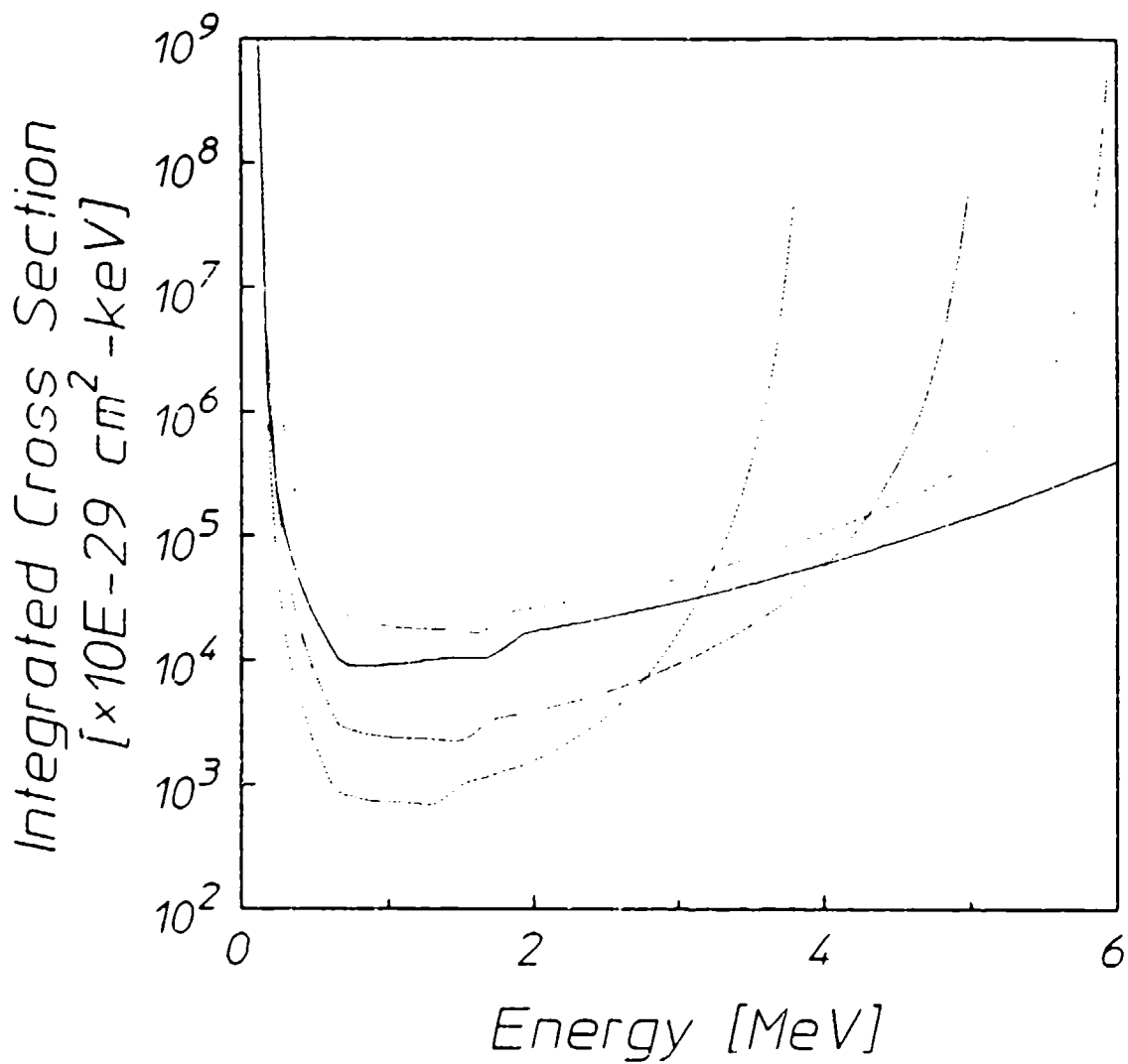


Figure 12: Cross section curves generated from the data taken with the Compton spectrometer and the modelled output spectral densities as shown in Figure 4.

The marked difference between these results and the synthetic curves of Fig. 6 suggests the presence of more than one gateway state, but may be due to experimental uncertainties. The data were analyzed using models incorporating both one and two gateways. In the case of one gateway, there are two unknowns -- the energy E_g and cross section σ for the single gateway -- and four simultaneous non-linear equations of the form

$$A_i' = \phi_i(E_g)\sigma \quad , \quad (19)$$

where the A_i' are the activation values of Eq. 15 normalized to the exposure time and the $\phi_i(E_g)$ are the spectral intensities (dI/dE) at the gateway energy E_g . This set of equations was solved using an iterated Marquardt procedure¹¹, yielding the values $E_g = 3.57 \pm 0.14$ MeV and $\sigma = 42000 \pm 4000 \cdot 10^{-29}$ cm²·keV.

If two gateway states are assumed to exist, then there are four unknown parameters to be found. These are the energies E_1 and E_2 and cross sections σ_1 and σ_2 associated with the lower and upper gateways. Again, a series of four simultaneous non-linear equations can be written relating these parameters to the observed levels of activation. A set of N simultaneous nonlinear equations in N unknowns may have no real solutions, a single solution, or a degenerate set of solutions. Unfortunately, when a solution was sought using the same Marquardt technique described above, successive iterations did not converge to a set of unique values, but instead produced results that were strong functions of the input estimates for the parameter values. Thus, experimental data at additional values of angle θ would be required to obtain an unique solution for the multi-gateway model.

Conclusions

The Compton spectrometer can be used to determine gateway energies and nuclear photo-activation cross sections when used with a linear accelerator producing a well-characterized continuous spectrum. The complexity of the model which can be used to analyze a given system is limited by the number of angles in the Compton spectrometer for which data are available. Models incorporating more gateway states require data at additional angles.

In the present work, a rudimentary analysis was made of the spectrum produced by the Compton spectrometer. This analysis would tend to underestimate the spectral intensity at lower energies, since it does not properly account for multiple Compton scattering in the spectrometer. Thus, the curves of Fig. 12 should lie lower than shown at the

lower photon energies. A comprehensive Monte Carlo transport calculation is planned to realistically estimate the total scattered spectral intensity at each of the sample positions.

Preliminary results from this work indicated that if a single gateway were responsible for the observed activation, the gateway would lie near 3.6 MeV and have a cross section of $4.2 \cdot 10^{-25} \text{ cm}^2\text{-keV}$. Although this is not inconsistent with the results of several other investigators^{12,13}, previous work in this Center¹⁴ and by Lukens¹⁵ also indicates the presence of at least one more gateway in the range between 1 and 3 MeV. Additional experiments with better angular resolution, statistical accuracy, and spectral characterization should further improve the understanding of the photoactivation mechanism in ¹⁹⁷Au.

While mathematical rigor cannot be maintained at any higher level of analysis, some further arguments can be presented based on physical insight. In the first place it must be recalled that the model error is not estimated by the Marquardt procedure. It was shown above that if there were only a single gateway within the interval between 1 and 6 MeV, then it would lie near 3.6 MeV. However, if there are two gateways, then neither is constrained to be near that energy.

Since the observation of any large gateways at all below the onset of the continuum of states was initially surprising, it is reasonable to propose a model with only a minimal number of them at lower energies. Lukens¹⁶ reported the excitation of ¹⁹⁷Au with bremsstrahlung having an endpoint energy of 3 MeV. If this activation observed by Lukens is assumed to be due to a single gateway below 3 MeV, several interesting conclusions may be drawn.

The intensities for energies above 3 MeV are relatively small for scattering at $\theta = 24^\circ$, and therefore the corresponding curve for σ in Fig. 12 approaches the vertical near this energy. Under the assumption made above, this curve represents the cross section of the single gateway observed by Lukens as a function of the energy at which it might lie. The correct choice of the energy can be approximated by considering the intersection of this curve with those obtained at other angles, in analogy to the situation shown in Fig. 6.

Wherever the higher energy gateways may lie, the data obtained at $\theta = 16^\circ$ will be that which is least affected by their presence. Therefore, the intersection near 2.6 MeV of the $\theta = 16^\circ$ and $\theta = 24^\circ$ curves¹⁶

in Fig. 17 should give the best approximation to the location of the gateway observed by Lukens. Consistent with this conclusion is the observation that the $\theta = 8^\circ$ curve, which shows elevated cross section values due to activation at higher energies, intersects the $\theta = 24^\circ$ curve near 3 MeV. If the $\theta = 8^\circ$ curve were corrected by removing the contributions of the higher gateways, the shape of the curve would be preserved, but its location would be translated downward on the plot of Fig. 12. This would shift the intersection down from 3 MeV toward the 2.6 MeV value noted above.

Of course, the $\theta = 16^\circ$ curve may also carry some contamination from higher gateways and thus require a similar downward correction if the effects of the upper gateways were to be removed. The extent of this correction cannot be determined, but its presence insures that 2.6 MeV is an upper limit for the energy of the assumed single gateway. Moreover, reference to Fig. 12 shows that below 1.5 MeV the cross section required by the $\theta = 24^\circ$ curve is $1000 \cdot 10^{-29} \text{ cm}^2\text{-keV}$ or more, which is much greater than the values¹⁵ obtained using the PITHON bremsstrahlung source operated with a 1.5 MeV endpoint energy. Thus, the gateway must be bracketed by these two points.

While the rigorous resolution of the merits of this interpretation must await additional data, there seems to be a strong argument that the gateway originally observed by Lukens lies near 2.6 MeV. This result has an interesting precedent in the literature¹⁷ that has largely been ignored as an anomaly. This is the discrete gateway for the reaction $^{87}\text{Sr}(\gamma, \gamma')^{87}\text{Sr}^*$, having an integrated cross section of $430 \cdot 10^{-29} \text{ cm}^2\text{-keV}$ at 2.66 MeV. This cross section was about one and a half orders of magnitude greater than any other reported for a discrete gateway and has remained unexplained for 20 years. Now it appears that there is a second such example in $^{197}\text{Au}(\gamma, \gamma')^{197}\text{Au}^*$.

Acknowledgements

The authors wish to acknowledge the contributions of our colleague Y. Paiss through many useful discussions concerning nuclear activation and the design of Compton spectrometers.

References

1. C. R. Collins, C. D. Eberhard, J. W. Glesner, and J. A. Anderson, *Phys Rev C* 37, 2267 (1988).
2. C. D. Eberhard, J. W. Glesner, Y. Paiss, J. A. Anderson, C. B. Collins, W. L. Hodge, E. C. Scarbrough, and P. P. Antich, Report GRL/8702, 89 (1987).
3. C. B. Collins, J. A. Anderson, C. D. Eberhard, J. F. McCoy, J. J. Carroll, E. C. Scarbrough, and P. P. Antich, Report GRL/8703, 37 (1988).
4. J. A. Anderson, C. D. Eberhard, J. F. McCoy, K. N. Taylor, J. J. Carroll, M. J. Byrd, C. B. Collins, E. C. Scarbrough, and P. P. Antich, Report GRL/8704, 11 (1988).
5. R. D. Evans, "Gamma Rays" in *American Institute of Physics Handbook*, ed. D. E. Gray (McGraw-Hill, New York, 1963).
6. R. Mohan, C. Chui, and L. Lidofsky, *Med. Phys.* 12, 592 (1985).
7. N. C. Ikoro, D. A. Johnson, and P. P. Antich, *Med. Phys.* 14, 93 (1987).
8. Y. Paiss, C. D. Eberhard, and C. B. Collins, Report GRL/8702, 71 (1987).
9. C. B. Collins, J. A. Anderson, Y. Paiss, C. D. Eberhard, R. J. Peterson, W. L. Hodge, *Phys. Rev. C* (accepted for publication).
10. J. A. Anderson, M. J. Byrd, and C. B. Collins, *Phys. Rev. C* (accepted for publication).
11. W. H. Press, B. P. Flannery, S. A. Teukolsky, and W. T. Vetterling, *Numerical Recipes*, (Cambridge University Press, Cambridge, 1986).
12. W. T. K. Johnson and C. E. Dick, *Nucl. Instr. and Meth.* 99, 221 (1972).
13. Zs. Nemeth, L. Lakosi, I. Pavlicsek, and A. Veres, *Appl. Radiat. Isot.* 37, 1155 (1986).

14. C. B. Collins and J. A. Anderson, Report GRL/8701, 35 (1987).
15. H. R. Lukens, Jr., J. W. Otvos and C. D. Wagner, Int. J. Appl. Radiat. and Isot. 11, 30 (1961).
16. The results shown in Fig. 12 and discussed in this chapter are the current values at press time, and are somewhat larger than preliminary values used elsewhere in this report.
17. E. C. Booth and J. Brownson, Nucl. Phys. A 98, 529 (1967).

DISSERTATIONS PRODUCED UNDER THIS CONTRACT

Bowen, Tracey S., A Compact Source Producing Doses of Kilorad/
Minute Delivered below 1 A in Pulses of Nanoseconds
Duration, Ph.D. Dissertation, (The University of Texas
at Dallas, 1988).

Sinor, Timothy W., Observation of Large Scale Nuclear Phase
Modulation Effects, Ph.D. Dissertation, (The University of
Texas at Dallas, 1988).

Reittinger, Peter W., A Frequency Modulation Spectrometer for
Mössbauer Studies, Ph.D. Dissertations, (The University
of Texas at Dallas, 1988).

Coogan, John J., A Flash X-Ray Source Driven by Stacked Blumleins
Producing 500 keV Photons, Ph.D. Dissertation, (The
University of Texas at Dallas, 1989).

APPENDIX I

"Calibration of Pulsed Bremsstrahlung Spectra with Photo-nuclear Reactions of ^{77}Se and ^{79}Br ," by J. A. Anderson and C. B. Collins, *Rev. Sci. Instrum.* 58, 2157-2160 (1987).

"Scaling to High Average Powers of a Flash X-Ray Source Producing Nanosecond Pulses," by F. Davanloo, T. S. Bowen, and C. B. Collins, *Rev. Sci. Instrum.* 58, 2103-2109 (1987).

"Frequency Modulation Spectrometer for Mössbauer Studies," by P. W. Reittinger, T. W. Sinor, S. S. Wagal, and C. B. Collins, *Rev. Sci. Instrum.* 59, 362-367 (1987).

"Calibration of Pulsed X-Ray Spectra," by J. A. Anderson and C. B. Collins, *Rev. Sci. Instrum.* 59, 414-419 (1987).

"Depopulation of the Isomeric State $^{180}\text{Ta}^m$ by the Reaction $^{180}\text{Ta}^m(\gamma, \gamma')^{180}\text{Ta}$," by C. B. Collins, C. D. Eberhard, J. W. Glesener, and J. A. Anderson, *Phys. Rev. C* 37, 2267-2269 (1988).

"Diamond-like Carbon Films Prepared with a Laser Ion Source," by S. S. Wagal, E. M. Juengerman, and C. B. Collins, *Appl. Phys. Lett.* 53, 187-188 (1988).

"Activation of $^{115}\text{In}^m$ by Single Pulses of Intense Bremsstrahlung," by C. B. Collins, J. A. Anderson, Y. Paiss, C. D. Eberhard, R. J. Peterson, and W. L. Hodge, *Phys. Rev. C* 38, 1852-1856 (1988).

"Flash X-Ray Source Excited by Stacked Blumlein Generators," by F. Davanloo, J. J. Coogan, T. S. Bowen, R. K. Krause, and C. B. Collins, *Rev. Sci. Instrum.* 59, 2260-2264 (1988).

"Activation of $^{111}\text{Cd}^m$ by Single Pulses of Intense Bremsstrahlung," by J. A. Anderson, M. J. Byrd, and C. B. Collins, *Phys. Rev. C* 38, 2838-2842 (1988).

"Comment on 'Mössbauer Sidebands from a Single Parent Line,'" by C. B. Collins, P. W. Reittinger, and T. W. Sinor, *Phys. Rev. B* 39, 9655-9659 (1989).

"Large Scale Effects of the Magnetic Phase Modulation of Recoilless Gamma Transitions," by T. W. Sinor, P. W. Reittinger, and C. B. Collins, *Phys. Rev. Lett.* 62, 2547-2551 (1989).

"Laser Plasma Source of Amorphic Diamond," by C. B. Collins, F. Davanloo, E. M. Juengerman, W. R. Osborn, and D. R. Jander, *Appl. Phys. Lett.* 54, 216-218 (1989).

"Mössbauer Isomer Shift Measurements without Mechanical Tuning," by T. W. Sinor, P. W. Reittinger, and C. B. Collins, *Rev. Sci. Instrum.* 60, 3258-3261 (1989).

"Accelerated Decay of $^{180}\text{Ta}^m$ and ^{176}Lu in Stellar Interiors through (γ, γ') Reactions," by J. J. Carroll, J. A. Anderson, J. W. Glesener, C. D. Eberhard, and C. B. Collins, *Astrophys. J.* 344, 454-459 (1989).

Calibration of pulsed bremsstrahlung spectra with photonuclear reactions of ^{77}Se and ^{79}Br

J. A. Anderson and C. B. Collins

The University of Texas at Dallas, Center for Quantum Electronics, P.O. Box 830688, Richardson, Texas 75083-0688

(Received 19 May 1987; accepted for publication 1 August 1987)

A new method is reported for calibrating bremsstrahlung spectra in the 200–1000-keV range with x-ray activation techniques. This approach is particularly significant for pulsed sources that cannot be characterized with conventional spectroscopy methods.

INTRODUCTION

Although (γ, γ') reactions have been investigated for the production of isomers for nearly 50 years,^{1,2} the punishing difficulties associated with this type of work have not allowed experimental reproducibility³ to develop to the level expected from other types of reactions. Only a few tens of papers can be found in the literature⁴ and results reported for the same reactions show extreme variances. The principal impediment to the quantitative study of (γ, γ') reactions seems to have arisen from the sources. Both accelerators and radioactive decay schemes have been traditionally used to provide electromagnetic excitation. Unfortunately, the combination of high flux and high photon energy in the excitation step did not permit the use of standard spectroscopic techniques, and thus the target had to be cycled between the irradiation device and the counting facility. In practice this has meant that studies were limited to the excitation of isomers with lifetimes of seconds to hours.

The difficulties in conducting (γ, γ') reactions are probably typified best by the excitation of the 269-min isomer of ^{113}In at 336 keV. The principal gateway state that is radiatively connected to both the initial and the final isomeric level lies at 1078 keV and can be conveniently excited by resonant absorption of the Compton continuum from a ^{60}Co source mounted in close proximity. Nevertheless, an experiment in 1981, carefully conducted in this way⁵ produced such an excess of isomeric population that it was necessary to postulate a new mechanism in the ^{113}In for nonresonant absorption of the undegraded lines from the ^{60}Co source. Theory has not yet provided a process of the needed magnitude, but discrepancies have been found⁶ as well in ^{111}Cd , in ^{113}In and ^{87}Sr , and even in ^{103}Rh , and $^{107,109}\text{Ag}$ and ^{197}Au excited by positrons annihilated by bound atomic electrons.⁸ However, the most recent repetition of this work³ has suggested that the excessive yield results not from dominance of an unknown process but rather from the difficulty in calibrating the effective dose in the input channel. In that 1986 experiment, excess production was not observed.³ Such problems attest to the need for a better means for the calibration of intense sources of continuum radiation.

Of the (γ, γ') reactions producing isomers through channels which have been more accurately characterized by studies of other types of reactions,^{9,10} those of ^{77}Se and ^{79}Br emerge as most completely described over the range of ener-

gies to 1 MeV. The relevant energy levels are shown in Fig. 1. We report the use of these materials to calibrate an intense bremsstrahlung source capable of delivering a peak dose of the order of 10^{12} keV/keV in a 20-ns pulse to a target volume of 10 cm^3 . The resulting system appears to have the potential for supporting studies of (γ, γ') reactions with a source whose characteristics are known with a level of precision sufficient to resolve concerns over the possible existence of dominant channels for nonresonant excitation in other materials.

I. METHOD AND EXPERIMENTAL DETAILS

The effective cross section for the resonant absorption of electromagnetic continua to produce a population of isomeric states is given by the expression

$$\int_{-\infty}^{\infty} \sigma(E)dE = \frac{\pi b_o b_0 \Gamma \sigma_0}{2}, \quad (1a)$$

where Γ is the total width of the gateway level with branching ratios of b_o and b_0 for decaying back into the ground state and into the isomer, respectively, and σ_0 is the Breit–Wigner cross section for photons

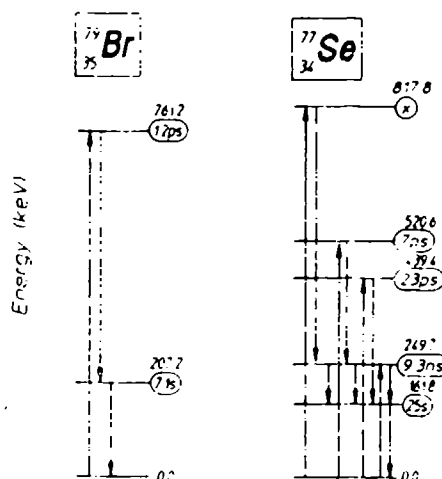


FIG. 1 Energy level diagram of the excited states of ^{79}Br and ^{77}Se important in the production of populations of their respective isomers. Lifetimes of the states are shown in the oval to the right of each and sequences of transitions corresponding to the (γ, γ') reactions leading to the isomers are shown by the arrows.

$$\sigma_0 = \frac{\lambda^2}{2\pi} \frac{2I_e + 1}{2I_g + 1} \frac{1}{\alpha_p + 1} \quad (1b)$$

In Eq. (1b), λ is the wavelength of the gamma ray at the resonant energy. E_0 , I_e and I_g are the nuclear spins of the excited and ground states, respectively; and α_p is the total internal conversion coefficient for the absorption transition.

With the exception of the α 's, which can reasonably be expected to be less than 0.01 at the energies involved, the parameters appearing in Eqs. (1a) and (1b) are reported⁹ for three of the four dominant transitions in ⁷⁷Se and for the single transition in ⁷⁹Br that produce isomers. The level in ⁷⁷Se which is incompletely characterized lies at 818 keV. Branching ratios have been reported⁹ but the lifetime of the state is unknown. We estimated this lifetime by scaling from the 521-keV level which has transitions of similar energies and multipolarities, obtaining 7 ps. Although large, the uncertainty in this estimate was subsequently found to have little effect on the results of the calibration of the continuum. Finally, results for the two ⁷⁷Se transitions at 440 and 521 keV were combined to represent an effective level at the average energy of 480 keV for convenience. The resulting absorption "standards" obtained from Eqs. (1a) and (1b) in these ways are summarized in Table I. As can be seen, the delayed fluorescence lines for ⁷⁹Br and ⁷⁷Se lie at 207 and 162 keV.

The bremsstrahlung x-ray source used in this work was a vacuum diode driven by a 10- Ω coaxial line resonantly charged from a Marx generator. The x-ray pulses from the tungsten foil anode were approximately 20-ns FWHM. Samples of LiBr and elemental Se in natural isotopic abundance were irradiated with a single pulse and then transferred to the counting chamber with a pneumatic shuttle (rabbit) system. A synchronization signal from the x-ray generator triggered the transfer system and started a transit-time clock, which was then stopped by an arrival sensor at the detector. Typical transit times were 700 ms or less. The rabbits and the transfer tube were made of acrylic tubing, which had a negligible x-ray attenuation at the energies involved here. Total sample volume in each rabbit was about 10 cm³. The cylindrical axis of the rabbit was approximately 2.8 cm behind the converter target during irradiation.

The counting system comprised a NaI(Tl) detector, its associated preamp/amplifier, and a dual analyzer that obtained both pulse-height spectra and multichannel scaler data for each shot. Counting was initiated by the arrival of the sample at the 7.6 \times 7.6 cm, well-type NaI(Tl) detector. The analyzers were ORTEC 918 multichannel buffers running on an IEEE-488 bus. Because of the severe RFI/EMI

TABLE I. Summary of nuclear fluorescence parameters used in this work.

Nuclide	E_{in} (keV)	$\pi b_e b_0 \Gamma \sigma_0 / 2$ (10^{-22} cm ² keV)	E_{out} (keV)
⁷⁹ Br	761	6.2	207
⁷⁷ Se	250	0.2	162
	480*	1.5	
	818	0.7	

*The effects of the 440- and 521-keV transitions have been combined.

TABLE II. Sample parameters for nuclear fluorescence experiments.

Sample	Sample weight (g)	Count time (s)	Transit time (s)	Number of shots
LiBr	16.8	20.0	0.73	9
Se	18.4	70.0	0.67	10

environments typically encountered in these experiments, the detector and analyzers were mounted in shielded enclosures and communicated via a fiber optics link with the PC/AT computer that served as the system controller.

II. RESULTS

In the experiment reported here, the x-ray device was operated with a nominal output voltage of 1.0 MeV. Sample weights, counting times, average transit times, and number of shots recorded for each material are shown in Table II.

After the indicated number of e-beam shots, the energy spectra for each material were summed together to produce a composite spectrum for that element. From these spectra of bromine and selenium, exemplified in Figs. 2 and 3, the final results were obtained by simple peak integration.¹¹ Corrections were then made for the photopeak efficiency of the well detector and for the counts lost during the rabbit transfer. Both raw photopeak counts and corrected values are listed in Table III. No corrections have been made for self-absorption of either the pump or the fluorescence radiation.¹²

Time spectra showing the decay of ^{79m}Br and ^{77m}Se appear in Figs. 4 and 5. The half-lives determined from these data are listed in Table III. Our measured half-lives are in reasonable agreement with the literature (compare Ref. 13 and the sources cited therein), as can be seen by comparing the solid lines—reflecting accepted values—with the data in Figs. 4 and 5.

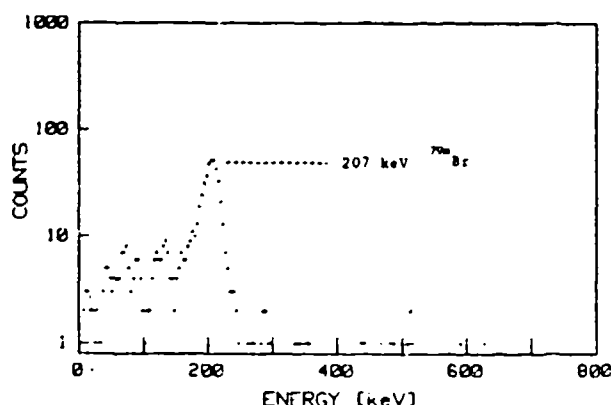


FIG. 2. Nuclear fluorescence spectrum of LiBr. The results of three 20-ns irradiations of the 16.8-g sample were added to obtain this spectrum. The main features of the spectrum are the 207-keV line from ^{79m}Br and the Pb x-ray peak at 75 keV.

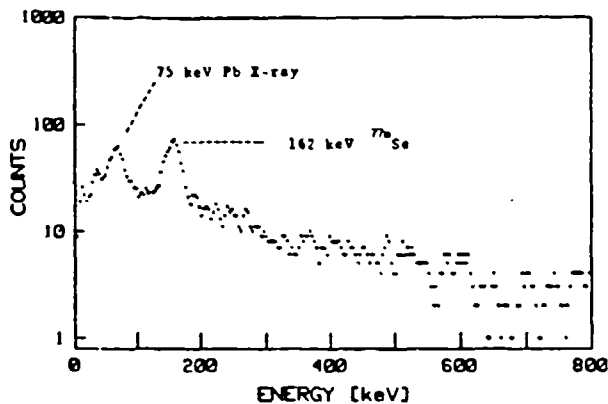


FIG. 3. Nuclear fluorescence spectrum of natural selenium. The spectra from ten 20-ns irradiations of the 18.4-g sample were stacked to produce this spectrum. The greater background in this spectrum, compared to that of Fig. 2, was due to buildup of the natural background over the longer counting period.

III. DISCUSSION AND CONCLUSIONS

Calibration of the bremsstrahlung spectrum required some initial assumptions about its functional form. The model is illustrated in Fig. 6. The high-energy portion of this curve is the linear Kulenkampff approximation¹⁴ with endpoint energy E_m . At energy E , this joins to a region of constant intensity that extends down to a cut-off level E_c . Thus, the model can be expressed by

$$\phi(E) = \phi_0(E_m - E)/(E_m - E_1), \quad E_1 < E < E_m, \quad (2a)$$

and

$$\phi(E) = \phi_0, \quad E_c < E < E_1. \quad (2b)$$

Cut-off level E_c was chosen to be 200 keV since all of the pump lines we considered lay above this value. The knee in the spectrum, E_1 , was placed at 350 keV, in rough agreement with calculations in which a Kulenkampff spectrum was convolved with the transmission spectrum of the tungsten converter foil in the accelerator. This was also consistent with the general form of spectra for pulsed x-ray machines as obtained by absorption techniques.¹⁵ Naturally, more complex models can be applied as additional lines are found to secure the fit.

The total isomeric population was calculated from Table I. By invoking the thin-layer approximation, the expect-

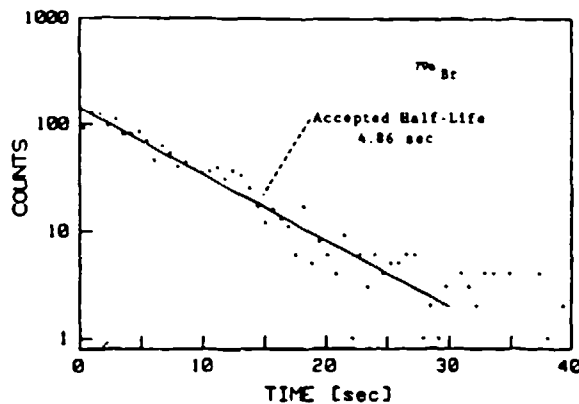


FIG. 4. Decay spectrum of ^{75m}Br obtained in this work. The decay curve calculated from the accepted value¹⁰ for the half-life, 4.86 s, is shown as a solid line.

ed signal (i.e., total isomeric population) produced by a single x-ray shot can be written as

$$S = \frac{\pi}{2} \frac{N}{A} \sum (b_a b_0 \sigma_0 \Gamma) \phi'(E_i), \quad (3)$$

where the summation is over all contributing intermediate gateway levels. In this equation, N is the total number of target nuclei in the sample and A is the area in cm^2 that the sample presents to the pump radiation. Note that $\phi'(E)$, the spectral density of the pump radiation, is expressed in terms of photons per keV. Thus to apply our model of the x-ray spectrum, the substitution

$$\phi'(E) = \phi(E)/E \quad (4)$$

must be used. Table I summarizes the values of the material parameters appearing in Eq. (3).

If substitutions from Eqs. (2a), (2b), and (4) are made, Eq. (3) can be reduced to a form that involves the material characteristics, the populations, and the parameters from the x-ray model. Inserting the experimentally obtained isomer populations for Se and Br from Table III and the energy and cross-section data from Table I then yield a system of equations in the unknowns ϕ_0 and E_m . The solutions are

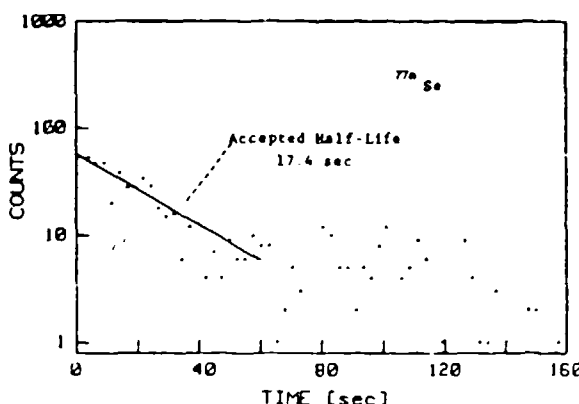


FIG. 5. Decay spectrum of ^{75m}Se . The solid line, drawn for comparison, was calculated using the accepted half-life of 17.4 s.¹⁰

TABLE III. Results for the nuclear fluorescence experiment, expressed in the number of counts observed per excitation pulse. The corrected values have been adjusted to reflect the transit time of the rabbit and the efficiency of the detector at the fluorescence line. The half-lives determined in this work are listed, but the accepted literature values⁹ were used to make the transit time corrections.

Sample	Energy (keV)	Counts observed (per shot)	Counts corrected (per shot)	Half-life observed (s)	Half-life Ref. 9 (s)
LiBr	207	125 ± 5	347 ± 13	16.4 ± 1.7	17.4
Se	162	36 ± 3	92 ± 8	4.4 ± 0.2	4.86

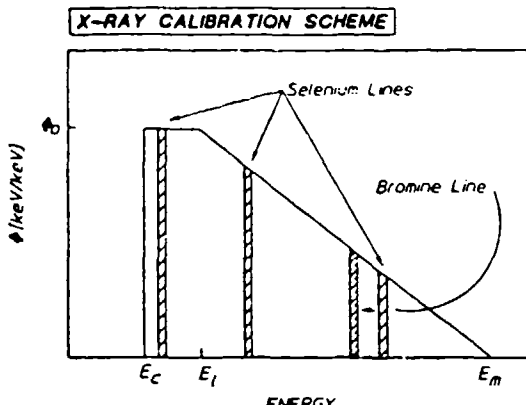


FIG. 6. Model x-ray spectrum used to calibrate the bremsstrahlung output. The locations of the Se and Br lines used in the calibration are shown. Most of the Se contribution occurs at the 480-keV line (actually two lines at 420 and 521 keV), and all of the Br contribution occurs at 761 keV.

$$\phi_0 = 2.05 \times 10^{12} \text{ keV/keV} \quad (5a)$$

and

$$E_m = 920 \text{ keV.} \quad (5b)$$

Note from Table I that these results will be heavily weighted by the contributions of the ^{77}Se "line" at 480 keV and the ^{79}Br line at 761 keV. Thus, the solution given above most realistically describes the intensity in the interval between these two lines.

Sensitivities of the results of Eqs. (5a) and (5b) to the explicit uncertainties in the model assumptions are not great. A change of 50% in the values estimated for the unknown cross section of the last entry of Table I perturbs the end-point energy in Eq. (5b) by only 0.6%. Changing the form of the curve of Fig. 6 to displace $\phi(250)$ upward to the maximum possible amount so that it lies on an extension of the linear portion affects the end-point energy by less than 3%.

The end-point energy $E_m = 920$ keV that was obtained from this characterization of the 450–761 keV interval is disturbingly lower than the 1.0-MV specification of the nominal output voltage. The insensitivity of the result to the explicit uncertainties in the model could imply relative inaccuracies between the parameters in the nuclear database from which the principal cross sections of Table I were computed, but such a conclusion would be premature. It seems more likely that this discrepancy suggests that a low-intensity tail extends upward from this effective end point, probably reflecting the integrated evolution and decay of the machine voltage during the x-ray pulse. The condition illustrates the desirability of employing a model with even

more degrees of freedom and with the attendant necessity of providing additional data points with other isomers. We plan to select other target materials that will enable us to explore the tailing region above 761 keV in greater detail.

Of primary importance is that substantial populations of isomeric states can be produced by pulsed bremsstrahlung irradiation with relatively modest sources. This technique has been exploited for the development of an important new method for characterizing pulsed, high-energy x-ray devices.

Ongoing research along these lines is focused on extending this technology further, so that nuclear fluorescence from short-lived states can be evaluated with smaller amounts of target isotopes.

ACKNOWLEDGMENTS

We gratefully acknowledge the suggestion of this concept for the calibration of pulsed electromagnetic continua by our colleague Y. Paiss. Support was provided by the Innovative Science and Technology Program of the Strategic Defense Initiative Office and was directed by the Naval Research Laboratory.

- ¹B. Pontecorvo and A. Lazard, C. R. Acad. Sci. 208, 99 (1939).
- ²G. B. Collins, B. Waldman, E. M. Stubblefield, and M. Goldhaber, Phys. Rev. 55, 507 (1939).
- ³K. Yoshihara, Zs. Nemeth, L. Lakosi, I. Pavlicek, and A. Veres, Phys. Rev. C 33, 728 (1986).
- ⁴Reference 3 contains a thorough review.
- ⁵A. Ljubicic, K. Pisk, and B. A. Logan, Phys. Rev. C 33, 2238 (1981).
- ⁶M. Kremar, A. Ljubicic, K. Pisk, B. A. Logan, and M. Vrtar, Phys. Rev. C 25, 2097 (1982).
- ⁷M. Kremar, A. Ljubicic, B. A. Logan, and M. Bistrovic, Phys. Rev. C 33, 293 (1986).
- ⁸References to earlier investigations are given in I. N. Vishnevskii, V. A. Zheltonozhskii, V. P. Svyato, V. V. Trishin, and A. I. Feoktistov, Sov. J. Nucl. Phys. 38, 161 (1983).
- ⁹Evaluuated Nuclear Structure Data File (Brookhaven National Laboratory, Upton, NY, 1986).
- ¹⁰C. M. Lederer and V. S. Shirley, *Table of Isotopes*, 7th ed. (Wiley, New York, 1987), Appendices 27 and 29.
- ¹¹P. A. Baedecker, Anal. Chem. 43, 403 (1971).
- ¹²As the mean-free paths for absorption of the pump radiations at the various energies were much greater than the sample sizes, no corrections were needed for the inputs. Numerical integration of the absorption integrals for the output fluorescences indicated that the corrections for these particular nuclei in the geometry employed should be less than 30%. However, the much greater and more ill-defined inaccuracy in the values of parameters appearing in Table I obviated the need for such a level of concern at this time. An ongoing recalibration of the critical nuclear properties is more important to overall accuracy.
- ¹³W. T. K. Johnson and C. E. Dick, Nucl. Instrum. Methods 99, 221 (1972).
- ¹⁴E. U. Condon, in *Handbook of Physics*, edited by E. U. Condon and H. Odishaw (McGraw-Hill, New York, 1967).
- ¹⁵S. G. Gorbics and N. R. Pereira (unpublished).

Scaling to high average powers of a flash x-ray source producing nanosecond pulses

F. Davanloo, T. S. Bowen, and C. B. Collins

Center for Quantum Electronics, University of Texas at Dallas, P. O. Box 830688, Richardson, Texas 75083-0688

(Received 2 September 1986; accepted for publication 24 July 1987)

Described here is the scaling of a repetitively pulsed, flash x-ray source to yield 140-mW average power in 15-ns pulses of radiation near 1 Å. Interchangeability of discharge anodes has provided for a significant fraction of the output to be extracted in the K lines of Cu, Mo, Nb, and Ag. In less than 1 min of experimental time, a peak spectral density is radiated that exceeds 1×10^{18} keV/keV. For some applications this device can offer a tabletop alternative to laser plasma x rays and to synchrotron radiation.

INTRODUCTION

The developing availability of synchrotron light sources has stimulated major areas of research requiring pulses of radiation in the x-ray region. Average x-ray powers can now be great enough so that many experimental responses can integrate above the noise in reasonable working periods. Unique features such as the collimation of the output seem to render the synchrotron irreplaceable for many applications. Nevertheless, the imbalance between demand and supply of such facilities motivates the development of alternative sources for at least some applications not needing all of the synchrotron's distinctive features. One such application of particular interest to our laboratory lies in examining the nuclear fluorescence from materials irradiated by x rays in the 1–100-keV range of energies.¹ Since we are using extended absorbers, collimation is not important. For us the essential figure of merit lies in the average x-ray power emitted¹ over the bandwidth of interest in pulses of duration of the order of 10 ns or less.

Although both laser plasmas and large e-beam discharges offer alternative solutions to the need for maximal emitted power in the x-ray region, those also are large and expensive devices requiring complex supporting facilities. A first major step in the realization of a laboratory-scaled, pulse x-ray source was the Blumlein-driven generators of Bradley² and co-workers.³ For pulses as short as 100 ns their devices performed successfully to the point limited by fundamental considerations,^{2,3} yet remained portable and self-contained. Nevertheless, those generators, together with the laser plasmas and e-beam devices, were characterized by very low repetition rates which would necessarily limit their usefulness in experiments dependent upon the integration of responses that occur with low probabilities.

Recently we reported⁴ a further step in the realization of a laboratory-scaled source of intense pulses of x rays delivered at high rates of repetition. We described a Blumlein-driven x-ray diode for which impedances had been controlled to yield output pulses of about 10-ns duration with reasonable efficiency. Moreover, commutation was effected with a hydrogen thyratron so that operation to high repetition rates could be realized. At 100 Hz an average x-ray

power of 35 mW was reported. Here we describe the scaling of this type of device to yield 140 mW of x rays while retaining the tabletop aspects.

I. DEVICE DESIGN AND CONSTRUCTION

As described in our previous report,⁴ the design of our flash x-ray device centers around three critical subassemblies: (1) a low-impedance x-ray tube, (2) a Blumlein power source, and (3) a commutation system capable of operation at high repetition rates. This basic organization was shown in our first report⁴ in a schematic, which is reproduced in Fig. 1 for convenience. Elements (2) and (3) differed little from drivers we had developed earlier for short-pulse nitrogen ion lasers.⁵

For the present investigation of the scaling of this flash x-ray device to higher powers, two larger systems were constructed: one with a nominal 1.8Ω line capable of storing about 7 J, the other with a 0.85Ω line storing 8 J. Because of the thicker dielectric layer giving the larger impedance, the first was capable of routine operation at higher voltages. In both cases the Blumlein was constructed from massive copper plates, potted with epoxy on outer surfaces to reduce corona, and separated by layered Kapton (polyimide) dielectrics. In operation the middle conductor was charged to a positive high voltage which could be varied to 30 kV, and commutation was effected by an EG&G 3202 hydrogen thyratron mounted in a grounded grid configuration. The average available input power was sufficient to support operation to a 100-Hz repetition rate in most configurations. Comparative values of line dimensions and parameters are summarized in Table I, with a description of the earlier system in the first column.

Charging of the Blumlein was accomplished with one of two systems, a dc power supply or a resonantly pulse charged source. The latter configuration is shown schematically in Fig. 2, together with a typical timing sequence of operation. Advantages of the pulse charged system were its physical compactness and the lessened duration over which high-voltage stress was applied to the Blumlein insulator. However, with either power supply, the integrated x-ray device could be operated to 30 kV in air in a tabletop mode.

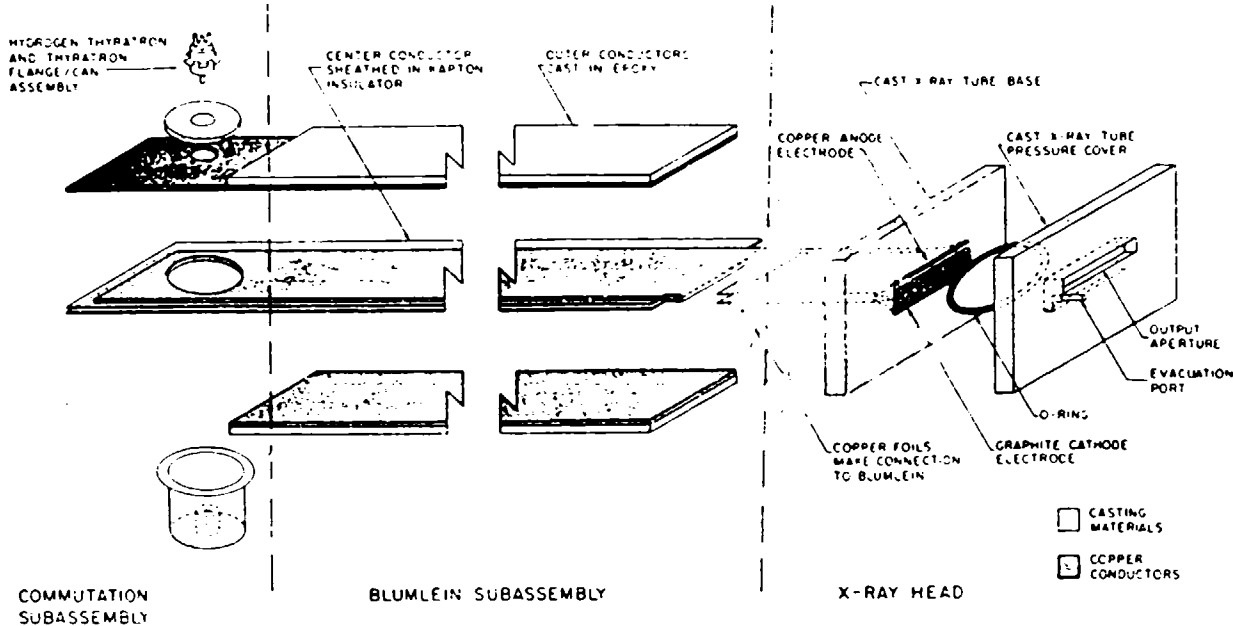


FIG. 1. Schematic drawing of the high repetition rate, flash x-ray device characterized in this work.

With emphasis on obtaining a singularly low inductance input to electrodes designed to give a filamentary source of radiation, the x-ray tube was constructed from cast materials selected to minimize erosion and maximize heat transfer. Copper foil strips 0.05 mm thick and 10 cm wide were fastened to the electrode mounts, then passed through the cast material of the base of the x-ray head before it hardened, and finally joined to the outermost copper plates of the Blumlein. In this way any transverse constriction of the path of the discharge current between the Blumlein and the electrodes was avoided.

The design of the x-ray tube for these scaling studies has evolved substantially from that used in the first models reported earlier.⁴ In that system the anode had been cast directly into the base to facilitate passage of the connecting foil. The first models of the x-ray tube were considered to be expendable, and the cost of construction was low enough to justify that conception. However, a recent refinement of objectives has created a potential need for the use of exotic metals, and it became necessary to develop the capability shown in Fig. 3 for the interchangeability of anodes. In this

design the anode is a simple cylinder of metal, 6.35 mm in diameter and 10 cm long, which is inserted into a socket as shown. The cathode is also demountable. As in the disposable version, it consists of a strip of 0.381-mm-thick graphite further ground with a bladelike edge 10 cm wide and is separated from the anode by a variable distance chosen to optimize performance. The electrical length of the strip was selected to give a resistance comparable to the line impedance but below it in order to assist in damping the ringing of the discharge current in the period following the initial pulse that produced the x rays. The position of the line of intersection between the midplane of the current sheet and the anode surface proved to be an important parameter, most probably because of a potential compensation between the angular distribution of the emitted x rays and the possible shadowing effect of the anode rod for some relative positions. Shims were inserted to raise the cathode blade in order to maximize the output.

The discharge space was enclosed by a pressure shell, also fabricated from cast materials, with an integral window of 0.076-mm-thick Kapton plastic film. The window aperture was covered with a graphite plate 0.127 mm thick to eliminate the emission of visible and UV light. Even with the cast construction and ready access to internal electrode spacings, operating pressures below 3.0 mTorr were routinely maintained with a small mechanical pump. Performance was not noticeably dependent upon the residual pressure in the x-ray tube unless it rose to approach 7 mTorr, a value beyond which outputs were progressively reduced.

II. OPERATION

Precise measurements of time-resolved voltages and currents were rendered difficult by the extremely low impedance of the Blumlein and by the commutation of the thyra-

TABLE I. Comparison of the dimensions and parameters of the Blumleins in the three devices used in these scaling studies.

System	0	A	B
Dielectric	Layered Kapton and epoxy	Layered Kapton and epoxy	Layered Kapton and oil
Thickness	0.66 mm	0.69 mm	0.38 mm
C(storage)	3.2 nF	7.2 nF	9.5 nF
C(switche)	3.5 nF	8.7 nF	9.1 nF
Line impedance	1.8 Ω	1.8 Ω	1.8 Ω
Transit time	5.5 ns	11.4 ns	6.8 ns

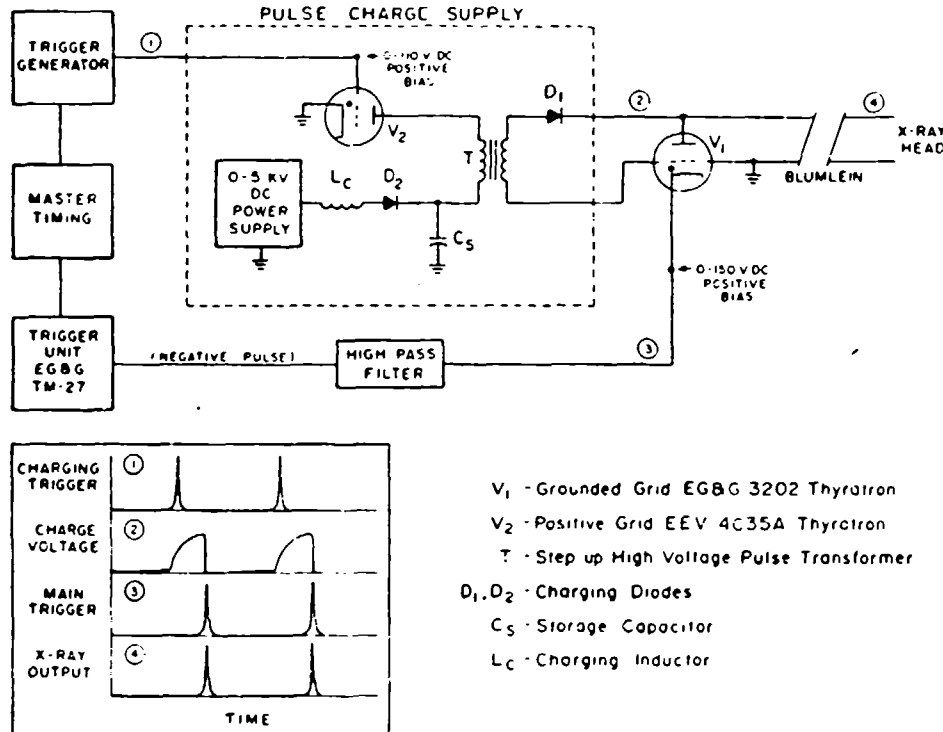


FIG. 2. Resonant pulse power supply used to charge the Blumlein in these experiments. The inset shows a typical timing sequence and the relationships between various events essential in the device operation.

V_1 - Grounded Grid EG&G 3202 Thyratron
 V_2 - Positive Grid EEV 4C35A Thyratron
 T - Step up High Voltage Pulse Transformer
 D_1, D_2 - Charging Diodes
 C_s - Storage Capacitor
 L_c - Charging Inductor

tron in a grounded grid configuration on this particular decade of time scales, 1–20 ns. With resonant pulse charging of the Blumlein it was possible to shunt the x-ray tube with a voltage divider constructed from a tapped water resistor of a sufficiently low impedance, around 200Ω , so that meaningful measurements of voltage as a function of time could be made with limited radio-frequency interference (RFI). Sampled voltages were suitably attenuated upon entry into a heavily screened room where they were recorded with a Tektronix 7912AD transient digitizer. Precautions notwithstanding,

there remained sufficient RFI to introduce triggering jitter of about ± 10 ns whenever absolute timing of signals was attempted.

Operation generally produced the switching waveforms of voltage expected of such Blumeins,³ with the charge voltage and the discharge gap separation emerging as the two most critical experimental variables. Figure 4 shows the dependence of the voltages measured across the x-ray diode as functions of time for the various spacings between anode and cathode for a charge voltage of 22 kV. In contrast to earlier

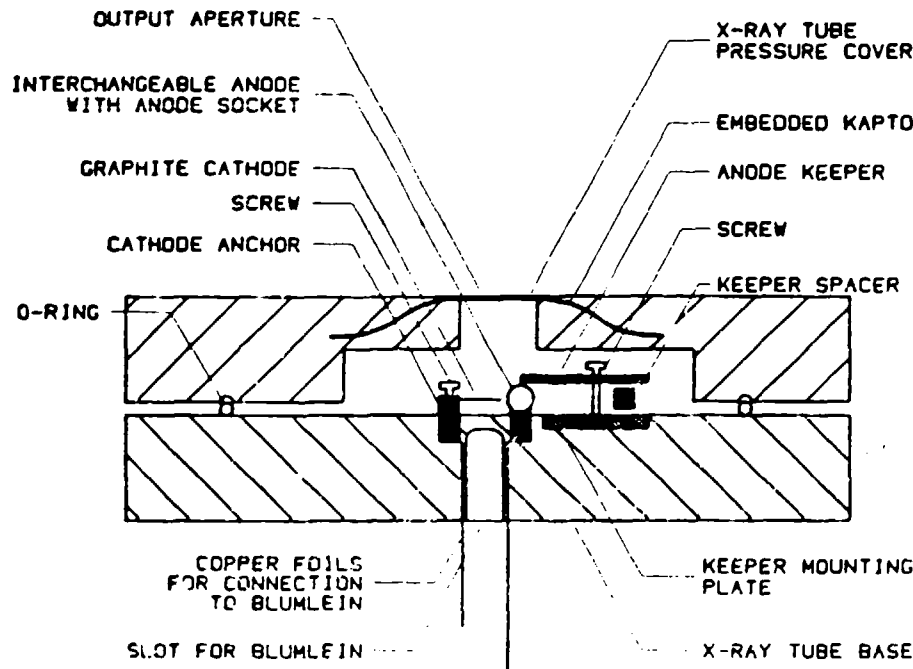


FIG. 3. Schematic drawing of a cross section of the x-ray diode used in this work emphasizing provisions for interchanging materials used as anodes.

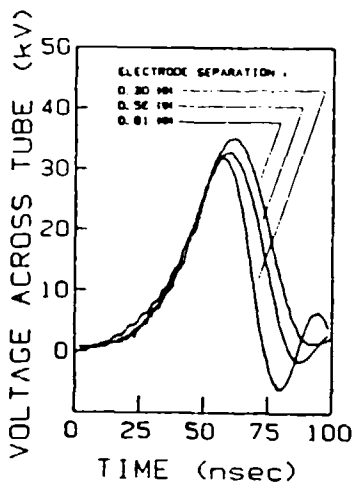


FIG. 4. Voltages measured across the electrodes of the x-ray diode driven by system B as functions of time for the various spacings of anode to cathode indicated. Charge voltage of the Blumlein before commutation was 22 kV.

impressions,⁴ it can be seen in Fig. 4 that significant voltage multiplication does develop before enough current is discharged through the x-ray diode, to limit further ringing of the voltage to even higher values. For electrode spacings producing useful amounts of x rays, the peak voltages typically reached values of about 1.5 times the charge voltage originally applied. Also seen clearly in Fig. 4 is the extent to which smaller discharge gaps facilitate the earlier initiation of the "switching" portion of the waveform, during which the multiplied voltage is rapidly falling as the current is presumed to be rising.

Outputs were detected with three different systems. Measurements of absolute pulse energies utilized a moderately fast scintillator plastic equivalent to NE114 with nominal 7.0-ns decay time. The resulting light output was detected with a photomultiplier having 1.5-ns resolution and was integrated with an EG&G/Ortec charge-sensitive preamplifier. Calibration was obtained by comparing the time-integrated fluorescence from the plastic detector when illuminated with geometrically attenuated x rays from the flash source directly with the level of excitation produced by a radioactive source emitting low-energy lines of known characteristics. This technique was used to determine the dependence of the total energies in the x-ray pulses as functions of the important experimental variables.

More direct measurements of the time-dependent evolution of the output intensities were made with the above two detection systems. In one the scintillator in the above system was replaced with a faster plastic equivalent to Pilot-U with a nominal 1.36-ns decay time, and the photomultiplier anode signal was input directly to a Tektronix 7912AD transient digitizer. Numerical deconvolution was subsequently employed to remove the combined time constants of the photomultiplier and plastic. Attention to the reconstruction of the base line after deconvolution identified an empirical time constant of 3.5 ns as the most probable value in reasonable agreement with the sum of the manufacturer's specifications cited above. Confirmation of the temporal dependence was

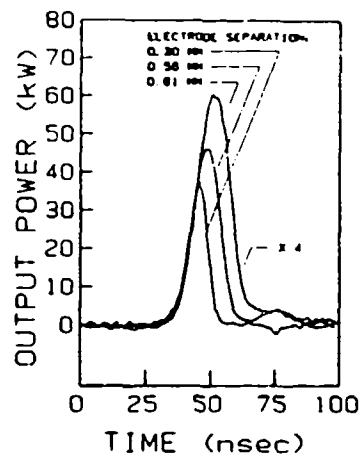


FIG. 5. Typical dependence of output x-ray power emitted by system B as a function of time for the different electrode spacings shown. Charge voltage of the Blumlein was 22 kV.

obtained with a Hamamatsu type S1722 PIN diode with 1-ns rise time connected to the Tektronix 7912AD digitizer without preamplification. While this last system proved preferable for the study of the dependence of the relative intensity upon time, long-term drift of the rather low sensitivity together with the absorption in the window made it difficult to use for the routine determination of absolute intensities.

Figure 5 shows the results of a typical measurement from system B of the output intensity as a function of time, made with the PIN diode cross calibrated with the scintillator plastic to obtain the absolute scale of intensities. Equivalent data taken entirely with the scintillator/photomultiplier combination agreed completely with such data but displayed a greater level of noise. From Fig. 5 it can be seen that the effect of electrode separation on x-ray output was comparable to its effect upon the voltage across the x-ray diode. Operation with smaller separations between anode and cathode resulted in earlier termination of the period during which power was effectively transferred to the load at a sufficiently high voltage to accelerate electrons to the energies needed to excite x-ray emission from the inner shells of the atoms of the anode material.

Relative times at which switching and x-ray emissions were found to occur are shown in Fig. 6. As mentioned earlier the triggering was not entirely stable. However, it alternated between several discrete positions rather than varying continuously. The data of Fig. 6 were obtained by selecting on the basis of histograms the most probable waveforms. The resulting standard deviation of the timing skew between curves shown in Fig. 6 was 3.1 ns.

For each of the three systems examined in this work, the x-ray fluence delivered to an external target would be visually examined for uniformity under both single pulse and higher repetition rate conditions by allowing it to fall upon a fluoroscopy screen of the type used in radiography. A uniform pattern, sharply delineated by the edges of the output aperture, could be readily seen to result from the great majority of discharges. Pinhole photographs of the output orifice showed the actual source to consist of a largely uniform

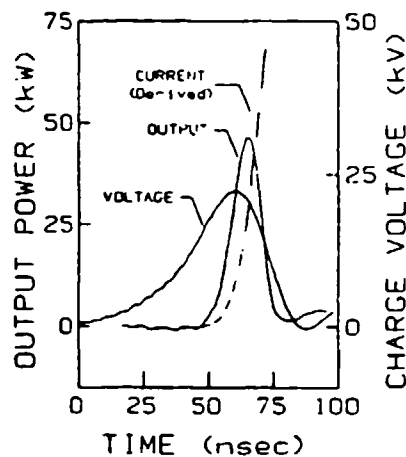


FIG. 6. Typical relationship for the voltage and output intensities measured at the x-ray diode. These particular data corresponded to a charge voltage of 22 kV applied to an electrode spacing of 0.56 mm by system B. The dashed line shows the development of the current waveform. The rising edge of the current waveform was obtained from the data using an iterative process as described in the text.

distribution of densely packed points along the length of the anode. Resolution was sufficient to show that the emission occurred primarily from the region between the anode and cathode, presumably from vaporized anode material being accelerated toward the cathode. Operationally the x-ray head was equivalent to a fast linear flash lamp for the x-ray region.

III. PERFORMANCE

For each of the three devices characterized in this work there was found to be an optimal value of anode to cathode spacing. Figure 7 shows the typical variation in x-ray pulse energy observed as that separation was changed. Such data presented the same general trend, thus refining the impression given in the preliminary report,⁴ with the exception that

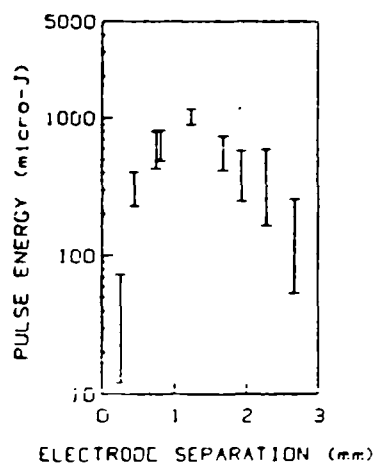


FIG. 7. Total x-ray pulse energy emitted near 1 Å under single-shot conditions (1.4 Hz) as a function of the separation between anode and cathode. These particular data were obtained from a Mo anode operated in system A initially charged to a voltage of 28 kV.

the datum in that work reported for the smallest gap was spurious and should have reflected a lower value. The trend displayed in Fig. 7 at smaller values of electrode spacing was entirely reproducible in this work and is readily comprehensible in the context of Figs. 4 and 5 showing a decreasing pulse width to result from more narrow separations.

The scaling with operating voltage of the outputs from flash x-ray devices has been the recent subject of an excellent review.⁶ It was shown that over the range of photon energies below 100 keV, the time derivative of the output dose \dot{D} could be parameterized

$$\dot{D}(t) = K_c I(t) V^2(t) + K_L I(t) [V(t) - V_K]^{1/2}, \quad (1)$$

where $I(t)$ and $V(t)$ denote the instantaneous values of current and voltage, respectively, at the x-ray diode and V_K is the potential of the K edge for the material of the anode. The first term of Eq. (1) describes the energy emitted as bremsstrahlung continuum, while the second describes emission of the characteristic lines of the anode.

In the experiments reported here, the voltage waveform could be measured directly but the tight coupling of the line to the diode prevented direct measurement of the current. In order to obtain a zeroth approximation to the behavior of the output energy expected for increased voltages, the time-dependent waveform for the current was obtained from measurement of $V(t)$ and $\dot{D}(t)$ and then was scaled to other voltages. Except for low voltages near the initiation of x-ray emission, results agreed with experiment to a degree that was better than might have been expected from the crude nature of the approximation.

The waveform for the current $I(t)$ through the x-ray diode was obtained from the data of Fig. 6 through the application of Eq. (1) in an iterative procedure. The n th approximation to the current was

$$I_n = \frac{K_{c(n-1)} + K_{L(n-1)}}{K_{c(n-1)} V^2 + K_{L(n-1)} (V - V_K)^{1/2}} \dot{D}, \quad (2a)$$

$$\frac{K_{cn}}{K_{Ln}} = 2.1 \frac{\int_0^\infty I_n (V - V_K)^{1/2} dt}{\int_0^\infty I_n V^2 dt}, \quad (2b)$$

where I_n and V were functions of time.⁷ To start the iteration it was assumed

$$K_{co} = 1, \quad K_{Lo} = 0. \quad (3)$$

Plotted in Fig. 6 is the waveform derived for I_4 which varied from I_1 by less than 3% at every value of time. Finally, it was assumed that

$$I = (U/22) I_4, \quad (4)$$

where U was the charge voltage on the line in kilovolts and the time integral of Eq. (1) was taken to approximate the total output dose for different values of U .

The results of this model are shown by the solid line in Fig. 8 together with a simple dependence upon V^3 shown as dashed for comparison to the actual data measured with the Cu anode. Undoubtedly, the disagreement at lower voltages is a consequence of the unrealistic approximations that neither the dynamic impedance nor the ratio of contributions from line to continuum are strong functions of voltage. The estimate of Fig. 8 is particularly useful in suggesting that

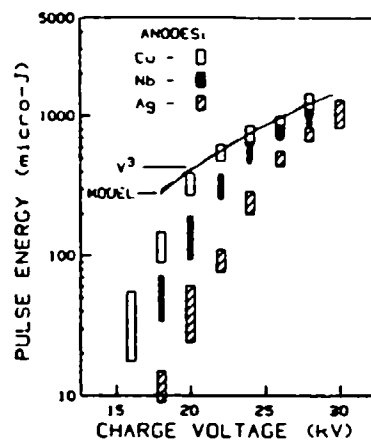


FIG. 8. Total x-ray pulse energies emitted near 1 Å under single-shot conditions (1.4 Hz) as functions of the charging voltage of the Blumlein in system A for anodes made from Cu, Nb, and Ag, as indicated. Electrode separations were 0.81, 1.2, and 1.4 mm, respectively. The solid line represents a model of the output as a function of the charge voltage based on the development of the current waveform derived from the data, as described in the text.

the strongest scaling of output with voltage is actually a threshold phenomenon restricted to the range of lower voltages. Roughly scaling output with V^3 would seem a reasonable means of projecting the performance to larger devices.

Rather curiously, it was found that the output pulse duration seemed to depend upon the anode material. In Fig. 9 it can be seen that the output pulse widths were anomalously brief when niobium was used as an anode. In that case pulse durations still depended strongly upon electrode spacing, but the scale of the variation was shifted by a significant amount.

The scaling of x-ray outputs to larger values with increased system size is illustrated in Fig. 10. It can be seen that whether obtained with a longer Blumlein or a thinner dielectric, a large value of stored energy resulted in greater out-

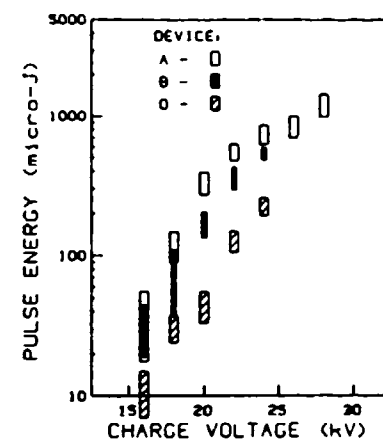


FIG. 10. X-ray pulse energies emitted as functions of the charging voltage of the Blumleins for the three different systems, A, B, and O described in Table I. For this comparison anodes were made of Cu and electrode spacings were 0.81, 0.56, and 0.81 mm, respectively.

puts. It was also observed that the emission of x rays into the output pulse persisted for longer times with the longer Blumlein of system A than for system O for the same electrode spacing. These results support the conclusion of the Bradley group² that useful emission can be obtained even after the closure of the electrode gap by the short-circuiting plasma formed from ions of the anode material.

With the larger devices considered in this work, x-ray pulse energies were found to remain largely constant as the pulse repetition rate was varied over the range from 1 to 100 Hz. Figure 11 shows this to be reflected in the measured values of average power output in the x-ray pulses from the largest of the devices. Limitations imposed by the primary power supply to the pulse-charged system prevented the actual operation simultaneously at both maximum repetition rate and voltages higher than shown in the figure. However, the absence of any significant variation in output pulse energy with repetition rate from Fig. 11 indicates that an average

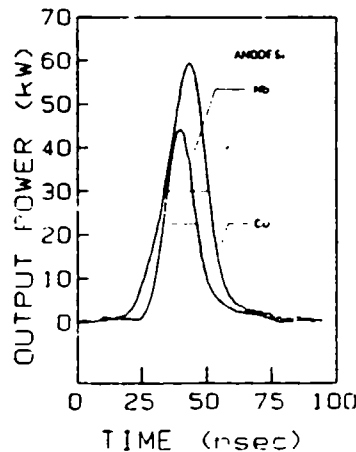


FIG. 9. X-ray power emitted as a function of time from two different anodes, Cu and Nb, in system A. Electrode spacings were 0.81 mm, and the horizontal lines indicate the full width half-maxima (FWHM) of the pulses. The origins of the time axes of the two pulses have been arbitrarily shifted to facilitate comparison of the FWHM's.

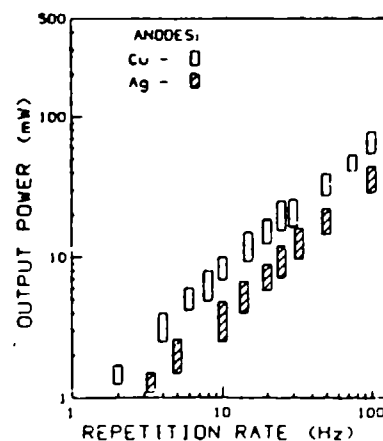


FIG. 11. Average powers emitted as x rays near 1 Å as functions of the pulse repetition rates for a charge voltage of 26 kV onto system A. Two different anode materials, Cu and Ag, were used as indicated, with electrode spacings of 0.81 and 1.4 mm, respectively.

power of 200 mW is readily within the capabilities of this device. Each data point in Fig. 11 was the average of a sequence of measurements.

IV. DISCUSSION

The results of this scaling study show that the principal variables determining the temporal morphology of the output x-ray pulse for these Blumlein-driven devices are actually the electrode spacings and material composition of the anode. This implies that the basic pulse shapes are determined by the characteristics of the process of closure of the diode gap by the plasma of ions ejected from the anode and accelerated to the cathode. However, in agreement with previous reports, the duration of useful output can be lengthened significantly by continuing to supply current from a low-impedance Blumlein, presumably even after the closure occurs.

The intensity level and thus, ultimately, the energy emitted into the output pulse seems to scale most strongly with the charge voltage. Unlike the analogous cases of lasers driven by low-impedance Blumleins, there appears to be no detrimental effect upon efficiency to result from operation at higher repetition rates. Having no gas to heat in the discharge or to sustain shock waves, such favorable contrast with laser performance as observed in these x-ray diodes is actually to be achieved.

Operation with these devices has been limited only by the primary sources of power available to date. It seems clear from these scaling studies that operation to much higher average powers with larger devices can be readily achieved.

Estimates continue to indicate²⁻⁴ that an amount of the order of 25% of the output energy generally lies in the characteristic x-ray lines of the anode material. With this assumption and the observation that relatively little output occurs at energies above the *K* edge, the spectral density in

the continuum in a single pulse from the largest device A corresponds to 8.4×10^{11} keV/keV. If it is assumed that with a copper anode the lines have their customary width of around 6 eV, best values of output energy correspond to about 2.2×10^{14} keV/keV when expressed in terms customary for reporting laser plasma yields. Thus, in less than a minute of experimental time at 100-Hz repetition, over 1.3×10^{18} keV/keV could be emitted. This would exceed the dose available from a shot of a large laser plasma system at these x-ray wavelengths corresponding to 8 keV.

As mentioned earlier, our own applications concern the use of such a device to excite nuclear transitions, and the ultimate signal-to-noise ratio will depend only upon the total keV/keV that can be delivered in a working period. It is reasonable to expect that some other applications as well may find benefit in this laboratory scaled alternative to either synchrotron radiation or laser plasma x rays.

ACKNOWLEDGMENTS

The authors gratefully acknowledge the support of this work in part by the Office of Naval Research and in part by the Innovative Science and Technology Program of the Strategic Defense Initiative Office, directed by the Naval Research Laboratory.

- ¹C. B. Collins, F. W. Lee, D. M. Shemwell, B. D. DePaola, S. Olariu, and I. I. Popescu, *J. Appl. Phys.* **53**, 4645 (1982).
- ²L. C. Bradley, A. C. Mitchell, Q. Johnson, and I. D. Smith, *Rev. Sci. Instrum.* **55**, 25 (1984).
- ³Q. Johnson, A. C. Mitchell, and I. D. Smith, *Rev. Sci. Instrum.* **51**, 741 (1980).
- ⁴C. B. Collins, F. Davanloo, and T. S. Bowen, *Rev. Sci. Instrum.* **57**, 863 (1986).
- ⁵C. B. Collins, *IEEE J. Quantum Electron.* **QE-20**, 47 (1984).
- ⁶P. Krehl, *Rev. Sci. Instrum.* **57**, 1581 (1986).

⁷The constant 2.1 appearing in Eq. (2b) was obtained from a separate measurement of the relative contribution from lines and continua under this one condition.

Frequency-modulation spectrometer for Mössbauer studies

P. W. Reittinger, T. W. Sinor, S. S. Wagal, and C. B. Collins

Center for Quantum Electronics, University of Texas at Dallas, Richardson, Texas 75080

(Received 30 July 1987; accepted for publication 13 October 1987)

A nuclear frequency-modulation spectrometer (NFMS) for high-resolution gamma-ray spectroscopy is described in this article. As the name implies, this device operates by modulating the cross section for gamma-ray absorption. The automation of this spectrometer required the development of an interface to an Apple computer which provides a real-time data display. This interface also enables the Apple computer to control up to two Mössbauer spectrometers at once, with a real-time data display for each. A nuclear frequency-modulation spectrometer makes it possible to observe directly the phenomenon known as "rf sidebands" in Mössbauer spectroscopy, without interference from the "parent transitions." The high resolution of NFMS makes it possible to examine the "rf sidebands" for any fine structure.

INTRODUCTION

As early as 1960 it had been noted that radio-frequency (rf) sidebands to the hyperfine structure of ^{57}Fe could be observed with a Mössbauer spectrometer.¹ The six lines (parent transitions) in a normal absorption spectrum of ^{57}Fe in iron [Fig. 1(a)] are accompanied by additional absorption peaks (rf sidebands) when the absorber is subjected to a rf field [Fig. 1(b)]. In 1960, Ruby and Bolef reported the observation of rf sidebands in iron produced by mounting a ^{55}Co Mössbauer gamma-ray source on an ultrasonic transducer driven at MHz frequencies.¹ It should be noted that the rf transducer was used in addition to a long-period oscillator which provided the energy range for the Mössbauer spectrum by introducing controlled Doppler shifts. In 1968, Perlow reported the generation of rf sidebands in iron directly, by subjecting the gamma ray source to a rf field without the involvement of any external ultrasonic source.² In that same year, Heiman, Pfeiffer, and Walker reported observing rf sidebands in iron as a result of subjecting the iron foil absorber to a rf field.³ Finally, in 1976, Chien and Walker presented a method for producing rf sidebands in a nonferromagnetic stainless-steel absorber with a rf field, by using nickel as a ferromagnetic nonabsorbing driver.⁴ In all cases, the rf sidebands appeared at integral multiples of the frequency of the applied rf (Fig. 2). Figure 2 shows rf sidebands produced in a stainless-steel foil driven by a nickel foil immersed in rf fields of different frequencies. The frequency dependence of these rf sidebands can be utilized to make a high-resolution adaptation of Mössbauer spectroscopy which is freed from many of the mechanical constraints tending to limit conventional devices.

In 1967, Bolef and Mishory reported the development of a spectrometer which was based upon rf sidebands induced in a Mössbauer source with a rf electromechanical transducer (an X-cut quartz crystal).⁵ As the frequency of the applied rf was changed, the energies of the sideband gamma-ray emissions changed. This phenomenon enabled Bolef and Mishory to obtain an absorption spectrum as a function of the frequency of the applied rf. In 1985, DePaolo, Wagal, and Collins reported success in developing a spectroscopic

technique using rf sidebands induced in a ferromagnetic absorber by a rf field.⁶ Modulating the absorber has numerous advantages over modulating the source. It is easier and safer to work with a stable isotope, and it is also easier to interpret a spectrum from a single line source, as opposed to a Zeeman split source or a source with rf sidebands. Therefore, we have improved the technique for a modulated gamma-ray absorption cross-section spectroscopy which we call nuclear frequency-modulation spectroscopy (NFMS).

The technique reported by DePaolo, Wagal, and Collins was slow and laborious, with data collection times on the order of months for tens of data points. We would like to report the automation of this technique, with resulting data collection times of two days for 1024 data points and a sig-

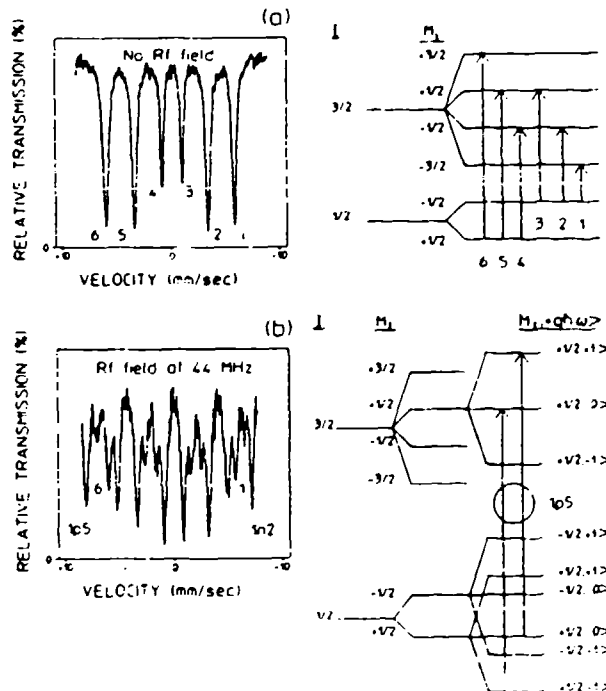


FIG. 1. Mossbauer absorption spectra and energy level diagrams for ^{57}Fe in iron, (a) with no rf field at the absorber, and (b) with a 4-Oe rf field applied to the absorber at a frequency of 44 MHz, showing the effect of the rf field.

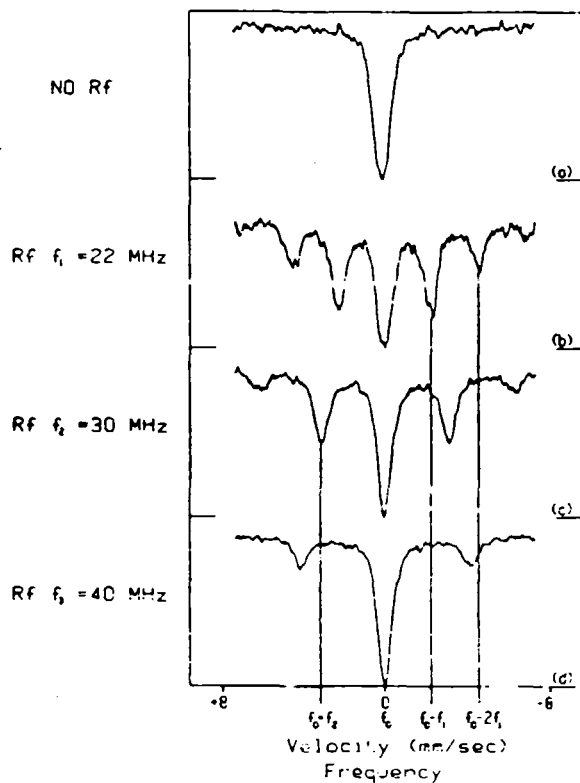


FIG. 2. Mossbauer absorption spectra of ^{57}Fe in 310-stainless-steel driven by a nickel foil, showing the effect of a rf field applied to the absorber-nonabsorber sandwich at frequencies of (b) 22 MHz, (c) 30 MHz, and (d) 40 MHz in comparison to (a) a no rf spectra. It can be seen from the figure that sidebands appear at integral multiples of the frequency of the rf field.

nal-to-noise ratio of 8:1 for a signal that represents a relative absorption of 3%. This article describes the NFMS apparatus, describes the interface to an Apple computer which automates NFMS data collection, and presents some typical NFMS data.

I. SPECTROMETER DESIGN

The NFMS is a modification of a conventional Mössbauer spectrometer comprised of the equipment in the dotted box in the schematic of Fig. 3. A Kr gas-filled proportional counter (ASA PC-KR-1) biased with 1.8 kV from a Bertran Associates model 303 dc voltage supply was used as our gamma-ray detector. The signal from the detector was amplified by an ASA CSP-400A preamp and ASA LA-200 amplifier. The amplified signal was then fed into an ASA LG-200 linear gate which produced 1- μ s TTL pulses for counting.

A 10-mCi ^{57}Co Mössbauer source in a Pd matrix was mounted on an ASA K-4 linear motor capable of operating at a constant velocity or with constant acceleration. A stable means of Doppler shifting the energy of the emitted gamma ray is needed, therefore, an ASA S-700 motor controller is used to produce the voltage waveforms which drive the linear motor. The constant acceleration voltage waveform is derived from a 5-Hz square wave which must be provided by the multichannel scalar (MCS). If the motor is driven at a constant velocity, then the motor controller gates off data to the MCS while the motor is rewinding.

The key to NFMS is the presence of the rf field at the absorber, for which a very stable rf signal generator and amplifier are needed. A Wavetek 3510 signal generator, with a frequency range of 1 MHz to 1 GHz, and a 100-Hz resolution with a 500-Hz/(10-min) stability, was used. The rf amplifier was an ENI 550L 50-W linear amplifier with a range of 1.5–400 MHz. There were two basic circuits used to generate the rf field at the absorber. One was a series LC circuit in parallel with an impedance matching capacitor (Fig. 3). This series-resonant tank circuit was designed to have either a low Q when used in a narrow-band NFMS, or a high Q when used to obtain a Mössbauer spectrum in the presence of a single-frequency rf field. It should be noted that narrow band in these instances refers to a 12 MHz or less bandwidth.

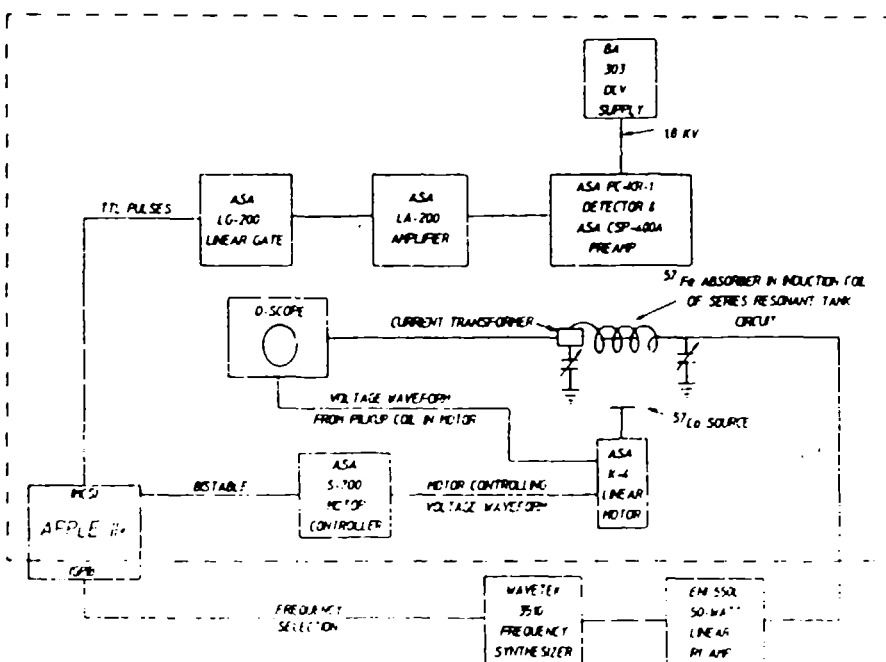


FIG. 3. This schematic shows the NFMS, while the portion of the apparatus which is in the dotted box can be used as a conventional Mossbauer spectrometer.

The other circuit, used in the wideband NFMS, simply incorporated an inductor in series with an impedance matching noninductive load. The absorber was then mounted in the induction coil of the appropriate circuit and subjected to field intensities on the order of 1–5 Oe.

In order to monitor the field intensity in the coil, a Pearson 2877 current transformer was used to measure the current flowing into the induction coil. This transformer outputs 1 V/A with a usable range of 300 Hz to 200 MHz and an insertion impedance of 0.02Ω . In order to monitor the velocity of the motor, there is a pickup coil mounted in the linear motor. The output from this pickup is used to stabilize the driving voltage waveform, but it can also be monitored on an oscilloscope. The velocity of the motor was established by correlating the pickup coil voltages to the positions of the peaks in the six-line spectrum of ^{57}Fe . Currently, work is underway building an interface to an Apple II+ from an ASA LC-9A laser interferometer. This interface will enable the computer to display real-time velocity information as well as track any drifting.

The heart of the NFMS, however, is the MCS/GPIB interface (Fig. 4). It enables an Apple II+ computer to be used for data acquisition and real-time data display with either the conventional Mössbauer spectrometer (constant acceleration mode) or with the NFMS (constant velocity mode with GPIB interface to signal generator). The MCS is a card designed around two VIAs, or versatile interface adapters (6522's). The GPIB, or IEEE-488 General Purpose Interface Bus (9914), is a commercially available interface card available for the Apple computer. The GPIB is necessary only for scanning frequencies of the signal generator. Therefore, the GPIB is not needed if one intends to use only the Mössbauer spectrometer.

The central components of the MCS are the two 6522's, the multiplexing logic, and a 12-bit counter. Each 6522 is a

40-pin chip which has a 16-bit counter with a 16-bit latch, a 16-bit counter with an 8-bit latch, two 8-bit parallel ports, and a serial port. The counter with the full latch can be set to count down in a free running mode and generate interrupts. In other words, the 6522 can be set to generate evenly spaced interrupts so that the Apple's CPU need not be wasted keeping track of time. The counter with the half-latch can be set to count negative logic pulses at one of the pins of the 6522. The multiplexing logic is an assortment of gates which channel the pulses to be counted to one of the 6522's while channelling the Apple's data bus to the other 6522. When an interrupt is generated, the pulses to be counted are gated to the other 6522 while the Apple's data bus is then channeled to the first 6522. As a result, the time it takes the Apple's CPU to add a count to the proper channel is not dead time for the MCS. The 12-bit counter, actually three 4-bit counters, is needed to count 512 interrupts. This counting produces the 5-Hz square wave which is used by the motor controller to generate a constant acceleration voltage waveform for the linear motor. Therefore, the time between interrupts, hence the dwell time per channel, must be $195 \mu\text{s}$ for a 1024 data point Mössbauer spectrum. The NFMS, on the other hand, does not require an accelerating source. Therefore, when using the MCS in a NFMS, the dwell time can be user selected. The optimum dwell time minimizes the total dead time, which arises from the time needed to allow the rf signal to stabilize each time the frequency is changed, without compromising the stability of the signal.

Use of this hardware as a NFMS or a Mössbauer spectrometer is determined by the software. Written in 6502 assembly language, the software for the two spectrometers is similar in principle but different in particulars. In both spectrometers the MCS transfers data to the Apple on an interrupt basis. Both programs consist of four basic routines: an initialization routine, a display routine, a keyboard-inter-

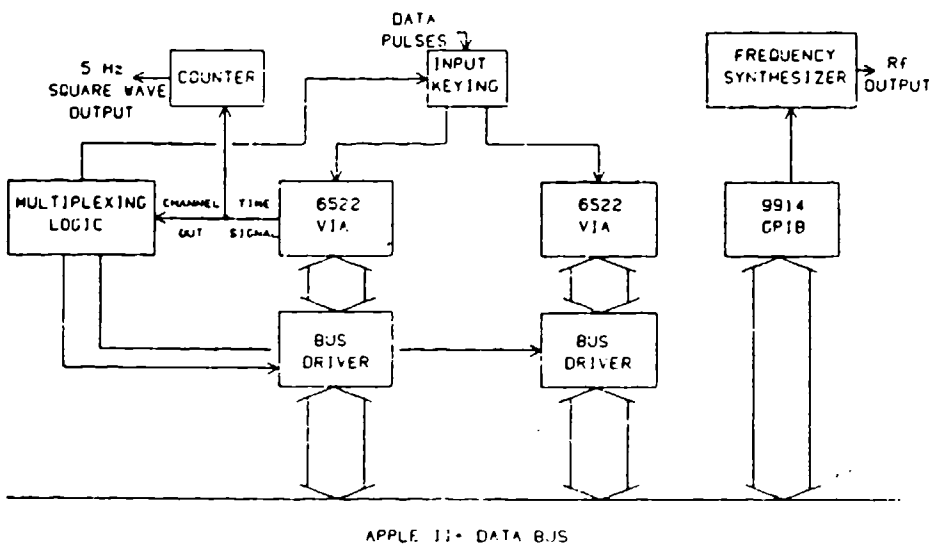


FIG. 4. This block diagram shows the basic components of the interface to the Apple II+ computer. This interface enables the computer to be used for automatic NFMS data acquisition, or it can enable one computer, with two cards, to control and collect data from up to two Mössbauer spectrometers.

MCS/GPIB INTERFACE

preting routine, and an interrupt routine. The initialization routine uses the multiplexing logic on the MCS card to address each of the 6522's and set the appropriate registers. The display routine has two options. The data can be displayed graphically at different resolutions, or counts can be displayed as counts per channel and total counts per sweep. The graphics data display uses table lookup and two graphics screens to provide a real-time data display. The initialization routine generates a table in memory which stores the address for a given vertical coordinate on the screen in a memory location which is correlated to the value of the vertical coordinate. The value of the horizontal coordinate is correlated to the memory address of the channel to be displayed. As the display routine scans through memory at the data, the datum value and the channel value are used to address indirectly the appropriate graphics screen coordinate through this table. Therefore, by using table lookup, all of the mathematical operations necessary to obtain the appropriate screen addresses (including a division by seven) are performed only once. While one graphics screen is displayed, the other is cleared and plotted with the current data. The updated screen is then activated and the first screen is cleared and replotted, and so on. The keyboard-interpreting routine allows one to change the display, change the resolution of the graphics display, or stop the spectrometer and store the data on a disk, all with single key codes. A table of these key codes is displayed at the bottom of the counts display screen, the default display. Finally, the interrupt routine collects the count from the currently accessible 6522 and stores it in the appropriate 3-byte location. The display and keyboard routines for the two spectrometers are identical, but the initialization and interrupt routines for the two spectrometers are necessarily very different.

In the Mössbauer spectrometer, the initialization routine must enable the MCS card to generate interrupts at 195- μ s intervals. Next, the interrupt routine must be capable of pushing all values in the CPU's registers to the stack, accessing the count from the appropriate 6522 and adding it to the appropriate memory locations, and then reloading the CPU's registers with their initial values, all in less than 195 μ s, with enough time left over to update the display between interrupts. This feat was best accomplished by using four separate interrupt routines. Since the spectrometer has 1024 channels, the data is stored in twelve 256-byte pages for 3 bytes per channel. Each interrupt routine addresses a channel comprising 3 bytes through the sum of base addresses plus a counter value. Upon completion, each routine stores the address of the next interrupt routine in the interrupt vector. The fourth routine stores the address for the first routine in the interrupt vector and increments the addressing counter. The result is an interrupt routine that lasts 50-60 μ s from interrupt to return, depending on the number of bytes which must be incremented. As a result, one Apple II+ computer can easily handle two Mössbauer spectrometers with a real-time data display for each.

In the NFMS, the initialization routine enables the MCS card to generate interrupts at $\frac{1}{2}$ of a second intervals. This routine also initializes the signal generator through the GPIB. The interrupt routine must then translate the number

of interrupts generated into an elapsed time and compare this time to the selected dwell time. In addition, this interrupt routine must perform all of the functions of the Mössbauer spectrometer interrupt routine. After the elapsed dwell time, the interrupt routine must step the frequency of the signal generator and change the address (channel) for data storage. When the frequency of the signal generator is changed, and for a time thereafter, the data to the MCS must be gated off and the timing stopped until the signal is stabilized. In the NFMS, the speed of the interrupt routine is no longer a major concern due to the significant increase in the time between interrupts and the fact that the data is gated off while the interrupt routine is delaying for the signal generator. Unfortunately, however, the time required to change the frequency is unavoidable dead time. Yet the total dead time in a run can be minimized by selecting a sufficiently long dwell time which does not allow the signal to drift significantly.

II. DATA AND DISCUSSION

Figures 1 and 2 show data collected with our Mössbauer spectrometer and processed with a five-point running average. These figures show rf sidebands in an iron foil absorber, and the frequency dependence of the rf sideband energies in a stainless-steel foil absorber. All NFMS spectra to be shown were obtained from a 1.5-cm \times 0.85-cm \times 2.5- μ m iron foil absorber enriched with 95% ^{57}Fe . This foil is the same absorber which gave us the spectra in Fig. 1. All spectra shown were obtained from an absorption geometry, using a ^{57}Co source in a Pd matrix. All NFMS spectra have been processed with a five-point running average.

The first set of NFMS data concentrates on the first-order sidebands from the 1 and 6 parent transitions (Fig. 5). The nomenclature for identifying the rf sidebands is as follows. The first digit corresponds to the order of the sideband. Radio-frequency sidebands of the j th order from a given parent transition are found at the sum and difference frequencies of the static field, or Zeeman splitting, and j times the frequency of the applied rf field. The letter after the first digit, either an "n" or a "p," indicates whether the sideband is a negative or positive sideband, respectively. A negative sideband appears at an energy lower than the energy of the parent transition, while a positive sideband is at a higher energy. The last digit identifies the parent transition of the sideband. There are six allowed transitions for ^{57}Fe in a metallic iron foil, of which the lowest-energy transition is identified as parent transition 1 and the highest-energy transition is identified as 6. The energy difference between parent transitions 1 and 6 is 123 MHz, therefore, at 61.5 MHz the 1n6 and 1p1 sidebands should overlap at the transition center of the spectrum. If the gamma-ray source is stationary, then the energy of the gamma rays emitted differ from the energy of the transition center of the absorber by the isomer shift. Therefore, a stationary source should provide a NFM spectrum of the 1n6 and 1p1 sidebands displaced from 61.5 MHz by plus and minus the isomer shift, respectively [Fig. 5(a)]. The source used was in a Pd lattice, which has an isomer shift of -0.185 mm/s relative to metallic iron. If the source is

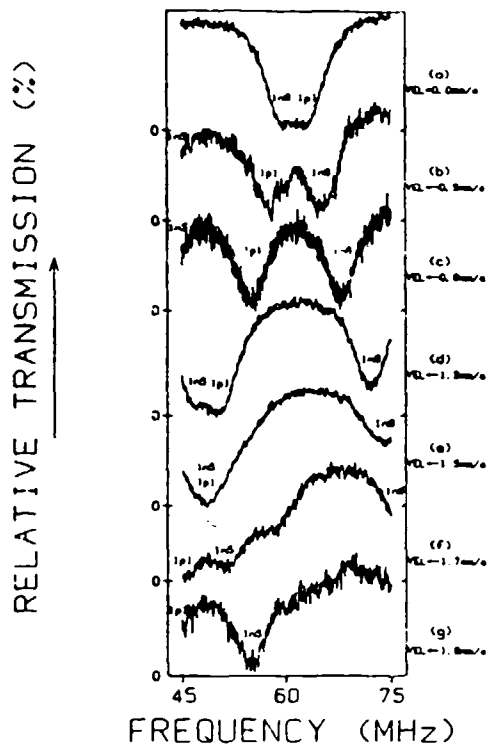


FIG. 5. Typical NFMS data showing first-order sidebands from the highest- and lowest-energy transitions of ^{55}Fe in iron, 1n6 and 1p1, respectively; (a) in the vicinity of the transition center of this Zeeman split absorber. An "n" in the sideband label indicates that the sideband is at a lower energy than its parent transition, whereas a "p" indicates that the sideband is at a higher energy. As the velocity of the source is decreased (b)–(g), the energy of the probe radiation is decreased, and as a result, the sideband from the lower-energy transition, 1p1, appears at lower frequencies. The sidebands from the higher energy transitions, 1n5 and 1n6, appear separated by the excited state splitting frequency of ^{55}Fe in iron, 26 MHz.

then given a constant velocity, the 1n6 and 1p1 sidebands should be displaced from 61.5 MHz by plus and minus (isomer shift – velocity), respectively [Figs. 5(b)–5(g)]. The sign convention is to define a velocity as negative when the source and absorber are moving away from each other. Note that the 1f sideband 1n5, which appears in Fig. 5, should be separated from 1n6 by 25.9 MHz, the excited state splitting frequency in metallic iron.

The second set of NFM spectra [Figs. 6(a)–6(c)] were obtained at a lower-frequency range. Higher-order sidebands add together at these lower frequencies and present significant cross sections. These particular spectra are comprised of 24 different sidebands, if one takes into account sidebands out to the fifth order. Following the spectra are computer-generated simulations [Figs. 7(a)–7(c)]. The model, a simple algorithm, shows remarkable agreement with the data. The frequency at which a sideband will appear is

$$f_{j,\text{ord}}(\text{MHz}) = [\text{vel} - (P_j + \text{iso})](K/\text{ord}), \quad (1)$$

where P_j is the position of the j th parent transition in mm/s, vel is the velocity of the source in mm/s, iso is the isomeric shift between the source and absorber, ord is the order of the sideband, and K is a conversion factor = 11.6 MHz/(mm/s) for the 14.4-keV gamma ray being detected.

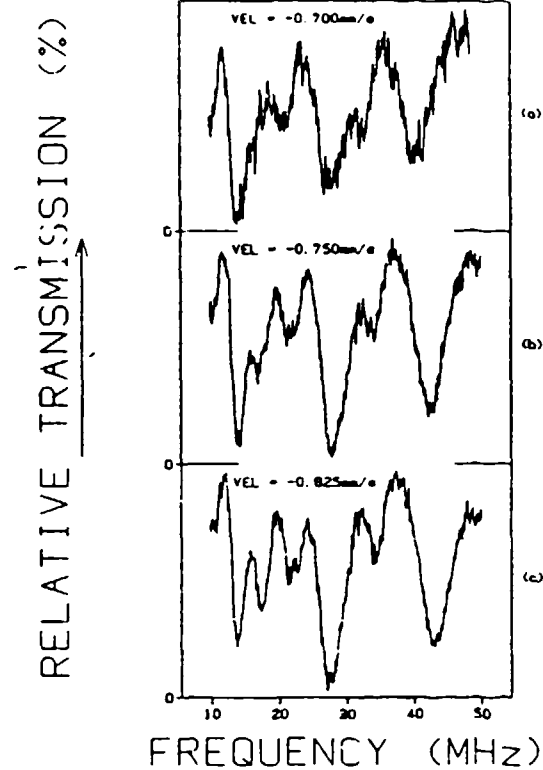


FIG. 6. Nuclear frequency-modulation spectrometer data obtained at lower frequencies has an appearance which belies the underlying complexity of the spectra. Sidebands add together to produce composite sidebands which have amplitudes, widths, and line shapes with a high degree of dependence upon the energy of the probing radiation. As a result, a small change in the source velocity can lead to a significant change in the appearance of a spectrum.

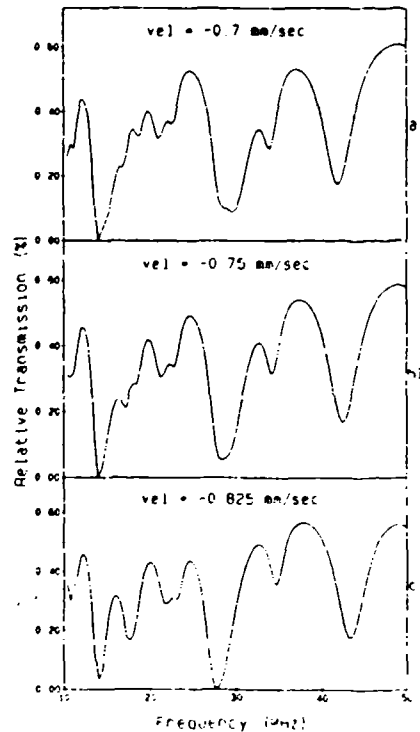


FIG. 7. Computer-generated simulations of the NFM spectra in Fig. 6 obtained from Eqs. (1)–(3). Each simulation is composed of 24 different sidebands.

The linewidth of the sideband as it will appear in the NFM spectrum is

$$\Gamma_{n,ord} = (\Gamma_p + \Gamma_g)/ord, \quad (2)$$

where Γ_p is the linewidth of the sideband's parent transition and Γ_g is the linewidth of the 14.4-keV gamma ray emitted by the source. The apparent linewidth's dependence on sideband order can be understood by realizing that an n th-order sideband will be displaced by n frequency units, while a first-order sideband is displaced by one frequency unit. Since we were concerned only with the relative amplitudes of a sideband within a given NFM spectrum, the amplitude of a sideband in a spectrum was assumed to be

$$A_{n,ord} = A_p/ord, \quad (3)$$

where A_p is the amplitude of the sideband's parent transition. By using this equation we have assumed that our spectra were not exhibiting the saturation effects discussed in Ref. 6. This assumption was a convenient mechanism for introducing a sideband amplitude dependence on the relative amplitudes of the parents. For the iron foil used, the relative amplitudes of the parents were taken as 2.2:1:1:2:2 [Fig. 1(a)]. The NFMS is a tool for directly measuring rf sideband position, width, and amplitude. This model shows that the NFMS is a powerful means of indirectly measuring isomeric shifts and the positions and relative amplitudes of the parent transitions.

The NFMS apparatus is versatile. This apparatus is a conventional Mössbauer spectrometer with or without a rf field, as well as a rf sideband spectrometer. A conventional

Mössbauer spectrometer is not capable of measuring rf sidebands when they overlap a parent transition, and resonances have been predicted for certain such overlappings. The NFMS enables one to observe the behavior of rf sidebands in the vicinity of a parent transition, with high enough resolution to discern any fine structure in the sideband which might result from such resonances, because in NFMS, the parent transition appears only as a base line due to its lack of any frequency dependence. With the NFMS, it is also possible to observe directly the effect of the rf field intensity on sideband position, amplitude, and width. It should also be noted that the MCS described in this paper may also be used in a spectrometer similar to the type described by Bolef and Mishory in Ref. 5.

ACKNOWLEDGMENTS

Support for this project was provided in part by the Office of Naval Research and in part by IST/SDIO, directed by the Naval Research Laboratory.

¹S. L. Ruby and D. I. Bolef, *Phys. Rev. Lett.* **5**, 5 (1960).

²G. J. Perlow, *Phys. Rev.* **172**, 319 (1968).

³N. D. Heiman, L. Pfeiffer, and J. C. Walker, *Phys. Rev. Lett.* **21**, 93 (1968).

⁴C. L. Chien and J. C. Walker, *Phys. Rev. B* **13**, 1876 (1976).

⁵D. I. Bolef and J. Mishory, *Appl. Phys. Lett.* **11**, 321 (1967).

⁶B. D. DePaolo, S. S. Wagal, and C. B. Collins, *J. Opt. Soc. Am. B* **2**, 541 (1985).

Calibration of pulsed x-ray spectra

J. A. Anderson and C. B. Collins

The University of Texas at Dallas, Center for Quantum Electronics, P. O. Box 830688, Richardson, Texas 75083-0688

(Received 17 August 1987; accepted for publication 8 November 1987)

A new technique has recently been described for the absolute calibration of intense sources of pulsed radiation in the 0.2–1-MeV range of photon energies. An x-ray activation technique, it depended upon the storage of samples of the irradiating spectrum in the form of populations of nuclei excited to isomeric states with lifetimes of seconds to hours. Accuracy was dependent upon the precision assumed for tabulated values of nuclear parameters. Described here is an extension of this technique to the larger range of photon energies, 0.2–1.5 MeV and to intensities from 10^{12} keV/keV to 10^{16} keV/keV using the target nuclei ^{75}Br and ^{75}Se . In this work self-consistency of the nuclear parameters was directly determined. Important changes were found to be necessary for improved accuracy, particularly over the larger ranges of experimental variables being considered. Values of the now-consistent set of nuclear parameters are reported.

INTRODUCTION

While particle reactions are routinely used for the precise measurement of nuclear parameters, the same levels of accuracy have not been reached in the applications of (γ, γ') reactions. Although examples have been known for over 50 years,^{1,2} only a few tens of papers can be found in the literature³ and results reported for the same reactions show extreme variance. To the nonspecialist this would seem surprising because the analogous optical double resonance techniques are among the most powerful investigative tools at the molecular level.

The principal impediment to the quantitative study of (γ, γ') reactions seems to have arisen from the difficulties in calibrating the sources. Both accelerators and radioactive decay schemes have been traditionally used to provide electromagnetic excitation to reaction sequences such as shown in Fig. 1. Unfortunately, the combination of high flux and high photon energy in the excitation step has not permitted the use of standard spectroscopic techniques, and thus the target has had to be cycled between the irradiation device and the counting facility. In practice this has meant that studies were limited to the excitation of isomers with τ_i lifetimes of seconds to hours.

The difficulties in conducting (γ, γ') reactions are probably typified best by the excitation of the 269-min isomer of ^{115}In at 336 keV. The principal gateway state that is radiatively connected to both the initial and the final isomeric levels lies at 1078 keV and can be conveniently excited by resonant absorption of the Compton continuum from a ^{60}Co source mounted in close proximity. Nevertheless, an experiment reported⁴ in 1981 produced such an excess of isomeric population that it was necessary to postulate a new mechanism in the ^{115}In for nonresonant absorption of the undegraded lines from the ^{60}Co source. Theory has not yet provided a process of the needed magnitude, and the most recent repetition of this work⁵ has suggested that the excessive yield resulted not from dominance of an unknown process but rather from the difficulty in calibrating the effective dose in the input channel. In that latest, 1986 experiment,

excess production was not observed.⁵ Such a chaotic level of contradiction between theory and experiment and among the experiments themselves is typical in the literature and attests to the need for a better means for the calibration of intense sources of continuum radiation at energies above 200 keV.

Because of the absence of dispersive materials for such energies and because of the similarity of the absorptive properties contributed by the electrons of the various elements above 200 keV, the absolute calibration of pulsed electromagnetic continua has been virtually impossible. All large-scale sources are currently "calibrated" by fitting a standard theoretical form for the intensity of bremsstrahlung continua as a function of energy to the end point energy and to the total dose.

Unfortunately, dosimeters are not uniform in their response to ionizing radiation. They are much more sensitive to the lower energy photons and thus weight by a large factor the area under the portion of the spectrum most likely to be distorted by effects of self-absorption which, themselves, have a complex dependence upon geometry. The consequence is that such "calibrations" are very sensitive to the particular structure of the spectrum at the low energies and so, in turn, are strongly affected by the accuracy of the parameterization of the individual converter being employed. It is not surprising that discrepancies as great as those affecting the ^{115}In experiments with ^{60}Co sources result from even the most careful efforts with accelerators.

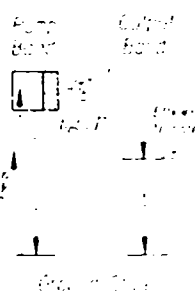


FIG. 1. Schematic representation of a typical (γ, γ') reaction sequence that could be used to populate an isomeric state with lifetime τ_i . Absorption of the gamma is assumed first to excite a state with a much shorter lifetime τ_e , which then either decays back to the original ground state with probability b_e or to the isomer with probability b_i .

A more direct means of calibration is offered by our approach to the nuclear analog of optical pumping.⁶⁻⁸ There are a few nuclei that are known to have absorption resonances that are broad enough to channel large populations to readily detected states but which remain narrow on the scale of spectral structure of available sources. These few nuclei have been characterized by other types of nuclear studies and can be used to sample narrow slices of the intensity of a continuum. We recently demonstrated⁶ the efficacy of this technique by activating targets of ⁷⁹Br and ⁷⁷Se for the characterization of a pulsed source of bremsstrahlung continua at spectral intensities of the order of 10^{12} keV/keV. Excitation was provided by an in-house pulsed electron beam generator having a nominal end point energy of 1 MeV. Accuracy was dependent upon the precision assumed for the tabulated values⁹ of nuclear parameters.

Reported here is an extension of this technique to the larger range of photon energies, 0.2 to 1.5 MeV, and for intensities to 10^{16} keV/keV using the same target nuclei, ⁷⁹Br and ⁷⁷Se. In this work the self-consistency of the nuclear parameters was directly determined. Important changes and additions were found to be necessary and these are reported. The resulting tabulation of the essential nuclear parameters is now self-consistent and capable of supporting the characterization of pulsed x-ray fluence over the larger range of energies and intensities.

I. EXPERIMENTAL METHOD

A schematic drawing of the apparatus used to calibrate the PITHON nuclear simulator at Physics International is shown in Fig. 2. Although only two counting systems are shown for the purposes of illustration, up to three samples could be irradiated during the x-ray pulse and then automatically transferred to the counters. The target-to-counter transit times for the pneumatic shuttles were measured for each shot, and averaged about 1.0 s.

For the work described here, a single sample that incorporated a mixture of LiBr and elemental selenium was used. Figure 3 shows the construction of the sample and lists the important parameters relating to it. After arrival at the counting station, the sample was analyzed for 80 s, which represented about four half-lives of the 17.4-s ^{77m}Se and 16 half-lives of the 4.8-s ^{79m}Br. Two NaI(Tl) spectrometers and

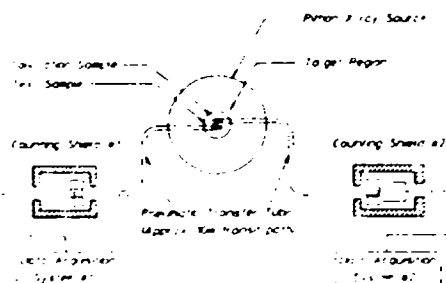


FIG. 2 Apparatus for nuclear fluorescence measurements with the PITHON bremsstrahlung machine. Most of the x-ray energy was emitted in a 20-cm pattern in which the samples were centered. The PITHON sequence timer was used to trigger the automatic transfer of samples from the irradiation volume to the counters.

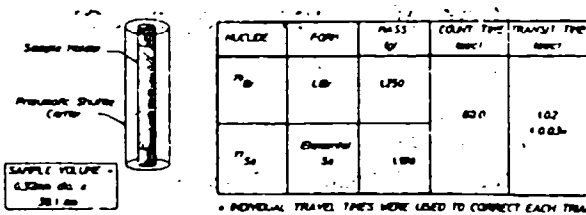


FIG. 3. Sample holder for mixed LiBr/Se target. The sample itself was in a 0.64-cm-diam tube capped with plastic plugs. This tube was centered in a polyethylene "rabbit" running in a 1.9-cm-diam transfer tube.

one HPGe system were employed in the experimental series, but the data presented here were obtained exclusively with one of the 3 × 3-in. NaI(Tl) detectors. Samples with longer half-lives (e.g., 4.49-h ^{115m}In) were manually inserted in the spectrometers after the short-lived materials were counted.

II. RESULTS AND ANALYSES

During the period of these experiments, 23 shots were successfully instrumented with the calibration target and pneumatic shuttles. The nominal variation of 20% in source performance was augmented by the deliberate programming of firing parameters. As a result, shots were obtained for end point energies ranging from 0.9 to 1.5 MeV. A spectrum of the fluorescence obtained from a typical irradiation is shown in Fig. 4.

Of paramount concern in the examination of data such as shown in Fig. 4 is whether the relative yields from ⁷⁹Br and ⁷⁷Se are in agreement with the accepted values for the nuclear parameters appearing in the most recent tabulations.¹⁰ The first step in the resolution of such a question is the extraction of the relative numbers of excited nuclei actually produced in the sample. This requires correction for the finite duration of the sampling period over which the fluorescence is counted, the efficiency of the detector, the probabilities for internal conversion rather than radiation of the fluorescence, and the fraction of fluorescence reabsorbed in the sample. While the first three corrections are readily obtained from tables or by calibration, the last is dependent upon geometry in a more complex fashion. To minimize the

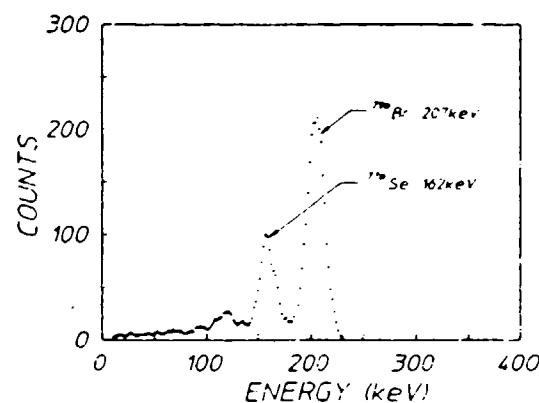


FIG. 4 Fluorescence spectrum from a target containing 1.25-g LiBr and 1.20 g of elemental Se, both in natural abundances excited with a single irradiation (Shot 4381) by the bremsstrahlung produced by the PITHON electron beam device. Acquisition time of these data was 80 s. Prominent lines are contributed by the isomeric transitions indicated.

importance of that particular correction, small samples were used for which the effects on the ^{79}Br and ^{77}Se data differed¹¹ by about 3%.

As described in the article⁶ reporting the previous implementation of this technique at lower energies, the number of excited nuclei produced in the course of an irradiation of the type shown in Fig. 1 can be computed from the expression

$$S = N \sum_i \frac{(\pi b_a b_0 \sigma_0 \Gamma / 2), \phi(E_i)}{E_i} \frac{\phi(E_i)}{A}, \quad (1)$$

where N is the number of absorbing nuclei in the sample and the summation is taken over the properties and pump fluxes characteristic of each of the i th broad pump bands centered at pump energy E_i . Only one such pump band is shown in the scheme of Fig. 1, but there could be several at different E_i , each funneling its population into the same output level.

In Eq. (1) the first ratio in the summation is composed of the nuclear parameters, while the second describes the intensities of the pump γ rays that are assumed to be continuous, at least without structure on the fine scale of the nuclear absorption. In particular, the combination $\phi(E_i)/A$ is the spectral fluence at the energy E_i in units of $\text{keV}/\text{keV}/\text{cm}^2$. Tacitly, it has been assumed that the duration of the pump source is less than the fluorescence lifetime τ_ϕ .

Of the nuclear parameters, Γ is the natural width in keV of the i th pump band, as shown in Fig. 1,

$$\Gamma = \hbar/\tau_\phi, \quad (2)$$

and the branching ratios, b_a and b_0 , give the probabilities for the decay of the broad level back into the initial and fluorescence level, respectively. The pump energy, E_i , is in keV and σ_0 is the Breit-Wigner cross section for the absorption transition,

$$\sigma_0 = \frac{\lambda^2}{2\pi} \frac{2I_e + 1}{2I_g + 1} \frac{1}{\alpha_p + 1}, \quad (3)$$

where λ is the wavelength in cm of the gamma ray at the resonant energy, E_i ; I_e and I_g are the nuclear spins of the excited and ground states, respectively; and α_p is the total internal conversion coefficient for the broad level of Fig. 1.

The nucleus ^{79}Br is unique in its utility to efforts at calibration. According to latest data,¹⁰ it has but a single broad level connecting to both ground and fluorescent states in the energy range 0–1.8 MeV. The relevant part of its scheme of energy levels is shown in Fig. 5. On the other hand, the ^{77}Se

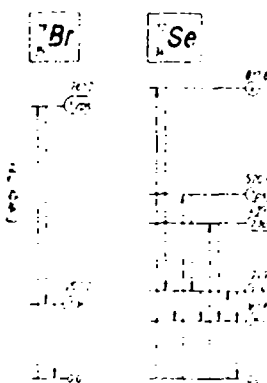


FIG. 5. Energy level diagram of the excited states of ^{79}Br and ^{77}Se important in the production of populations of their respective isomers. Half-lives of the states are shown in the ovals to the right of each and sequences of transitions corresponding to the (γ, γ') reactions leading to the isomers are shown by the arrows. Downward γ transitions also include effects of cascading through levels other than those shown.

TABLE I. Summary of nuclear fluorescence reconciled by this work

Nuclide	E_i (keV)	$\pi b_a b_0 \Gamma \sigma_0 / 2$ ($10^{-29} \text{ cm}^2 \text{ keV}$)		E_{out} (keV)
		Ref. 6	This work	
^{79}Br	761	6.2	6.2	207
^{77}Se	250	0.20	0.20	162
	480 ^a	1.50	0.87	
	818	0.7	0.7	
	1005		30	
^{113}In	1078		20 ^b	337

^aThe effects of the 440- and 521-keV transitions have been combined.

^bFrom Ref. 15.

nucleus is more complex having at least four levels funneling to the same fluorescent transition at 161.8 keV, as shown in Fig. 5. The highest at 818 keV is insufficiently characterized, and the Γ parameter appearing in Eq. (1) must be estimated. This was done and reported previously.^{6,7} The "best" values¹² of the parameters of Eq. (1) are listed in Table I for convenience, together with sources of the basic data and the values confirmed by this experiment.

An additional difficulty encountered in the use of Eq. (1) to model the performance of targets pumped with the device used in these experiments accrues from the geometry of the diode producing the bremsstrahlung γ rays. Since it is configured as a pinched diode, electrons do not arrive at the converter foil with normal incidence. In such cases the linear, Kulenkampff approximation to the spectrum used previously⁶ is expected to become markedly concave.¹³

Of the 23 shots instrumented in this experimental series, five benefited from additional diagnostics. From records of the time-dependent voltage and current, the spectral fluence was calculated with the one-dimensional coupled electron/photon Monte Carlo transport code, TIGER, an established procedure in the e-beam community.¹⁴ Results supplied by Physics International are shown in Fig. 6 for a selection of those five shots. If plotted on a linear scale, those spectra would be considerably more concave than the idealized approximation⁶ used for normal incidence. However, the ratio of fluence at a particular energy to that at some standard can be readily parameterized from curves such as shown in Fig. 6. In doing this, the energy of the single absorption line of ^{79}Br at 761 keV was chosen as a standard. Shown in Fig. 7 are the resulting curves for the empirical estimation of the relative spectral intensity $\zeta(E_i)$,

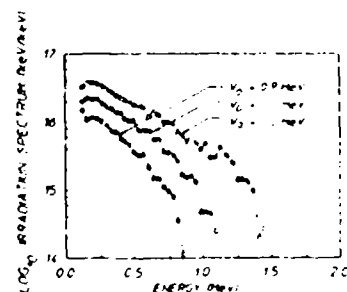


FIG. 6. Plot of three bremsstrahlung spectra computed with the TIGER code for the particular characteristics of three electron beam discharges from PITHON having the end point energies K_0 , as indicated.

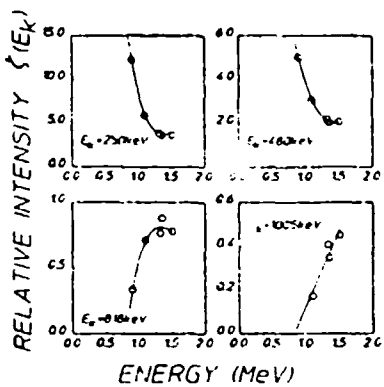


FIG. 7. Graphs of the relative spectral intensities $\zeta(E_k)$ at the photon energy E , plotted as functions of the end point energy of the electron beam producing the bremsstrahlung. Curves were obtained by smoothing and interpolating between the data points representing the results of TIGER code computations, three of which are shown in Fig. 6. Intensities are normalized to the spectral intensity at the reference energy $E = 760$ keV.

$$\zeta(E_k) = \phi(E_k)/\phi(760 \text{ keV}), \quad (4)$$

plotted as functions of the end point energy E_k , for four different E_k : 250, 480, 818, and 1005 keV. Data points record the values supplied by the TIGER code, and the curves were obtained by a smoothing procedure.

From data such as presented in Fig. 7 the fluorescent yield expected from ^{77}Se can be readily computed in terms of that actually observed from ^{79}Br . The degree to which the calculated yield agrees with the measured fluorescence is a direct indication of the level of consistency between the values compiled for the nuclear parameters in Table I. This can be appreciated by writing Eq. (1) for the irradiation of a sample of ^{79}Br ,

$$S(\text{Br}) = N(\text{Br}) \xi_{760}(\text{Br}) [\phi(760)/A], \quad (5)$$

where

$$\xi_k = (\pi b_0 b_0 \sigma_0 \Gamma / 2) / E_k, \quad (6)$$

from Eq. (1), and $\phi(760)$ is the spectral intensity at the target. The corresponding expression for the ^{77}Se is

$$S(\text{Se}) = N(\text{Se}) \left(\xi_{250}(\text{Se}) \frac{\phi(250)}{A} + \xi_{480}(\text{Se}) \frac{\phi(480)}{A} + \xi_{818}(\text{Se}) \frac{\phi(818)}{A} + \xi_{1005}(\text{Se}) \frac{\phi(E_k)}{A} \right), \quad (7)$$

where the possibility of an extra contribution from an unexpected band at E_k has been included.

Dividing Eq. (7) by Eq. (6) and substituting from Eq. (4) yields after some rearrangement,

$$\frac{S(\text{Se})}{S(\text{Br})} = \frac{N(\text{Se})}{N(\text{Br})} \left(\frac{\xi_{250}(\text{Se})}{\xi_{760}(\text{Br})} \zeta(250) + \frac{\xi_{480}(\text{Se})}{\xi_{760}(\text{Br})} \zeta(480) + \frac{\xi_{818}(\text{Se})}{\xi_{760}(\text{Br})} \zeta(818) \right) = \frac{N(\text{Se})}{N(\text{Br})} \frac{\xi_k(\text{Se})}{\xi_{760}(\text{Br})} \zeta(E_k). \quad (8)$$

While formidable in appearance, Eq. (8) has a very straightforward interpretation, namely,

$$R(\text{exp}) - R(\text{model}) = \frac{N(\text{Se})}{N(\text{Br})} \frac{\xi_k(\text{Se})}{\xi_{760}(\text{Br})} \zeta(E_k). \quad (9)$$

where R is the ratio of the numbers of excited nuclei produced in ^{77}Se and ^{79}Br .

Several points warrant comment. While $\phi(E_k)$ in Eq. (5) depends upon the poorly characterized geometric efficiency through which the fluences of Fig. 6 are actually coupled to the target, the relative fluence, $\zeta(E_k)$, does not. Neither does it depend upon the entrance aperture of the target, A , another uncertain quantity in real configurations.

In actual experiments, the residues between experimental data and the results of the model appearing on the left-hand side of Eq. (9) should be scattered about zero, regardless of the end point energy of the irradiation—provided the model is complete. If an unknown channel is contributing, or if one of the $\xi_k(\text{Se})$ is incorrect, then the residue should have a dependence upon experimental variables as shown to the right-hand side of Eq. (9). Since the $\zeta(E_k)$ of Fig. 7 have considerably different functional dependencies upon E_k , it should be possible to identify the particular E_k contributing the residue, provided enough variation of E_k can be introduced into the experiment.

For the 23 data points of this experiment, the residues computed from Eq. (9) do not scatter about zero. Figure 8 shows a plot of the resulting residues as functions of end point energies. The functional dependence is striking and fits a line intercepting the horizontal axis near 1 MeV. Inspection of the right-hand side of Eq. (9) suggests that this would be consistent with the contribution from an additional transition with a threshold energy for excitation near 1 MeV.

The complete set of nuclear parameters appearing in Eq. (6) is not known for any of the transitions of ^{77}Se lying above 818 keV. However, the branching ratios are available for many of them. While optimal branching ratios could be offset by poor lifetimes, in principle, it is most reasonable to expect a significant new channel of excitation to correspond to a level for which branching ratios were, at least, favorable. Table II records the product $b_0 b_0$ for levels of ^{77}Se above 818 keV, and the close correlation between the large value seen at 1005 keV and the intercept of Fig. 8 is extremely persuasive.

Once the excitation energy of the "new" channel was determined from Fig. 8 and Table II, the functional dependence of $\zeta(1005)$ upon end point energy could be determined. This was done and the result is shown in Fig. 7. Again there is a striking similarity between the functional dependencies upon E_k of the residues and of the $\zeta(1005)$, as would be required by Eq. (9).

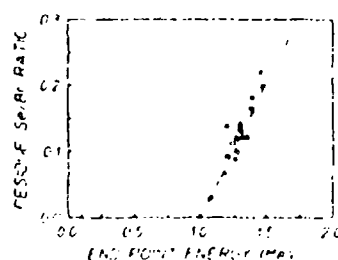


FIG. 8. Plot of the residues obtained from the application of Eq. (9) to the data for a model containing the three lowest energy gates as levels of ^{77}Se plotted as a function of the end point energies of the electron beam discharges producing the bremsstrahlung.

TABLE II. Compilation from Ref. 10 of the products of the branching ratios, $b_0 b_0$, appearing in Eq. (6) for the transitions of ^{77}Se lying above 818 keV. Corresponding values of Γ have not been reported in the literature.

Level (keV)	$b_0 b_0$
818	0.0063
825	0.00025
911	0.017
1005	0.031
1128	0.0012
1160	0.047
1230	0.0024

Once the level missing from the model is identified as corresponding to $E_k = 1005$ keV, all of the terms of Eq. (9) are known except $\zeta_{1005}(\text{Se})$. In Fig. 9 the model residues are plotted as functions of $\zeta(1005)$ for the 19 shots of this experiment having end point energies above 1 MeV. From Eq. (9) it can be seen that the slope of such a plot should correspond¹⁶ to $\zeta_{1005}(\text{Se}) N(\text{Se}) / \zeta_{760}(\text{Br}) N(\text{Br})$. The least-squares fit to the data including the origin is shown by the heavy line in Fig. 9, together with the lighter lines bounding acceptable alternatives. These lead to a value

$$\zeta_{1005}(\text{Se}) = (30 \pm 7.5) \times 10^{-32} \text{ cm}^2, \quad (10a)$$

which from Eq. (6) gives

$$\pi b_0 b_0 \sigma_0 \Gamma / 2 = (30 \pm 7.5) \times 10^{-29} \text{ cm}^2 \text{ keV}, \quad (10b)$$

in turn yielding

$$\tau_{1/2}(1005) = 0.36 \text{ ps}. \quad (10c)$$

As a final step of analysis, the residues of Eq. (9) were recomputed, including the term of Eq. (10a), into the model estimate $R(\text{model})$, on the left-hand side of Eq. (9). Figure 10 shows the resulting residues as functions of the end point energies. This time the data appear¹⁶ to scatter around the ζ axis, indicating that the model now contains a sufficient number of terms to predict the fluorescent yields up to an end point energy of 1.5 MeV to an accuracy of better than 10%.

III. DISCUSSION

The principal conclusion of this work is that the 1986 version¹⁰ of the nuclear parameters is completely consistent. Provided no significant component of the x-ray flux lies above 1 MeV, those data are sufficient to predict the fluorescent yields from ^{79}Br and ^{77}Se . However, for the irradiation of samples with bremsstrahlung produced by electrons with

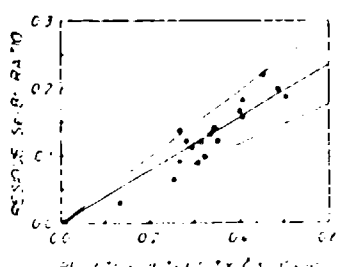


FIG. 9. Plot of the residues of Fig. 8 as functions of the relative intensity of irradiation at 1005 keV.

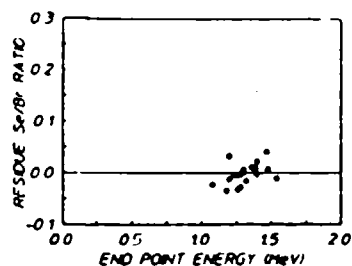


FIG. 10. Plot of the residues obtained from the application of Eq. (9) to the data for a model containing the three lowest energy gateway levels of ^{77}Se together with the new level at 1005 keV, plotted as a function of the end point energies of the electron beam discharges producing the bremsstrahlung.

end point energies above 1 MeV, the more complete set of parameters of Table I must be used. In such cases it is appropriate for all end point energies below 1.5 MeV.

The difference between the 1986 data and Table I lies in the inclusion of the pump channel in ^{77}Se at 1005 keV found in the course of this work. Corresponding to the considerable transition strength of 0.011 Weisskopf units for an M1 transition in the absorption channel, it is well connected to both initial and fluorescent levels. As can be seen from Table I it will rapidly become the dominant channel for funneling population into the fluorescence level as the number of pump photons above 1 MeV increases in a source.

The striking consistency between the results from ^{79}Br and those from ^{77}Se argues favorably for the utility of this technique of selective nuclear excitation over a wider field of experimental variables than originally described.⁶ It does not require an initial computer model. A measurement of the activation of ^{79}Br would determine the fluence at 761 keV at the position of the sample. Activation of ^{77}Se is more complex but tractable, once the ^{79}Br results are known. Assuming $\zeta(818) \sim \zeta(761)$ the contribution to ^{77}Se from the small 818 channel can be easily removed. The immediate residue is a weighted sample of the low-energy portion of the irradiating spectrum and of the energies near 1 MeV. To separate these effects in cases where the end point energy lies above 1 MeV, recourse must be made to a third nuclei sampling only high energies. An ideal candidate is ^{113}In , which is the subject of a subsequent article.¹⁷ It samples only the fluence at 1078 keV and the consistent value¹⁷ for the corresponding reaction has also been included in Table I for convenience. From the activation of an ^{113}In component of the sample, the contribution to ^{77}Se activation from the new 1005 keV channel can be removed. From the resulting second residue, the average fluence in the range 250–480 keV can be isolated.

As a demonstration of the efficacy of nuclear activation, such a procedure was performed on the activation of a composite target irradiated with a typical shot (4379) from PITHON. As expected, absolute measurements of the flux at the target could be obtained for three energies¹⁸: 433, 761, and 1078 keV. Then by multiplying those values of flux by the area of the forward (2π) hemisphere upon which the target was conceived to rest during irradiation, the absolute spectral intensity emitted by the source was determined. Results are plotted in Fig. 11 together with the predictions of the TIGER code calculations for that shot. Agreement is

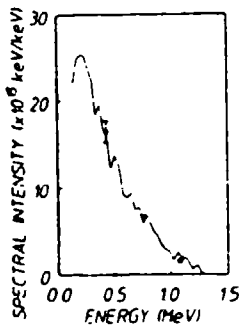


FIG. 11. Data points plot the spectral intensities measured directly with the nuclear activation technique using the parameters of Table I in comparison to the spectrum computed with the TIGER code for a typical PITHON shot, 4379. Vertical bars show uncertainty in the measurement at the one point for which that uncertainty was larger than the plotted size of the symbol.

perhaps better than is warranted by the inherent level of mechanical inaccuracy in target positioning.

Uncertainty in the direct measurement of spectral intensity at the target arises from two sources: statistical error in the number of fluorescent counts and unknown error in the nuclear data of Table I. Results of the former are plotted in Fig. 11, but appear larger than the plotted symbol only at the lower energy point arising as a result of so many differences of data. Uncertainty due to residual inconsistency in the data of Table I is of unknown magnitude but should be less than the error introduced by the statistical uncertainty in the counts as a result of these efforts in determining consistency of the entries of Table I.

The results of this work indicate that (γ, γ') reactions can be studied with a high level of precision if the sources are carefully characterized. The existing data for the transitions of ^{75}Br and ^{75}Se , together with others to be discussed, clearly offer a convenient means of sampling the spectra of intense pulsed sources.

ACKNOWLEDGMENTS

This work was supported by IST/SDIO and directed by NRL. It was made possible through the efforts of many people within the Center for Quantum Electronics. The original concept for the calibration of pulsed electromagnetic continua was suggested by our colleague Y. Paiss. The implementation of the project depended on the contributions of K. Taylor, C. Dutta, M. Byrd, and P. Phillips from the Detector Physics group and of J. Carroll, C. Shippy, D. Tipton, M. Wright, and K. Renslow in the Engineering group. C. Eberhard provided theoretical support for this work.

The authors wish to convey their sincere appreciation to M. Krishnan and his colleagues, R. Schneider and J. Hilton at Physics International of San Leandro, CA, for their direc-

tion of the PITHON irradiation facility and for the TIGER code calculations and to the DNA for sponsorship of the irradiation time.

Acknowledgment is gratefully given to the ORNL isotope facility for their generosity in loaning samples of separated isotopes.

- ¹B. Pontecorvo and A. Lazard, *C. R. Acad. Sci.* **208**, 99 (1939).
- ²G. B. Collins, B. Waldman, E. M. Stubblefield, and M. Goldhaber, *Phys. Rev.* **55**, 507 (1939).
- ³K. Yoshihara, Zs. Nemeth, L. Lakosi, I. Pavlicek, and A. Veres, *Phys. Rev. C* **33**, 728 (1986) contains a thorough review.
- ⁴A. Ljubicic, K. Pisk, and B. A. Logan, *Phys. Rev. C* **33**, 2238 (1981).
- ⁵K. Yoshihara, Zs. Nemeth, L. Lakosi, I. Pavlicek, and A. Veres, *Phys. Rev. C* **33**, 728 (1986).
- ⁶J. A. Anderson and C. B. Collins, *Rev. Sci. Instrum.* (to be published).
- ⁷J. A. Anderson and C. B. Collins, *Proof of the Feasibility of Coherent and Incoherent Schemes for Pumping a Gamma-Ray Laser*, University of Texas at Dallas, Report #GRL/8602, Innovative Science and Technology Directorate of Strategic Defense Initiative Organization, April 1987, pp. 29-46.
- ⁸We recently learned that apparently the first demonstration of the feasibility of the principle of this technique was made in 1971 before tabulations of nuclear parameters had matured to the point of being able to provide adequate practical guidance. See L. Cohen and E. A. Wolicki, *NRL Report 7306*, 1971.
- ⁹*Table of Isotopes*, edited by C. M. Lederer and V. S. Shirley (Wiley, New York, 1978).
- ¹⁰*Evaluated Nuclear Structure Data File* (Brookhaven National Laboratory, Upton, NY, 1986).
- ¹¹The actual values for the fractions of the fluorescent photons unaffected by self-absorption were calculated to be 91% and 88% for ^{75}Br and ^{75}Se , respectively.
- ¹²As seen in Table I, the best values of nuclear parameters differ from those used in Refs. 6 and 7. Our earlier reports used data from Ref. 9, while more recently we used Ref. 10, current to 1986.
- ¹³W. Miller, J. W. Motz, and C. Ciaella, *Phys. Rev.* **96**, 1344 (1954).
- ¹⁴J. A. Halbleib and T. W. L. Sanford, Sandia Report SAND83-2572, 1983.
- ¹⁵Data actually plotted in Figs. 8-10 are ratios of the numbers of detected photons corrected for the finite period of counting, while the analyses of Eqs. (1)-(10) are written in terms of the ratios of the numbers of active nuclei produced in the target. Slopes obtained from the figures must be multiplied by 1.50, the product of the ratios of corrections for detector and fluorescence efficiencies and for self-absorption in the target before being used in the equations.
- ¹⁶The scatter of the residues in Fig. 10 does not appear completely random and a trend might be perceived as indicating another gateway opening around 1.2 MeV. It is tempting to identify this with the level at 1186 keV favored in Table II. However, more shots ≈ 1 , higher end point energies would be needed to obtain a meaningful assessment of such a possibility.
- ¹⁷C. B. Collins, J. A. Anderson, Y. Paiss, and C. D. Eberhard, *Phys. Rev. C* (to be published).
- ¹⁸The first, 433 keV, is the average of the energies of the lowest two transitions in ^{75}Se weighted by their respective ξ , from Eq. (6). Pragmatically this corresponds to an average line at 433 keV having $\xi_{433}(\text{Se}) = 3.9 \times 10^{-12}$.

Rapid Communications

The Rapid Communications section is intended for the accelerated publication of important new results. Manuscripts submitted to this section are given priority in handling in the editorial office and in production. A Rapid Communication may be no longer than 3½ printed pages and must be accompanied by an abstract. Page proofs are sent to authors, but, because of the rapid publication schedule, publication is not delayed for receipt of corrections unless requested by the author.

Depopulation of the isomeric state $^{180}\text{Ta}^m$ by the reaction $^{180}\text{Ta}^m(\gamma, \gamma')^{180}\text{Ta}$

C. B. Collins, C. D. Eberhard, J. W. Giesener, and J. A. Anderson

Center for Quantum Electronics, The University of Texas at Dallas, Richardson, Texas 75083

(Received 27 October 1987)

The irradiation of an enriched sample of $^{180}\text{Ta}^m$ with bremsstrahlung from a linear accelerator having an end-point energy of 6 MeV has excited a strong channel for the reaction $^{180}\text{Ta}^m(\gamma, \gamma')^{180}\text{Ta}$, which requires a total spin change of $8\hbar$. An integrated cross section of $4.8 \times 10^{-25} \text{ cm}^2 \text{ keV}$ has been found. This is a large value exceeding by two orders of magnitude known cross sections for (γ, γ') reactions producing isomers of other species.

The isotope $^{180}\text{Ta}^m$ carries a dual distinction. It is the rarest stable isotope occurring in nature¹ and it is the only naturally occurring isomer.² The actual ground state of ^{180}Ta is 1^+ with a half-life of 8.1 h, while the tantalum nucleus of mass 180 occurring with 0.012% abundance is the 9^- isomer $^{180}\text{Ta}^m$. It has an adopted excitation energy of 75.3 keV and half-life in excess of 1.2×10^{15} yr.²

The stellar *s* process^{3,4} for nucleosynthesis has steadily gained favor for the production of $^{180}\text{Ta}^m$ and the role of the most critical intermediary $^{180}\text{Hf}^m$ has been well established.^{2,5} However, the viability of this cosmic mechanism rests upon the absence of any reactive channel $^{180}\text{Ta}^m(\gamma, \gamma')^{180}\text{Ta}$ which could destroy the isomeric population in the photon bath present in the stellar interior at the time of creation. Prior experiments^{6,7} have failed to show such a channel having any gateway for excitation below 1332 keV, but the rarity of the target material limited the sensitivity of those measurements. Reported here is the measurement of a very large cross section for the photonuclear deexcitation of $^{180}\text{Ta}^m$ through a gateway level at an energy $E \geq 1.4$ MeV. This definitive observation of such a strong radiative coupling between isomeric and ground states of ^{180}Ta may affect explanations for the natural occurrence of $^{180}\text{Ta}^m$.

The energy-level diagram of ^{180}Ta and its daughters is shown in Fig. 1, together with a schematic representation of the individual steps in the excitation and detection of the $^{180}\text{Ta}^m(\gamma, \gamma')^{180}\text{Ta}$ reaction. As can be seen in Fig. 1, the principal means for the detection of the ^{180}Ta ground state lies in observing the *Ka* lines of its daughter ^{180}Hf , following the decay by electron capture of the parent ^{180}Ta . The efficiency for the emission of *Ka* photons relative to the number of ^{180}Ta decays is about 57%.⁸

Two targets were used in these experiments. One con-

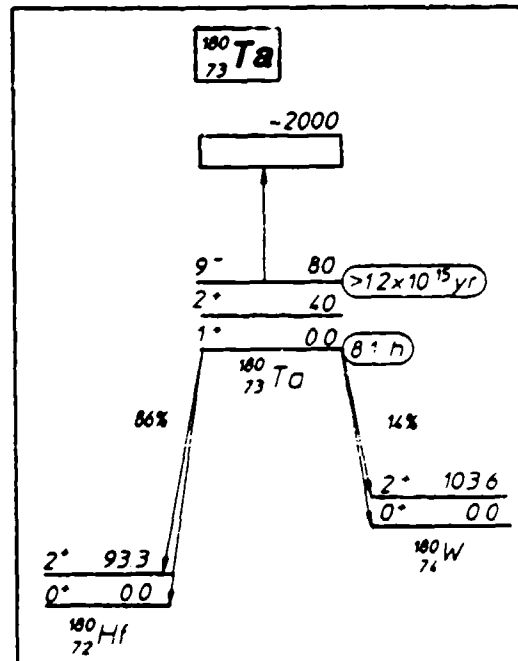


FIG. 1. Schematic energy-level diagram of ^{180}Ta and its daughters. Half-lives are shown in ovals to the right of the ground and isomeric levels. Energies are in keV. The initial transition of the (γ, γ') reaction is shown by the arrow pointing upward to the broad state represented by the rectangle. Cascade through the levels of ^{180}Ta is not known, but leads finally to the ground state. Electron capture to the left and beta decay to the right are indicated by the diagonal downward arrows. The final debris from pumping down the isomer is found principally in the *Ka* fluorescence from the ^{180}Hf characterized by the 8.1 h lifetime of its ^{180}Ta parent.

sisted of a disk 5 cm in diameter of tantalum in natural isotopic abundance. It contained about 0.5 mg of $^{180}\text{Ta}^m$ in the surface layer of thickness equal to the mean distance for escape of a 55 keV x-ray photon. The second target was enriched to contain 1.3 mg of $^{180}\text{Ta}^m$ in 24.7 mg of ^{181}Ta . Deposited as a dusting of oxide near the center of the surface of a 5 cm disk of Al and overcoated with a 0.25 mm layer of Kapton, this second sample was believed⁹ to be free from self-absorption of the x-rays from the daughter Hf.

The samples were exposed to bremsstrahlung radiation from a Varian Clinac 1800 linear accelerator (LINAC) operated with an end-point energy of 6 MeV. This device has been well characterized,^{10,11} and its output dose rate has been calibrated with an accuracy of $\pm 3\%$. After irradiation, the samples were counted with an *N*-type, HPGe spectrometer having a beryllium entrance window. Conventional techniques were used to calibrate the counting system with isotopic standards.

Figure 2 shows the spectra of the enriched target before and after 4 h irradiation. The spectrum from the other target was entirely similar with the Hf signal reduced by the ratio of the masses of the $^{180}\text{Ta}^m$ and the background increased by the appearance of *K* lines of Ta excited in the large mass of diluent ^{181}Ta by the decay of natural activity in the counting shield.

Figure 3 shows the dependence upon time of the counting rate observed in the Hf(*K*_α) peaks after irradiation. Data points are plotted at the particular times at which the instantaneous counting rate equals the average counting rate measured over the finite time interval shown. The figure shows the close agreement of the measured rates to the decay expected for a half-life assumed to be 8.1 h.

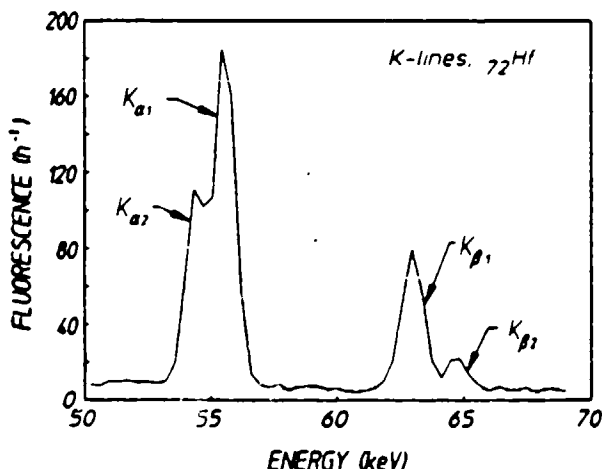


FIG. 2. Dotted and solid curves show, respectively, the spectra obtained before and after dumping some of the isomeric $^{180}\text{Ta}^m$ contained in a target sample enriched to 5%. An HPGe detector was used to obtain the dotted spectrum before irradiation. The feature at 63 keV is from traces of natural activity in the counting shield. The solid curve shows activity resulting from the transmutation of the pumped ^{180}Ta measured in the same sample and counting system after irradiation. The prominent additions are the *K*_α and *K*_β hafnium x-ray lines resulting from electron capture in the ^{180}Ta .

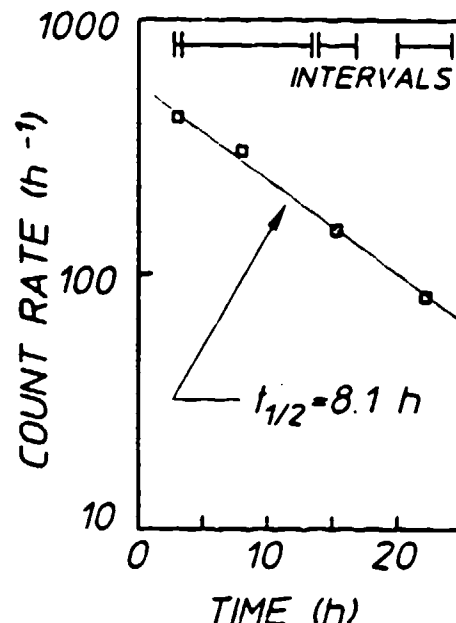


FIG. 3. Plot of the counting rates measured for the Hf(*K*_α) fluorescence from the target fabricated from natural tantalum as functions of the time elapsed from the end of the irradiation. The vertical dimensions of the data points are consistent with 1σ deviations of the measured number of counts accumulated during the finite counting intervals shown at the top of the graph. The dotted line shows the rate expected for a half-life of 8.1 h.

The spectrum of the bremsstrahlung pumping the fluorescence seen in Fig. 2 was taken from the literature¹⁰ and was normalized to the total dose measured in this experiment. In this way, the time-integrated spectral intensity producing the fluorescence was found to be constant¹² to within a factor of 2 over the range 1-5 MeV at a value of 2×10^{14} keV/(keV cm²). The number of counts observed in the Hf *K*_α lines were corrected for finite irradiation and counting times, the absolute counting efficiency of the spectrometer, and the 57% emission intensity from the parent ^{180}Ta to obtain the total number of nuclei pumped to the ground state. Assuming self-absorption in the enriched target to be negligible, the integrated cross section for the deexcitation of the isomer can be readily calculated if the reaction is assumed to occur through a gateway state narrow in comparison to the range of energies spanned by the irradiation. A value of $\sigma\Gamma = 4.8 \times 10^{-25}$ cm² keV is obtained for the integrated cross section if the gateway energy is arbitrarily assumed to be near the lowest value consistent with prior⁷ negative results, 2.0 MeV. Even larger cross sections would result from the assumption that the gateway lies at higher energies where the pumping flux is decreased or from the inclusion of an exact self-absorption correction. Once the gateway energy is fixed, experimental error in the integrated cross section is bounded on the lower side by a total uncertainty of 15% contributed by the calibrations of source and detector and on the upper side by a factor of 2 arising from the possible loss of signal because of self-absorption of the Hf x-rays.

The results of this work show a radiative connection between the isomer $^{180}\text{Ta}^m$ and the ^{180}Ta ground state of remarkable strength. Comparative values for the deexcitation of other isomers are not available as it appears this is the first such measurement. However, the inverse process for the excitation of isomers by (γ, γ') reactions typically proceeds¹³⁻¹⁵ with integrated cross sections at least two orders of magnitude smaller. The value reported here for the reaction $^{180}\text{Ta}^m(\gamma, \gamma')^{180}\text{Ta}$ is inexplicably large and may have several consequences. If the gateway level through which it proceeds is not sufficiently above the thermal energies expected to characterize the *s* process of

nucleosynthesis, current models of the stellar production of $^{180}\text{Ta}^m$ will be severely affected.

The authors gratefully acknowledge the support of this work by the Innovative Science and Technology Directorate of the Strategic Defense Initiative Organization through direction by Naval Research Laboratory. Sincere appreciation is conveyed to Dr. P. P. Antich and E. C. Scarbrough of the University of Texas Southwestern Medical Center at Dallas for use of the linear accelerator and to the Oak Ridge National Laboratory isotope facility for the loan of the enriched $^{180}\text{Ta}^m$ sample.

¹A. G. W. Cameron, in *Essays in Nuclear Astrophysics*, edited by C. A. Barnes, D. D. Clayton, and D. N. Schramm (Cambridge Univ. Press, Cambridge, 1982), p. 23.

²E. Browne, Nucl. Data Sheets 52, 127 (1987).

³K. Yokoi and K. Takahashi, Nature 305, 198 (1983).

⁴H. Beer and R. A. Ward, Nature 291, 308 (1981).

⁵E. Runte, W. D. Schmidt-Ott, W. Eschner, I. Rosner, R. Kirchner, O. Klepper, and K. Rykaczewski, Z. Phys. A 328, 119 (1987).

⁶J. Law and F. A. Iddings, J. Radioanalytical Chem. 3, 53 (1969).

⁷E. B. Norman, S. E. Kellogg, T. Bertram, S. Gil, and P. Wong, Astrophys. J. 281, 360 (1984).

⁸E. Browne and R. B. Firestone, in *Table of Radioactive Isotopes*, edited by V. S. Shirley (Wiley, New York, 1986), pp. 180-182.

⁹Although the grain size of the Ta_2O_5 was small compared to es-

cape lengths for the 55 keV x-ray, close examination of the target subsequent to the experiment indicated that some clumping of the material had occurred. As discussed in the text, this could cause our result to become a lower limit for the integrated cross section.

¹⁰R. Mohan, C. Chui, and L. Lidofsky, Med. Phys. 12, 595 (1985).

¹¹N. C. Ikoro, D. A. Johnson, and P. F. Antich, Med. Phys. 14, 93 (1987).

¹²Since the spectral intensity is roughly constant, the flux decreases as E^{-1} toward the end point with a final more rapid drop between 5 and 6 MeV.

¹³E. C. Booth and J. Brownson, Nucl. Phys. A98, 529 (1967).

¹⁴M. Boivin, Y. Cauchios, and Y. Heno, Nucl. Phys. A137, 520 (1969).

¹⁵M. Boivin, Y. Cauchios, and Y. Heno, Nucl. Phys. A176, 626 (1971).

Diamond-like carbon films prepared with a laser ion source

S. S. Wagal, E. M. Juengerman, and C. B. Collins

Center for Quantum Electronics, University of Texas at Dallas, P.O. Box 830688, Richardson, Texas 75083-0688

(Received 31 March 1988; accepted for publication 13 May 1988)

Diamond-like carbon films have been deposited onto clean, unseeded substrates using a hybrid ion beam technique. In this method the ion fluences available for acceleration were particularly enhanced by the use of laser ablation plumes ejected from highly purified graphite targets. The combination of levels of purity characteristic of ultrahigh vacuum environments, large ratios of ion to neutral concentrations, and high fluences showed considerable merit for the growth of large-area (10 cm^2) films of optical quality and uniformity at deposition rates approaching $20 \mu\text{m/h}$.

Interest in diamond-like carbon (DLC) films is motivated by their unique combinations of physical hardness, electrical strength, high thermal conductivity, and optical transparency. Studies have been recently accelerated by prospects of commercial application for optics and semiconductors, but no single technique has yet produced films with uniform properties at practical rates of growth.

Four methods remain at the focus of current interests: ion beam deposition,¹⁻⁴ chemical vapor deposition (CVD),⁵⁻⁷ plasma-enhanced CVD (PECVD),⁸⁻¹¹ and sputtered deposition.¹²⁻¹⁵ Contamination is minimized in the first because only the ions of carbon are accelerated to selected energies and deposited on a substrate in a high vacuum environment. In such systems differential pumping and mass separation further reduce the level of the inclusion of impurities into the films. Layers of high quality can be obtained, but at the cost of very slow rates of growth.

In CVD and PECVD both ions and neutral atoms of carbon are produced by the dissociation of organic vapors, such as CH_3OH , C_2H_2 , and CH_3OHCH_3 , and deposited on substrates. The unwanted collateral products of dissociation provide ready sources of contamination. While growth rates reach practical levels, no one has yet reported the preparation in this way of DLC films of optical quality. The sputtering technique requires two ion sources, one for sputtering carbon from a graphite source with enough velocity to reach the substrate and another for breaking the unwanted graphite bonds which may otherwise remain in the growing film. The two ion sources make the system cumbersome and the higher pressures (10^{-3} – 10^{-4} Torr) needed to support the sputtering process introduce problems of contamination that degrade the films to a level comparable to those encountered in CVD and PECVD. In two cases^{16,17} lasers have been used in a variant of the sputtering process, but with similar results and problems.

Here we report a hybrid method in which the modest rate of growth that characterizes the cleaner ion beam method is enhanced by the high fluence of carbon ions that can be separated from a discharge plume excited by a laser beam focused upon a cold graphite source. The free expansion of the carbon plume into a UHV chamber rapidly attenuates the flux of neutrals impinging upon a substrate positioned at some distance, while the ions are accelerated directly to the

surface of the growing film. Since the laser is pulsed for 10 ns periods the peak growth rates are very high. The duty cycle is low but average growth rates can still reach $20 \mu\text{m/h}$. Films of DLC produced in this way show a mirror-smooth surface finish and a uniformity of optical quality. Most surprising is that the growth of these films does not require any seeding of the substrate with debris from abrasive treatment with either diamond or any other particles. Areas of 10 cm^2 have been coated with uniform optical quality on a variety of substrates with only routine cleaning.

Our technique is shown schematically in Fig. 1. As seen there, the output from a Nd-glass laser was focused on a graphite target placed in a UHV environment. The effect of the laser beam was to eject a plume of carbon vapor and then to ionize that portion of it still being illuminated. The neutral cloud expanded isotropically, as evidenced by the pervasive coating of soot which developed in the UHV chamber. The ions were drawn out of the plume and accelerated by the static fields between the graphite target which was grounded and the negatively charged grid structure shown in Fig. 1. The use of highly purified graphite (99.999%) ensured that only the ions of carbon were collected without any necessity for the mass separation techniques often required when using molecular sources of C^+ . The substrate was contained in a Faraday cage connected to the accelerating grid. A drift space was incorporated in the cage making the path from the laser plume to the substrate total 15 cm.

In operation the laser could be used in either a triggered mode giving 10 J of energy in a $10 \mu\text{s}$ pulse or a Q-switched mode producing a nominal 1 J of output in a 10 ns pulse. Accelerating potentials typically ranged from 300 to 2000 V. The substrates used in most of the studies reported here were

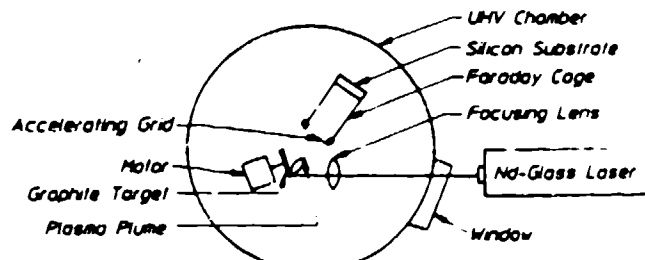


FIG. 1. Schematic representation of the experimental apparatus.

cut from Si(111) disks, 7.5 cm in diameter, but DLC films of comparable quality could be grown on a variety of materials including Ge and quartz. Without any seeding or abrasion of the surfaces, films grown in this way were mirror smooth and uniform, producing no perceptible distortion in reflected images and test patterns. The coloration of a particular sample depended upon the combination of source proximity and accelerating voltage used to prepare it. A brownish cast appeared under conditions which would have increased the proportions of neutral carbon atoms and clusters in the plasma being transported to the growing film.

The predominance of DLC in the films was indicated by Raman spectra such as shown in Fig. 2. The particular signature of the DLC¹⁴ is the broad triangular structure peaking at 1560 cm^{-1} with a base stretching from 1000 to 1600 cm^{-1} . The thickness of this film was only about 200 Å and the DLC spectrum is well developed for such a thin film, probably because of the optical quality. The same spectrum was obtained at different locations sampled on the film. The prominent lines in Fig. 2 were contributed by the Si and were found to be much stronger than were produced by an uncoated substrate. This enhancement has been reported previously¹⁵ and is attributed to the matching of the indices of refraction by the DLC coating.

Ellipsometry measurements showed the index of refraction to be uniform across a single film, but to be dependent upon the accelerating voltage that had been used to deposit the DLC. Several films were grown with different accelerating voltages, each chosen to produce a DLC with a different index of refraction lying within the range 1.5 – 2.15. The ellipsometry measurements also confirmed that the thickness of the films corresponded to a nominal deposition rate of 1 Å/pulse of the laser for a substrate placed 15 cm from the plasma plume. The particular sample characterized in Fig. 2 was found to have a thickness of 180 Å with a surface roughness of only $\pm 1 \text{ \AA}$.

Tests of chemical and physical parameters showed the films to be completely intact after immersion in boiling water for 1 h and 10% HCl solution for 1/2 h. The resistance measured on the surface was found to vary from a value for freshly prepared films larger than could be measured with

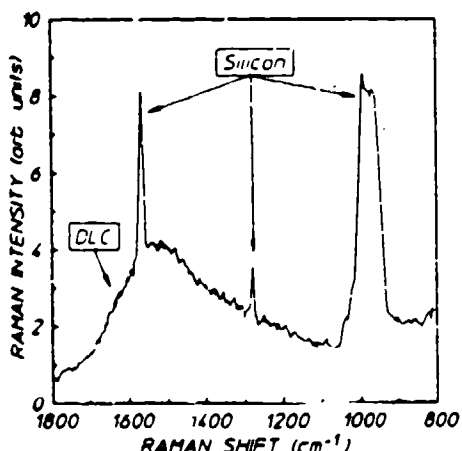


FIG. 2. Spectrum of the Raman scattering of the 514.5 nm output of an argon ion laser from a 180-Å-thick film of DLC grown on a Si(111) substrate from carbon ions from the laser ion source.

available methods, $> 40 \text{ M}\Omega/\text{cm}$ to less than $500 \text{ }\Omega/\text{cm}$ in films annealed at 600°C . This agrees with previous observations⁴ of the graphitization of DLC films.

Similar levels of improvement in the optical qualities of the diamond-like films were obtained by cratering the graphite target and by *Q* switching the laser. Either adjustment should have increased the ratio of ions to neutrals in the ablated plasma, emphasizing again the predominant importance of the carbon ions to the growth mechanism. Rotating the graphite target ensured that each triggered discharge fell on a clean planar surface and under such conditions films were formed which were mostly soot. The contrasting approach of triggering successive discharges into the same crater ensured that the plume reached higher temperatures because of confinement and that a larger proportion of the vapor remained in the illumination to be subsequently ionized. Optical quality films were obtained in this way that matched the best produced with the much greater power densities available from the *Q*-switched operation.

Our tentative conclusions are that the high proportions of ions to neutrals in the plasmas² formed by laser ablation are responsible for the uniform optical quality of the DLC films grown by the hybrid technique we are reporting. In this way the advantages of the ion beam method for the deposition of DLC are enhanced by the greater fluences available from laser plasma sources. At deposition rates currently realized of 1 Å/pulse over tens of cm^2 a growth rate of DLC approaching $20 \mu\text{m}/\text{h}$ could be realized with commercially available lasers.

The authors wish to convey their sincere appreciation to colleagues who generously shared their diagnostic capabilities, in particular M. Green and T. D. Black of the Physics Department of the University of Texas at Arlington for the Raman spectroscopy and S. Lambert of Varo, Inc. for the ellipsometry. This work was supported by the Innovative Science and Technology Directorate of the Strategic Defense Initiative Organization and directed by the Naval Research Laboratory.

- ¹S. Aisenberg and R. Chabot, *J. Appl. Phys.* **42**, 2953 (1971).
- ²E. G. Spencer, P. H. Schmidt, D. C. Joy, and F. J. Sansalone, *Appl. Phys. Lett.* **29**, 118 (July 1976).
- ³T. Mori and Y. Namba, *J. Vac. Sci. Technol. A1*, 23 (1983).
- ⁴S. Kashi, H. Kang, and J. Wayne Rabalais, *Phys. Rev. Lett.* **59**, 75 (1987).
- ⁵B. V. Spitsyn, L. L. Bouilov, and B. V. Derjaguin, *J. Cryst. Growth* **52**, 219 (1981).
- ⁶S. Matsumoto, Y. Sato, M. Kamo, and M. Sakata, *Jpn. J. Appl. Phys.* **21**, (1982) L183.
- ⁷A. Sawabe and T. Inuzuka, *Appl. Phys. Lett.* **46**, 2 (1985).
- ⁸L. Holland and S. M. Ojba, *Thin Solid Films* **58**, 107 (1979).
- ⁹J. Vora and T. J. Moravec, *J. Appl. Phys.* **52**, 6151 (1981).
- ¹⁰S. Matsumoto, M. Hino, and T. Kobayashi, *Appl. Phys. Lett.* **51**, 737 (1987).
- ¹¹K. Kurihara, K. Sasaki, M. Motonobu, and N. Koshino, *Appl. Phys. Lett.* **52**, 437 (1988).
- ¹²C. Weissmantel, K. Bewilogua, D. Dietrich, H. J. Erler, H. J. Hinnerberg, S. Klose, W. Nowich, and G. Reisse, *Thin Solid Films* **72**, 19 (1980).
- ¹³T. Miyasato, Y. Kawakami, T. Kawano, and A. Miraki, *Jpn. J. Appl. Phys.* **23**, L234 (1984).
- ¹⁴M. Kitabatake and K. Wada, *J. Appl. Phys.* **58**, 1693 (1985).
- ¹⁵M. Mirtich, Dan Nir, D. Swec, and B. Bank (unpublished).
- ¹⁶K. Kitahama, K. Hirata, H. Nakamatsu, and S. Kawi, *Appl. Phys. Lett.* **49**, 643 (1986).
- ¹⁷T. Sato, S. Furuno, S. Iguchi, and M. Hanabusa, *Jpn. J. Appl. Phys.* **26**, L1487 (1987).

Activation of $^{115}\text{In}^m$ by single pulses of intense bremsstrahlung

C. B. Collins, J. A. Anderson, Y. Paiss, and C. D. Eberhard

University of Texas at Dallas, Center for Quantum Electronics, Richardson, Texas 75083

R. J. Peterson

University of Colorado, Nuclear Physics Laboratory, Boulder, Colorado 80309

W. L. Hodge

High Energy Laser Associates, 6114 LaSalle Avenue, Ste. 426, Oakland, California 94611

(Received 13 October 1987)

A new technique has been recently described for the absolute calibration of intense sources of pulsed radiation in the 0.2–1.5 MeV range of photon energies. An activation technique, it depended upon the storage of samples of the irradiating spectrum in the form of populations of nuclei excited to isomeric states with lifetimes of seconds to hours. Described here is the use of such a calibrated source to resolve severe conflicts in previous studies of the reaction $^{115}\text{In}(\gamma, \gamma')^{115}\text{In}^m$ through the 1078 keV $J^\pi = \frac{5}{2}^+$ level; this mode has traditionally served as the archetype for (γ, γ') reactions. We report an integrated cross section of $(18.7 \pm 2.7) \times 10^{-29} \text{ cm}^2 \text{ keV}$ with no evidence of any importance of nonresonant channels of excitation.

I. INTRODUCTION

For the study of (γ, γ') reactions that produce isomeric products, ^{115}In has a particularly favorable combination of characteristic properties. Having only a few channels for reaction at energies below 1.4 MeV, it nevertheless displays a large integrated cross section for excitation of the 269 min isomer at 336 keV. For these pragmatic reasons ^{115}In has served as the archetype material for the study of this type of reaction and a number of efforts have been reported^{1–13} in the past 48 years.

The relevant part of the energy level diagram¹⁴ of ^{115}In is shown in Fig. 1, indicating only three levels through which a (γ, γ') reaction of multipolarity $E1$, $M1$, or $E2$ could proceed to populate the isomeric state for photons below 1.4 MeV. The importance of the lowest gateway level at 941 keV is negligible because it has a particularly small integrated cross section¹⁵ for excitation in comparison to that of the nearby 1078 keV level, and the 934 keV $\frac{7}{2}^+$ level has a yet smaller cross section because of its longer lifetime.

In practical cases in which ^{115}In samples are excited either with gamma rays from a source or by bremsstrahlung from an accelerator operating below 1.4 MeV, the absorption spectrum for (γ, γ') reactions producing isomers is thus essentially monochromatic at 1078 keV. Nevertheless, measurements by different investigators have shown considerable variance. Table I presents a summary of values reported in the literature together with the results of this measurement in terms of the integrated cross section as usually reported,¹⁶ $\pi b_e b_0 \Gamma \sigma_0 / 2$, where Γ is the natural width in keV of the pump band, where the branching ratios b_e and b_0 give the probabilities for the decay of the gateway level back into the initial and isomeric level, respectively, and σ_0 is the Breit-Wigner cross section for the absorption transition,

$$\sigma_0 = \frac{\lambda^2}{2\pi} \frac{2I_e + 1}{2I_g + 1} \frac{1}{\alpha_p + 1}, \quad (1)$$

where λ is the wavelength in cm of the gamma ray at the resonant energy, E_i , I_e , and I_g are the nuclear spins of the excited and ground states, respectively, and α_p is the total internal conversion coefficient for the absorption transition. The α 's can reasonably be expected to be less than 0.01 for the transitions discussed here.

It has been recently argued¹⁶ that the principal cause of such a large degree of variance among previous measurements of the ^{115}In excitation has been the generally inadequate level of characterization of the spectrum of the pump source. It is particularly awkward to specify the spectrum from a line source. In a previous paper¹⁵ we showed that the spectrum from a pulsed source of intense bremsstrahlung could be determined to a level of accuracy sufficient for the quantitative description of the reactions $^{77}\text{Se}(\gamma, \gamma')^{77}\text{Se}^m$ and $^{79}\text{Br}(\gamma, \gamma')^{79}\text{Br}^m$. This agreement now provides a reliable scheme to normalize other results to the pumping spectrum.

It is the purpose of this paper to report the reexamination of the reaction $^{115}\text{In}(\gamma, \gamma')^{115}\text{In}^m$ with the same pulsed bremsstrahlung source used for the reconciliation of the absorption cross sections to $^{79}\text{Br}^m$ and $^{77}\text{Se}^m$. The quantitative value for the integrated cross section we report is in good agreement with the value reported most recently as the result of excitation with a radioactive source.¹²

II. METHODS AND APPARATUS

In this method based on the results of Refs. 13 and 16, the uncertainty in the absolute value of the geometric coefficient coupling the source of pump radiation to the absorbing target is eliminated by normalizing both the

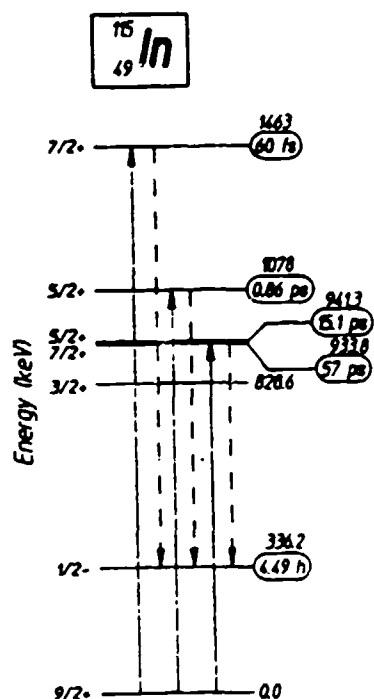


FIG. 1. Energy level diagram of the excited states of ^{115}In important in the production of populations of the isomer (Ref. 14). Half-lives of the states are shown to the right of each and sequences of (γ, γ') reactions leading to the isomer are shown by the arrows. Dashed γ' transitions occur by cascading through levels not shown.

pump fluence and the fluorescence counts to some standard material having a monochromatic excitation spectrum. The reaction $^{79}\text{Br}(\gamma, \gamma')^{79}\text{Br}^m$ is that standard, having an integrated cross section of $6.2 \times 10^{-29} \text{ cm}^2 \text{ keV}$ and a convenient radioactivity in the isomer. Following the formalism reported earlier,¹³ the number of $^{115}\text{In}^m$ nuclei, $S(\text{In})$, which could be excited by a flash of intense bremsstrahlung can be expressed as a ratio,

$$\frac{S(\text{In})}{S(\text{Br})} = \frac{N(\text{In})}{N(\text{Br})} \frac{\xi_{1078}(\text{In})}{\xi_{761}(\text{Br})} \cdot \xi(1078), \quad (2)$$

where $S(x)$ and $N(x)$ are the number of nuclei produced and the number of target nuclei of material x , respectively, $\xi(1078)$ is the ratio of pumping intensity in units of (keV/keV) at 1078 keV to the intensity in (keV/keV) at 761 keV, and the $\xi_E(x)$ are the combinations of nuclear parameters involved in the excitation of the gateway level at energy E .

$$\xi_E(x) = \frac{(\pi b_e b_0 \Gamma \sigma_0 / 2)_E}{E} \quad (3)$$

The collection of terms in parentheses in Eq. (3) comprises the integrated cross section for excitation as usually reported and the calibration value¹³ for ^{79}Br is $\xi_{761}(\text{Br}) = 8.2 \times 10^{-32} \text{ cm}^2$.

The source of excitation in these experiments¹³ was the bremsstrahlung produced by the DNA PITHON nuclear simulator at Physics International. For these particular experiments the nominal firing parameters were deliberately perturbed so that successive irradiations could be obtained with end point energies varying from 0.9 to 1.5 MeV.

Intensities at the target were determined by measuring the nuclear activation of the ^{79}Br component of a sample of LiBr containing isotopes in natural abundance. This calibrating target was run in a pneumatic transfer system which enabled the population of $^{79}\text{Br}^m$ produced by a single irradiation to be subsequently counted with a NaI(Tl) detector of known efficiency at a quiet location 30 m removed from the source. Activation lost during the 1.0 s transit time could be readily corrected during analysis.

The ^{115}In sample under study was in the form of a thin foil taped to a fiduciary mark near the pneumatic system. Since the $^{115}\text{In}^m$ had a substantially longer half-life, it could be manually detached after exposure and transferred to the spectrometer which consisted of a 3" x 3" NaI(Tl) detector with associated electronics. In typical cases a counting time of 1 h gave better than 2%

TABLE I. Summary of integrated cross sections reported for the reaction $^{115}\text{In}(\gamma, \gamma')^{115}\text{In}^m$ through the 1078 keV $J^\pi = \frac{5}{2}^+$ level.

Cross Section $\pi b_e b_0 \Gamma \sigma_0 / 2$ ($10^{-29} \text{ cm}^2 \text{ keV}$)	Method ^a	Reference
23 \pm 4	S	Ikeda and Yoshihara (Ref. 4)
20 \pm 4	S	Veres (Ref. 5)
7.1 \pm 2.3	A	Chertok and Booth (Ref. 6)
11.5 \pm 4.0	A	Booth and Brownson (Ref. 7)
30(X + 40, - 20)	A	Boivin, Cauchois, and Heno (Ref. 8)
10.5 \pm 2.7	S	Lakosi, Csuros, and Veres (Ref. 9)
19 \pm 1	S	Watanabe and Mukoyama (Ref. 10)
5.39 \pm 0.64	S	Ijubici, Pisk, and Logan (Ref. 11)
18.1 \pm 1.5	S	Yoshihara <i>et al.</i> (Ref. 12)
14 \pm 1		Calculated from lifetimes and branching ratios (Ref. 14)
18.7 \pm 2.7	A	This work

^a A is bremsstrahlung from an accelerator; S is radiation from ^{60}Co source.

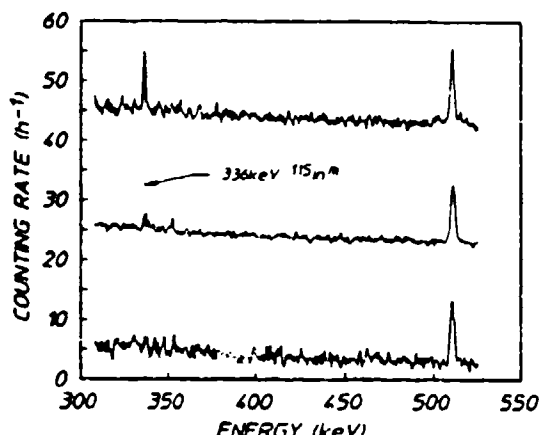


FIG. 2. Three sequential spectra from an intrinsic Ge detector begun at times 6.5, 9.2, and 19.0 h after the irradiation with a flash of bremsstrahlung with an 1.3 MeV end point. Data have been offset by 40, 20, and 0 counts/h, respectively. The 336.2 keV peak is seen to decay with the appropriate half-life of 4.49 h for $^{115}\text{In}^m$. The other structure is the annihilation peak at 511 keV, present in the background at a constant rate.

typical cases a counting time of 1 h gave better than 2% statistical accuracy in the $^{115}\text{In}^m$ peak after removal of background. In the course of this experimental series 12 shots were obtained for sufficiently high end point energies to yield fluorescent isomeric activity for ^{115}In .

To confirm that the fluorescence being detected resulted only from decay of the $^{115}\text{In}^m$ activity, additional foils were irradiated and then examined with an intrinsic Ge spectrometer, carefully shielded. In Fig. 2 we show spectra from an In foil irradiated by bremsstrahlung with an endpoint of 1.3 MeV. The fluorescence peak is at 336.2 keV, with a half-life seen to be consistent with a tabulated value of 4.49 h.

The relative bremsstrahlung intensity emitted at 1078 keV was a strong function of end-point energy of the accelerator as shown in Fig. 3. These data were obtained

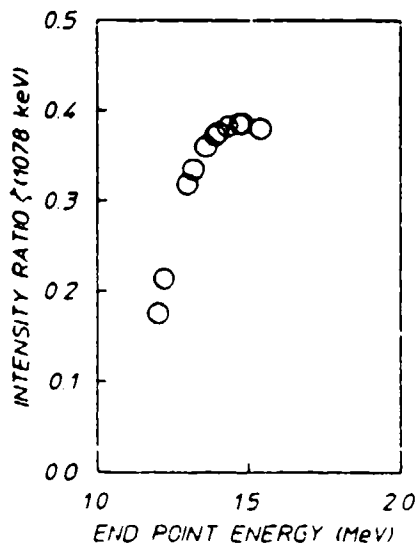


FIG. 3. Plot of the ratio of intensities of the bremsstrahlung spectrum at 1078 keV to that at 761 keV as a function of the end-point energy of the electron beam producing the photons. Statistical uncertainties are smaller than the data points.

by numerically fitting theoretical computations of bremsstrahlung spectra. A sample computed spectrum and the verification points from ^{75}Br and ^{75}Se are shown in Ref. 13. For each shot of the PITHON simulator the voltage and current were integrated in a bremsstrahlung modeling code to normalize the activity induced. As described previously,¹³ confidence in the present method was established by examining quantitatively the number of fluorescent nuclei produced by successive irradiations of samples of ^{75}Br and ^{75}Se at a variety of end-point energies. The monotonic results in Fig. 3 indicate that the end point determination is reliable to within ± 50 keV from shot to shot.

III. RESULTS

Because of a physical displacement between the ^{115}In sample and the mixed $^{75}\text{Br}/^{75}\text{Se}$ calibrator, the observed activities required correction for the different x-ray intensity obtained at these two points. This was done by mounting thermoluminescent dosimeters (TLD's) at both positions and comparing delivered doses for each shot. Using the assumption that the relative spectral distribution was constant even though the intensity was varying with position, the ^{115}In activity was scaled by the ratio of the calibrator dose to that of the indium sample. This correction ranged from 1.40 to 0.69 for the shots used in this work. The relative reversals of the positions of calibrator and sample with respect to the center of the irradiation source gave the same results, thus supporting the validity of the method of correction.

The indium sample was optically thin (0.183 g/cm^2) at the 336 keV energy of the fluorescence from the $^{115}\text{In}^m$ thus obviating corrections for self-absorption. Data were corrected for fluorescence and detector efficiencies. The resulting values of $S(\text{In})/S(\text{Br})$ are obtained from Fig. 4 by multiplying the ratios of fluorescent counts shown there by 0.75, the ratio of correction factors for these effects.

The linear form of the dependence of the relative yield of fluorescence from the indium isomers seen in Fig. 4 between 1.0 and 1.45 MeV is a strong indication of the dominance of a single channel of excitation through a gateway level lying at an energy given by the value of intercept. From the data of Fig. 4 it is seen that the intercept lies between 1000 and 1200 keV in agreement with the known $\frac{5}{2}^+$ state at 1078 keV. Also indicated in Fig. 4 is the energy of the next higher gateway state, $\frac{7}{2}^+$ at 1463 keV. It is interesting to observe that for end-point energies above this value there may be a tendency of the data to depart from the simple linear fit because of the availability of this additional gateway. A greater number of measurements at successively higher end-point energies would be needed to confirm this indication.

Once the data below 1.4 MeV are established as being consistent with the model of excitation through a single level at 1078 keV, Eq. (2) provides a means of determining the absolute cross section for the excitation. In Fig. 5 data for the measured values on the left side of Eq. (2) are plotted as functions of the relative intensities, $\xi(1078)$, appearing on the right.¹⁷ The scatter in the counting ra-

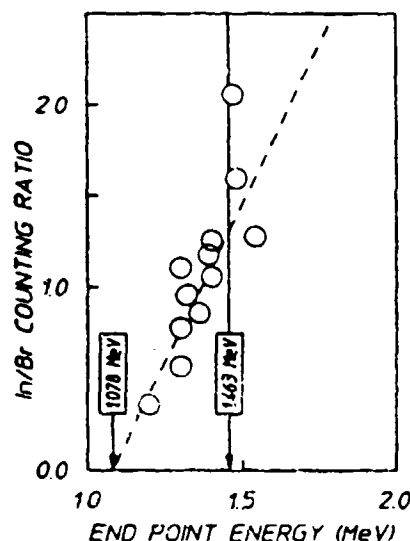


FIG. 4. Ratios of fluorescent photons from ^{115}In to those from ^{75}Br , produced by single discharges from PITHON, as corrected for the finite duration of the counting interval and plotted as a function of the end-point energies of the electrons producing the bremsstrahlung. The dashed line shows a linear fit to the data intercepting the x axis at a single gateway energy of 1.078 MeV. The excitation energy of the next higher gateway is also shown at 1.463 MeV. Statistical uncertainties are smaller than the data points.

tio is not due to the 2% counting statistics, but to the scatter in the modeled normalized fluxes, for which consistency provides the best estimate of the uncertainty. Note that it is the shape, not the absolute intensity of the pumping spectrum that enters as $\xi(1078)$. As can be seen from Eq. (2), the best slope around which the data of Fig. 5 scatter would represent our experimental determination of the product of the first two terms on the right of Eq. (2).

From the linear fit to the data of Fig. 5 shown as the heavy line, Eqs. (2) and (3), and the value of integrated cross section for ^{75}Br mentioned earlier, we obtain $\xi_{1078}(\text{In}) = (17.3 \pm 2.5) \times 10^{-32} \text{ cm}^2$. The uncertainty was obtained from application of the same analyses to the lighter lines in Fig. 5 bounding the scatter from the least-squares fit to the data. The lines shown were obtained by determining the extent to which the fit to the data points of Fig. 5 would be displaced horizontally if the corresponding abscissae were varied by the maximum extent of the uncertainty in the value of $\xi(1078)$ arising from the nature of the calibration and the interpolations being employed,¹³ that is, by the uncertainty in the slope of the pumping spectrum. The scatter of the data is within the bounds established by this uncertainty in intensity. Not explicitly shown in $\xi_{1078}(\text{In})$ is the $\pm 16\%$ uncertainty in the reference value of $\xi_{76}(\text{Br})$ taken from the literature.¹⁴

Finally, substituting the result for $\xi_{1078}(\text{In})$ into Eq. (3) and solving for the integrated cross section gives for the 1078 keV transition in ^{115}In , $\pi b_a b_b \Gamma \sigma_0 / 2 = (18.7 \pm 2.7) \times 10^{-29} \text{ cm}^2 \text{ keV}$. This is the value we report in Table I.

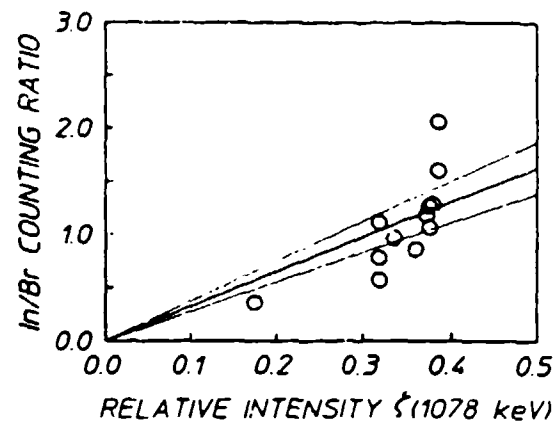


FIG. 5. Plot of the ratios of ^{115}In to ^{75}Br fluorescence observed as a function of the relative intensity of irradiation at 1078 keV normalized to the intensity at 761 keV. The heavy line shows the least-squares fit including the origin and the lighter lines indicate the uncertainty in such a fit introduced by varying the characterization of the intensities of Fig. 3 over the uncertainties in the characterization of the source. Slopes must be multiplied by 0.75, the product of the ratio of corrections for detector and fluorescence efficiencies and for self-absorptions in the targets before used in expressions such as Eq. (2).

IV. CONCLUSIONS

The detailed characterization of the spectrum emitted by the intense source of pulsed bremsstrahlung described earlier¹³ has been found to be sufficient to determine the yield of the reaction $^{115}\text{In}(\gamma, \gamma')^{115}\text{In}$. Table I shows this value to agree with some of the prior measurements. In this work there was no need to invoke any nonresonant reaction channels of the type sometimes used¹¹ in the description of this reaction.

In addition to providing further evidence against the occurrence of nonresonant reactions in ^{115}In , the results of this work have important implications for the calibration of intense sources of pulsed continua. By providing a means for storing a sample of the illuminating intensity at a single well-defined energy of 1078 keV for subsequent measurement at a later, quieter time, a sample of ^{115}In can readily complement the information supplied^{11,16} by ^{75}Br about the intensity at 761 keV. Moreover, both together can be used to identify the component of excitation contributed by the higher energy lines of ^{77}Se so that the remainder can be used to characterize the intensities at lower energies.¹³

Finally, it seems this technique of using single pulses of intense continua to measure integrated cross sections for the production of measurable populations of isomers can provide data of use in astrophysical modeling. Cross section at photon energies as low as 1 MeV are quite large for such elements as Se, Br, and In and might provide viable photonuclear channels for the production of enough isomeric population to be important in cosmic nucleosynthesis. It seems that the experiments reported here give evidence that it is possible to advance the precision for the characterization of (γ, γ') reactions toward that enjoyed by other types of particle reactions at comparable energies.

ACKNOWLEDGMENTS

This work was supported by the Innovative Science and Technology Directorate of the Strategic Defense Initiative Organization and directed by the Naval Research Laboratory. It was made possible through the efforts of many people within the Center for Quantum Electronics. The implementation of the project depended on the contributions of K. Taylor, C. Dutta, M. Byrd, and P. Phil-

lips from the Detector Physics group and of J. Carroll, C. Shippy, D. Tipton, M. Wright, and K. Renfrow in the Engineering group. The authors wish to convey their sincere appreciation to M. Krishnan and his colleagues, R. Schneider and J. Hilton at Physics International of San Leandro, California, for their direction of the PITHON irradiation facility and to the Defense Nuclear Agency for sponsorship of the irradiation time.

¹B. Pontecorvo and A. Lazard, *C. R. Acad. Sci.* **208**, 99 (1939).

²G. B. Collins, B. Waldman, E. M. Stubblefield, and M. Goldhaber, *Phys. Rev.* **55**, 507 (1939).

³G. Harbottle, *Nucleonics* **12**, 64 (1954).

⁴N. Ikeda and K. Yoshihara, *Radioisotopes* **7**, 11 (1958).

⁵A. Veres, *Int. J. Appl. Radiat. Isot.* **14**, 123 (1963).

⁶B. T. Chertok and E. C. Booth, *Nucl. Phys.* **66**, 230 (1965).

⁷E. C. Booth and J. Brownson, *Nucl. Phys.* **A98**, 529 (1967).

⁸M. Boivin, Y. Cauchois, and Y. Heno, *Nucl. Phys.* **A137**, 520 (1969).

⁹L. Lakosi, M. Csuros, and A. Veres, *Nucl. Instrum. Methods* **114**, 13 (1974).

¹⁰Y. Watanabe and T. Mukoyama, *Bull. Inst. Chem. Res.* **57**, 72 (1979).

¹¹A. Ljubicic, K. Pisk, and B. A. Logan, *Phys. Rev. C* **23**, 2238 (1981).

¹²K. Yoshihara, Zs. Nemeth, L. Lakosi, I. Pavlicek, and A. Veres, *Phys. Rev. C* **33**, 728 (1986).

¹³J. A. Anderson and C. B. Collins, *Rev. Sci. Instrum.* **59**, 414 (1988).

¹⁴*Evaluated Nuclear Structure Data File* (Brookhaven National Laboratory, Upton, New York, 1986).

¹⁵In the units usually employed the integrated cross section $\pi b_0 b_0 \Gamma \sigma_0 / 2$ for the 941 keV level is computed from Ref. 14 to be $0.72 \times 10^{-29} \text{ cm}^2 \text{ keV}$.

¹⁶J. A. Anderson and C. B. Collins, *Rev. Sci. Instrum.* **58**, 2157 (1987).

Flash x-ray source excited by stacked Blumlein generators

F. Davanloo, J. J. Coogan, T. S. Bowen, R. K. Krause, and C. B. Collins

University of Texas at Dallas, Center for Quantum Electronics, P.O. Box 830688, Richardson, Texas 75083-0688

(Received 30 December 1987; accepted for publication 16 June 1988)

Eight triaxial Blumleins have been stacked in series at one end while being synchronously commuted at the other end with a single hydrogen thyratron. Significant voltage gain has been maintained in the stack for periods of the order of 20 ns. Having no other switching elements, operation has been possible at repetition rates to 100 Hz. An x-ray diode has been matched to this pulse power source, making possible the emission of an average bremsstrahlung dose of 5.8 R/s from a sequence of 20-ns pulses. In less than 4 min of operation at 100 Hz, a dose of 1 kR could have been delivered to a target sample. When operated at 50-kV charging voltage, spectral measurements show the output to be a true continuum, peaking at intensities in excess of 2×10^4 keV/keV/shot and containing useful intensities of photons having energies of 150 keV.

INTRODUCTION

Recently we described¹⁻³ a flash x-ray source producing intense nanosecond pulses at high repetition rates. The principal innovation lay in the development of an x-ray diode of such low geometric profile that it could be matched to Blumlein pulsers having impedances as low as 1Ω . Output pulses were found to have durations comparable to the transit times of the lines and the combination of pulse duration and line impedance represented entry into a new region of parameter space.⁴

Despite the successes of these x-ray sources, one aspect differed little from devices we had developed earlier for short pulse nitrogen ion⁵ and XeF lasers.⁶ Each was driven by a Blumlein charged by a resonantly pulse charged power supply, and each line was tightly coupled to a diode load adapted to the application.² Commutation was effected by a fast, low inductance thyratron; ringing periods of the order of 100 ns could be realized in the switching cycle. Operating parameters were most strongly constrained by the limitations on peak currents and the voltage tolerances of existing commercial thyratrons. At present the limits are 20 kA and 150 kV, respectively.

Reported is a next step in scaling such impulsive devices to potentials greatly exceeding 100 kV, while retaining the capabilities for operation at high repetition rates. The example we describe is a pulsed x-ray generator, driven by stacked Blumleins that could be charged in parallel at the opposite end and commuted with a single thyratron. The output diode was matched to the series stack so that the endpoint energy of the bremsstrahlung approached the sum of the voltages launched on each individual line. No output switches were needed and x-ray pulse durations were comparable to the transit time of the lines. The only breakdown device was the single thyratron providing the primary commutation. In these aspects, the device we report offers some synthesis of individual advantages optimized in prior efforts.

Pulse-forming lines have long been used in the production of high power electron beams in accelerators and e-beam discharges.⁷⁻¹⁰ Their specific function is to provide impedance transformation between a power source and a diode

load. To do this they must generally be isolated, with fast-closing switches at one or both ends. These lines commonly consist of coaxial or triaxial Blumleins, with dielectrics composed of water, oil, mylar, or a combination of these. In the archetype pulse power system, they are generally not required to provide voltage multiplication as well.

If very high voltages are required, Marx generators with several spark gaps are often used to charge the pulse-forming lines. Examples are found in accelerators and large e-beam machines. It has been reported that the number of spark gaps can be reduced somewhat by using a high-voltage transformer pulsed from a capacitor bank.⁷ In either case, inputs to the lines typically consist of voltage pulses of the order of several megavolts from impedances high enough to require durations of 0.1–1.0 μ s for charging.

In attempts to combine the functions of voltage multiplication and impedance transformation, Blumlein pulse-forming networks constructed from capacitors and inductors have been used; in this case the lines themselves have successfully multiplied the charging voltages. Ivers *et al.*⁸ designed a pulse generator that utilized seven artificial Blumlein pulse-forming networks which were charged in parallel by a 30- to 50-kV power supply and discharged in a series configuration, avoiding conventional high-voltage Marx generators as a power source. However, the use of this type of artificial Blumlein led to triggering problems. Short commutation time between the load and trigger circuit prevented operation with a single switch. As a consequence Marx triggering columns had to be used, which inevitably limited repetition rates by reintroducing the Marx concept.

In this work, an array of eight triaxial Blumleins were successfully stacked to add voltage pulses for tens of nanoseconds in a configuration that could be switched with a single hydrogen thyratron without impedance transformation. Operation of a prototype device produced discharge voltages to 200 kV in an x-ray diode at peak currents of 0.5 kA for a 60-kV charging voltage. At 100 Hz an average x-ray dose of 5.8 R/s was obtained from x-ray pulses of 20-ns duration each. Developed here to excite nuclear fluorescence for the study of (γ, γ') reactions, the ultimate signal-to-noise ratio will depend only upon the total radiation that can be delivered.

ered to an extended absorber in a working period. This laboratory-scaled alternative to either synchrotron radiation or to bremsstrahlung from large e-beam machines may be useful in a more general class of experiments that require access to an extended source of radiation with wavelengths below 0.1 Å.

I. DEVICE DESIGN AND CONSTRUCTION

Here we describe a prototype device consisting of three basic sections that comprised a pulse-forming system, which was then matched to a diode load. The essential sections of the pulse-forming system were (i) the commutation assembly, (ii) the transmission lines, and (iii) the pulse stacking module. When integrated, the system with load extended over a nominal length of 4 m. This basic organization is shown schematically in Fig. 1. It was immersed in a closely fitting pan filled with transformer oil. The outer surface of the diode load was sealed with a gasket into the wall of the pan, so that the output could emerge without passage through the insulating oil.

The commutation assembly is shown in Fig. 2. As usual, the thyratrons provided the impulsive connection of two massive copper plates constructed from 3.2-mm stock with rounded edges. Their purpose was to distribute the switching current to each of the Blumleins in a manner designed to avoid both transit time inequalities and path constrictions, which could bias the distribution. As shown in Fig. 2, the plates were separated by layered Kapton dielectrics and were connected to the Blumleins with a closely lapped joint.

Both plates and dielectric were pierced to permit insertion of a thyratron. Edges of the lower plate were insulated by fingerlike extensions of the Kapton dielectric layer. Connection from the lower plate to the anode well of the thyratron was accomplished with one of several low inductance cans, each designed for a different one of three possible thyratrons.

Details of the construction of the Blumleins are seen in Fig. 2. The eight individual Blumleins consisted of top and bottom (switching and storage) copper plates 3.8 cm in width. The center high-voltage plates were similar, but only 2.5-cm wide to reduce field stresses at the edges and to increase dielectric lifetimes. All lines were made of 3.2-mm-thick copper and were 3.1-m long with rounded edges.

A laminated Kapton (polyimide) dielectric consisting of thirteen 0.127-mm-thick layers separated the plates. These insulators were manufactured using an in-house la-

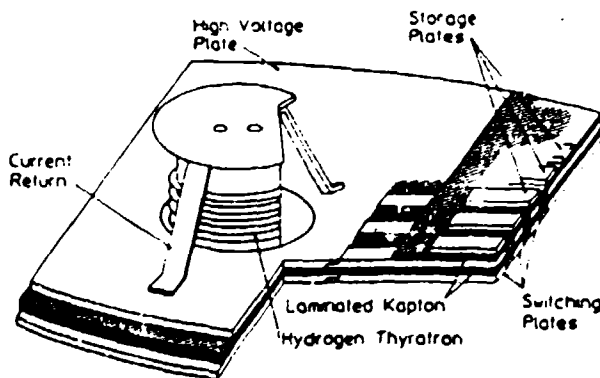


FIG. 2. Layered configuration of the thyratron assembly is presented in a cutaway scheme. The lap joints of the lines to the thyratron plates are shown. The shaded portion of the figure consists of laminated Kapton film.

mination process. Alternate layers of Kapton and high dielectric epoxy were pulled through a press consisting of heavy steel rollers. The finished sheet had an average thickness of 2.3 mm, giving a line impedance of 26Ω .

The plates and the Kapton were lapped to "plug in" at both the thyratron and series ends, as seen in Fig. 3. These plates were completely sheathed in dielectric. In addition to the layer between the plates, 3.2-mm-thick Lexan (polycarbonate) sheets enclosed the copper on the sides; the Kapton walls were placed between each line to prevent interline flashover.

The Blumleins were switched from parallel to series with the rather complex structure shown in Fig. 4. The conductive lines were lapped to lengths of copper foil cut into curves in the plane of the foil so that the conductors from successive lines could be displaced toward the center, where they would lie one above the other. Dielectric sheets were curved along the same lines to isolate the foils and to try to maintain a reasonably constant transmission line impedance of each Blumlein section being stacked. The resulting series section at the head of the lines was then cast to minimize corona. Figure 4 depicts this in a cutaway view.

Also incorporated into the pulse stacking module were a current transformer and an anode cooling system. Accommodations were made for a water-resistor voltage divider, as well. The top and bottom foils leading to the electrodes were conveyed through high-temperature ceramic directly set into the cast material that formed the base wall of the diode load specific to the particular application.

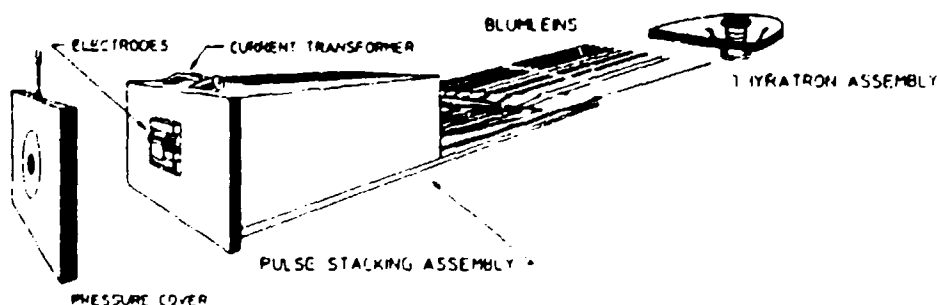


FIG. 1. Schematic drawing of the flash x-ray device

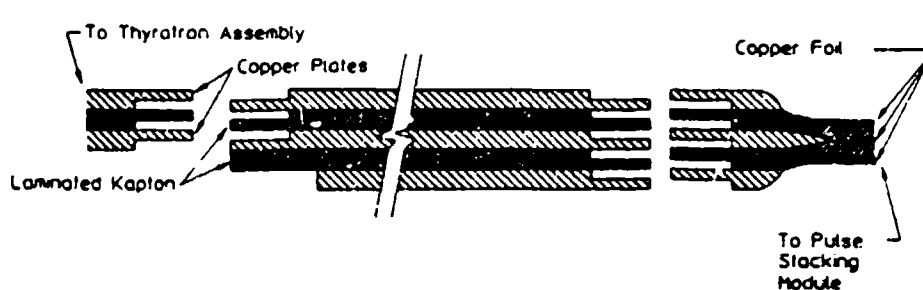


FIG. 3. Side view of each transmission line connecting the commutation assembly and the pulse stacking module.

It is well known that the line and continuous x-ray emission intensities are angularly distributed with respect to incident electron direction. The bremsstrahlung becomes more peaked in forward directions as the incident electron energy increases.¹⁰ Thus in the high-voltage pulsing of x-ray diodes, the most energetic photons of the continuum of x rays are observed in the direction of the discharge electrons.

In this work, the load matched to the voltage-multiplying lines was an x-ray diode configured with two different electrode assemblies, as shown in Fig. 5. In the high-voltage configuration, electrodes were connected to the foils emerging from the base wall from the series part of the lines. A 2.5-cm-wide graphite blade of 0.38-mm thickness was connected to the cathode foil, while the anode foil emerged from the ceramic inset in the wall to connect to an assembly for interchanging anodes. The useful part of the x-rays emerged from the output window in the direction of the incident electron beams colliding with the anode foil. The spacing between the anode and cathode was adjusted by varying the ceramic shim under the anode. An alternative electrode assembly similar to the one described in earlier works¹⁻³ is shown in Fig. 5. This configuration was used in the low-voltage operation of the device and useful x rays were observed from an output window perpendicular to the direction of the discharge electrons.

A vacuum cover was sealed to the particular head being used by an O-ring. The pressure cover was machined out of

Delrin plastic and the completed diode could be routinely evacuated to pressures below 5μ . An output window made of layered Kapton and graphite was placed directly in front of discharge area, as seen in Fig. 1. In operation, all components except for the pressure cover with an output window were immersed in transformer oil.

II. OPERATION AND PERFORMANCE

In operation, the Blumleins were resonantly pulse charged with a source capable of bringing the 16-nF total capacitance of the system to a selected voltage in the range of 3-75 kV in 100 μ s.¹¹ The middle conductors were charged to a positive high voltage. For the performances described here, commutation was effected by a three-stage EG&G 5353 hydrogen thyratron mounted in a grounded cathode configuration.

Both the voltages launched on individual lines and the voltage pulse appearing across the series stack at the head were measured with tapped water resistors, as shown in Fig. 5. They were connected to a Tektronix 7912AD transient digitizer. A comparison of pulses launched and received at the stack for both open and loaded circuits is shown in Fig. 6. As can be seen, the output voltage into a matched load approached four times the charging voltage of each line.

The temporal evolution of the x-ray output from the diode is shown in Fig. 7, together with the time dependence

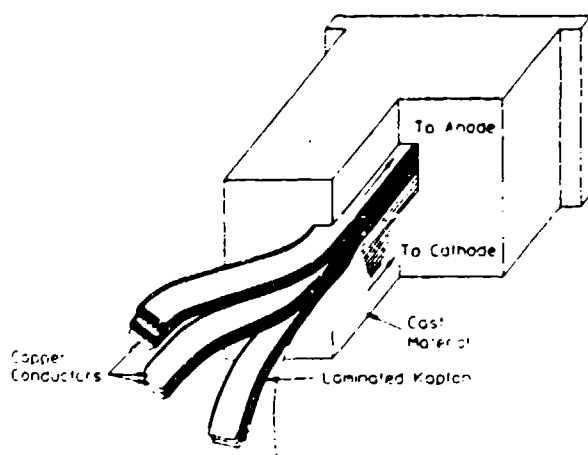


FIG. 4. Three full sets out of a total of eight Blumleins are shown as they are stacked in series when entering the casting material at the base of the x-ray diode. The top set shows the layering of the conductor and dielectric components. The laminated Kapton layers have been shaded for clarity.

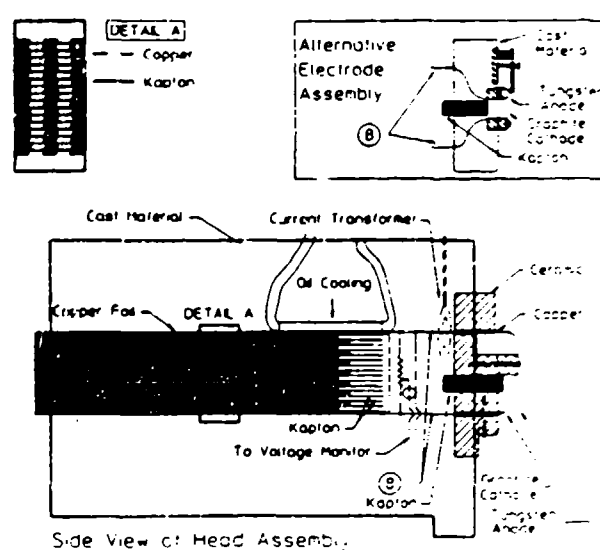


FIG. 5. Schematic drawing of a cross section of the pulse stacking module. An alternative electrode assembly for low-voltage pulsing is shown.

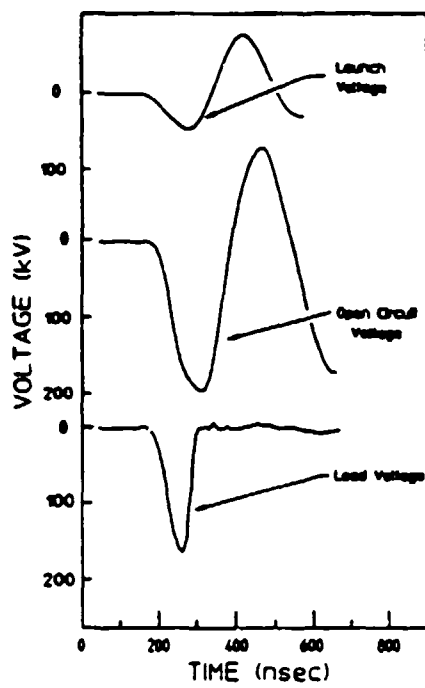


FIG. 6. Voltages measured across the individual lines and across the series stack with and without load as a function of time. The top pulse is typical of the voltage launched down each line by commuting the thyratrons. These particular data correspond to a charging voltage of 50 kV.

of the voltage and current at the diode. For this measurement, the x rays were detected with a PIN diode directly coupled to the Tektronix 7912A.D. Electrical performance was recorded with the integral diagnostics described above.

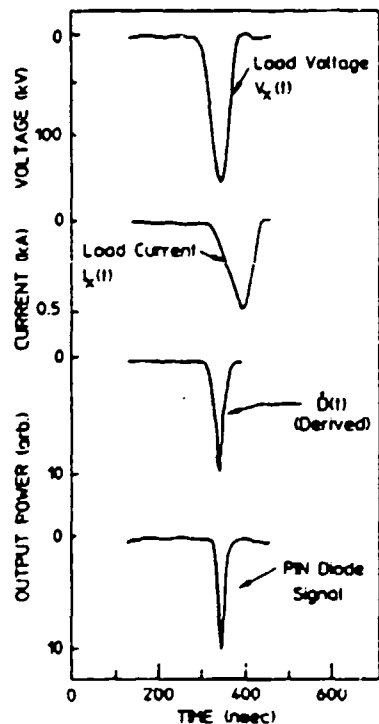


FIG. 7. Typical relationship between the load voltage, load current, and x-ray output emitted from the tungsten anode. These particular data correspond to a charging voltage of 60 kV. The derived x-ray output was obtained from the data as described in the text.

Synchronization was readily maintained between records of voltages and PIN diode signals, but the current monitor required a different grounding arrangement, which disturbed the triggering. The relative phase of the current pulse on the time scale of Fig. 6 had to be determined from the relationship² between instantaneous power and the corresponding time derivative of the x-ray dose, \dot{D} :

$$\dot{D}(t) = K_c I(t) V^2(t) + K_L I(t) [V(t) - V_K]^{1/2}, \quad (1)$$

where $I(t)$ and $V(t)$ denote the instantaneous values of current and voltage at the x-ray diode, respectively, and V_K is the potential of the K edge for the material of the anode. The first term of Eq. (1) describes the energy emitted as bremsstrahlung continuum, while the second describes emission of the characteristic lines of the anode. The constants K_c and K_L denote the relative efficiencies for the emission of continuum and line radiation, respectively.

For the purposes of synchronizing $I(t)$ with $V(t)$ it was assumed that

$$K_c = 2.1 K_L, \quad (2)$$

in general agreement with previous results. Then Eq. (1) was evaluated for values of load voltage $V(t)$ input from Fig. 7 and for $I(t + \tau)$, where $I(t)$ was taken from the raw data and τ was an adjustable phase shift. Shown in Fig. 7 is the $\dot{D}(t)$ computed for the particular value of τ , giving the current waveform plotted for comparison; this $\dot{D}(t)$ represented the best agreement that could be obtained by this procedure. It seems to be reasonably phased with the voltage waveform since appreciable amounts of current are seen to start at the time $V(t)$ begins to break from the form of the open circuit ringing.

The x-ray spectra emitted by this device were sampled with an imaging system formed with a pinhole. The output window was heavily masked with lead collimators and the detector was similarly masked to admit only the image of the open aperture at the source. In this way the contribution from spurious Compton scattering was minimized. A test for the magnitude of the remaining Compton intensity not originating in the source itself was conducted by blocking only the open aperture at the source. No counts were detected on the scale used for the presentation of the spectra.

The detector used to observe the image of the source aperture was a NaI(Tl) crystal mounted to a photomultiplier whose output was connected to an ORTEC preamplifier/amplifier combination servicing a multichannel analyzer. By adjusting the size of the imaging pinhole, the intensity at the scintillator was reduced to the point at which one photoelectron was counted by the electronics on the average of every three discharges. In this way pulse pileup was avoided. These data comprised a pulse-height spectrum that reasonably approximated the desired spectrum of intensity as a function of photon energy. Radioactive sources emitting lines at convenient energies were used to calibrate the relationship between photon energy and detected pulse height. Since the deviation from simple proportionality was less than 4% over the range of energies of interest, a linear relationship was used in the final analysis of the spectral data.

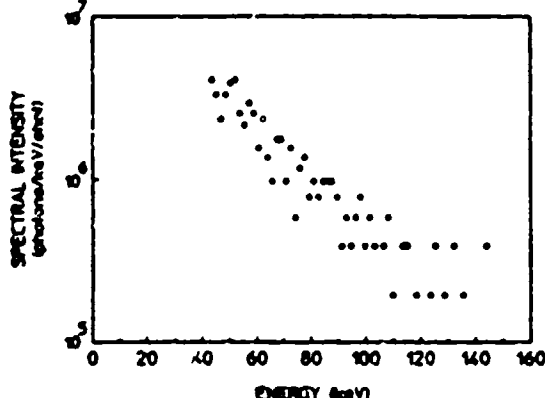


FIG. 8. Typical spectral distribution of flux emitted from the tungsten anode at a charging voltage of 50 kV.

The spectrum of the counting rate detected at each photon energy was multiplied by the ratio of $2\pi/\Omega$, where Ω was the measured solid angle of the pinhole. The resulting spectrum is shown in Fig. 8. Data at lower energies than those shown were rendered uncertain by levels of Compton scattering in the detector and thus were not plotted. Errors in the intensities accrued primarily from statistical uncertainties in the numbers of photons n collected in each of the discrete windows in photon energies. A reasonable expectation is that the statistical error in intensity is \sqrt{n} . This can be estimated in Fig. 8 from the identification of the lowest intensity, with the accumulation of a single photon in the corresponding window in energy. Experimentally, this uncertainty is seen in the scatter of the data in Fig. 8.

With this first prototype device, x-ray pulse energies were found to remain largely constant as the pulse repetition rate was varied over the range of 1–100 Hz. Figure 9 shows this to be reflected in the measured values of average dose output in the x-ray pulses of 20-ns duration emitted from a tungsten anode.

Average x-ray powers at 100 Hz resulting from the operation of this device with a charging voltage of 50 kV showed that in less than 4 min, a dose of 1 kR could be delivered to a target sample. This would exceed the dose available in the bremsstrahlung from a shot of a large laser plasma or small e-beam machine.

ACKNOWLEDGMENTS

We wish to express our sincere appreciation to Dr. John McCoy and Jennifer Young for their splendid efforts in data

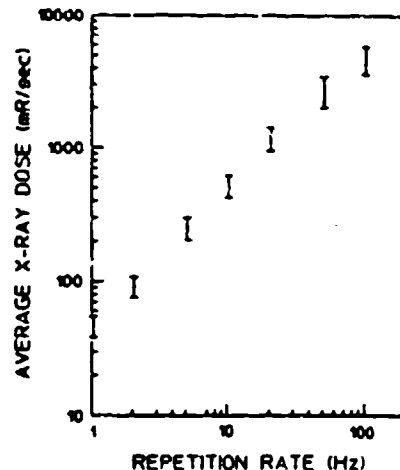


FIG. 9. Average dose outputs emitted as x-rays near 1 Å as a function of the pulse repetition rates for a charge voltage of 50 kV.

processing and to Dr. Jon Anderson for his loan of the detector, together with invaluable advice. This work was supported by the Innovative Science and Technology Directorate of the Strategic Defense Initiative Organization and directed by the Naval Research Laboratory.

- ¹C. B. Collins, F. Davanloo, and T. S. Bowen, *Rev. Sci. Instrum.* **57**, 563 (1986).
- ²F. Davanloo, T. S. Bowen, and C. B. Collins, *Rev. Sci. Instrum.* **58**, 2163 (1987).
- ³F. Davanloo, T. S. Bowen, and C. B. Collins, in *Advances in Laser Science I*, edited by W. C. Swalley and M. Lapp (AIP Conference Proceedings No. 146, New York, 1986), pp. 60–61.
- ⁴P. Krehl, *SPIE Rev.* **689**, 26 (1986).
- ⁵C. B. Collins, *IEEE J. Quantum Electron.* **QE-20**, 47 (1984).
- ⁶R. Sadighi-Bonabi, F. W. Lee, and C. B. Collins, *J. Appl. Phys.* **53**, 375 (1982).
- ⁷J. R. Smith, R. F. Schneider, M. J. Rhee, H. S. Uhm, and W. Nankung, *J. Appl. Phys.* **60**, 4119 (1986).
- ⁸M. T. Buttrom and G. J. Rohwein, *IEEE Trans. Electron Devices* **ED-26**, 1503 (1979).
- ⁹J. D. Ivers and J. A. Nation, *Rev. Sci. Instrum.* **54**, 1509 (1983).
- ¹⁰E. C. Booth and J. Brownson, *Nucl. Phys.* **A98**, 529 (1967).
- ¹¹F. Davanloo, T. S. Bowen, J. J. Coogan, and C. B. Collins, in *Central Quantum Electronics Report No. GRL/8602*, University of Texas at Dallas, Dallas, 1987, pp. 47–70.

Activation of $^{111}\text{Cd}^m$ by single pulses of intense bremsstrahlung

J. A. Anderson, M. J. Byrd, and C. B. Collins

University of Texas at Dallas, Center for Quantum Electronics, Richardson, Texas 75083

(Received 9 August 1988)

Described here is the use of a calibrated bremsstrahlung source to resolve conflicts in previous studies of the reaction $^{111}\text{Cd}(\gamma, \gamma')^{111}\text{Cd}^m$ through a level located near 1200 keV. We report an integrated cross section of $(9.8 \pm 2.5) \times 10^{-29} \text{ cm}^2 \text{ keV}$ with no evidence of any importance of non-resonant channels of excitation.

I. INTRODUCTION

Fifty years ago it was first reported¹ that (γ, γ') reactions could produce isomeric nuclei. It is interesting to note that even after such an advance of technology as has occurred over the intervening time, attempts at quantitative measurements still do not converge. For example, the most recent three measurements of the integrated cross sections for the reaction $^{111}\text{Cd}(\gamma, \gamma')^{111}\text{Cd}^m$ were conducted in 1979, 1982, and 1987 with results of 35, 5.8, and 14, as reported in Refs. 2–4, respectively, in the usual units of $10^{-29} \text{ cm}^2 \text{ keV}$. Probable errors were quoted as varying only from 7 to 14% and, yet, no two of the measurements were even within a factor of 2 of each other.

The $^{111}\text{Cd}^m$ isomer at 396 keV has a 48.6 min half-life and is readily detected by observing the 150.6 and 245.4 keV gammas radiated in the cascade from the isomer.^{5,6} Experimentally this is an almost ideal vehicle for the study of (γ, γ') reactions since the lifetime of the isomer is long enough to collect a substantial dose from any one of a variety of excitation sources during the activation cycle and short enough to count with reasonable signal-to-background ratio afterward.^{7,8} Experiments appear to have been carefully executed^{2–4} and the drastic disagreement in the results has been attributed³ to the controversial⁴ proposal that some mechanism of nonresonant nuclear absorption dominates the excitation step. However, the data that support this intriguing proposal³ and the data that seem to refute⁴ it agree only in indicating that the (γ, γ') reaction producing $^{111}\text{Cd}^m$ is not well understood.^{2–4,9–12}

The relevant part of the energy level diagram⁵ of ^{111}Cd is shown in Fig. 1. All of the adopted levels⁵ between 1000 and 1500 keV are shown together with the gamma transitions that have been observed⁶ in reactions other than (γ, γ') . Additional transitions to the 1190 and 1330 keV levels have been inferred^{9,10} from (γ, γ') studies, but those reports depend upon the validity of arguments which do not support all of the data. Moreover, even the existence of the 1330 keV level might reasonably be questioned, since it is based upon a single report¹³ of a reaction not dependent upon the interpretations of (γ, γ') data.

For levels in Fig. 1 which might be excited by photons with energies in the range 1000 to 1500 keV, there are a

number of possible cascades to the $\frac{11}{2}^-$ isomer through levels below 1000 keV which are not shown. However, no particular path has been proposed.

It has been recently argued⁷ that the principal cause of such a large degree of variance among previous measurements of isomeric excitation has been the generally inadequate level of characterization of the spectrum of the pump source. In a previous paper⁸ we showed that the spectrum from a pulsed source of intense bremsstrahlung could be determined to a level of accuracy sufficient for quantitative description by the reactions $^{77}\text{Se}(\gamma, \gamma')^{77}\text{Se}^m$ and $^{79}\text{Br}(\gamma, \gamma')^{79}\text{Br}^m$.

Subsequently we reexamined¹⁴ the reaction $^{115}\text{In}(\gamma, \gamma')^{115}\text{In}^m$ with the same pulsed bremsstrahlung source used for the reconciliation of the absorption cross sections to $^{79}\text{Br}^m$ and $^{77}\text{Se}^m$. For ^{115}In , the quantitative value for the integrated cross section we found was in good agreement with the other value reported most recently as the result of excitation with a radioactive source.¹⁵ Reported here is an extension of this technique to the reaction $^{111}\text{Cd}(\gamma, \gamma')^{111}\text{Cd}^m$. We find an integrated cross section of $(9.8 \pm 2.5) \times 10^{-29} \text{ cm}^2 \text{ keV}$ for reaction through a gateway level near 1200 keV.

II. METHODS AND APPARATUS

As usually reported⁷ the integrated cross section for a (γ, γ') reaction yielding an isomeric product state is $\pi b_o b_n \Gamma \sigma_0 / 2$, where Γ is the natural width in keV of the pump band, where the branching ratios b_o and b_n give the probabilities for the decay of the gateway level back into the initial and isomeric level, respectively, and σ_0 is the maximum of the Breit-Wigner cross section for the absorption transition.¹⁴ Unlike our previous study¹⁴ of ^{115}In from which this present work has been extended, none of the elementary nuclear properties entering into the computation of the integrated cross section were known for ^{111}Cd . Although it is uniformly assumed^{2–4,9–12} that the dominant gateway level lies at 1330 keV, this is not strongly supported by prior data. Early experiments^{9,10,16,17} using bremsstrahlung from accelerators with variable end point energies indicated that the reaction turns on between 1200 and 1400 keV. However, the apparent sharpness seen in some early data at 1330 keV is strongly affected by the logarithmic presentation of a linear threshold and the sensitivity of the in-

strumentation to low levels of activation. In more recent experiments using ^{60}Co sources, the high level of activation produced and the proximity of the 1330 keV level of ^{111}Cd to the strong 1332 keV line of ^{60}Co made it attractive to identify the (γ, γ') reaction as occurring through the 1330 keV level of undetermined symmetry. Since the experiments reported here were conducted with an accelerator producing a known⁸ bremsstrahlung spectrum it was decided to try to determine experimentally the energy of the gateway needed, as well as the integrated cross section.

In a previous report^{7,8} it was shown that the uncertainty in the absolute value of the geometric coefficient coupling the source of pump radiation to the absorbing target could be eliminated by normalizing both the pump

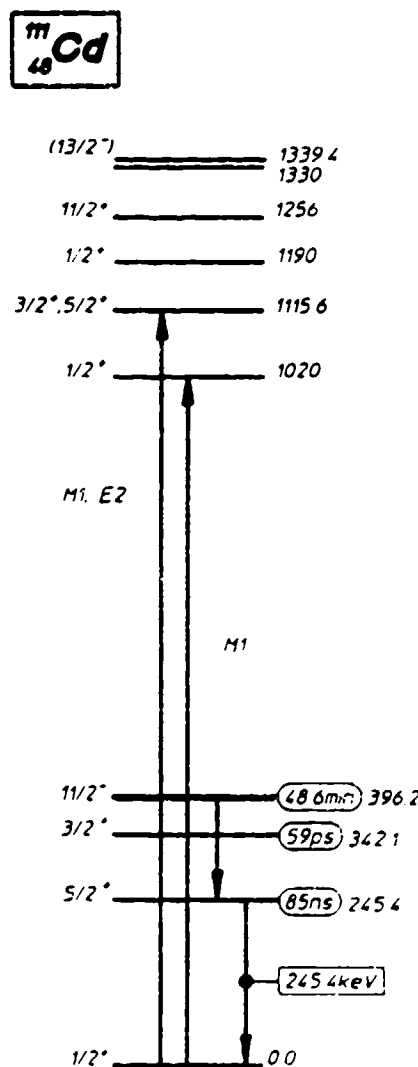


FIG. 1. Energy level diagram of the excited states of ^{113}Cd between 1000 and 1500 keV which may be important in the production of the 48.6 m isomer as reported in Ref. 5. Also shown are all excited states below 400 keV. Half-lives of the states are shown to the right of each state and known (Ref. 6) gamma transitions are shown by the arrows. Populations of the 48.6 m isomer are most conveniently detected by the 245.4 keV fluorescent transition as indicated.

fluence and the fluorescence counts to some standard material having a monochroimatic excitation spectrum. The reaction $^{79}\text{Br}(\gamma, \gamma')^{79}\text{Br}^m$ was found to be an ideal standard, having a single pump level at 761 keV, an integrated cross section of $6.2 \times 10^{-29} \text{ cm}^2 \text{ keV}$, and a convenient radioactivity in the isomer.

Following the formalism reported earlier,⁸ the number of $^{111}\text{Cd}^m$ nuclei, $S(\text{Cd})$, which could be excited through a single gateway state at an energy E by a flash of intense bremsstrahlung can be conveniently expressed as a ratio,

$$\frac{S(Cd)}{S(Br)} = \frac{N(Cd)}{N(Br)} \frac{\xi_E(Cd)}{\xi_{76}(Br)} \xi(E), \quad (1)$$

where $S(x)$ and $N(x)$ are the number of nuclei produced and the number of target nuclei of material x , respectively; $\xi(E)$ is the ratio of pumping intensity at the gateway energy E in keV to the intensity at 761 keV and the $\xi_E(x)$ are the combinations of nuclear parameters involved in the excitation.

$$\xi_E(x) = \frac{(\pi b_0 b_0 \Gamma \sigma_0 / 2)_E}{E} . \quad (2)$$

The collection of terms in parentheses in Eq. (2) comprises the integrated cross section for excitation as usually reported, and the calibration value for ^{79}Br is $\xi_{761}(\text{Br}) = 8.2 \times 10^{-12} \text{ cm}^2$. Still more convenient for analysis is the weighted activation ratio, R , obtained by multiplying Eq. (1) by the ratio of the number of target nuclei.

$$R = \frac{N(\text{Br})S(\text{Cd})}{N(\text{Cd})S(\text{Br})} = \frac{\xi_E(\text{Cd})}{\xi_{\text{Br}}(\text{Br})} \xi(E) . \quad (3)$$

The source of excitation in these experiments⁸ was the bremsstrahlung produced by the DNA/PITHON nuclear simulator at Physics International. The deliberate perturbation of the firing parameters provided for a sequence of irradiations with end point energies varying from 1.3 to 1.54 MeV.

Intensities at the target were determined by measuring the nuclear activation of the ^{79}Br component of a sample of LiBr containing isotopes in natural abundance. The ^{111}Cd sample under study occurred in natural isotopic abundance in a thin Cd foil taped to a fiduciary mark near the pneumatic system used to convey the LiBr calibrator to a counting system. Since the $^{111}\text{Cd}^{m}$ had a substantially longer half-life than the calibrating Br, it could be manually detached after exposure and transferred to the spectrometer which consisted of an intrinsic germanium detector with associated electronics. In typical cases a counting time of 1 h gave better than 5% statistical accuracy in the area of the $^{111}\text{Cd}^{m}$ peak. In the course of this experimental series, six shots were obtained for sufficiently high end-point energies to yield statistically significant numbers of fluorescent isomeric activity.

To confirm that the fluorescence being detected resulted only from decay of the $^{111}\text{Cd}^m$ activity, the spectra from irradiated foils were first examined for traces of interference from the 238 keV line from ^{212}Pb contaminating the counting environment. The clear separation of the 238 keV line from the 245 keV line obtained from

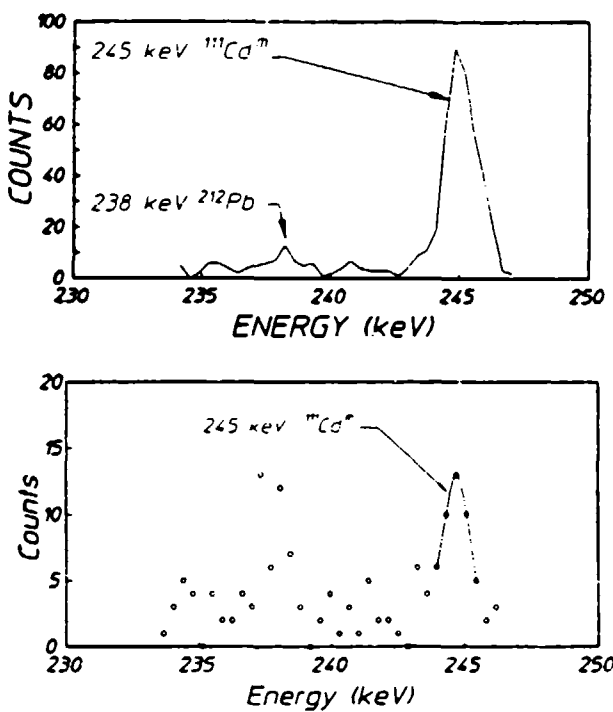


FIG. 2. Spectra showing the 245 keV line from the decay of $^{111}\text{Cd}^m$. The spectra were obtained from an 8.02 gm, natural Cd foil sample. The small peak near 238 keV is due to the decay of naturally occurring ^{212}Pb in the counting environment. (a) Fluorescence from $^{111}\text{Cd}^m$ following irradiation with a single bremsstrahlung pulse having an end point energy of 1.4 MeV. Counting time was 3600 sec. (b) Fluorescence following excitation with an end point of 1.3 MeV; counting time was 2700 sec.

$^{111}\text{Cd}^m$ following irradiation with a 1.4 MeV end point bremsstrahlung pulse is shown in Fig. 2(a). At an end point energy of 1.3 MeV, where the spectral intensity at the 1330 level in $^{111}\text{Cd}^m$ should have been negligible, the 245 keV line is weak but clearly observable, as shown in Fig. 2(b).

In order to determine an experimental value of the $\xi_E(\text{Cd})$ by fitting Eq. (3) to measurements of the fluorescence yields from the sample and from the LiBr calibrator, the relative bremsstrahlung intensity, $\zeta(E)$, emitted

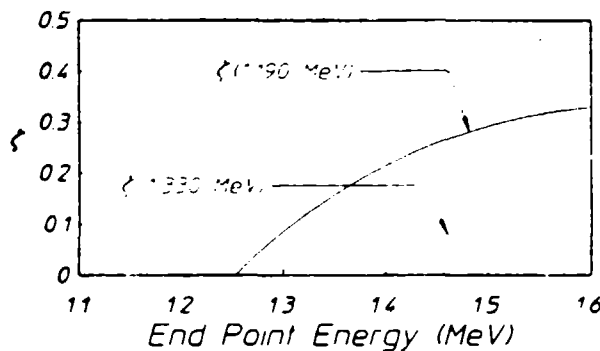


FIG. 3. Plots showing the ratio of the spectral density at energy E normalized to the spectral density at the 761 keV gateway of $^{79}\text{Br}^m$ for varying end-point energies. The solid and dotted lines show the ratio for energies $E = 1.190$ and 1.330 MeV.

at E must be known. For these experiments, these data were obtained by numerically fitting theoretical computations of bremsstrahlung spectra. As reported previously,⁸ confidence was established by examining quantitatively the number of fluorescent nuclei produced by successive irradiations of samples of ^{79}Br and ^{77}Se at a variety of end-point energies. The relative bremsstrahlung intensity emitted at a particular energy was found to be a strong function of the end-point energy of the accelerator; two examples are shown in Fig. 3.

III. RESULTS

Because of a small physical displacement of the ^{111}Cd sample from the mixed $^{79}\text{Br}/^{77}\text{Se}$ target providing calibration, the observed number of fluorescent photons counted had to be corrected for the different source intensities. This was done by mounting thermoluminescent dosimeters (TLD's) at both positions and then comparing the total dose recorded at the different points for each shot.¹⁴ The number of photons from $^{111}\text{Cd}^m$ was scaled by the value of relative dose received at the ^{111}Cd and at the calibrating positions.

The cadmium sample was optically thin (0.5–0.7 gm/cm²) at both the 150 and 245 keV fluorescence energies, requiring relatively small factors of 1.645 and 1.222 for the self-absorption correction. Data were corrected for fluorescence and detector efficiencies, as well as for variations in measurement time. Fluorescent counts from each line were used to calculate the total number of nuclei pumped for each exposure. Good agreement was

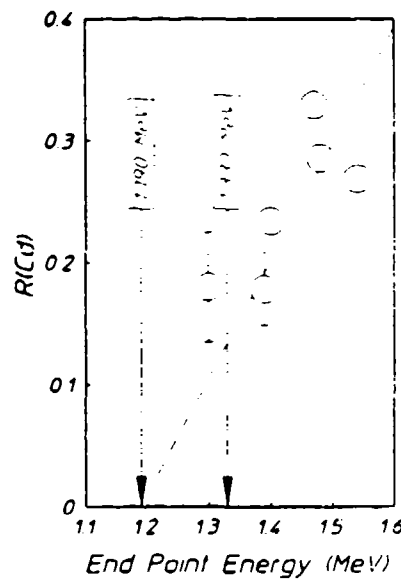


FIG. 4. Ratios of isomeric fractions produced in $^{111}\text{Cd}^m$ to those in $^{79}\text{Br}^m$, as corrected for the finite duration of the counting interval and plotted as a function of the end-point energy of the bremsstrahlung. Error bars show the counting statistical uncertainty. The dashed line shows a linear fit to the data intercepting the x axis at a gateway energy of 1.19 MeV. Excitation energy of the next higher gateway is shown at 1.33 MeV. In this figure and in Fig. 5, the error bars for the two least precise points have been shown. The statistical errors for the other points are commensurate with the plotting symbols in the figures.

found and the weighted average was taken to reduce statistical error. The resulting values of weighted activation ratio, R , from Eq. (3) are shown in Fig. 4.

The linear form of the dependence of the relative yield of fluorescence from the cadmium isomers seen in Fig. 4 between 1.1 and 1.6 MeV is a strong indication of the dominance of a single channel of excitation through a gateway level lying at an energy given by the value of the x intercept. While uncertainties in the actual endpoint energy of the electrons could be as great as ± 100 keV, the agreement between the intercept obtained in a similar experiment¹⁴ for the activation of ^{113}In and the known energy of the predominant gateway at 1078 keV support the values given for end points in this energy range.

From the data of Fig. 4 it is seen that the intercept lies near 1200 keV, in agreement with the known $\frac{1}{2}^+$ state at 1190 keV. Also shown in Fig. 4 is the energy of the next higher gateway state having an acceptable J^π , the poorly characterized level at 1330 keV. It is interesting to observe that for end-point energies above this value there seems to be no clear tendency of the data to depart from the simple linear fit because of the availability of this additional gateway. A greater number of measurements at successively higher end-point energies would be needed to confirm this indication that the 1330 keV level has no particular role in the excitation of ^{111}Cd .

Once most of the data are established as being consistent with the model of excitation through a single level at 1190 keV, Eq. (3) provides a means of determining the absolute cross section for the excitation. In Fig. 5(a) data for the measured values on the left side of Eq. (3) are

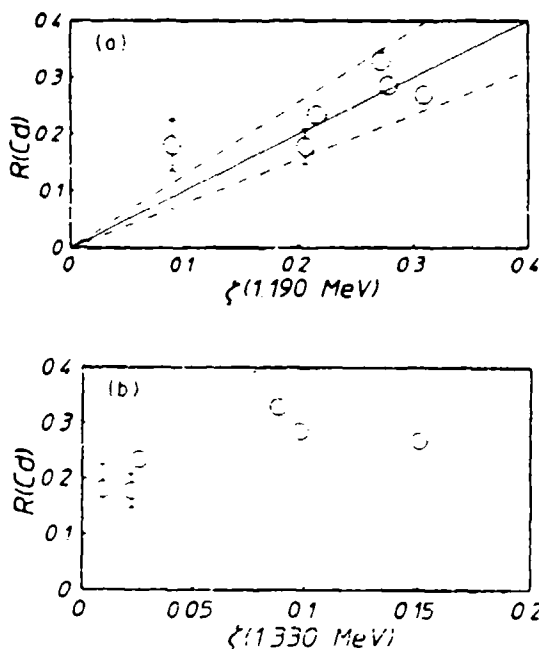


FIG. 5. Plots of the weighted activation ratio $R(\text{Cd})$ as a function of the spectral intensity at energy E normalized to the intensity at the 761 keV gateway in ^{75}Br . (a) Plot for $E = 1190 \text{ keV}$. The heavy line shows the least squares fit through the origin, and the lighter lines bound the uncertainty in such a fit. (b) Plot for $E = 1330 \text{ keV}$, showing the absence of a reasonable fit that would include the origin.

TABLE I. Summary of integrated cross sections reported for the reaction $^{111}\text{Cd}(\gamma, \gamma')^{111}\text{Cd}$ through a level near 1200 keV.

Cross section $\pi b_0 b_0 \Gamma \sigma_0 / 2$ ($10^{-29} \text{ cm}^2 \text{ keV}$)	Reference
8(+4, -0.5)	Cauchois, Heno, and Boivin (Ref. 9)
6±2	Boivin, Cauchois, and Heno (Ref. 10)
15±3	Yoshihara (Ref. 11)
10.2±2.6	Lakosi, Csuros, and Veres (Ref. 12)
35±4	Watanabe and Mukoyama (Ref. 2)
5.8±0.8	Krcmar <i>et al.</i> (Ref. 3)
14±1	Bikit <i>et al.</i> (Ref. 4)
9.8±2.5	This work

plotted as functions of the relative intensities, $\zeta(1190)$, appearing on the right. As can be seen from Eq. (3), the best slope around which the data of Fig. 5(a) scatter would represent our experimental determination of the product of the first two terms on the right of Eq. (3). For comparison, the same approach is repeated in Fig. 5(b) to show the difficulty in attempting to force the interpretation that the principal gateway level is the state at 1330 keV. In Fig. 5(b) the weighted activation ratios are plotted as functions of $\zeta(1330)$. It is difficult to consider these data as approximating a linear dependence of R upon ζ , and particularly one which extrapolates to the origin as required by Eq. (3).

From the linear fit to the data of Fig. 5(a) shown as the heavy line, Eqs. (2) and (3), and the value of integrated cross section for ^{75}Br mentioned earlier, we obtain

$$\zeta_{1190}(\text{Cd}) = (8.2 \pm 2.1) \times 10^{-32} \text{ cm}^2.$$

The uncertainty was obtained from application of the same analyses to the lighter lines in Fig. 5(a) bounding the scatter from the least squares fit to the data. The scatter in the data is within the bounds established by this uncertainty in intensity.

Finally, substituting the value for $\zeta_{1190}(\text{Cd})$ into Eq. (2) and solving for the integrated cross section gives for the 1190 keV transition in ^{111}Cd ,

$$\pi b_0 b_0 \Gamma \sigma_0 / 2 = (9.8 \pm 2.5) \times 10^{-29} \text{ cm}^2 \text{ keV}.$$

This is the value we report in Table I.

IV. CONCLUSIONS

The detailed characterization of the spectrum emitted by the intense source of pulsed bremsstrahlung described earlier⁸ has been found to be sufficient to determine the quantitative yield of the reaction $^{111}\text{Cd}(\gamma, \gamma')^{111}\text{Cd}$. Table I shows that value to fall within the interval over which the prior measurements have scattered. In this work there was no need to invoke any theory of nonresonant reaction channels of the type sometimes used¹ in the description of this reaction.

In addition to providing further evidence against the occurrence of nonresonant reactions in ^{111}Cd , in concordance with the conclusions for ^{113}In , the results of this work have important implications for the calibration of intense sources of pulsed continua. By providing a pho-

toactivation channel with a well-defined gateway at 1190 keV, a sample of ^{111}Cd can readily complement the information supplied^{7,8} by ^{79}Br about the intensity at 761 keV and by ^{115}In at 1078 keV.¹⁴ Moreover, the results of this work may indicate why previous work gave such disparate results, no matter how carefully done. The most recent experiments^{3,4} with ^{60}Co sources were strongly model dependent. In those efforts the irradiating intensity and its dependence upon experimental variables were assumed to be a result of Compton scattering from the ^{60}Co line at 1332 keV to the absorption energy at 1330 keV. From Fig. 4 it can be seen that the actual excitation energy is nearer 1200 keV. In the ^{60}Co experiments the intensities at the real gateway must have differed drastically from what had been calculated because of the substantial differences in energies assumed for the gateway.

ACKNOWLEDGMENTS

This work was supported by the Innovative Science and Technology Directorate of the Strategic Defense Initiative Organization and directed by the Naval Research Laboratory. It was made possible through the efforts of many people within the Center for Quantum Electronics. The implementation of the project depended on the contributions of K. Taylor and C. Dutta from the Detector Physics group and of J. Carroll, C. Shippy, D. Tipton, M. Wright, and K. Renfrow in the Engineering group. The authors wish to convey their sincere appreciation to M. Krishnan and his colleagues, R. Schneider and J. Hilton at Physics International of San Leandro, California, for their direction of the PITHON irradiation facility and to the Defense Nuclear Agency for sponsorship of the irradiation time. We are grateful to Professor R. J. Peterson for his insights and for stimulating discussions.

¹B. Pontecorvo and A. Lazard, *C. R. Acad. Sci.* **208**, 99 (1939).

²Y. Watanabe and T. Mukoyama, *Bull. Inst. Chem. Res.* **57**, 72 (1979).

³M. Kremar, A. Ljubicic, K. Pisk, B. Logan, and M. Vrtar, *Phys. Rev. C* **25**, 2097 (1982).

⁴I. Bikit, J. Slivka, I. V. Anicin, L. Marinkov, A. Rudic, and W. D. Hamilton, *Phys. Rev. C* **35**, 1943 (1987).

⁵B. Harmatz, *Nucl. Data Sheets* **27**, 453 (1979).

⁶*Evaluated Nuclear Structure Data File* (Brookhaven National Laboratory, Upton, New York, 1986).

⁷J. A. Anderson and C. B. Collins, *Rev. Sci. Instrum.* **58**, 2157 (1987).

⁸J. A. Anderson and C. B. Collins, *Rev. Sci. Instrum.* **59**, 414 (1988).

⁹Y. Cauchois, Y. Heno, and M. Boivin, *C. R. Acad. Sci. Ser. B* **262**, 503 (1966).

¹⁰M. Boivin, Y. Cauchois, and Y. Heno, *Nucl. Phys.* **A137**, 520 (1969).

¹¹K. Yoshihara, *Isot. Radia. Technol.* **3**, 464 (1960).

¹²L. Lakosi, M. Csuros, and A. Veres, *Nucl. Instrum. Methods* **114**, 13 (1974).

¹³B. Rosner, *Phys. Rev.* **136**, B664 (1964).

¹⁴C. B. Collins, J. A. Anderson, Y. Paiss, C. D. Eberhard, R. J. Peterson, and W. L. Hodge, *Phys. Rev. C* **38**, 1852 (1988).

¹⁵K. Yoshihara, Zs. Nemeth, L. Lakosi, I. Pavlicsek, and A. Veres, *Phys. Rev. C* **33**, 728 (1986).

¹⁶M. L. Wiedenbeck, *Phys. Rev.* **67**, 92 (1945).

¹⁷E. C. Booth and J. Brownson, *Nucl. Phys.* **A98**, 529 (1967).

Comment on "Mössbauer sidebands from a single parent line"

C. B. Collins, P. W. Reittinger, and T. W. Sinor

Center for Quantum Electronics, University of Texas at Dallas, P.O. Box 830688, Richardson, Texas 75083-0688

(Received 25 March 1988)

Foils composed of alternating layers of ferromagnetic and nonmagnetic materials immersed in magnetic fields oscillating at radio frequencies display sidebands on Mössbauer transitions from the nuclei contained in the nonmagnetic regions. Attributed by Chien and Walker [Phys. Rev. B 13, 1876 (1976)] to the transfer into the nonmagnetic layer of acoustic phonons excited by magnetostriction in the ferromagnetic layers, this accepted cause of such effects is challenged by new data resulting from a reexamination and extension of that classical experiment.

The paper of Chien and Walker¹ was of such critical importance that it warrants comment over a decade later. Generally perceived as reporting an unarguable proof of a certain basic proposition, it has now been found to have rested upon a demonstrably false assumption. A reexamination of the original experiment shows it to have been so flawed that any conclusions drawn from it must now be considered unproven.

The point of inception had been the original proposal of Mitin^{2,3} that Mössbauer transitions could be excited as part of a multiphoton process in nuclei immersed in intense radio-frequency (rf) fields. In those cases the Mössbauer spectrum was expected to show additional sum and difference frequency lines displaced from the normal lines by integral multiples of the perturbing frequency. In appearance such multiphoton spectra are expected to resemble the transmission spectra which Ruby and Bolef⁴ obtained by imposing periodic Doppler shifts of purely mechanical origin upon the Mössbauer source. This unfortunate similarity in appearance between phenomena arising from such different origins provided the basis for years of critical controversy seemingly resolved by the work of Chien and Walker.¹ The purpose of this comment is to report new data from a repetition and extension of the Chien and Walker experiment that shows their conclusions to be unjustified. Without the force of conviction conveyed by their work, the controversy must be reopened to further investigation.

The earliest experiment in radio-frequency sideband production, reported by Perlow⁵ in 1968, focused upon the components of the 14.4-keV transition in ⁵⁷Fe. Several ⁵⁷Co sources diffused into ferromagnetic hosts were immersed into intense magnetic fields oscillating at radio frequencies. Those results were attributed⁵ to successive jumps in the hyperfine energies of the radiating states that had been caused by rotations of the local direction of the magnetization at the nucleus. Those jumps were assumed

to occur at the random times when domain walls passed, but with an average periodicity which was treated as a fitted parameter. Such a treatment could be termed a magnetodynamic model of sideband development which anticipated the results of the more complex propagation of the rotations of the magnetization in foils and tapes that was subsequently developed.^{6,7} It generally conformed to the Mitin hypothesis for multiphoton transitions. Two of the three groups who initially documented this phenomena favored the magnetodynamic explanation which required no mechanical action^{5,8,9} while the other group began to develop an alternative based entirely upon magnetostriction.^{10,11} Most of the actual experiments had used ferromagnetic hosts to enhance the applied magnetic fields, and such materials are almost invariably magnetostrictive. In the model finally synthesized, periodic Doppler shifts were assumed to be driven by acoustic phonons which were excited by magnetostriction along the greatest dimensions of the material and scattered onto the axis connecting source and absorber. To be effective, this mechanism required the sample to have a large acoustic *Q* so that displacements of the active nuclei could build to significant values.

Despite the accretion over the years of a large body of phenomenology presumed to describe rf sidebands on Mössbauer transitions, the magnetostrictive-acoustic theory never quantitatively predicted the amplitudes of the sidebands as functions of either applied power or frequency. However, the magnetodynamic models of that time fared no better, and attention turned to "proving" a magnetostrictive origin by distressing the alternative explanations.¹² The obvious difficulty with proving a theory by distressing the alternatives is that those other explanations may not have reached comparable levels of maturation. The magnetodynamic models of the late 1960's were relatively easy to destroy.¹² However, the recent successes of ferromagnetodynamics^{6,7} show the early models⁵ of

sideband formation to have been inspired, but inadequate approximations. Those models simply did not embody the level of sophistication necessary to describe the complex switching behavior of magnetization in ferromagnetic foils subjected to various combinations of static and oscillating fields in those geometries employed.

More recent experiments^{13,14} have shown that the applications of such oscillating magnetic fields to Mössbauer nuclei embedded in nonmagnetic hosts do produce radio-frequency sidebands by directly modulating the phases of the nuclear states involved in the transitions. However, amplitudes were rather small in those experiments because the driving forces depended only upon the value of applied field $\mu_0 H$. In 1984, we extended such approaches further by deriving the phase modulation of a nuclear state in a magnetic material.¹⁵ In this case driving forces were proportional to the magnetization $\mu_0 M$ and effects were found to be large.¹⁵⁻¹⁷ It appears that many prior results attributed exclusively to acoustic effects driven by magnetostriction could have also benefited from an unrecognized contribution from direct phase modulations of the nuclear states involved.

From a current perspective it is the experiment reported by Chien and Walker¹ that forms the bulwark of the magnetostrictive-acoustic explanation of Mössbauer sidebands. In that experiment an absorbing foil composed of ferromagnetic and nonmagnetic layers was used to study transport of the causitive agent from the ferromagnetic layer into the nonmagnetic region where the sidebands were produced upon Mössbauer transitions of embedded ⁵⁷Fe nuclei. Very clear evidence showed that the cause did arise in the ferromagnetic Ni layers, producing sidebands in the nonmagnetic stainless-steel layers. The most ready explanation at that time was a transport of phonons from one layer to the next with a high acoustic Q . Those experiments were repeated in the work reported here, but with extensions which contradict the classic interpretation of Chien and Walker.¹

Although not unique for all sidebands in a spectrum,¹ the idea of a modulation index m as a measure of the strength of the development of the sidebands offers practical convenience for descriptions. For a magnetostrictive origin,¹

$$m = x_0/\lambda, \quad (1)$$

where x_0 is the amplitude of the periodic displacement of the nuclei and $\lambda = 0.137 \text{ \AA}$ for the 14.4 keV line of ⁵⁷Fe. In the corresponding magnetodynamic model,¹³

$$m = bH, \quad (2)$$

where H is the applied magnetic field and b provides proportionality between M_s , the saturation magnetization of the medium, and H . For relatively small m , the ratio of the magnitude of the first order sidebands to the intensity in the original parent line is proportional to m^2 , which in turn is proportional to P , the applied radio-frequency power.

One of the most compelling results presented by Chien and Walker¹ was a demonstration supposed to show the enhancement of m^2 afforded by tighter acoustic coupling of the layers. They found that electroplating Ni upon a

stainless-steel foil produced much higher values of m^2 in absorption experiments than could be obtained by gluing a Ni foil to the stainless foil. They attributed the difference to the obviously poorer acoustic properties of the glue. However, as part of this report we observe that their stainless-steel foil was electroplated on both sides with Ni while the epoxied bond was used to join a single Ni foil to one side of the stainless absorber. While the m defined by Eq. (1) for a single foil could not be additive if produced in different magnetostrictive layers, in principle the H upon which m depends in Eq. (2) could add coherently. Two sources of m arising from distinctly separate sources could give a resulting modulation of $4m^2$ in a magnetodynamic model. Chien and Walker failed to recognize¹ that even in the magnetostrictive model two sources of m generated in the two electroplated layers should give a modulation index of $2m^2$ in the absorber foil. Instead, they attributed the increased sideband intensity developed by the two plated sources in comparison to the one glued source only to the advantage they assumed for a plated contact over a glued interface. They reported no comparison of the effects of gluing or plating the same number of ferromagnetic layers to the absorber foil. Reported here is a repetition of the Chien and Walker experiment which showed that the effect of two foils varied from two to four times that produced by a single foil joined in the same fashion, depending upon the static magnetic bias applied.

In our experiment the absorber was a $2.5 \mu\text{m}$ paramagnetic stainless-steel (SS) foil with 90.6% enrichment of ⁵⁷Fe. For the nonabsorbing ferromagnetic drivers, $2.5 \mu\text{m}$ Ni foils were used, all of which were cut from a single sheet of polycrystalline Ni. The stainless-steel absorber was sandwiched between two Ni foils and held in rigid contact by mounting the foils between glass cover slides of $100 \mu\text{m}$ thickness. A conventional Mössbauer spectrometer, modified for rf experiments (Fig. 1), utilized a 25-mCi source in a Rh matrix to obtain the ⁵⁷Fe absorption spectra. The 14.4-keV gamma rays were detected with a Kr gas filled proportional counter biased with 1.8 kV.

A 25 MHz rf magnetic field was applied by mounting the foils in the cylindrical induction coil of an L-C tank circuit. In obtaining data for a direct comparison between the effect of one Ni driver versus two, the product of the applied rf power P and the electrical Q of the circuit containing the rf induction coil was maintained at constant values. Elementary analysis shows that if PQ is constant the rf current in the coil of such a circuit is also constant and hence the two absorber arrangements are subjected to applied fields of the same intensity H . The results of the first experiment verified the linearity of the first-order sideband amplitudes at 25 MHz for SS with two Ni drivers with PQ products of 75, 150, and 300 W as shown in Fig. 2. The spectra are scaled so that the intensity of the central Mössbauer absorption peak of ⁵⁷Fe in SS is held constant in order to make direct comparisons of the sideband amplitudes.

Having established the linearity of the first-order sidebands in the Ni-SS-Ni sandwich, one of the Ni drivers was removed and the experiment was repeated with the same PQ products as before. Figure 3 shows a comparison of the sideband amplitude for two Ni drivers versus

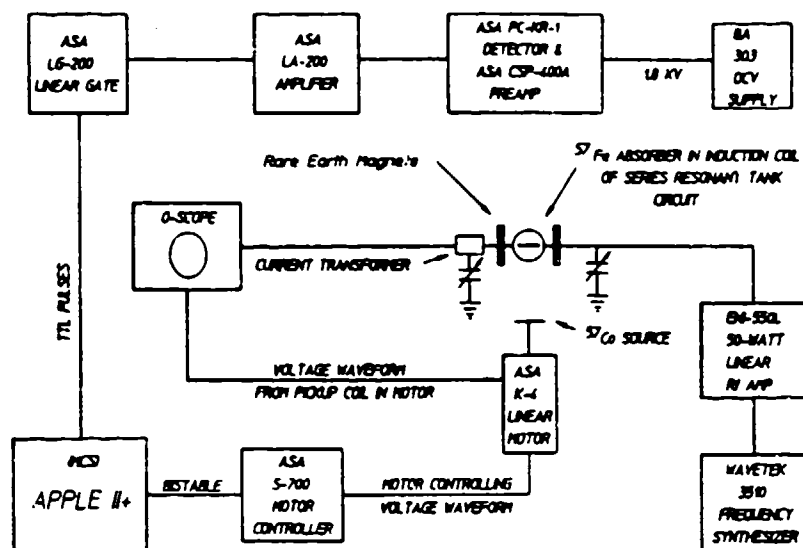


FIG. 1. Schematic drawing of the experimental arrangement used.

one; in this configuration two Ni drivers give twice the effect of one driver foil.

In the next experiments a comparison was made between the effect of one source of excitation with that from two sources when both were biased with a static magnetic field. Rare-earth element magnets were placed about the induction coil such that the static magnetic field was mutually orthogonal to the rf magnetic field and to the direction of gamma-ray propagation.

The linearity of the sideband amplitudes at 25 MHz as a function of PQ was again established as shown in Fig. 4 to insure that the introduction of the static magnetic field did not introduce any nonlinearities into the system. The scale thus established was used to measure the decrease in the sideband amplitude when one of the sources of excitation was removed from this biased sandwich. As is clearly shown in Fig. 5, the sideband amplitudes obtained with two driver foils are four times the amplitudes obtained with one driver foil. Therefore, with the application of a

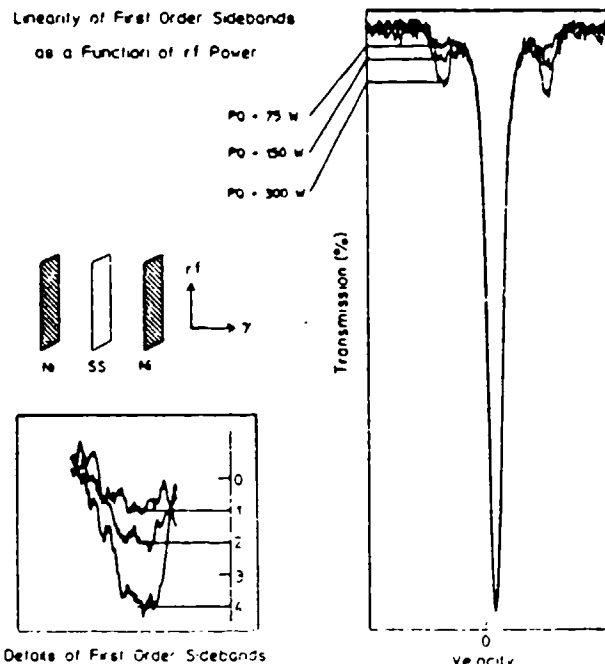


FIG. 2. Experimental verification of the linearity of the first-order sidebands at 25 MHz as a function of the applied rf power. The product of the applied rf power P and the quality factor Q of the circuit are used to insure reproducibility of the rf field strengths.

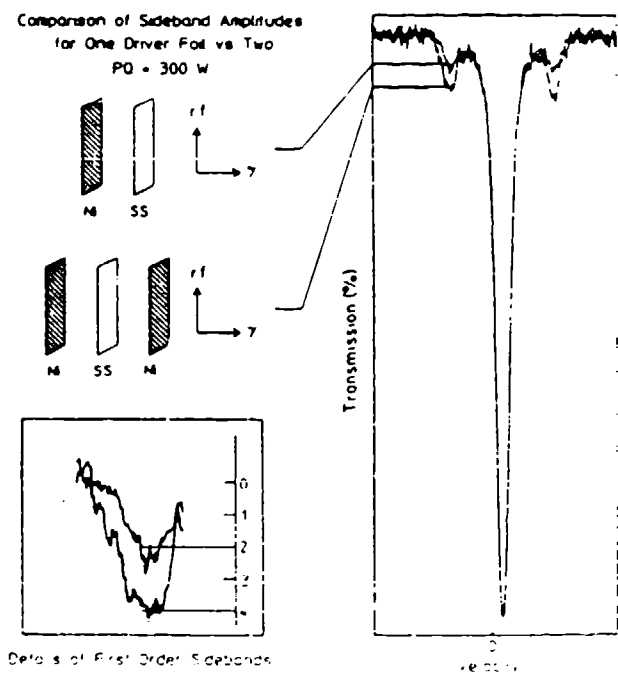


FIG. 3. Comparison of first-order sideband amplitudes for one Ni driver foil vs two at 25 MHz with a PQ product of 300 W.

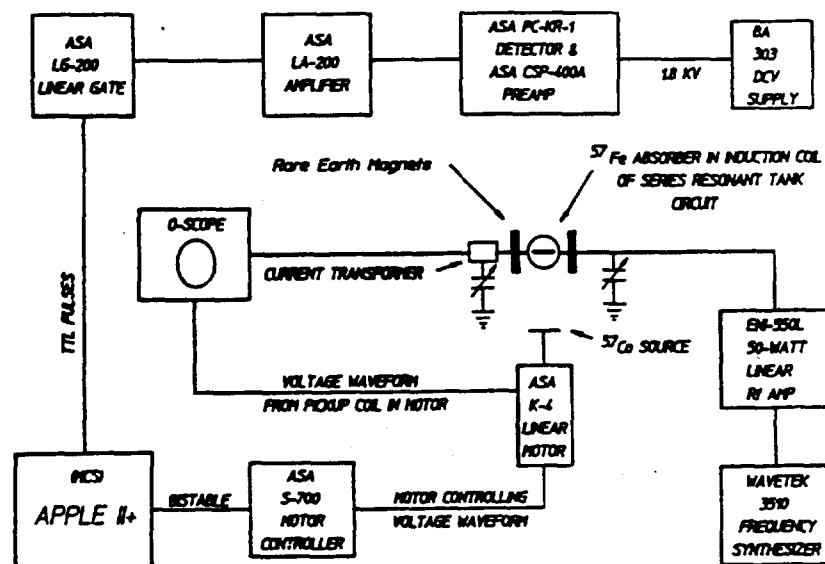


FIG. 1. Schematic drawing of the experimental arrangement used.

one; in this configuration two Ni drivers give twice the effect of one driver foil.

In the next experiments a comparison was made between the effect of one source of excitation with that from two sources when both were biased with a static magnetic field. Rare-earth element magnets were placed about the induction coil such that the static magnetic field was mutually orthogonal to the rf magnetic field and to the direction of gamma-ray propagation.

The linearity of the sideband amplitudes at 25 MHz as a function of PQ was again established as shown in Fig. 4 to insure that the introduction of the static magnetic field did not introduce any nonlinearities into the system. The scale thus established was used to measure the decrease in the sideband amplitude when one of the sources of excitation was removed from this biased sandwich. As is clearly shown in Fig. 5, the sideband amplitudes obtained with two driver foils are four times the amplitudes obtained with one driver foil. Therefore, with the application of a

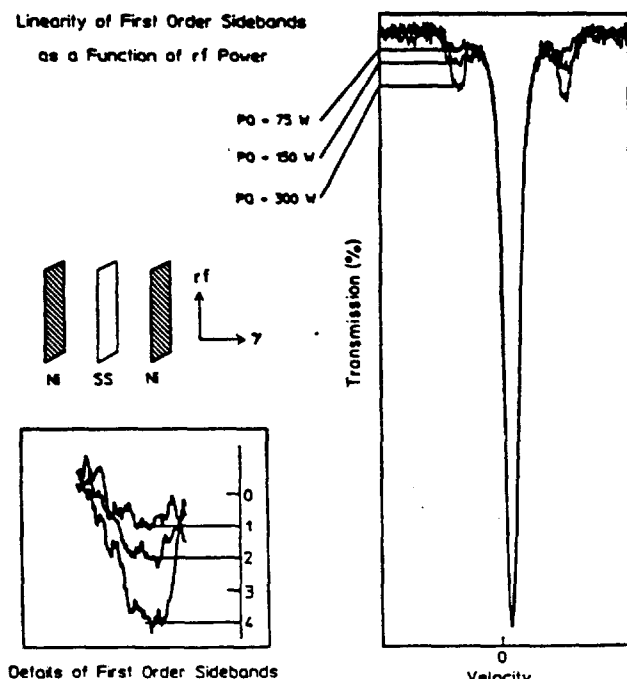


FIG. 2. Experimental verification of the linearity of the first-order sidebands at 25 MHz as a function of the applied rf power. The product of the applied rf power P and the quality factor Q of the circuit are used to insure reproducibility of the rf field strengths.

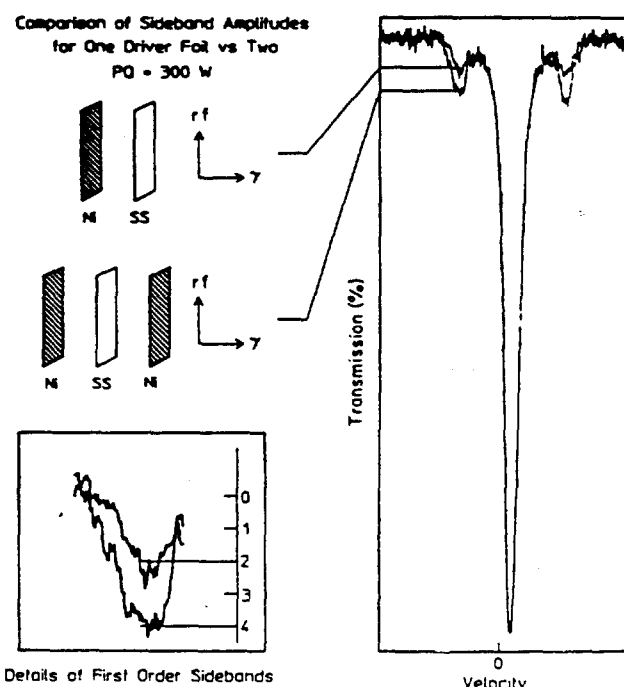


FIG. 3. Comparison of first-order sideband amplitudes for one Ni driver foil vs two at 25 MHz with a PQ product of 300 W.

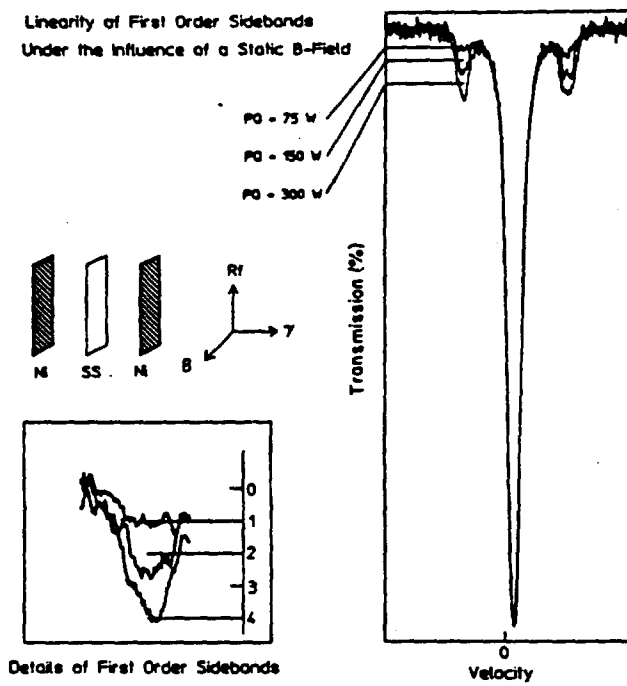


FIG. 4. Establishment of linearity of the first-order sidebands at 25 MHz with $PQ = 75$, 150, and 300 W when the foils are biased with a static B field.

static B field, two sources of excitation give four times the effect.

The results of this reexamination of the Chien and Walker experiment support only the first conclusion reached in that original work, namely that the causitive agent of rf sidebands can be produced in a ferromagnetic layer and then transported into a nonmagnetic layer. Their other conclusion is completely refuted by this demonstration because the effects they attributed to the type of coupling between layers most probably resulted from the relative numbers of magnetic and nonmagnetic layers.

These new results go beyond the propositions tested by Chien and Walker¹ and display behaviors completely inconsistent with the traditional magnetostriuctive-acoustic origin of Mössbauer sidebands. In experiments such as these, acoustic phonons are the bosons associated with vector fields driven by tensor forces, *not vector forces*. Without invoking stimulated emission, we can conceive of no way in which tensor sources which are physically separated can produce coherent vector fields in a space between them, even if they are temporally synchronized. As the fields increase the magnetostriuctive foils will become stressed along parallel axes which are displaced by the thickness of the stainless layer between them. There is no mechanism to produce a displacement vector in a particular transverse direction as a consequence of the resulting strains in the Ni foils. Only a small scale bulging or buck-

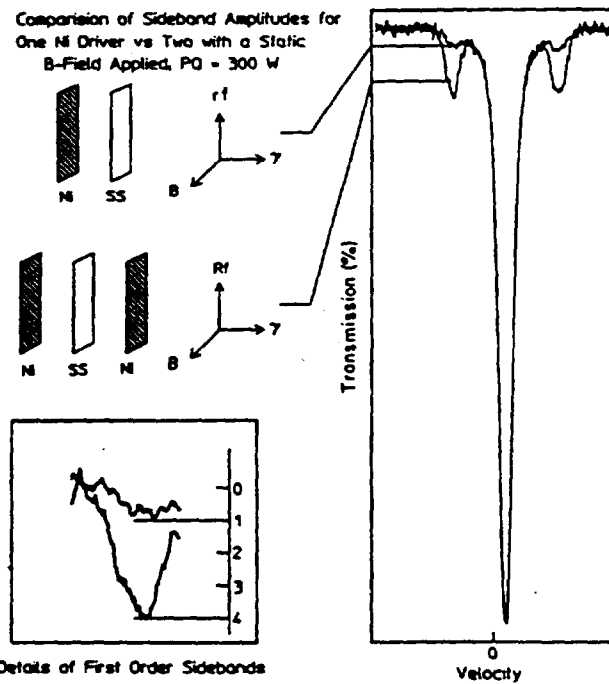


FIG. 5. Comparison of sideband amplitudes for one driver vs two when both are biased by a static B field with $PQ = 300$ W. Here two foils give four times the effect of one thus giving a modulation index of $4m^2$.

ling of each Ni foil is to be expected and this is usually described as the scattering of phonons at right angles to the source. Without the stimulated emission of such phonons, there is no way to insure that one foil buckles toward the stainless layer at a particular point while the other buckles away.

The stimulated emission of phonons that would be necessary to produce coherent additions of the displacements arising from the different sources would imply the existence of a threshold of power, above which two modulation indices of m would give an effect of $4m^2$ and below which only $2m^2$. No such threshold was suggested by data similar to that of Fig. 5 which was obtained over an adequate range of powers.

In view of the growing number of successes of the model for the direct modulation of the phases of the nuclear states and these new results which question the validity of the conclusions of the Chien and Walker¹ experiment, it would appear that the controversy over the origin of Mössbauer sidebands must be reopened.

The authors gratefully acknowledge the support of this work by the Office of Naval Research, by the Naval Research Laboratory, and by the Innovative Science and Technology Directorate of the Strategic Defense Initiative Office.

¹C. L. Chien and J. C. Walker, *Phys. Rev. B* **13**, 1876 (1976).
²A. V. Mitin, *Zh. Eksp. Teor. Fiz.* **52**, 1596 (1967) [*Sov. Phys. JETP* **25**, 1062 (1967)].
³A. V. Mitin, *Dokl. Akad. Nauk SSSR* **194**, 59 (1971) [*Sov. Phys. Dokl.* **15**, 827 (1971)].
⁴S. L. Ruby and D. I. Bolef, *Phys. Rev. Lett.* **5**, 5 (1960).
⁵G. L. Perlow, *Phys. Rev.* **172**, 319 (1968).
⁶T. H. O'Dell, *Ferromagnetodynamics* (Wiley, New York, 1981), Chap. I.
⁷C. W. Chen, *Magnetism and Metallurgy of Soft Magnetic Materials* (North-Holland, Amsterdam, 1977).
⁸G. Asti, G. Albanese, and C. Bucci, *Nuovo Cimento B* **57**, 531 (1968).
⁹G. Asti, G. Albanese, and C. Bucci, *Phys. Rev.* **184**, 260 (1969).
¹⁰N. D. Heiman, L. Pfeiffer, and J. C. Walker, *Phys. Rev. Lett.* **21**, 93 (1968).
¹¹N. D. Heiman and J. C. Walker, *Phys. Rev.* **184**, 281 (1969).
¹²L. Pfeiffer, N. D. Heiman, and J. C. Walker, *Phys. Rev. B* **6**, 74 (1972).
¹³P. J. West and E. Matthias, *Z. Phys. A* **288**, 369 (1978).
¹⁴E. Ikonen, P. Helistö, J. Hietaneni, and T. Katila, *Phys. Rev. Lett.* **60**, 643 (1983).
¹⁵C. B. Collins and B. D. DePaola, *Opt. Lett.* **10**, 25 (1985).
¹⁶B. D. DePaola and C. B. Collins, *J. Opt. Soc. Am. B* **1**, 812 (1984).
¹⁷B. D. DePaola, S. S. Wasal, and C. B. Collins, *J. Opt. Soc. Am. B* **2**, 541 (1985).

Large-Scale Effects of the Magnetic Phase Modulation of Recoilless γ Transitions

T. W. Sinor, P. W. Reittinger, and C. B. Collins

Center for Quantum Electronics, University of Texas at Dallas, P.O. Box 830688,
Richardson, Texas 75083-0688
(Received 6 July 1988)

The excitation of coherent transients in Mössbauer spectra has been previously limited by the high powers required to modulate the nuclear phases. Reported here is an orders-of-magnitude increase in the efficiency through which such phenomena can be produced. Magnetic modulation of the quantum phases of ^{57}Fe nuclei in paramagnetic media has been produced by spin waves of large amplitude transported from ferromagnetic sources.

PACS numbers: 76.80.+y

A recent Letter¹ reported variations in recoilless γ -ray spectra produced by directly modulating the interaction energies arising from the couplings of the nuclear magnetic moments to the hyperfine fields. Described in terms of the phase modulation of the nuclear states involved in the transition, these results represent important realizations of some of the general possibilities for developing nuclear analogs^{1,2} of coherent transient effects studied in quantum optics.

An example is found in the frequency domain in the excitation of sidebands on γ -ray transitions, and precursive work^{2,4} had treated that problem in a manner equivalent to an application of the phase modulation formalism.³ For cases in which there is no static magnetic field⁵ or in which the modulation is parallel to the static field,⁶ the effect of the time-varying component $H_0 f(t)$ upon an eigenstate of the nucleus, $\Psi_{e,m}^{(0)}$, can be written

$$\Psi_{e,m} = e^{-i\phi_e(t)} \Psi_{e,m}^{(0)}, \quad (1)$$

where $\phi_e(t)$ is the modulation angle of the phase.

$$\phi_e(t) = m\omega_e \int_0^t f(t') dt', \quad (2)$$

and the Larmor frequency ω_e is

$$\omega_e = \mu_N g_e H_0 / \hbar, \quad (3)$$

where μ_N is the nuclear magneton, g_e is the gyromagnetic ratio for the e th excited or ground state of the nucleus, and m is the magnetic quantum number of the eigenstates.

In principle, the difference in phase modulation between the ground state, g , and an excited state, e , may be observed during an absorption transition because the Fourier components of $\phi_g(t) - \phi_e(t)$ will be manifested as sidebands. However, since the transition will have a width Γ associated with the time-dependent decay of the states, unless

$$\hbar\omega_e \geq \Gamma, \quad (4)$$

the sidebands will be buried in the natural wings of the probing transition.

Only the ingenuous use of the ultranarrow, 93-keV line of ^{67}Zn permitted the quantitative study of the

coherent phase modulation effects recently described.¹ That benchmark achievement required field amplitudes reaching 13.4 mT for sinusoidal modulation at applied frequencies ω up to 10 kHz and effects were reported¹ to scale as $(H_0/\omega)^2$.

The conceptual key to orders-of-magnitude enhancement of phase modulation effects has been reported⁷⁻⁹ to lie in the use of smaller powers to manipulate the greater magnetic fields arising from the natural correlations of individual spins in ferromagnetic materials. However, the modulation $\partial M/\partial t$ of the magnetization M of a ferromagnetic material is rarely parallel to either the applied field H_0 or even to M itself.¹⁰ For such cases of nuclei in ferromagnetic media, the modulation angle of Eq. (2) takes a more complex form,⁷ and one which causes a mixing of the eigenstates $\Psi_{e,m}^{(0)}$. Nevertheless, the principal parameter is still a Larmor frequency ω_e which for magnetic environments becomes

$$\Omega_e = \mu_N g_e M / \hbar. \quad (5)$$

a value much larger than that found in Eq. (3) for non-magnetic samples. Unfortunately, magnetic materials are almost invariably magnetostrictive and the concern has lingered that even the enhanced effects of phase modulation might always be overwhelmed by the periodic Doppler shifts produced by vibration in the lattices excited by magnetostriction.

The propagation of magnetoelastic waves is a complex problem which has been intensively studied since 1958.¹¹ For many magnetic media the dispersion equation for such waves displays several branches^{12,13} which can be individually identified with spin waves, magnetostatic waves, or elastic waves. Mixed waves coupling magnons and phonons occur principally when branches intersect, so that the frequencies and wavelengths for both are nearly equal.¹¹ Away from those values of parameters magnetic and acoustic waves can be separated. In principle this offers a means to propagate only the former to some remote part of a sample where it is desired to magnetically modulate the phases of the states of the nuclei without carrying acoustic noise along to the same place.

The most convenient of the Mössbauer transitions for modulation experiments is the 14.4-keV transition of

^{57}Fe diluted in a thin metal foil. The propagation of magnetic waves in conductive foils presents a special problem because of eddy-current losses; Kittel has given an approximation¹¹ which would limit the mean free path for a magnon to a few wavelengths for the frequencies of tens of MHz which would be interesting for use with ^{57}Fe . For this reason the preferred choices for the propagation of magnetization in such thin metallic foils are the magnetostatic waves characterized by long wavelengths and high group velocities^{12,14} that are quite removed from intersections with acoustic branches. Wavelengths can readily reach the scale of millimeters, and it has been demonstrated that dispersion properties are little affected by raising the temperature of the foil above the Curie point.¹⁵ Thus, if they can be excited at the boundaries, such spin waves should propagate in paramagnetic foils as well as they do in conductive ferromagnetic foils.

A stainless-steel foil $10\text{ mm} \times 20\text{ mm} \times 2.5\text{ }\mu\text{m}$ was used in these experiments. It was rolled from a nonmagnetic alloy, 310, which was expected¹⁶ to have a susceptibility of about 4000×10^{-6} cgs. When enriched in ^{57}Fe , it displayed a single absorption line at 14.4 keV. Relatively recently, it has been shown¹⁷ how to communicate the large values of magnetization characteristic of ferromagnetic materials into thin foils of paramagnetic media, such as stainless steel at room temperature, by sandwiching it between ferromagnetic layers. Grünberg demonstrated that at small separations ferromagnetic foils switch coherently so that lines of fringing flux emerging from one continue across to the other. Flux refraction insures that this small normal component is compressed in the separating layer by a factor comparable to its ratio of length to thickness, an aspect ratio of about 10^4 in these experiments. In this way a wave of

oscillating magnetization was launched into a stainless-steel tape, enriched in ^{57}Fe so that nuclear phase modulation might be observed at a distance from the source of the disturbance that was greater than the range for the transport of acoustic phonons.

This experiment employed a conventional Mössbauer spectrometer with a 2 mCi ^{57}Co source in a Pd matrix to obtain the ^{57}Fe resonance spectra in a transmission geometry. To detect the 14.4-keV γ rays we used a high-resolution EG&G high-purity Ge detector. A Wavetek Model 3000 signal generator and a 50-dB FNI-325LA linear radio-frequency (rf) amplifier provided the oscillating magnetic field.

To calibrate the contributions from ultrasonic and from phase modulation effects two independent techniques of sideband generation were used. As a basis for comparison, ultrasonic sidebands were excited on the un-split absorption line of ^{57}Fe nuclei in the same stainless-steel foil by sinusoidal vibrations injected with two different 25-MHz piezoelectric transducers. One was X cut and the other AT cut in order to inject the widest possible variety of phonons of vibration for transmission to the point of observation in the geometry of Fig. 1(a).

As shown in the lower panel of Fig. 1(b) an $8 \times 10\text{ mm}^2$ section of the foil was acoustically bonded to each of the transducers used in this experiment. The remaining length was gently curved, forming a 90° angle with the plane of the transducer. Mechanical support was provided for the remote section of foil by mounting it between glass cover slides which were then fastened to the transducer cell.

In the usual geometry for a transmission experiment arranged to sample excitation at the source, a convenient level of input power of 0.06 W to the X -cut crystal produced the reference level of sideband development seen

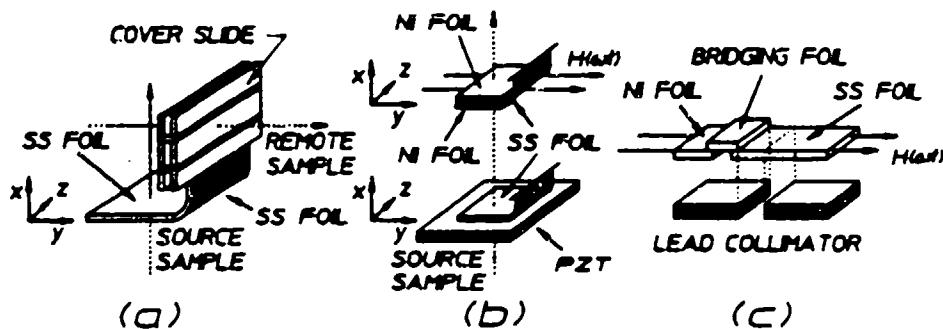


FIG. 1. Schematic representation of the mounting arrangements used in the excitation of sidebands on the Mössbauer absorption line of ^{57}Fe in the 2.5- μm -thick stainless-steel (SS) foil. (a) The optical path from γ source to detector is shown by the dotted arrow for the orthogonal x and y directions arranged to sample sideband development at the source of the phenomenon and at a remote point, respectively, as marked. Excitation is injected into the horizontal face of the SS foil and the vertical face is mechanically stabilized by the 100- μm -thick glass cover slides sandwiching the absorber foil. (b) Upper: spin waves injected by the periodic oscillation of the Ni foils pressed onto the absorber foil by additional cover slides not shown and excited by the magnetic field in an inductor containing the Ni foils. The vertical section protrudes from the coil between windings. Lower: vibrational excitation injected by the X -cut quartz-crystal transducer connected to a radio-frequency oscillator. (c) Geometry used in the experiments designed to bridge a break in the conductive path with 25- μm -thick foils of various materials.

in Fig. 2 in which the fourth order contained 34% of the intensity remaining in the parent transition. Nevertheless, the effect of phonons transported in the foil about 1 cm around a bend of 90° could not be detected even with a tenfold increase in power above the reference level. Nor could they be observed at the remote sampling point when excitation was provided by the *AT*-cut transducer which required a larger input power of 2.9 W in order to obtain the same reference level of sideband development at the source position. The presence of a high level of phonon excitation *in the stainless-steel foil at the source end* was clearly demonstrated by the strong development of the sidebands seen there, but evidently those phonons could not propagate to the remote point of observation. If there had been any low-loss modes for the transport of purely elastic waves in the stainless-steel foil, the population of phonons already in the foil at the source end should have coupled into them. However, the absence of phonon transport actually observed seems consistent with the difficulties expected in propagating transverse vibrations through a medium which is very thin in comparison to a wavelength and one in which the local acoustic Q is expected to be high.¹⁸

In the experimental arrangement used to launch spin waves, the piezoelectric transducer was replaced with a pair of 2.5- μm foils of ferromagnetic Ni ($8 \times 10 \text{ mm}^2$) which were periodically magnetized as shown in the upper panel of Fig. 1(b). The foils (Ni-SS-Ni) were held in rigid contact by sandwiching them between glass cover slides at the source end. Only the source end of the experiment was changed and the protruding section of the stainless-steel foil was again bent at an angle of 90° and enclosed between glass cover slides in the same way as before. Mechanical rigidity was provided to the absorber assembly by a plastic frame.

An rf magnetic field of 0.07 mT was applied to the absorber via a flattened induction coil of a tuned *LC* circuit. During observation in the *x* direction at the source end the rf power level was adjusted to give about the

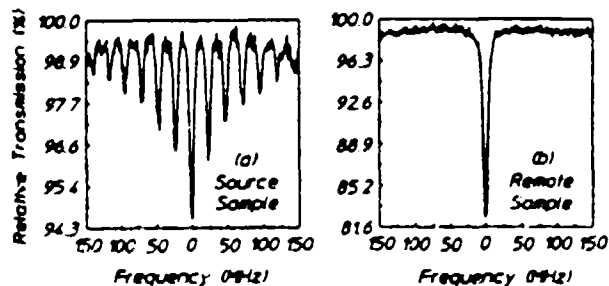


FIG. 2. Absorption spectra of ^{57}Fe in stainless steel showing sidebands developed by phonons present in the sample foil. (a) Reference spectrum observed in the *x* direction at the source at a level of excitation of 0.06 W in the piezoelectric crystal. (b) Spectrum observed in the *y* direction at the remote point shown in Fig. 1(a) for an excitation level of 0.7 W. Only the unsplit parent line is seen.

same reference level of sideband development as had been generated with the piezoelectric transducer. This insured the same ambient level of phonons in the foil at the source end and thus provided for a direct comparison of the phase modulation effects propagated by magneto-static waves with the null level of acoustic noise that had reached the same point of observation during calibration.

The spectra obtained in the samples of the source and remote points in the geometry of Fig. 1(b) are shown in Fig. 3. At the remote point for this same level of input power, first-order sidebands containing about 22% of the intensity of the parent line developed. This represents a level 10 times the threshold for detection and hence 100 times any component contributed by acoustic phonons as determined from the data of Fig. 2. It seems that these experiments have shown that an oscillating alignment of spins can be propagated through a paramagnetic foil better than mechanical vibrations can be transported under the same conditions.

Moreover, such effects of spin waves were not sensitive to mechanical pressures or spurious damping and the complete disassembly, substitution of foils, and reassembly served to reproduce closely the levels of excitation seen in Fig. 3. Only the thickness and length of the foil, together with the level of input power, were found to be variables that significantly affected the result.

Finally, to confirm the magnetic nature of the transport of the cause of the sidebands, the Ni foil generating the spin waves was separated from the SS foil by a gap which was then bridged as shown in Fig. 1(c) by foils having various magnetic and acoustic properties. To insure reliable and reproducible contact of the foils the layers were pressed between two thin glass plates. As expected, these plates alone were unable to communicate the spin waves from the Ni to the SS and no sidebands could be produced without a bridging foil.

All of the bridging foils were of a uniform size and thickness, being 4 mm by 10 mm by 25 μm , respectively. They differed only in acoustic and magnetic properties.

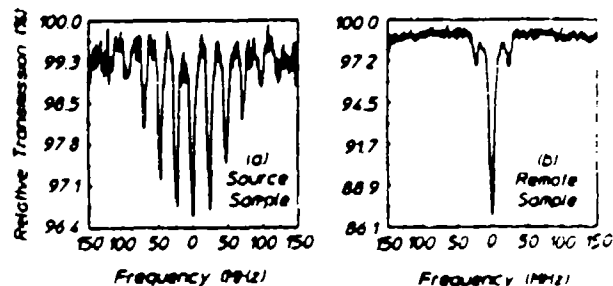


FIG. 3. Absorption spectra of ^{57}Fe in stainless steel showing sidebands resulting from the modulation of nuclear phases by spin waves present in the sample foil. (a) Reference level of excitation observed at the source in the *x* direction shown in Fig. 1(b) at a field amplitude of 0.07 mT. (b) Sidebands observed in the *y* direction at the remote point for the same driving field of 0.07 mT.

TABLE I. Summary of experimental results for the rf bridging experiments.

Bridging material	Susceptibility $\chi (10^{-6} \text{ cgs})$	Acoustics impedance $Z = pc (10^3 \text{ g/cm}^2 \text{ sec})$	Effect transported
Aluminum	+16.5	17.33	Yes
Copper	-5.46	44.74	No
Silver	-19.5	37.96	No
310-SS	+4000	45.4	Yes
Tin	-37.0	24.24	No
Titanium	+153	27.32	Yes

As shown in Table I, the transport of the spin waves correlated completely with the susceptibility of the bridge and showed no dependence upon the matchings of acoustic impedances.

For example, consider the case for Al which has a magnetic susceptibility of $+16.5 \times 10^{-6} \text{ cgs}$ but which offers a very poor matching of its acoustic impedance to that of either Ni or SS. With an Al bridge there was a strong transport of the cause of the sidebands as seen in Fig. 4(a). In contrast Cu which is diamagnetic, as indicated by its negative susceptibility, should have been unable to propagate spin waves across the gap, despite its very close match of acoustic properties to both Ni and SS. Figure 4(b) shows that sidebands did not develop with the Cu bridge.

While it is expected that the transport of purely acoustic waves should be quite sensitive to interface contacts and damping effects, the spin waves propagated in these experiments were not found to be affected by the contact pressure or by the mechanical mounting. The area of contact and length of the bridge were important parameters but the pressure of the cover glasses and placement of the supports were not important. The data of Fig. 4(a) were routinely reproduced to within the noise level even after disassembly and rearrangement of the mechanical parts.

In these experiments the driving amplitude H_0 in the Ni was around 0.07 mT while the frequency was 23.74 MHz. Without the excitation of spin waves the effect should have been smaller by at least the ratios of the scaling parameters, $(B_0/\omega)^2$, a factor of 10^{11} for this case. The great enhancement in the effects of coherent modulation which spin waves produce makes possible the examination of many other coherent phenomena predicted at practical ranges of tuning and accessible levels of input powers.

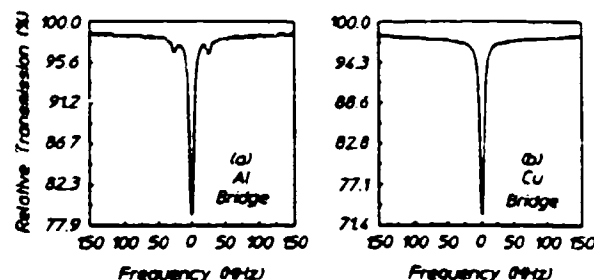


FIG. 4. Absorption spectra of ^{55}Fe in stainless steel in the geometry of Fig. 1(c) for a certain constant level of radio-frequency input. (a) Sidebands developed with an Al bridge. (b) Null effect obtained with a Cu bridge.

The authors acknowledge the support of this work by ONR and by Strategic Defense Initiative Office of Innovative Science and Technology (SDIO/IST) with direction by the NRL.

¹E. Ikonen, P. Helisto, J. Hietaniemi, and T. Katila, Phys. Rev. Lett. **60**, 643 (1988).

²P. Helisto, E. Ikonen, T. Katila, and K. Riski, Phys. Rev. Lett. **49**, 1209 (1982).

³E. Ikonen, P. Helisto, T. Katila, and K. Riski, Phys. Rev. A **32**, 2298 (1985).

⁴A. V. Mitin, Zh. Eksp. Teor. Fiz. **52**, 1596 (1967) [Sov. Phys. JETP. **25**, 1062 (1967)].

⁵P. J. West and E. Matthias, Z. Phys. A **228**, 369 (1978).

⁶S. Olariu, I. Popescu, and C. B. Collins, Phys. Rev. C **23**, 1007 (1981).

⁷C. B. Collins and B. D. DePaola, Opt. Lett. **10**, 25 (1985).

⁸B. D. DePaola and C. B. Collins, J. Opt. Soc. Am. B **1**, 812 (1984).

⁹B. D. DePaola, S. S. Wagal, and C. B. Collins, J. Opt. Soc. Am. B **2**, 541 (1985).

¹⁰T. H. O'Dell, *Ferromagnetodynamics* (Wiley, New York, 1981), Chap. 2.

¹¹C. Kittel, Phys. Rev. **110**, 836 (1958).

¹²P. C. Fletcher and C. Kittel, Phys. Rev. **120**, 2004 (1960).

¹³E. Schliemann, J. Appl. Phys. **31**, 1647 (1960).

¹⁴R. W. Damon and J. R. Eshback, J. Appl. Phys. Suppl. **31**, 1045 (1960).

¹⁵H. A. Mook, J. W. Lynn, and R. M. Nicklow, Phys. Rev. Lett. **30**, 556 (1973).

¹⁶T. Lyman, *Metals Handbook* (American Society for Metals, Metals Park, OH, 1961), 8th ed., Vol. I, p. 792.

¹⁷P. Grünberg, J. Appl. Phys. **51**, 4338 (1980).

¹⁸L. Pfeiffer, N. D. Heiman, and J. C. Walker, Phys. Rev. B **6**, 74 (1972).

Laser plasma source of amorphic diamond

C. B. Collins, F. Davanloo, E. M. Juengerman, W. R. Osborn, and D. R. Jander
Center for Quantum Electronics, The University of Texas at Dallas, P. O. Box 830688, Richardson,
Texas 75083-0688

(Received 5 October 1988; accepted for publication 7 November 1988)

Amorphous diamond films characterized by a high percentage of sp^3 bonds have been prepared in an UHV environment with a laser plasma source of carbon ions. Peak power densities in excess of 10^{11} W/cm^2 were found necessary to produce films at growth rates of $0.5 \mu\text{m/h}$ over areas of 20 cm^2 having optical quality sufficient to show bright interference colors.

The past few years have witnessed a renaissance in the preparation and study of thin films of carbon having diamond-like properties.¹ However, while natural diamond is a well-defined substance, these diamond-like films are not. In many cases different materials result from the different methods of preparation and this has contributed much complexity to the evaluation of the merits of the different techniques of growth.

From a structural viewpoint, Spencer² has identified six allotropes of carbon, two for each of the numbers of dimensions through which the carbon atoms may bond. The ones most important in the formation of thin films of diamond-like carbon (DLC) are the two-dimensional sp^2 bonds which characterize graphite and the three-dimensional sp^3 bonds which give cubic diamond its unique properties.

From the standpoint of mechanical and electrical properties the best results have been obtained with a class of DLC materials denoted as α -C:H, the α suggesting an amorphous structure. They can be grown by a variety of techniques for chemical vapor deposition (CVD) at rates practical for commercial applications. Surprisingly, these materials contain hydrogen in amounts which vary from about 20 to 60%. Within these limits the amount of hydrogen correlates with the proportions of sp^3 to sp^2 bondings and thus, with the prevalence of diamond-like properties. A reduction in the amount of hydrogen in such a film degrades it toward graphite. At 20% there is a discontinuity in stability and only pure carbon films can exist with less than this limiting amount of hydrogen.¹

Denoted as α -C films, these unhydrogenated DLC films have received relatively little attention, although they have been known for quite some time. As early as 1971, Aisenberg and Chabot³ reported the quenching of a beam of C^+ ions in the presence of Ar and Ar^+ on a cold substrate to form an amorphous layer containing no hydrogen, yet having some diamond-like properties. Spencer *et al.*² continued this line of development in 1976, attributing the favorable properties of the deposited layers to the selective destruction of exposed sp^2 bonds by the bombarding ions. However, with these early ion beam methods the growth rates were extremely slow and the material they produced remained only a curiosity until relatively recent times.

With a high fluence ion source Miyazawa *et al.*⁴ brought growth rates up to about 360 A/h on a 1 cm^2 substrate, while Savvides^{5,6} achieved 500 A/h on a 20 cm^2 area with a sputtered source of carbon ions and atoms. Even higher growth

rates were demonstrated at the cost of degraded film quality. The resulting availability of samples of a tangible scale together with the potential importance of such films in optical applications seems to have motivated an intensive study of their optical properties. Unlike the α -C:H materials these unhydrogenated DLC films were moderately clear in the visible wavelengths and Miyazawa recorded the observation of colored interference fringes.⁴ The resulting indices of refraction reported by Miyazawa and Savvides⁶ are collected in Figs. 1(a) and 1(b).

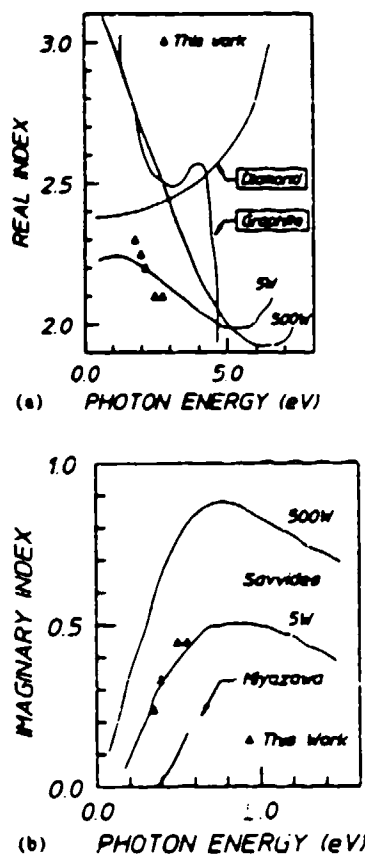


FIG. 1. Symbols plot the real and imaginary parts of the refractive indices of α -C films produced by the laser plasma source described in this work as functions of photon energy. (a) Real parts plotted together with comparative values for diamond and graphite as indicated. Dotted curves show the results reported in Ref. 6 for films prepared with a sputtered ion source operated at the powers shown. (b) Imaginary components of the refractive indices of α -C films reported by Savvides in Ref. 6 are shown by the dotted lines for the two powers used in his process while results reported by Miyazawa in Ref. 4 are plotted by the solid curve.

While the real parts of the indices in Fig. 1(a) are interesting in their approaches to the value of 2.42 for natural diamond, the greatest diagnostic significance lies in the imaginary parts, shown in Fig. 1(b). Savvides has shown^{5,6} how at small values this extinction coefficient is reasonably proportional to the fraction of sp^2 bondings in the film, provided the real part is reasonably constant. Purely diamond-like sp^3 bonding would give no loss at these photon energies. The lower curve, identified by the 5 W of input power to the sputtering source in Savvides' system, provides a calibration that is identified with a 25% content of graphitic, sp^2 bonds. Though not computed previously, it can be seen that Miyazawa's films should have contained only about 10% of the sp^2 bonding. This compares favorably with the best results¹ attained by using hydrogen to minimize to 14% the proportions of sp^2 bonds in α -C:H. Since the latter material is black in the visible because of the hydrogen bonding, the α -C films might be the preferred choice for some applications, if the growth rates were of practical magnitudes. Moreover, if the residual sp^2 bonds could be shown to be an artifact of the production, as opposed to being a necessary ingredient for stability, then the direction would be shown toward the development of truly amorphous diamond containing only sp^3 bonds.

Reported here are the deposition and characterization of several α -C films grown at rates of $0.5 \mu\text{m}/\text{h}$ on 20 cm^2 areas with a laser plasma source. The experimental arrangement is shown in Fig. 2. As can be seen, it represents a substantial evolution from the laser plasma device we described earlier,⁷ both in the electronics and in the laser. The laser plasma source of Wagal,⁷ together with the earlier sources of Richter⁸ and Sato,⁹ had been limited to peak intensities at the graphite feedstock of a few $\times 10^{10}$, 10^8 , and 10^9 W/cm^2 , respectively. The system shown in Fig. 2 uses a Q-switched Nd-YAG laser to deliver 250 mJ to the focus at a repetition rate of 10 Hz. Because of an improved optical system it produces $5 \times 10^{11} \text{ W/cm}^2$ in a 15 ns pulse at the graphite target. While Sato⁹ and Wagal⁷ used supplementary electrodes for cleaning the substrate and for steering the ions, respectively, the system in Fig. 2 incorporates an auxiliary discharge to further increase the plasma temperature by Joule heating in the small volume of the ablation plume.

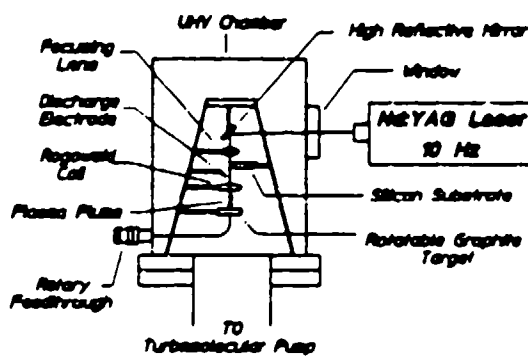


FIG. 2. Schematic representation of the laser plasma source used in this work to prepare amorphous diamond films.

The current which was passed from electrode to the ablation plume was measured with a Rogowski coil, electrically isolated from the deposition system. A typical result is shown in Fig. 3 where it can be seen that currents peak in the 1-10 A range in a pulse are found to have FWHM of the order of 2 μs . From the time dependence of the current it appears that it flows only when the ejected material is filling the space between the point of ablation and the electrode, as would be expected.

The current-voltage (I - V) characteristics seen in Fig. 3 are typical for a gas-filled diode with the "forward" direction for conduction that is shown in the first quadrant being established when the plume is negative, and so able to function as a hot filament. The selection of either positive or negative voltages to give the same absolute values of current generally yielded very similar depositions on Si(100) substrates. Usually a value of 10 A was used. There was no particular sensitivity of the results to the placement of the collecting electrode, but no effect of the discharge current unless it passed through the small volume at the laser focus.

The characterization of such thin lossy films as produced in this work requires particular attention to the fact that ellipsometry, as customarily employed, does not give a unique result, when both real, n_0 and imaginary indices, n , are to be measured together with the thickness z . In our experiments, ellipsometry was used at 632.8 nm and reflectance spectroscopy was employed to obtain uniqueness. Measurements of reflectance spectra at normal incidence were fitted to the (book) expressions¹⁰ to give values of $(n_0 z)$ and (n_z/n_0) and with these a unique result could be obtained from the ellipsometry data.

Phenomenology was examined over a wide range of process variables. All experiments were conducted in an UHV environment operated around 10^{-6} Torr, as residual pressures seemed of little actual significance. The only variables of particular importance were the peak laser intensity in the ablation plume and the peak discharge current. Generally, lower current could be compensated by higher laser power. Consistent with this was the observation that cratering the graphite or defocusing the laser gave larger plumes and high-

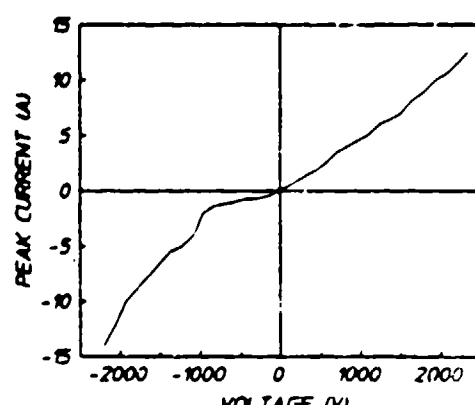


FIG. 3. Plot of the current and voltage characteristics of the diode formed by the graphite target and the electrode containing the conductive plasma ablated from the graphite by the laser.

er growth rates at the substrate but the resulting *a*-C film had much greater loss. Characteristics of films deposited at the lower power densities of Wagal,⁷ Richter,⁸ and Sato⁹ could not be plotted on the scale of Fig. 1(b).

Optical constants for a typical film prepared at 5×10^{11} W/cm² are plotted in Figs. 1(a) and 1(b). In each case the substrate was 5.5 cm from the laser plasma source and radial expansion of the ejected material produced a domed profile of thickness which could be appreciated by the visual appearance of bright Newton's rings of interference. Optical constants were measured to be consistent across the 20 cm² over which thickness varied from 0.1 to 0.2 μ m.

The laser pulse energies used here were not particularly different from those employed previously,⁷ but the power densities developed at the graphite feedstock were much greater in the present work. The fact that a smaller growth rate was observed supports the expectations that a tighter focus gives a higher temperature to a smaller amount of carbon material. This in turn strengthens the perception of Miyazawa⁴ that the carbon ions are the critical precursors of *sp*³ bonding, but refute his conclusion that the concurrent transport of electrons is detrimental. At these densities the ablated material must be traveling as largely neutral plasma. However, in agreement with Savvides¹ these results suggest that such sputtering techniques depending upon ion beam sources may be intrinsically limited by the inability to reach high-power densities at high enough values of fluence to be

practical. Losses indicate that the proportion of *sp*² bonding in our material is comparable to the best of Savvides' samples and can be reduced further with lasers of higher power that are commercially available. It is believed that this material can be reasonably described as amorphous diamond with 25% impurities and that the *sp*² inclusions serve no necessary role.

The authors gratefully acknowledge the contributions of R. K. Krause in arranging the deposition system. This work was supported by Innovative Science and Technology/Strategic Defense Initiative Organization and directed by the Naval Research Laboratory.

¹An excellent review can be found in J. C. Angus and C. C. Hayman, *Science* **241**, 913 (1988).

²F. G. Spencer, P. H. Schmidt, D. C. Joy, and F. J. Sensalone, *Appl. Phys. Lett.* **29**, 118 (1976).

³S. Aisenberg and R. Chabot, *J. Appl. Phys.* **53**, 2953 (1971).

⁴T. Miyazawa, S. Misawa, S. Yoshida, and S. Gonda, *J. Appl. Phys.* **55**, 188 (1984).

⁵N. Savvides and B. Window, *J. Vac. Sci. Technol. A* **3**, 2386 (1985).

⁶N. Savvides, *J. Appl. Phys.* **58**, 518 (1985); **59**, 4133 (1986).

⁷S. S. Wagal, E. M. Juengerman, and C. B. Collins, *Appl. Phys. Lett.* **53**, 187 (1988).

⁸A. Richter, H. J. Scheibe, W. Pompe, K. W. Brzezinka, and I. Muhling, *J. Non-Cryst. Solids* **88**, 131 (1986).

⁹T. Sato, S. Furuno, S. Iguchi, and M. Hanabusa, *Jpn. J. Appl. Phys.* **26**, L1487 (1987).

¹⁰M. Born and E. Wolf, *Principles of Optics*, 6th ed. (Pergamon, Oxford, 1980), Sec. 13.4.1.

Mössbauer isomer shift measurements without mechanical tuning

T. W. Sinor, P. W. Reittinger, and C. B. Collins

Center for Quantum Electronics, University of Texas at Dallas, P. O. Box 830688, Richardson, Texas 75083-0688

(Received 16 March 1989; accepted for publication 28 June 1989)

A technique is described which demonstrates how a frequency modulation spectrometer (FMS) can be used to measure the isomer shift of ferromagnetic absorbers without mechanical tuning. As an example, the isomer shift of an iron sample relative to a ^{57}Co source in a Pd matrix was measured and found to be $-(0.1869 \pm 0.003)$ mm/s compared to the literature value of $-(0.185 \pm 0.02)$ mm/s.

INTRODUCTION

The high Q of a Mössbauer resonance, approximately 10^{12} for ^{57}Fe , provides photons of well-defined energy in the keV range that are useful for probing phenomena involving very small changes of energies. In this way Mössbauer spectroscopy can provide a highly detailed account of the way in which the nucleus interacts with its environment. It is only through the existence of the Mössbauer effect that a practical source of narrow line radiation can be produced at these wavelengths, and with such a source very small changes in frequency can be measured.

With Mössbauer techniques there is sufficient frequency resolution that spectral changes produced by magnetic perturbations to the nucleus can be observed in the short wavelength limit where quantum effects are dominant. In particular the Mössbauer effect is ideally suited to the study of the interaction of the nucleus with a rapidly oscillating magnetic field. Mitin^{1,2} was the first to propose that Mössbauer transitions could be excited as part of a multiphoton interaction for nuclei immersed in intense radio-frequency fields. The earliest experiments investigating the influence of radio-frequency magnetic fields on Mössbauer transitions was reported by Perlow³ in 1968. In his experiment, Perlow subjected several ^{57}Co sources of the 14.4-keV transition of ^{57}Fe to intense magnetic fields oscillating at rf frequencies and was able to demonstrate the destruction of the Mössbauer hyperfine pattern by the action of the rf field. Later researchers⁴ soon found that when a ferromagnetic iron absorber was subjected to long wavelength photons of an alternating magnetic field with frequency Ω (MHz), the Mössbauer spectrum contained additional absorption lines, known as rf sidebands, at frequencies $\omega \pm n\Omega$ where ω is the frequency of the parent transition and $n = 1, 2, \dots$, but these were shown to be artifacts produced by spurious acoustic noise generated in the absorber. True sum and difference frequency lines were not found in Mössbauer spectra until much later.⁵⁻¹⁰ The origin of these tunable sidebands in multiphoton or nuclear phase modulation effects was established even more recently.¹¹⁻¹⁴

The frequency dependence of these rf sidebands provides the basis for development of a high resolution gamma-ray spectrometer which operates by modulating the cross section for the gamma-ray absorption. A prototype of this Frequency Modulation Spectrometer (FMS) was first de-

scribed¹⁰ by our laboratory in 1985 with subsequent refinements¹⁵ reported in 1988.

A FMS spectrum of ^{57}Fe provides a direct measurement of rf sideband positions and intensities without interference from the parent transitions. It does this by scanning the frequency of the probing sidebands¹⁵ as opposed to the shifting of the transition energy conventionally employed. In such a spectrum one can extrapolate information about the transitions between Zeeman split energy levels (parent transitions) and the nuclear isomer shift between the source and absorber. In particular, it provides a technique for accurately measuring the isomer shift directly in terms of frequency; a quantity which can be measured more precisely than the customary Doppler velocity.

The heart of the Frequency Modulation Spectrometer is, an Apple II + computer which serves as a Multichannel Scaler (MCS) and an IEEE-488 GPIB interface as shown in Fig. 1. The GPIB enables the spectrometer to sweep continuously through the frequencies of the rf magnetic field which is controlled by a Wavetek frequency synthesizer. A Mössbauer linear motor allows the frequency of the incident gamma rays to be biased by a constant Doppler shift, if desired. The spectrometer currently has an instrumental resolution of 100 Hz and a frequency range of 1 MHz-1 GHz with a stability of 0.1 Hz/s when used with a stationary source.

In Fig. 2(a) a conventional Mössbauer spectrum of ^{57}Fe showing the six allowed magnetic transitions is shown without external perturbation. Component lines are labeled 1 through 6 with the transition of lowest energy identified as number 1. In the spectrum of the same absorber subject to the excitation of rf sidebands as shown in Fig. 2(b), the sidebands have been labeled using the following nomenclature. The first digit corresponds to the order of the sideband n , with the second number corresponding to its particular parent transition, p . The sign of n indicates whether the sideband appears at a higher ($+n$) or lower ($-n$) energy than its parent transition. For example, $-1;5$ denotes the first order sideband displaced to lower energies from parent transition 5.

The parent transitions 1 and 6 of Fig. 2(a) are symmetric about the centroid of the resonance pattern and are separated by 123.68 MHz. The application of a 61.84 MHz alternating magnetic field to the ^{57}Fe absorber produces $+1;1$ and $-1;6$ sidebands which overlap at the center of the hyperfine structure of the Mössbauer spectrum. The energies of

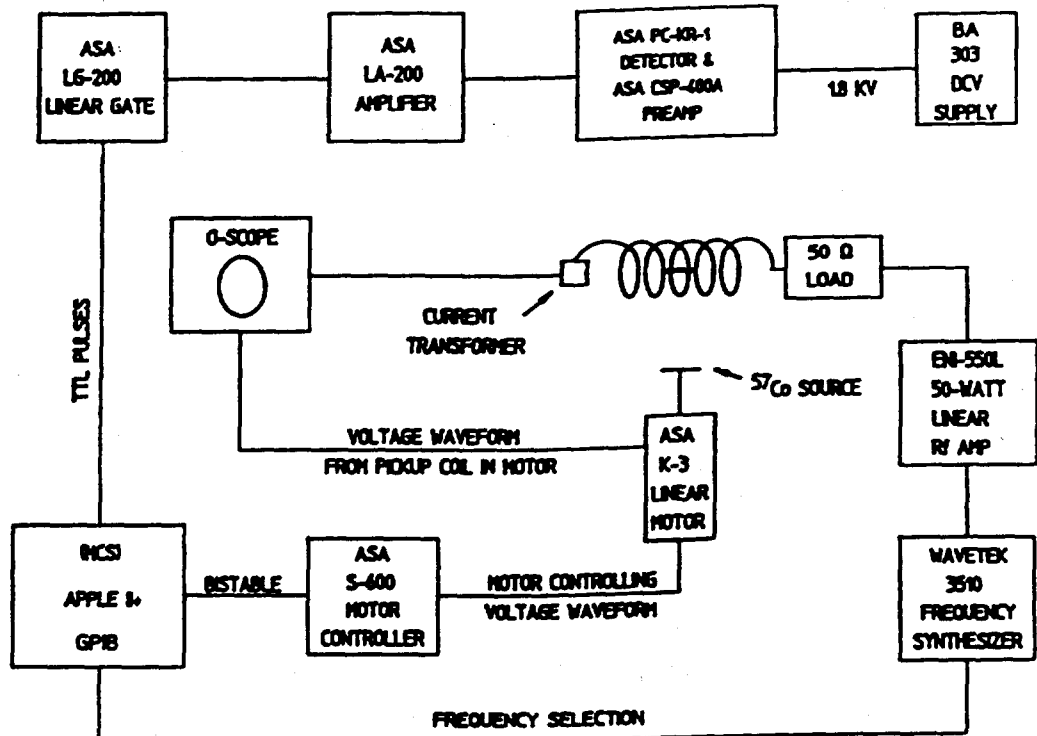


FIG. 1. Schematic representation of a frequency modulation spectrometer (FMS).

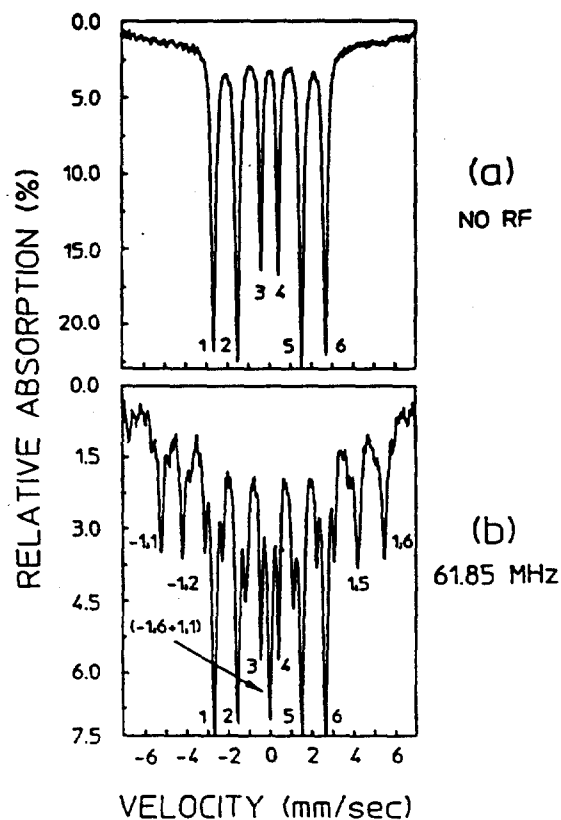


FIG. 2. (a) Mössbauer absorption spectrum of a 2.5- μm foil of iron isotopically enriched with 95.8% ^{57}Fe obtained with a ^{57}Co source in a Pd matrix. The six allowed magnetic dipole transitions are labeled 1 through 6 going from the lowest- to the highest-energy transition. (b) Spectrum of the same foil subjected to an oscillating radio-frequency field with a frequency of 61.85 MHz.

the incident gamma rays from the source will differ from the transition center of the absorber by the isomer shift, Δ . In a FMS spectrum the sidebands $+ 1;1$ would be observed at a frequency of $(61.85 - \Delta)$ MHz while the sideband $- 1;6$, would be detected at a frequency of $(61.85 + \Delta)$ MHz. Therefore, the FMS spectrum will produce two absorption peaks as shown in Fig. 3(a), around 62 MHz with a separation equal to twice the isomer shift, 2Δ . If the Mössbauer source is given a constant velocity Doppler shift, the FMS spectrum will show two peaks near 62 MHz, separated by $2(\Delta + \delta)$, where δ is the Doppler shift of the incident gamma rays. In this way very precise measurements of the nuclear isomer shift can be obtained using FMS. The accuracy of the measurement is dependent upon the resolution and stability of the signal generator used to produce the rf magnetic field and the quality of the curve fitting routine used to fit the data.

I. THEORY

In a Mössbauer absorption spectrum taken in the velocity domain the isomer shift appears as a displacement of the centroid of the resonance pattern from the nominal zero position. The isomer shift is the result of an electric monopole interaction between the Mössbauer nuclei and its surrounding electrons. More specifically, the excited and ground-state nuclei differ in radius by a small yet significant amount ($\Delta R / R = -0.8 \times 10^{-3}$ in ^{57}Fe). It is this change in the radius of the nucleus which causes the electrostatic interaction between the nucleus and its surrounding electrons to change upon excitation of the nucleus. Therefore, if the Mössbauer nuclei in the source and absorber are in different

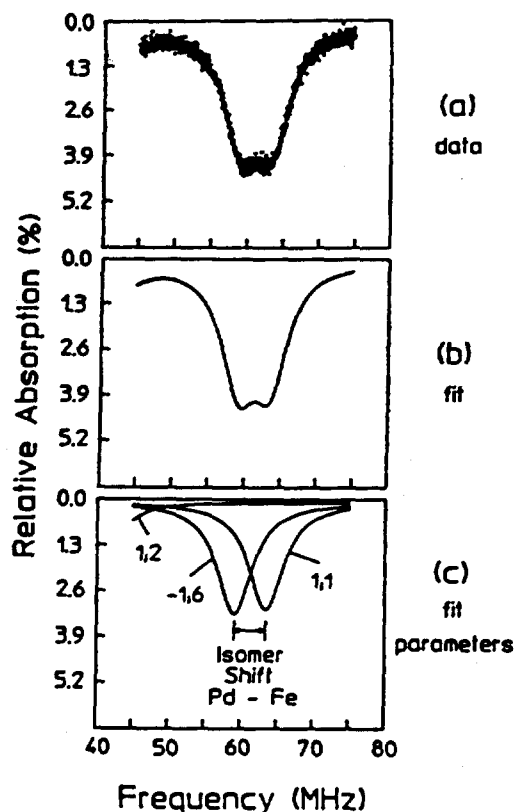


FIG. 3. (a) FMS spectrum of the same enriched foil. The two peaks represent sidebands +1;1 and -1;6. The separation of these peaks is equal to twice the isomer shift of an iron foil relative to a ^{57}Co source in Pd. (b) Spectrum constructed from fitting the data of Fig. (a) using the Levenberg-Marquardt method for a nonlinear least-squares fit. (c) Spectral components resulting from the fitting procedure shown before summation.

chemical environments such that different electronic distributions are experienced, the isomer shift has been shown to be¹⁶

$$\Delta = (4\pi c Z e^2 R^2 / 5E_\gamma) [\rho_s(0) - \rho_a(0)] (\Delta R / R) \text{ mm/s,} \quad (1)$$

where Z is the atomic number, e is the electronic charge, R is the effective nuclear radius, c is the velocity of light, $\rho_s(0)$ and $\rho_a(0)$ are the electronic charge densities at the nucleus for the source and absorber, and $\Delta R = R_{\text{excited}} - R_{\text{ground}}$.

In addition to the isomer shift displacement of the centroid of the resonance pattern there is also a temperature shift of the spectrum which arises due to time dilation resulting from the motions of the emitting and absorbing nuclei. This temperature shift is given by¹⁷

$$\delta E / E = C_p / 2c^2 \quad (2)$$

where C_p is the specific heat of the material and c is the velocity of light. At room temperature, for iron the above expression yields $\delta E / E = -2.21 \times 10^{-15} / ^\circ\text{C}$. The experimentally observed value¹⁸ is $-(2.09 \pm 0.24) \times 10^{-15} / ^\circ\text{C}$. In the work being reported here the source and absorber were at essentially the same temperature. Therefore, the temperature shift was considered negligible.

The frequency, f_n , at which sidebands appear in a FMS spectrum is given by

$$f_n = (v - P_i + \Delta)(K/n), \quad (3)$$

where v (mm/s) is the Doppler velocity of the source, P_i (mm/s) is the position of the i th parent transition, Δ (mm/s) is the isomer shift, K ($= 11.605 \text{ MHz/mm/s}$) is the conversion factor for the 14.4-keV gamma rays being detected and n is the order of the sideband of interest. Furthermore, it is known that the frequency displacement Ω of sidebands 1;1 and -1;6 is given by

$$\Omega(1;1) = \Omega(-1;6), \quad (4)$$

with respect to the center of the resonance pattern. Therefore, for a stationary source and absorber we have

$$\Omega(1;6) - \Omega(1;1) = |\Omega(P_6) + \Delta|$$

$$- |\Omega(P_1) + \Delta| = 2\Delta. \quad (5)$$

The absolute value of the Ω 's are used since Eq. (3) can result in a negative frequency. However, the sign of f_n is merely a convention to indicate whether the sideband has a lesser or greater energy than its parent transition. The sign convention used for isomer shift measurements is that a negative isomer shift indicates the source has a higher nuclear energy level than the absorber.

II. DATA AND DISCUSSION

The isomer shift between a ^{57}Co source in a Pd matrix relative to an iron foil absorber was measured using FMS and found to have a value of $-(0.1869 \pm 0.003) \text{ mm/s}$ compared to the literature value¹⁹ of $-(0.185 \pm 0.02) \text{ mm/s}$. The ^{57}Co source in a Pd matrix had an initial activity of 25.4 mCi and was purchased from New England Nuclear. The absorber was a $1.5 \text{ cm} \times 0.85 \text{ cm} \times 2.5 \mu\text{m}$ foil of iron isotopically enriched with 95.8% ^{57}Fe . The rf signal was produced by a Wavetek signal generator, Model 3520, which was equipped with an IEEE-488 GPIB interface to allow the frequency to be automatically scanned. The resolution and stability of this signal generator are those previously stated. The rf signal from the Wavetek was amplified by an ENI-5506 50db linear amplifier and this amplified signal was then used to drive an inductor in which the absorber was mounted. A five-turn flat coil was constructed as the field induction coil with a separation of 4.5 mm between turns and a cross-sectional area of 20 mm^2 . This led to a small inductance ($< 1 \mu\text{H}$) and a minimum capacitance between turns while producing a reasonable field intensity ($\sim 4\text{G}$) at 50 W. This inductor was then mounted in series with a $48\text{-}\Omega$ noninductive load to match the impedance of the amplifier output and cable. The result was a circuit having a reasonably broad band tunability and a Q of approximately one. The heat produced in the absorber by eddy currents was minimal for the rf powers employed. However, in critical measurements of the isomer shift using FMS, this minimal rf heating of the absorber can be eliminated by simultaneously pulsing the rf and directing a cool flow of nitrogen over the absorber.

The data from which the fitted parameters were obtained is shown in Fig. 3(a). The data was fit to seven parameters using the Levenberg-Marquardt method²⁰ for a nonlinear least squares fit. In the fitting procedure, it was assumed that the spectra were composed of three sidebands; the -1;6, +1;1, and -1;5. It was further assumed that

the sidebands had a uniform linewidth. Figure 3(b) shows the spectrum constructed from the fit parameters and Fig. 3(c) shows the spectral components before summation. The standard deviation of the fit parameters was obtained from the covariance matrix derived from the fitting procedure and are valid only with the assumption of normally distributed measurement error.

As can be seen from this example, FMS is a high-resolution Mössbauer technique which provides a direct measurement of rf sideband positions and intensities without interference from the parent transitions. Furthermore, from an FMS spectrum, information can be obtained without mechanical tuning about the linewidth or positions of Zeeman split energy levels in addition to accurate measurement of the nuclear isomer shift. Recently¹⁴ it has been demonstrated how to excite large-scale magnetic phase modulation effects in paramagnetic materials by exciting magnetostatic spin waves in the sample under study. With this refinement frequency modulation spectroscopy can now be extended to the study of paramagnetic materials. Then, FMS can provide a viable alternative for precision isomer shift measurements in a variety of environments.

ACKNOWLEDGMENTS

The authors acknowledge the support of this work by the Office of Naval Research and by the Innovative Science and Technology Directorate of the Strategic Defense Initia-

tive Organization with direction by the Naval Research Laboratory.

- ¹A. V. Mitin, *Zh. Eksp. Teor. Fiz.* **52**, 1596 (1967) [Sov. Phys. JETP **25**, 1062 (1967)].
- ²A. V. Mitin, *Dok. Akad. Nauk SSSR* **194**, 59 (1971) [Sov. Phys. Dokl. **15**, 827 (1971)].
- ³G. J. Perlow, *Phys. Rev.* **172**, 319 (1968).
- ⁴N. D. Heiman, L. Pfeiffer, and J. C. Walker, *Phys. Rev. Lett.* **21**, 93 (1968).
- ⁵P. J. West and E. Matthias, *Z. Phys. A* **288**, 369 (1978).
- ⁶O. Olariu, I. Popescu, and C. B. Collins, *Phys. Rev. C* **23**, 50 (1981).
- ⁷O. Olariu, I. Popescu, and C. B. Collins, *Phys. Rev. C* **23**, 1007 (1981).
- ⁸B. D. DePaola and C. B. Collins, *J. Opt. Soc. Am. B* **1**, 812 (1984).
- ⁹C. B. Collins and B. D. DePaola, *Opt. Lett.* **10**, 25 (1985).
- ¹⁰B. D. DePaola, S. S. Wagal, and C. B. Collins, *J. Opt. Soc. Am. B* **2**, 541 (1985).
- ¹¹T. W. Sinor, Ph.D. thesis, University of Texas at Dallas, 1988.
- ¹²E. Ikonen, P. Helistö, J. Hietanieni, and T. Katila, *Phys. Rev. Lett.* **60**, 643 (1988).
- ¹³E. Ikonen, J. Hietanieni, and T. Katila, *Phys. Rev. B* **38**, 6380 (1988).
- ¹⁴T. W. Sinor, P. W. Reittinger, and C. B. Collins, *Phys. Rev. Lett.* **62**, 2547 (1989).
- ¹⁵P. W. Reittinger, T. W. Sinor, S. S. Wagal, and C. B. Collins, *Rev. Sci. Instrum.* **59**, 362 (1988).
- ¹⁶See, for example, G. K. Shenoy and F. E. Wagner, Eds. *Mössbauer Isomer Shifts* (North-Holland, Amsterdam, 1978).
- ¹⁷B. D. Josephson, *Phys. Rev. Lett.* **4**, 341 (1960).
- ¹⁸R. V. Pound and G. A. Rebka, Jr., *Phys. Rev. Lett.* **4**, 274 (1960).
- ¹⁹A. H. Muir, Jr., K. J. Ando, and H. M. Coogan, *Mössbauer Effect Data Index, 1958-1965* (Wiley-Interscience, New York, 1966).
- ²⁰B. P. Flannery, S. A. Teukolsky, and W. T. Vetterling, *Numerical Recipes: The Art of Scientific Computing* (Cambridge University Press, Cambridge, 1985).

ACCELERATED DECAY OF $^{180}\text{Ta}^m$ AND ^{176}Lu IN STELLAR INTERIORS THROUGH (γ , γ') REACTIONS

J. J. CARROLL, J. A. ANDERSON, J. W. GLESENER, C. D. EBERHARD, AND C. B. COLLINS

University of Texas at Dallas, Center for Quantum Electronics

Received 1987 November 25; accepted 1989 February 13

ABSTRACT

It has been suggested that the long-lived nuclei $^{180}\text{Ta}^m$ and ^{176}Lu may be used as stellar *s*-process chronometers. However, the recent reports of large cross sections for the reactions $^{180}\text{Ta}^m(\gamma, \gamma')^{180}\text{Ta}$ and $^{176}\text{Lu}(\gamma, \gamma')^{176}\text{Lu}^m$ raise the concern that the evolution of these species may have been affected by the bath of thermal photons present at the *s*-process temperatures. The recent experimental results did not identify the energies at which the (γ, γ') reactions occurred, so in this work the effective half-lives of $^{180}\text{Ta}^m$ and ^{176}Lu in a stellar environment are calculated as a function of the possible energies of states mediating the resonance reactions. The time scales indicate that, unless these large "gateway" states lie at relatively high energies, the *s*-process cannot be effectively dated from the observed abundance of these nuclei.

Subject headings: nuclear reactions — nucleosynthesis

I. INTRODUCTION

The study of naturally occurring radioactive isotopes such as ^{176}Lu and ^{180}Ta has become increasingly important to the astrophysical community since these species have been envisioned as stellar chronometers. Provided the mechanisms of nucleosynthesis are sufficiently understood, the creation of these types of nuclei can be dated from their predicted initial abundance, their presently observed abundance and their half-lives.

The analysis for ^{176}Lu and ^{180}Ta is complicated by the fact that each possesses an isomer. In these cases stellar nucleosynthesis may branch to both the ground state and the isomer, providing a different initial population in each state than would result were only a single level present. This branching is critical to the observation of $^{180}\text{Ta}^m$, nature's rarest stable isotope (Cameron 1982), because the isomer ($T_{1/2} \geq 1.2 \times 10^{15}$ yr) is the surviving state rather than the shorter lived ground state ($T_{1/2} = 8.152$ hr).

The presence of an isomer produces an additional effect when the excited nucleus can undergo transmutation without first decaying radiatively to the ground state. If there is a sufficiently strong channel for the transfer of a population of nuclei between the ground state and the isomer, the effective half-lives of the states will be drastically different in the stellar environment than those measured in the laboratory. Processes which may provide such a channel include photoexcitation, positron annihilation excitation, inelastic neutron scattering, and Coulomb excitation. In particular, for ^{176}Lu and ^{180}Ta , photoexcitation through (γ, γ') reactions has been investigated.

Critical early works (Norman *et al.* 1984, 1985) described experiments in which samples containing naturally abundant lutetium and tantalum were irradiated with medical ^{137}Cs and ^{60}Co sources. Following exposure, the X-ray spectra of the samples were examined for signatures of the decays of $^{176}\text{Lu}^m$ and ^{180}Ta . No activation of the tantalum sample was in evidence, but some activation of the lutetium sample was observed. In order to calculate the reaction cross section for ^{176}Lu from the observed activation and to estimate an upper bound on the cross section for $^{180}\text{Ta}^m$, it was assumed that the reactions were nonresonant, threshold processes in keeping

with conclusions from previous experiments (Krcmar *et al.* 1981; Ljubicic, Fisk, and Logan 1982) on ^{115}In and ^{111}Cd . The irradiating spectrum was therefore integrated above the assumed threshold, and the large number of available photons resulted in the report of small values for the cross sections. The absence of larger cross sections was then used to imply the usefulness of ^{176}Lu and $^{180}\text{Ta}^m$ nuclei as stellar chronometers.

In contrast to earlier work, the most recent studies of the reactions $^{115}\text{In}(\gamma, \gamma')^{115}\text{In}^m$ and $^{111}\text{Cd}(\gamma, \gamma')^{111}\text{Cd}^m$ have shown no evidence for the appearance of nonresonant effects (Anderson, Byrd, and Collins 1988; Bikit *et al.* 1987; Collins *et al.* 1988a; Yoshihara *et al.* 1986). Instead it was reported that previous evidence for threshold processes could be attributed to departures of the experimental photon sources from expectations. Evidently (γ, γ') reactions proceed through relatively narrow resonant "gateway" levels rather than through nonresonant excitation. In this context, the most recent measurements (Anderson *et al.* 1988; Collins *et al.* 1988b) of the cross sections for the reactions $^{176}\text{Lu}(\gamma, \gamma')^{176}\text{Lu}^m$, and $^{180}\text{Ta}^m(\gamma, \gamma')^{180}\text{Ta}$ make possible a reevaluation of the degree to which these nuclei are useful as stellar chronometers.

II. EXPERIMENTAL DETAIL AND ANALYSIS

A set of experiments was performed by exposing lutetium and tantalum samples to the bremsstrahlung from a Varian Clinac 1800 medical linear accelerator operating in a 6 MeV mode. An enriched tantalum sample containing 1.3 mg of $^{180}\text{Ta}^m$ in 24.7 mg of ^{181}Ta was used. The tantalum was deposited as a dusting of oxide near the center of a 5 cm square plate of aluminum. This sample composition was chosen in order to minimize the self-absorption of fluorescent X-rays. Following irradiation, the sample was transported to an N-type HPGe spectrometer system for counting. As the ground and isomeric states of ^{180}Ta decay by β^- emission and electron capture as shown by the partial decay level diagram of Figure 1a, the 4096 channel pulse-height spectra contained X-ray peaks emitted from the daughter nucleus ^{180}Hf . The identities of the observed photopeaks were verified by their energies and counting rate decays. A typical spectrum for the tantalum sample showing the ^{180}Hf K_{α} and K_{β} peaks is given in Figure 2.

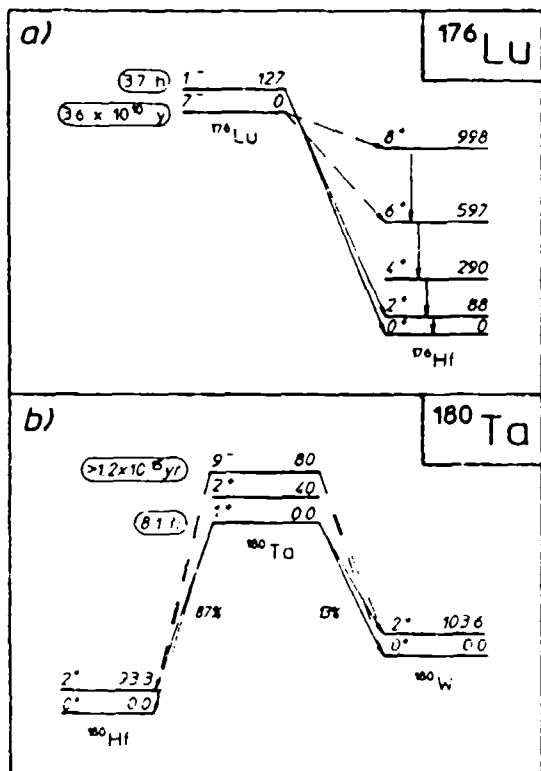


FIG. 1--Partial decay level diagrams of (a) ^{176}Lu and (b) ^{180}Ta depicting parent and daughter nuclei. Half-lives are shown in ovals to the left of the ground and isomeric levels. The nuclear spins, parities, and energies in keV of each state is given. Electron capture decays are shown by diagonal arrows on the left and β^+ decays are shown by diagonal arrows on the right of the parent levels.

Each lutetium sample consisted of approximately 5 g of LuCl_3 dissolved in distilled water to make about 20 ml of solution contained within a polyethylene scintillation bottle. The samples were fashioned in this way in order to employ an

alternate detection scheme which was better suited to the examination of ^{176}Lu . The ground state of ^{176}Lu β^- decays with an endpoint energy of 565 keV and the isomer with endpoint energies of 1313 keV (39.6%) and 1225 keV (60.4%), as depicted in the partial decay level diagram of Figure 1b. Since these nuclei were suspended in solution, the particles emitted in these decays produced Cerenkov radiation in the water with efficiencies dependent on the differences in the particle energies and the Cerenkov threshold energy at about 250 keV.

In these experiments the efficiency for production of Cerenkov radiation from isomeric decays was over 10 times larger than that from ground-state decays. This made possible an accurate measurement of the number of isomeric decays, and thus of isomeric production from the ground state, by counting the Cerenkov events with a detector consisting of two RCA 8850 photomultiplier tubes in EG & G 9201 bases. The tubes were operated in a coincidence mode by connecting the time synchronized outputs through a 150 MHz Phillips 755 logic unit. This ensured that only events detected in coincidence by both tubes were counted, improving the signal-to-noise ratio. Then, the number of coincident counts as a function of time was stored as a 4096 channel multichannel scalar spectra with a 40 s dwell time. A typical spectrum is shown in Figure 3. The counter was calibrated with a $^{40}\text{KCl}_3$ solution of known activity which emitted β^- particles having roughly the same endpoint energy as $^{176}\text{Lu}^m$.

The rate of excitation of nuclei, dN_{excited}/dt , was determined for each sample from the observed photopeak counts for the pulse-height spectra and from the decay of the counting rate for the coincidence spectra. These were corrected for self-absorption of fluorescent photons, detector efficiency, signature photon or β^- decay intensity, and finite times for counting, transport, and irradiation. From the viewpoint of photoexcitation through resonant gateways, the excitation rate is given by

$$\frac{dN_{\text{excited}}}{dt} = N_T \sum (\sigma \Gamma)_i \Phi(E_i), \quad (1)$$

where N_T is the number of target nuclei in the sample, $\Phi(E)$ is

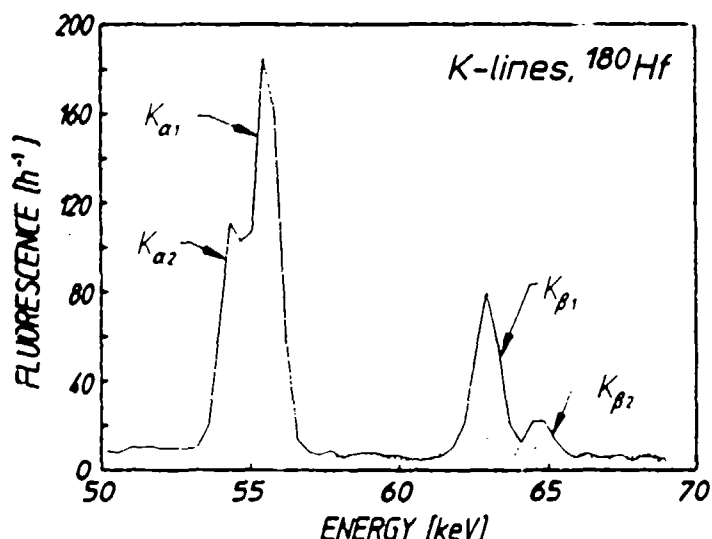


Fig. 2 - Dotted and solid curves show, respectively, the spectra obtained before and after irradiation of a tantalum sample containing ^{180}Ta enriched to 5%. An HPGe detector was used to obtain the spectra. The feature of 61 keV is due to traces of natural activity in the counting shield. The solid curve shows activity resulting from the transmutation of ^{180}Ta ground-state nuclei measured in the sample following irradiation. The prominent additions are the ^{180}Hf , K_α , and K_β X-ray lines resulting from electron capture in the ^{180}Ta .

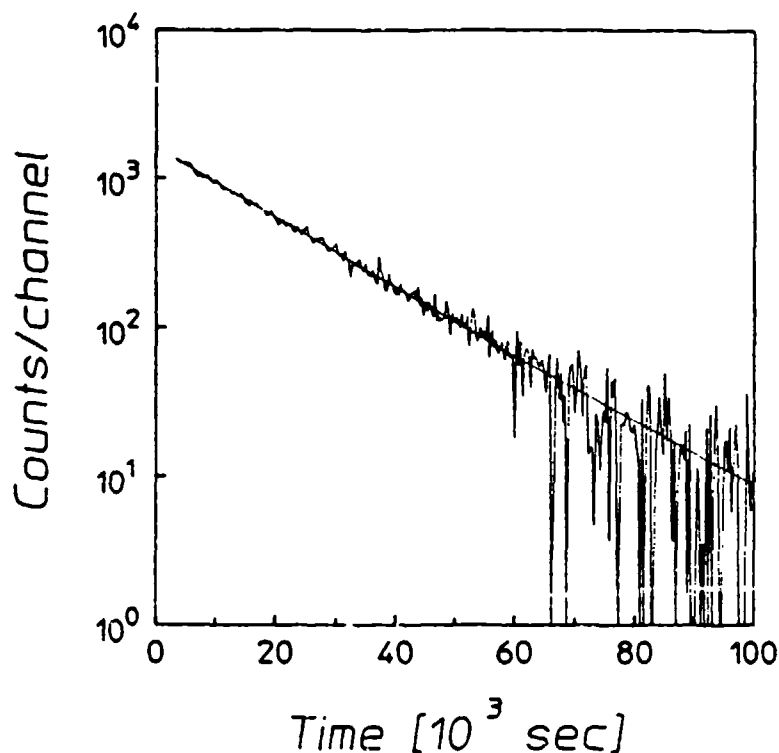


FIG. 3.—A typical decay spectrum from a lutetium sample following a 40 minute irradiation. Each channel represents an interval of 320 s. The solid line indicates a fit to the data which gives a half-life for ^{176}Lu of 3.58 ± 0.05 hr; the literature value is 3.68 hr.

the incident photon flux in photons $\text{cm}^{-2} \text{ keV}^{-1} \text{ s}^{-1}$ at the gateway energy E_i , and $(\sigma I)_i$ is the integrated cross section in $\text{cm}^2 \text{ keV}$,

$$(\sigma I)_i = \int \sigma_i(E) dE \quad (2)$$

The quantity Γ_i represents the natural width of the i th gateway state, given by $\Gamma_i \geq h/\tau_i$, where τ_i is the lifetime of the state. Determinations of the integrated cross sections depend primarily on knowledge of the E_i , since the output of the linac is well characterized (Ikoro, Johnson, and Antich 1987; Mohan, Chui, and Lidofsky 1985). The relative spectral intensity normalized to unit total flux for the linac operating in the 6 MeV mode is shown in Figure 4.

The fixed endpoint of the linac did not allow the gateways to be located. However, by assuming the excitation proceeds through a single gateway state, cross sections were found as functions of the possible gateway energies. Previous examinations (Dewberry *et al.* 1981; Warde *et al.* 1983; Wasson and Chrien 1970) of known nuclear states have indicated that the lowest likely gateway states lie at about 1 MeV for ^{176}Lu and about 750 keV for $^{180}\text{Ta}^m$. Consistent with these suggestions, the cross sections for ^{176}Lu and $^{180}\text{Ta}^m$ are shown in Figure 5. The gateway energies indicated by the data points are located at the centers of energy bins corresponding to mesh points at which intensities are available from published linac spectra.

It is difficult to directly compare the results of Figure 5 with the cross sections of Norman *et al.* (1984, 1985) since the irradiating spectra used in those experiments are not known. However, as a point of contact between the two approaches, for $^{180}\text{Ta}^m$ a single resonant gateway at 750 keV would correspond to an integrated cross section of $27,700 \times 10^{-29} \text{ cm}^2 \text{ keV}$, while a nonresonant process with a threshold at 750

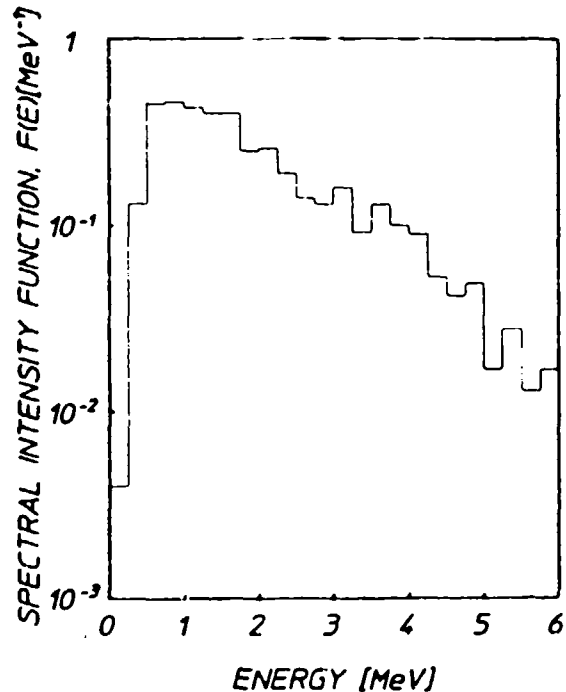


FIG. 4.—Relative spectral intensities of the bremsstrahlung from the Varian Clinac 1800 used in these experiments. The function $F[\text{MeV}^{-1}]$ is normalized to the total delivered flux, which for linac operation in the 6 MeV mode at 300 Hz is 2.28×10^7 photons $\text{cm}^{-2} \text{ s}^{-1}$ at a distance of 63.7 cm from the X-ray source.

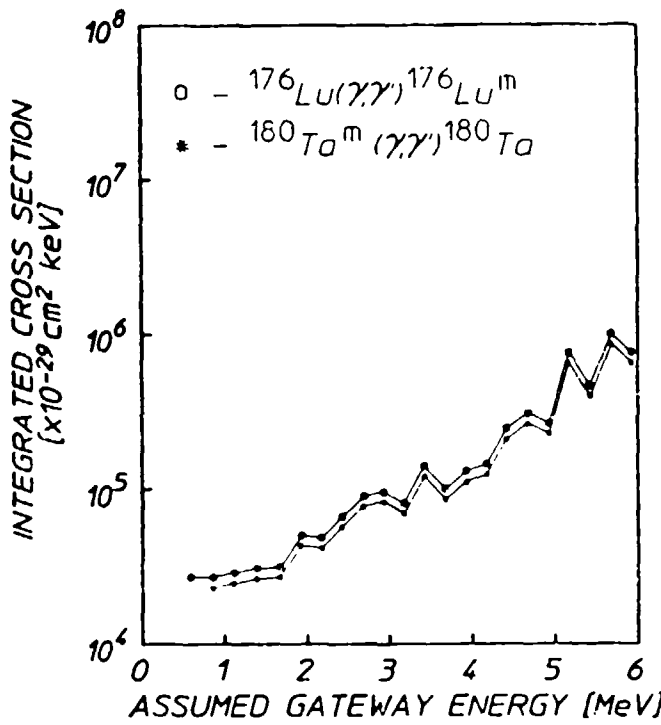


FIG. 5—Integrated cross sections for the reactions $^{176}\text{Lu}(\gamma, \gamma')^{176}\text{Lu}^m$ and $^{180}\text{Ta}^m(\gamma, \gamma')^{180}\text{Ta}$, each plotted as a function of the energies at which a single gateway state could be assumed.

keV would have a cross section of $148 \mu\text{barns}$. This is more than 3 orders of magnitude larger than the cross section reported in Norman (1984).

III. EFFECTIVE HALF-LIFE OF ^{176}Lu

The ground and isomeric states of ^{176}Lu can be considered to comprise two components of a coupled system of populations governed by the standard rate equations for radioactive decay. For the ground and metastable populations N_0 and N_1 , these are

$$\frac{dN_1}{dt} = -(R_1 + R_{10})N_1 + R_{01}N_0, \quad (3)$$

and

$$\frac{dN_0}{dt} = -(R_0 + R_{01})N_0 + R_{10}N_1. \quad (4)$$

The quantities R_0 and R_1 are the radioactive decay rates for these states, taken from laboratory values for the half-lives, $(T_{1/2})_0 \geq 3.59 \times 10^{10} \text{ yr}$ and $(T_{1/2})_1 = 3.635 \text{ hr}$. The R_{01} and R_{10} are the total transfer probability rates from ground to isomer and from isomer to ground states through (γ, γ') reactions.

The rate for excitation to the isomer through a single gateway is found by recognizing that $R_{01} = N_1^{-1} \times dN_{\text{excited}}/dt$, where N_T is the number of target nuclei. Equation (1) then gives

$$R_{01} = (\sigma_{01}\Gamma M E_{01}), \quad (5)$$

where E_{01} is the gateway energy relative to the ground state, and the width of the gateway has been assumed to be sufficiently narrow so that the flux may be considered as constant over

the gateway. Employing the Planck distribution to represent the stellar interior at temperature T ,

$$\Phi(E_{01}) = \frac{8\pi E_{01}^2}{h^3 c^2} [\exp(E_{01}/kT) + 1]^{-1}. \quad (6)$$

Thus, in terms of the experimentally measured integrated cross section,

$$R_{01} = \frac{8\pi}{h^3 c^2} (\sigma_{01}\Gamma) E_{01}^2 [\exp(E_{01}/kT) + 1]^{-1}. \quad (7)$$

The rate for the inverse reaction is found by considering the question of thermal equilibrium. If it were possible for both states to come into equilibrium with the photon bath, the net photoexcitation rate would vanish,

$$\left(\frac{dN_1}{dt} + R_1 N_1 \right)_{\text{eq}} = 0. \quad (8)$$

This indicates that as a function of the ground and isomeric state angular momenta J_0 and J_1 and the energy of the isomer relative to the ground state, E_1 , the ratio of populations would become

$$\left(\frac{N_1}{N_0} \right)_{\text{eq}} = \frac{R_{01}}{R_{10}} = \frac{2J_1 + 1}{2J_0 + 1} \exp(-E_1/kT). \quad (9)$$

For the ^{176}Lu isotope, $J_0 = 7$, $J_1 = 1$, and the isomer energy is $E_1 = 126 \text{ keV}$. Then, the solution to the rate equations (3) and (4) is given by

$$\frac{N_1}{N_0}(t) = \frac{a + b \coth(bt/2)}{2R_{10}}, \quad (10)$$

where

$$a = R_0 + R_{01} - R_1 - R_{10},$$

and

$$b = \sqrt{a^2 + 4R_{01}R_{10}}.$$

The effective half-life of ^{176}Lu nuclei in the stellar environment is finally evaluated for this two-level system from the expression,

$$(T_{1/2})_{\text{eff}} = \left\{ 1 + \frac{N_0}{N_1} [(T_{1/2})_1] \right\} (T_{1/2})_1. \quad (11)$$

Figure 6 shows the effective half-life as a function of temperature for several assumed gateway energies.

IV. EFFECTIVE HALF-LIFE OF ^{180}Ta

The possibility of decay of ^{180}Ta nuclei by electron capture introduces an additional temperature dependence. The half-life of the isomer is so long that an accurate result can be obtained by considering it to be temperature independent. However, the depletion of its electron shells at stellar temperatures will appreciably alter the half-life of the ground state. Detailed calculations of this effect have been made (Takahashi and Yokoi 1987), but the nuclear data that were used are now dated. Considering the simpler problem of the depletion of the K shell only, the ground-state half-life may be written as (Stromgren 1932)

$$(T_{1/2})_0 = [(T_{1/2})_{0\text{lab}} [b_{\alpha} R(T) + b_{\beta}]]^{-1}, \quad (12)$$

where $b_{\alpha} = 0.87$ and $b_{\beta} = 0.13$ are the branching ratios for the

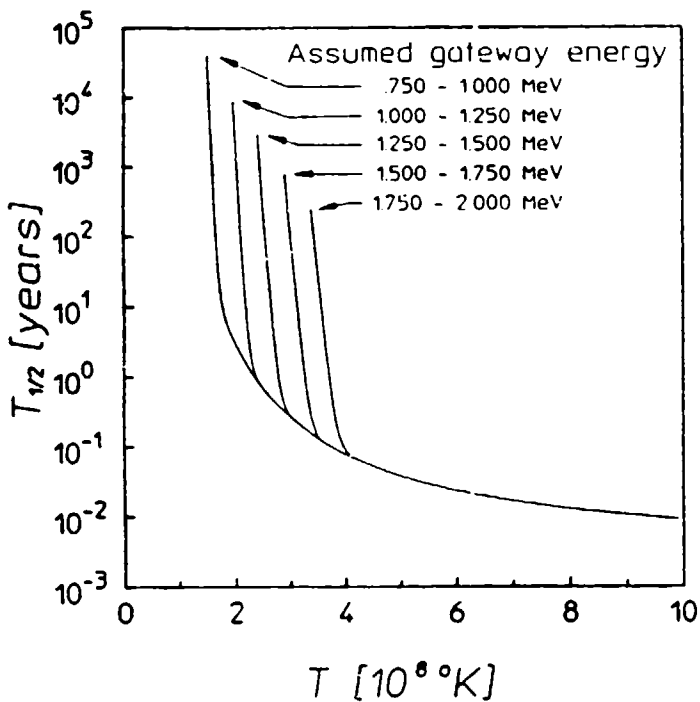


FIG. 6.—Effective half-life of ^{176}Lu nuclei as a function of the temperature of the stellar environment in which it is immersed. The different curves are parameterized by the energies of several assumed gateway states which lie within the indicated energy ranges.

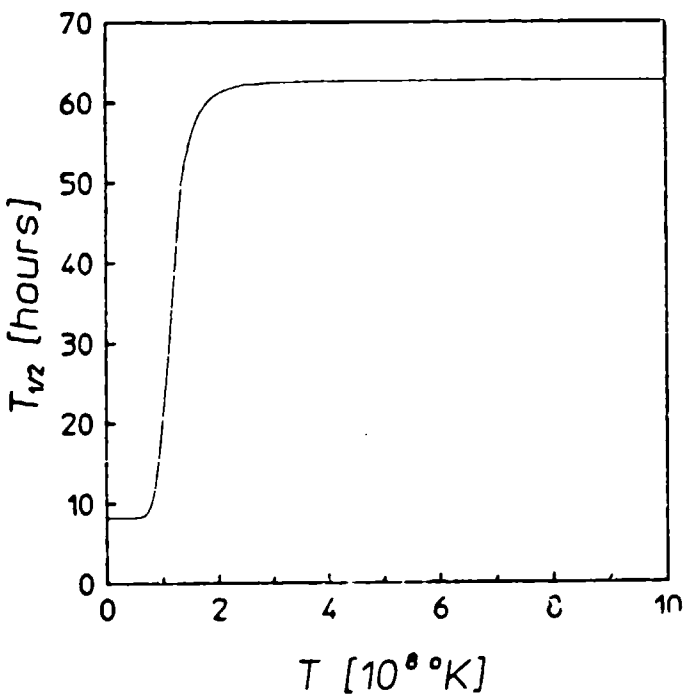


FIG. 7

FIG. 7.—Half-life of ground state nuclei of ^{176}Ta as a function of temperature in the surrounding stellar environment. At temperatures above 2×10^8 K, the K shell is completely depleted and the nuclei decay only through β^- emission.

FIG. 8.—Effective half-life of ^{180}Ta nuclei as a function of the temperature of the stellar environment in which it is immersed. The different curves are parameterized by the energies of several assumed gateway states which lie within the indicated energy ranges.

two decay modes. The ratio $r(T)$ of K shell occupancy at T to that as $T \rightarrow 0$ is given by

$$r(T) = [\exp(\mu - E_K/kT) + 1]^{-1}, \quad (13)$$

where $E_K = 67.416$ keV is the K shell energy and μ is the fermion chemical potential.

$$e^\mu = \frac{2}{h^3 N_e} (2\pi m_e kT)^{3/2}, \quad (14)$$

where N_e is the number density of electrons in pure He stellar matter, for which a typical value of 10^3 g cm^{-3} is taken and m_e is the electron mass. The half-life of the ^{180}Ta ground state as a function of temperature is given in Figure 7.

With the inclusion of this mechanism, the previous analysis is used to determine the half-life of ^{180}Ta for which $J_0 = 1$, $J_1 = 9$, and $E_1 = 180$ keV from

$$(T_{1/2})_{\text{eff}} = \left\{ 1 + \frac{N_1}{N_0} (T_{1/2})_0 \right\} (T_{1/2})_0. \quad (15)$$

These results are displayed in Figure 8.

V. DISCUSSION

An origin which is strictly s-process in character has been proposed (Arnould 1973; Audouze, Fowler, and Schramm 1972) for ^{176}Lu and the appropriate neutron capture chain has been examined (Allen, Lowenthal, and de Laeter 1981; Beier *et al.* 1981). This isotope is shielded from the r-process by ^{176}Yb , which is stable against β^- decay. The s-process of stellar

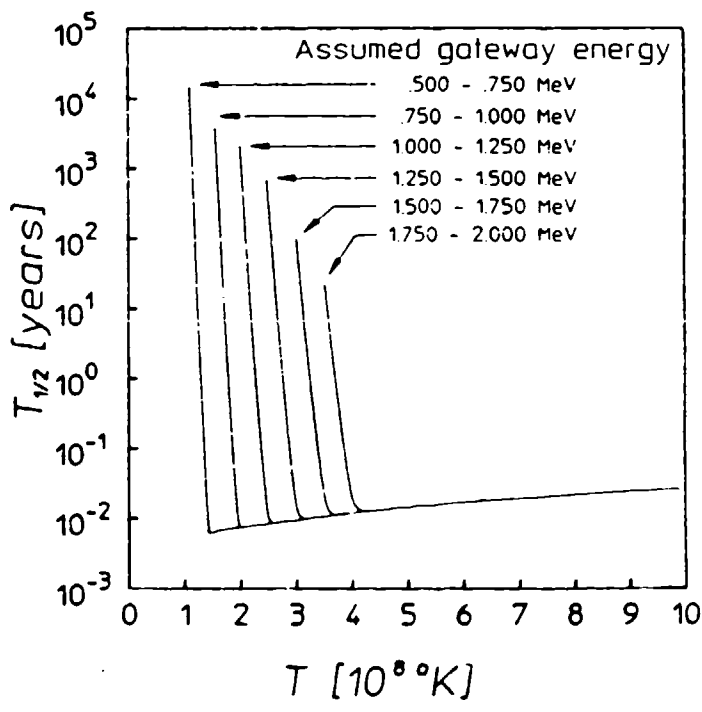


FIG. 8

nucleosynthesis is thought to require temperatures (Normal *et al.* 1984) of around 3.5×10^8 K and to occur primarily in stable red giants (Audouze and Vauclair 1979), possibly during thermal relaxation oscillations (Rose 1973). Examination of Figure 6 indicates that at this temperature at least partial equilibration of the ground state and isomer of ^{176}Lu will occur unless the gateway is located at an energy above about 1.5 MeV. Should the gateway lie within the 1–1.25 MeV range as has been suggested, an *s*-process origin may still apply. However, the strong temperature dependence of the half-life would render ^{176}Lu useless as an *s*-process chronometer.

Many mechanisms have been suggested to be responsible for the production of ^{180}Ta , although none has been firmly established (Audouze 1970; Hainebach, Schramm, and Blake 1976). Recently an *s*-process origin for ^{180}Ta has been suggested (Beer and Warde 1981; Yokoi and Takahashi 1983) and the necessary reactions demonstrated (Kellogg and Norman 1985). The rarity of $^{180}\text{Ta}^m$ was concluded to be a consequence of the fact that this nucleus lies aside the main path of cosmic nucleosynthesis (Runte *et al.* 1987). Figure 8 clearly shows again that equilibrium will occur at the canonical *s*-process temperature of 3.5×10^8 K unless the gateway lies above 1.5 MeV. The discovery of a gateway lying below 1.5 MeV would then imply

that ^{180}Ta could not be employed as an *s*-process chronometer. This could be avoided only if the *s*-process can proceed at temperatures below 1.5×10^8 K.

These interesting results point to the importance of locating the participating gateways more precisely. This could be accomplished if a variable endpoint linac were available that was capable of delivering sufficient dosage. Indeed, should multiple gateways be found below 6 MeV the results of this analysis may be drastically altered. Also of importance is the more manageable problem of determining the linac spectrum for smaller bin sizes. Each curve in Figures 6 and 8 must represent a range in possible gateway locations rather than simply one gateway energy. Smaller bin sizes would enable more exact examination of the temperatures at which equilibration becomes important for given gateway locations.

This work was supported through the Innovative Science and Technology Directorate of the Strategic Defense Initiative. It was administered by the Naval Research Laboratory. We thank P. P. Antich and E. C. Scarbrough, our colleagues at the University of Texas Southwestern Medical Center, for their help in irradiating the samples on the UTSMC linac facility.

REFERENCES

Allen, B. J., Lowenthal, G. C., and de Laeter, J. R. 1981, *J. Phys. G*, **7**, 1271.
 Anderson, J. A., Byrd, M. J., and Collins, C. B. 1988, *Phys. Rev. C*, **38**, 2838.
 Anderson, J. A., Taylor, K. N., Carroll, J. J., Byrd, M. J., Collins, C. B., Scarbrough, E. C., and Antich, P. P. 1988, Center for Quantum Electronics Report No. GRL/8803, University of Texas at Dallas, unpublished.
 Arnould, M. 1973, *Astr. Ap.*, **22**, 311.
 Audouze, J. 1970, *Ast. Ap.*, **8**, 436.
 Audouze, J., Fowler, W. A., and Schramm, D. N. 1972, *Nature*, **238**, 8.
 Audouze, J. and Vauclair, S. 1979, *An Introduction to Nuclear Astrophysics* (Boston: Reidel).
 Beer, H., Kappeler, F., Wissak, K., and Ward, R. A. 1981, *Ap. J. Suppl.*, **46**, 295.
 Beer, H. and Ward, R. A. 1981, *Nature*, **291**, 308.
 Bikit, I., Slivka, J., Anicin, I. V., Marinkov, L., Rudic, A., and Hamilton, W. D. 1987, *Phys. Rev. C*, **35**, 1943.
 Cameron, A. G. W. 1982, in *Essays in Nuclear Astrophysics*, ed. C. A. Barnes, D. D. Clayton, and D. N. Schramm (Cambridge: Cambridge University Press), p. 23.
 Collins, C. B., Anderson, J. A., Paiss, Y., Eberhard, C. D., Peterson, R. J., and Hodge, W. L. 1988a, *Phys. Rev. C*, **38**, 1852.
 Collins, C. B., Eberhard, C. D., Giesener, J. W., and Anderson, J. A. 1988b, *Phys. Rev. C*, **37**, 2267.
 Dewberry, R. A., Sheline, R. K., Lanier, R. G., Mann, L. G., and Struble, G. L. 1981, *Phys. Rev. C*, **24**, 1628.
 Hainebach, K. L., Schramm, D. N., and Blake, J. B. 1976, *Ap. J.*, **205**, 920.
 Ikoro, N. C., Johnson, D. A., and Antich, P. P. 1987, *Med. Phys.*, **14**, 93.
 Kellogg, S. E., and Norman, E. B. 1985, *Phys. Rev. C*, **31**, 1505.
 Krcmar, M., Ljubicic, A., Pisk, K., Logan, B., and Vrtar, M. 1981, *Phys. Rev. C*, **25**, 2097.
 Ljubicic, A., Pisk, K., and Logan, B. A. 1982, *Phys. Rev. C*, **23**, 2238.
 Mohan, R., Chui, C., and Lidosky, L. 1985, *Med. Phys.*, **12**, 595.
 Norman, E. B., Bertram, T., Kellogg, S. E., Gil, S., and Wong, P. 1985, *Ap. J.*, **291**, 834.
 Norman, E. B., Kellogg, S. E., Bertram, T., Gil, S., and Wong, P. 1984, *Ap. J.*, **281**, 360.
 Rose, W. K. 1973, *Astrophysics* (New York: Holt, Rinehart, and Winston).
 Runte, E., Schmidt-Ott, W. D., Eschner, W., Rosner, I., Kirchner, R., Klepper, O., and Rykaczewski, K. 1987, *Z. Phys. A*, **328**, 119.
 Strömgren, B. 1932, *Zeits. für Ap.*, **4**, 118.
 Takahashi, K., and Yokoi, K. 1987, *At. Data and Nuc. Data Tables*, **36**, 375.
 Warde, E., Seltz, R., Costa, G. J., Magnac, D., and Gerardin, C. 1983, *Phys. Rev. C*, **27**, 98.
 Wasson, O. A., and Chrien, R. E. 1970, *Phys. Rev. C*, **2**, 675.
 Yokoi, K., and Takahashi, K. 1983, *Nature*, **305**, 198.
 Yoshihara, K., Nemeth, Zs., Lakosi, L., Pavlicsek, I., and Veres, A. 1986, *Phys. Rev. C*, **33**, 728.

J. A. ANDERSON, J. J. CARROLL, C. B. COLLINS, C. D. EBERHARD, and J. W. GLESENER: University of Texas at Dallas, Center for Quantum Electronics, P.O. Box 830688, Richardson, TX 75083-0688

Center for Quantum Electronics
The University of Texas at Dallas
P.O. Box 830888, MS NB11
Richardson, Texas 75083-0688
(214) 690-2863
An Equal Opportunity/Affirmative Action University